Structural Geological Controls And Timing Of Ag-Pb-Zn Mineralisation At The Keno Hill Deposit, Yukon

by

Simon David Craggs

B.Sc. University of Leeds, 2004

M.Sc. University of New Brunswick, 2008

A Dissertation Submitted in Partial Fulfillment
of the Requirements for the Degree of

Doctor of Philosophy

in the Graduate Academic Unit of Earth Sciences

Supervisor: David R. Lentz, Ph.D., Departrment of Earth Sciences
Joseph C. White, Ph.D., Department of Earth Sciences

Examining Board: John A. Kershaw, Ph.D., Faculty of Forestry and Environmental Management
Adrian Park, Ph.D., Natural Resources and Energy Development New Brunswick
Chris R. M. McFarlane, Ph.D. Department of Earth Sciences

External Examiner: Stephen T. Johnston, Ph.D. Department of Earth and Atmospheric Sciences, University of Alberta

This dissertation is accepted by the
Dean of Graduate Studies

THE UNIVERSITY OF NEW BRUNSWICK

March, 2022

©Simon David Craggs, 2022

ABSTRACT

The structural history of the Keno Hill district is comprised of three discrete phases of deformation that record the ductile to brittle-ductile deformation, exhumation, and subsequent brittle deformation of the Keno Hill district between at least the Early Cretaceous (likely Late Jurassic) and the Eocene. Pre-Ag-Pb-Zn-mineralisation, D_1 deformation is characterised by ductile to brittle-ductile structural elements and is associated with greenschist facies metamorphism. Syn-Ag-Pb-Zn-mineralisation, D_2 deformation is characterised by ENE-striking, sinistral strike-slip faults, and NE- to NNE-striking, sinistral-normal oblique-slip linking faults that developed in a regional sinistral strike-slip fault system. Ag-Pb-Zn mineralisation is associated with fault dilation along NE- to NNE-striking fault segments with additional high-grade zones at D_2 fault intersections. Post-Ag-Pb-Zn-mineralisation, D_3 deformation is characterised by unmineralised SE-striking faults that are associated with development of the Cenozoic Tintina Fault.

Ag-Pb-Zn-mineralisation occurred coevally with D_2 fault propagation, and mineralisation is primarily controlled by the complex interplay between fault geometry and orientation, and the rheological contrast between varying rock types in the district. F_1 fold and thrust repetition thickened units prior to D_2 fault propagation and provided a larger volume of preferential host rock that focussed brittle deformation and localised economic Ag-Pb-Zn deposits. $^{40}Ar/^{39}Ar$ (sericite) geochronological data from D_2 associated rocks produce two sets of dates at circa 81 to 78 Ma and circa 69 Ma, respectively. These represent mica

growth during the Ag-Pb-Zn-mineralising event, and a subsequent hydrothermal overprinting event.

Airborne magnetic data indicates that the Keno Hill district is located within a left-stepping, releasing bend of a major sinistral strike-slip fault system. Palinspastic restoration of remote sensing data to its position pre-Tintina fault movement indicates the presence of a through-going ENE-trending, lineament that extends east of the Selwyn Basin margin. The lineament is coincident with, and may indicate a structural link between numerous deposits, including the Keno Hill, and the Fort Knox IGRS deposits.

DEDICATION

For my parents, Lindsay, and Isabel. Thanks for your belief and patience. Dad, I wish you could've seen this.

ACKNOWLEDGEMENTS

Thesis writing is commonly a lonely process and requires the support of a vast number of people. This thesis has taken over a decade to complete and could not have been written without the support and patience of my supervisors Dr. Dave Lentz and Dr. Joe White. Thanks are conveyed to all at UNB, in particular Dr. Chris MacFarlane for his review and advice on the geochronology sections of this thesis, and Dr. Adrian Park, Dr. Donovan Blissett, and Dr. Hubert Mvondo for their advice and lively discussions.

Alexco Resource Corp. provided financial and logistical support, and data for the project. Special thanks are given to Al McOnie, Stan Dodd, and Seymour Isles, with thanks also given to my field assistants Kathleen Gould, Natasha Morris, Linette MacInnis, Jared Chipman, Travis Murphy, Kristin Chislett, Genevieve Gay, Tim Hall, Karen Anderson, and Stephanie Nicholls. Additionally, Melanie Roberts, Dick Lippoth, Mike Burke, Rick Dutka, Bruce Otto, and Peter Read are thanked for their support, and discussion. Metallic Minerals Corp. are thanked for allowing me to include their data in my analysis, in particular Scott Petsel, Bill Harris, Greg Johnson, and Debbie James.

The Yukon Geological Survey provided financial and logistical support with special thanks conveyed to Don Murphy, Maurice Colpron, and Venessa Bennett for their insight and frequent, lively debates. Jim Ryan and Nathan Hayward at Natural Resources Canada are thanked for providing me with a new perspective on my data.

Samples were prepared by Calvin Nash, Ansell Murphy, and Carlin Lentz. Dr. Doug Hall and Suporn Boonsue provided assistance during SEM analysis, and Ven Reddy provided assistance during XRD analysis. XRF analysis was conducted by the Earth Resources Research and Analysis Facility (TERRA) at Memorial University Newfoundland. U-Pb CA-TIMS analysis was completed by Dr. Richard Friedman at the University of British Columbia, and $^{40}Ar/^{39}Ar$ analysis was completed by Dr. Doug Archibald at Queens University.

My current employers, SRK Consulting (Canada) Inc., have shown great patience throughout the thesis writing process. In particular, Dr. James Siddorn, Blair Hrabi, Anna Fonseca, Matt Grimshaw, and Jos Hantelmann have provided encouragement, and invaluable insight into all aspects of this thesis.

Finally, the greatest thanks are given to my family and friends, without whom none of this would have been possible. My mother, father, and sister were a constant source of encouragement and belief; I will be forever in their debt. Dad, I wish you could be here to see this. To Lindsay, and my daughter, Isabel, your patience and support has been unbelievable, without you I would have given up years ago.

Table of Contents

ABSTRACT ii
DEDICATION iv
ACKNOWLEDGEMENTS v
Table of Contents vii
List of Tables xi
List of Figures xiii
List of Symbols, Nomenclature or Abbreviations xxvii
1. Introduction 1
1.1 Rationale 3
1.2 Objectives and Scope of Work 5
1.3 Significance 7
1.4 Thesis Structure 9
1.5 Location and Access 12
2. Geological Setting 14
2.1 Tectonic Assembly of the North American Cordillera 14
2.1.1 Tectonic Realms 19
2.1.2 Late Proterozoic to Late Triassic Cordilleran (Passive Margin) Tectonics 21
2.1.3 Late Triassic to Middle Cretaceous Cordilleran (Terrane Accretion) Tectonics 23
2.1.4 Late Cretaceous to Eocene Tectonics – The Baja BC Controversy 30
2.2 Geology of the Selwyn Basin 39
2.2.1 Metasedimentary Rocks 41
2.2.2 Intrusive rocks 47

2.2.3 Structure and Tectonics 52

2.3 Geology of the Keno Hill District 55

2.3.1 Metasedimentary Rocks 57

2.3.2 Intrusive Rocks 62

2.3.3 Structure 64

3. Methodology 69
3.1 Field Data Collection 69

3.1.1 Statistical Analysis of Field Data 77

3.2 Additional Available Data 77

3.3 Two-dimensional (2D) Analysis 79

3.4 Three-dimensional (3D) Analysis 87

3.5 Laboratory Analytical Techniques 90

3.5.1 Optical and Scanning Electron Microscopy 91

3.5.2 Geochemical Analysis 92

3.6 Geochronology 94

3.6.1 $^{40}Ar/^{39}Ar$ Analytical Methodology 95

3.6.2 U-Pb Analysis 95

4. Field- and laboratory-based descriptions of lithological units, and associated geometric relationships 97
4.1 Metasedimentary Units 100

4.1.1 Yusezyu Formation - Hyland Group 100

4.1.2 Earn Group 100

4.1.3 Keno Hill Quartzite 104

4.2 Intrusive Rocks 118

4.2.1 Metamafic Intrusive Rocks 118

4.2.2 Mid-Cretaceous Intrusive Rocks 133

4.2.3 Lamprophyre 134

5. Structural Geology of the Keno Hill District 135
5.1 Structural Elements of Deformation 137

5.1.1 A Note on Fault Age and Order Nomenclature 137

5.1.2 Pre-Ag-Pb-Zn-Mineralisation (D_1) 139

5.1.3 Syn-Ag-Pb-Zn-Mineralisation (D_2) 165

5.1.4 Post-Ag-Pb-Zn-Mineralisation (D_3) 195

5.2 2D and 3D Interpretation of Structural Geology 203

5.2.1 District-Scale Interpretation of Airborne Magnetic Data 203

5.2.2 Regional-Scale Interpretation of Airborne Magnetic Data 214

5.2.3 District-Scale Interpretation of Digital Elevation (DEM) Data 217

5.2.4 2D Vein Geometry 220

5.2.5 3D Vein Geometry 224

6. Geochronological Analysis 232
6.1 Previous Geochronological Studies in the Keno Hill District and Surrounding Area 232

6.2 Sampling for the Geochronological Study 234

6.3 Sample Descriptions and Results 237

6.3.1 $^{40}Ar/^{39}Ar$ Analysis 237

6.3.2 U-Pb CA-TIMS Analysis 252

6.4 Summary and Discussion of Geochronology Analysis 254

7. Discussion 258
7.1 Controls on Ag-Pb-Zn-Mineralisation 260

7.2 Deformation Phases 262

7.2.1 Pre-Ag-Pb-Zn-Mineralisation Structural Elements and Associated Tectonism 262

7.2.2 Syn-Ag-Pb-Zn-Mineralisation Structural Elements and Associated Tectonism 264

7.2.3 Post-Ag-Pb-Zn-Mineralisation Structural Elements and Associated Tectonism 273

7.3 Post-Ag-Pb-Zn-Mineralisation Transport and its Impact on Regional Prospectivity 275

7.3.1 Palinspastic Restoration of the Tintina Fault 276

7.4 Potential Precambrian Control on Mesozoic Mineralisation 283

8. Conclusions 292
8.1 Deformation in the Keno Hill District 292

8.2 Structural Controls and Timing of Ag-Pb-Zn-Mineralisation 295

Bibliography 303

Appendix 324

Curriculum Vitae

List of Tables

Table 1.1: Keno Hill Camp. Total recorded production - 1913 to 1990 (listed in order of decreasing Ag ounces (Modified after Cathro, 2006). 2

Table 1.2: The main factors influencing the geometry of precious and base metal lode deposits (modified after Robert et al., 1994). 4

Table 2.1: Summary of estimated northward displacement of outboard terranes based on paleomagnetic data, listed in chronological order of publication date. 33

Table 2.2: Correlative geological elements offset by the Tintina Fault summarised from Gabrielse et al. (2006) and references therein. 38

Table 3.1: Collar locations and initial orientations of logged boreholes. All values rounded to nearest whole number; collar co-ordinate datum is NAD83 UTM Zone 8N. 75

Table 3.2: Fault definitions, characteristics, and kinematics 86

Table 5.1: Characteristics of deformation events in the Keno Hill district. 136

Table 5.2: Criteria for field characterisation of fault order. 138

Table 5.3: Characteristics of faults defined in the interpretation of airborne magnetic data 205

Table 6.1: Summary of geochronology studies within 50 km of Keno Hill district (data from Breitsprecher and Mortensen, 2004). 235

Table 6.2: Summary of $^{40}Ar/^{39}Ar$ dates for sample K-ON-003. 239

Table 6.3: Summary of $^{40}Ar/^{39}Ar$ dates for sample K-ON-004. 241

Table 6.4: Summary of $^{40}Ar/^{39}Ar$ dates for sample 187-005. 244

Table 6.5: Summary of $^{40}Ar/^{39}Ar$ dates for sample U0160-009. 247

Table 6.6: Summary of $^{40}Ar/^{39}Ar$ dates for sample K-BX-007. 249

Table 6.7: U-Pb isotopic ages for sample K-KH-003 253

List of Figures

Figure 1.1: Regional geology of the northern Cordillera in Yukon, British Columbia, and eastern Alaska (Modified after Mair et al., 2006)..... 3

Figure 1.2: Locations of selected mines and deposits in the Keno Hill district overlain on five metre resolution digital elevation model. 7

Figure 1.3: Shaded relief image of the Yukon showing location of Keno Hill, selected municipalities, and the major road network. Inset map of NW North America. 13

Figure 2.1: Regional geology of the northern Cordillera in the Yukon Territory, British Columbia, and eastern Alaska. Modified from Mair et al. (2006). 15

Figure 2.2: Position of the Cordilleran orogen of western North America along the Circum-Pacific orogenic belt. 16

Figure 2.3: Sequential east-west cross-sections through Canada, summarising the changes in the plate-tectonic regime during the Phanerozoic. Modified from Miall and Blakey (2019). 17

Figure 2.4: Map showing framework of terranes in the northern Cordillera. Modified from Colpron and Nelson (2011). 18

Figure 2.5: Map showing framework of tectonic realms in the northern Cordillera. Modified from Colpron and Nelson (2011). 19

Figure 2.6: Paleogeographic reconstruction of A) Late Paleozoic (Pennsylvanian to Early Permian), and B) end Paleozoic (Late Permian to Early Triassic). 22

Figure 2.7: Schematic cross sections across the northern Cordilleran orogen (approximately through the west-central Yukon) illustrating the development of the Cordilleran margin. Modified after Mair et al. (2006)..... 24

Figure 2.8: Paleogeographic reconstructions of the; A) Late Triassic and B) Early Jurassic during exhumation of the Yukon-Tanana terrane. 25
Figure 2.9: Paleogeographic reconstruction of the Middle Jurassic. 26
Figure 2.10: Distribution of regional, orogen-parallel, strike-slip faults in the Canadian Cordillera. 28
Figure 2.11: Map of Yukon showing distribution of plutons by age, with a focus on Mesozoic plutons. 29
Figure 2.12: Schematic map of the northern Cordillera during the Late Cretaceous showing palinspastic restoration of 430 km of dextral strike-slip movement along the Tintina Fault. Extension during magmatism in Selwyn basin NE of the Tintina Fault accounts for an additional 60 km of offset of Inconnu thrust fault. YTT = Yukon-Tanana terrane. Modified from Gabrielse et al. (2006). 37
Figure 2.13: Simplified geological map of Yukon highlighting the bedrock geology of the Selwyn Basin and selected lithological units. 40
Figure 2.14: Simplified geological map of Yukon and eastern Alaska illustrating the geological features on opposite sides of the Tintina Fault and the distribution of Cretaceous-age intrusions. 50
Figure 2.15: Simplified geological map of the northern Selwyn Basin showing locations of the Dawson, Tombstone, and Robert Service thrusts, the Tombstone High Strain Zone, and gold and silver occurrences. Modified after Hart (2007). 53
Figure 2.16: Stratigraphic units of the McQuesten River region and their relationship with regional structures and intrusive episodes. Modified from Murphy (1997). 54

Figure 2.17: Simplified geological map of the Keno Hill district. Modified after Boyle (1965), Murphy (1997), and Alexco (2021). 56
Figure 2.18: Comparison and correlation of stratigraphic logs for the KHQ from various localities compiled from data of Boyle (1965), Tempelman-Kluit (1966), McOnie and Read (2009), and Otto (2010). 60
Figure 2.19: Photograph of macro-scale boudinage of greenstone unit on north flank of Keno Hill. Photograph looking SW from UTM 490325 mE, 7091887 mN. 63
Figure 2.20: Summary of depositional, deformational, and intrusive events in the Keno Hill district. 66
Figure 2.21: Schematic cross-section through Sourdough and Keno Hill. Not to scale. Modified from McOnie and Read (2009). 67
Figure 3.1: Map showing study area defined by limit of mining leases currently held by Alexco (data obtained from http://mapservices.gov.yk.ca/GeoYukon, January 26, 2016). 70
Figure 3.2: Map of the Keno Hill district showing selected locations for data collection overlaid on digital elevation model (DEM). 72
Figure 3.3: Collar locations of logged boreholes overlaid on digital elevation model. Reference numbers refer to Table 3.1. 76
Figure 3.4: Map showing limits of the Alexco's 2006 helicopter magnetic and THEM survey and Metallic Mineral's 2011 SkyTEM survey. 80
Figure 3.5: Levelled 1VD data used for 2D interpretation of airborne magnetic data. Dashed lines indicate data supplied by Metallic Minerals. 82
Figure 3.6: Shaded-relief image of DEM data 83

Figure 3.7: Map showing locations of mineralised domains 88
Figure 3.8: Georeferenced scan of composite level plan (A) and digitized faults and vein in the Hector and Calumet deposits. Original composite level plan was produced by United Keno Hill Mines (UKHM; date unknown) and supplied to the author by Alexco in November 2008..... 90
Figure 3.9: Simplified geological map of the Keno Hill district showing sample locations for analysis by SEM. Base map modified from Murphy (1997). 92
Figure 3.10: Simplified geological map of the Keno Hill district showing sample locations for analysis by INAA, XRD, and XRF. Base map modified from Murphy (1997). 93
Figure 3.11: SEM-BSE images of metamict zircon grain (A) and baddeleyite grain (B) in metagabbro from the Calumet open pit (sample K-CA-003). 96
Figure 4.1: Column showing stratigraphic units by age and associated tectonostratigraphic column (modified after McOnie and Read, 2009). 98
Figure 4.2: Simplified geological map of the Keno Hill district showing sample locations. Base geological data modified after Boyle (1965), Murphy (1997), and Alexco (2021). 99
Figure 4.3: Examples of Earn Group “grey schist” rocks in (A) thin section (transmitted light scan), (B and C) drill core, and (D) outcrop. 102
Figure 4.4: Examples of Earn Group “chlorite ± sericite schist” rocks in thin section, and outcrop. 103
Figure 4.5: Photograph of massive, grey, homogenous, equigranular quartzite in drill core (borehole BKUD09-0153, depth 68.60 m, Bellekeno deposit). 105

Figure 4.6: Photographs of thick quartzitic units within the Keno Hill Quartzite. Purple dashed line: Fold enveloping surface. 106
Figure 4.7: Long-section of the SE wall of the Onek open pit. Mapping data collected by the author draped onto topographic data supplied by Alexco. 108
Figure 4.8: Examples of isoclinally folded, thin-layered quartzite intercalated with schist. 108
Figure 4.9: Examples of foliation-parallel quartz veins in underground workings and drill core. 109
Figure 4.10: Characteristics of sericite schist in A) polished thin section, and B) drill core. 111
Figure 4.11: Simplified outcrop map and interpretation of the Bermingham deposit. ... 111
Figure 4.12: Panorama photograph of the SE wall of the Bermingham open pit showing sericite schist overlying graphitic schist (both Earn Group) and in fault contact with the KHQ. Red dashed lines show trace of faults, white dashed lines show approximate contact between sericite and graphitic schist. 112
Figure 4.13: Simplified outcrop map and interpretation of the Onek deposit. 112
Figure 4.14: Examples of graphitic schist in polished thin section (A and B) and outcrop (C and D) 114
Figure 4.15: Characteristics of foliation-oblique veins 117
Figure 4.16: Photograph of macro-scale boudinage of greenstone unit on the north flank of Keno Hill. Photograph looking SW from UTM 490325 mE, 7091887 mN. 119
Figure 4.17: Examples of greenstone rocks in outcrop and drill core. 119

Figure 4.18: Map showing location of greenstone samples collected for geochemical analysis. 120
Figure 4.19: Photomicrographs of selected greenstone samples. 123
Figure 4.20: SEM-EDS images of greenstone samples. 124
Figure 4.21: Geochemical discrimination plots showing classification of metamafic samples. 130
Figure 4.22: Geochemical discrimination plots showing geotectonic classification of metamafic samples. 131
Figure 4.23: Primitive mantle normalized multi-element spider diagrams of high field strength elements (after Swinden, 1996; Sun and McDonough, 1989). Samples tend to show an E-MORB signature. 132
Figure 4.24: Photographs of outcrop of felsic intrusive rock on north flank of Keno Hill (UTM 490420mE, 7091898 mN). 133
Figure 5.1: Lambert equal area lower hemisphere projections of F_1 fold axes in the Keno Hill district. 141
Figure 5.2: F_{1a-b} fold interference patterns. 142
Figure 5.3: Density contoured, Lambert equal area lower hemisphere projection of measured $S_{0-1a-1b}$ foliations in the Keno Hill district; peak orientation 31°/096°; polar data, 1520 measurements, contour intervals 2σ. 144
Figure 5.4: Density contoured Lambert equal area lower hemisphere projections of L_1 lineations in the Keno Hill district. 144
Figure 5.5: Meso- to micro-scale examples of S_{1a-b} crenulation cleavage development across the Keno Hill district. 145

Figure 5.6: Examples of meso- to micro-scale C-S fabric development across the Keno Hill district. C-fabric: yellow dashed lines, S-fabric: blue dashed lines, red arrows: movement direction. 146

Figure 5.7: Examples of D_1 associated boudin development across the Keno Hill district. 147

Figure 5.8: Examples of D_1 associated quartz veins across the Keno Hill district. 150

Figure 5.9: Examples of meso- to micro-scale strain partitioning associated with D_1 deformation. 152

Figure 5.10: Examples of pre- to syn-D_1 pyrite sulfidation. 153

Figure 5.11: Lambert equal area projections of D_1 fault measurements and associated inversions using FaultKin™ software (Marrett and Allmendinger, 1990; Allmendinger et al., 2012). 155

Figure 5.12: Density peak subtraction methodology for analysis of potentially D_1-associated joints in the Galena Hill and Keno Hill/Sourdough Hill areas. 157

Figure 5.13: Density peak subtracted, contoured, Lambert equal area projections of joint data for the (A) Galena Hill and (B) Keno Hill/Sourdough Hill areas showing results of density peak subtraction process to analyse potential D_1-associated joints. 158

Figure 5.14: Examples and analysis of D_1-associated joints in the Onek deposit. 160

Figure 5.15: Geometric relationships between planar and linear, D_1 associated, structural elements. 163

Figure 5.16: Lambert equal area lower hemisphere projections and rose diagram of D_2 faults in the Keno Hill district. 167

Figure 5.17: Examples of major D_2, Pb-Zn ± Ag mineralised veins in pits and trenches within the Keno Hill district. 168
Figure 5.18: Photographs showing examples of fault breccia associated with D_2 fault in the Bellekeno deposit. 169
Figure 5.19: Examples of slickenlines, slickenfibres, and associated steps on D_2 faults across the Keno Hill district. 170
Figure 5.20: Simplified geological maps of the No.6 and No.9 faults at the summit of Keno Hill with associated foliation, lineation, and fault orientation data. 173
Figure 5.21: Simplified geological map of the 1st order Nabob and Comstock-Porcupine fault network on Keno Hill. First order faults are hard-linked by a set of 2nd order faults including the No.9 Fault. Fault network geometry is compiled from field observations by the author, Boyle (1965), and Murphy (1997). Overlaid on regional geological map of Alexco (2021). 174
Figure 5.22: Fault strike and dilation on Galena Hill. 176
Figure 5.23: Simplified geological maps of the Sime open pit with associated foliation, lineation, and fault orientation data. 177
Figure 5.24: Simplified geological maps of the Calumet open pit with associated foliation, lineation, and fault orientation data. 178
Figure 5.25: Simplified geological maps of the Bermingham open pit with associated foliation, lineation, and fault orientation data. 179
Figure 5.26: Simplified geological maps of the Onek open pit with associated foliation, lineation, and fault orientation data. 180

Figure 5.27: Cross-section view of bladed calcite on open fracture surface at the Onek open pit. Vein orientation 77°/217° (UTM 485713mE, 7087405mN). 181
Figure 5.28: Panoramic photograph (A) of a cross-section through an Ag-Pb-Zn vein at the 750-1 cross-cut in the Bellekeno underground workings with close-up photographs (B to E) showing characteristics of vein. 182
Figure 5.29: Quartz veins associated with D_2 faults at the Homestake prospect. 184
Figure 5.30: Examples of fluid overpressure-mineralisation at the Sime and Onek open pits. 185
Figure 5.31: Lambert equal area lower hemisphere projections of F_2 fold axes, and L_2 lineation in the Keno Hill district. 186
Figure 5.32: F_2 fold architecture at the Bermingham open pit (UTM: 478897 mE, 7086836 mN). 187
Figure 5.33: Examples of F_2 folding across the Keno Hill district. 188
Figure 5.34: Variations in L_{1int} orientation across the Keno Hill district. Numbers refer to equivalent density contoured Lambert equal area lower hemisphere projection showing orientations of L_{1int} lineations. Red arrows show approximate azimuth for density peak. Base data from Alexco (2021). 190
Figure 5.35: Variations in $S_{0\text{-}1a\text{-}1b}$ orientation across the Keno Hill district. Numbers refer to equivalent density contoured Lambert equal area lower hemisphere projection showing poles to $S_{0\text{-}1a\text{-}1b}$. Red arrow shows approximate location of regional F_2 fold axis. Base data from Alexco (2021). 191
Figure 5.36: Photographs showing examples of veins exploiting boudin necks and fold axes. 192

Figure 5.37. Anisotropic model of Ag grade at the Calumet mine shows steep SE plunge to high-grade zones (A), with grade highest along a NE-striking splay fault and at intersection of faults (B and C). Grade isoshells: Green > 400 g/t Ag; Red > 600 g/t Ag. D: Location map showing line of section for Figure A and plan view area of Figures B and C. 194

Figure 5.38: Lambert equal area lower hemisphere projections of D_3 faults and L_{3sl} lineations in the Keno Hill district. 196

Figure 5.39: Example of a D_3 fault measured in both north and south walls of the Bellekeno East mine access drive. 198

Figure 5.40: Photographs showing D_3 fault characteristics in the Bermingham open pit. 200

Figure 5.41: Lambert equal area lower hemisphere projections of F_3 fold axial surfaces, and F_3 fold axes in the Bermingham deposit. 201

Figure 5.42: Characteristics of F_3 folds in the Bermingham deposit. 202

Figure 5.43: District-scale form line interpretation of 1VD data showing interpreted lazy-s-shaped restraining bend. Inset rose diagram showing trend of all interpreted form lines. 206

Figure 5.44: District-scale fault interpretation of 1VD data (A) with rose diagrams showing the trends of all interpreted D_1 (B), D_2 (C), and D_3 (D) faults. 207

Figure 5.45: District-scale fault interpretation overlain on simplified geological map (combined from Murphy, 1997; and Alexco, 2021) showing variations in interpreted fault frequency dependant on underlying lithology. 209

Figure 5.46: District-scale fault interpretation showing only D_2 faults. 211

Figure 5.47: Fault density analysis for D_2 faults interpreted from district-scale 1VD data. 211
Figure 5.48: Fault density analysis for D_2 faults overlain by all interpreted faults. 212
Figure 5.49: District-scale fault interpretation showing D_2 faults classified by orientation. 213
Figure 5.50: Fault density analysis for D_2 faults with a strike of $\leq 050°$ interpreted from district-scale 1VD data. 213
Figure 5.51: Location (A) and 1VD regional airborne magnetic data (B) used for the regional fault interpretation. 214
Figure 5.52: Regional-scale form line interpretation of 1VD data. Red dashed line: Tintina Fault; Blue dashed line: Dawson Thrust. 215
Figure 5.53: Regional-scale fault interpretation of 1VD data. 216
Figure 5.54: Regional-scale fault interpretation showing interpreted left-stepping releasing bends. 217
Figure 5.55: Lineament interpretation of DEM data. 219
Figure 5.56: Plan view of all supplied assay data for the Keno Hill district. Assay data show a pattern of en echelon, anastomosing vein systems. 222
Figure 5.57: Interpretation of 2D vein geometry based on borehole assay data and regional, historic vein mapping (modified after Boyle, 1965). 223
Figure 5.58: Sketch of small-scale en echelon vein architecture defined by sphalerite stringer veins in KHQ outcrop at the Sime deposit (UTM 482374mE, 7088658mN). .. 224
Figure 5.59: Plan view of 3D model of D_2 faults/veins and cross-cutting D_3 faults in the Galena Hill area. 226

Figure 5.60: Plan view slice through 3D fault/vein model. 1160 masl..... 227
Figure 5.61: Vertical (A and B) and inclined (C) sections through the 3D fault/vein model. D: location map showing lines of section at surface..... 229
Figure 5.62: Anisotropic modelling of Ag grade in D_2 veins in 3D fault/vein model. Model created in Leapfrog Geo^{TM}. 231
Figure 6.1: Simplified geological map showing locations of samples collected for geochronological analysis. Base data from Murphy (1997). 237
Figure 6.2: Inverse isochron (A) and age spectrum (B) for sample K-ON-003. 240
Figure 6.3: Age spectrum for sample K-ON-004. 242
Figure 6.4: Inverse isochron (A) and age spectrum (B) for sample 187-005. 245
Figure 6.5: Age spectrum for sample U0160-009. 247
Figure 6.6: Inverse isochron and age spectra for sample K-BX-007. A: inverse isochron for analysis D-700; B: age spectrum for analysis D-700; C: inverse isochron for analysis JF-151617; D: age spectrum for analysis JF-151617. 251
Figure 6.7: Photomicrographs (XPL) of sample K-KH-003 showing (A) calcite in a biotite-quartz-feldspar groundmass; and (B) example of zircon crystals present..... 252
Figure 6.8: Concordia diagram and weighted six-point average chart for sample K-KH-003..... 254
Figure 6.9: Comparison between $^{40}Ar/^{39}Ar$ and U-Pb ages acquired in this study, and K-Ar and U-Pb ages acquired in or near the Keno Hill district by previous authors. 257
Figure 7.1: Schematic block models showing the essential elements and structural architecture of D_1 (A), D_2 (B), and D_3 (C) deformation in the Keno Hill district. Not to scale..... 259

Figure 7.2: Lambert equal area projections of D_2 fault measurements and associated inversions using FaultKin™ software (Marrett and Allmendinger, 1990; Allmendinger et al., 2012). 266

Figure 7.3: Time series chart showing publicly available geochronological data for Ancestral North American (Laurentian Realm) basinal rocks. 269

Figure 7.4: Lambert equal area projections of D_3 fault measurements and associated inversions using FaultKin™ software (Marrett and Allmendinger, 1990; Allmendinger et al., 2012). 273

Figure 7.5: Palinspastic restoration of 430 kilometres of dextral strike-slip movement along Tintina Fault of geological mapping data (N. Hayward, personal communication, January 27, 2017). 277

Figure 7.6: Palinspastic restoration of 430 kilometres of dextral strike-slip movement along Tintina Fault of 1VD airborne magnetic data (A) and interpretation of through-going ENE-trending lineaments in palinspastically restored (B). Interpretation shows potential structural link between the Keno Hill and Fort Knox deposits. Source data: Oneschuk et al. (2019). 280

Figure 7.7: A: Geological map (Wiltse et al., 1995) overlain on DEM data; and B; interpretation of 1VD airborne magnetic data (Oneschuk et al., 2019) showing ENE-striking faults linked by NNE-striking faults in an apparent left-stepping, releasing bend approximately 30 km WSW of Central, AK. 282

Figure 7.8: Distribution of major precious and base metal deposits in the northern Cordillera, and their spatial association with orogen-oblique, likely Paleoproterozoic-age faults. 285

Figure 7.9: Proposed location of Precambrian basement structure that controls deformation in overlying basinal rocks, based on observations from regional free air gravity anomaly data (A), regional airborne magnetic RTF data, and topographic data.291

List of Symbols, Nomenclature or Abbreviations

1VD	First vertical derivative
2D	Two dimensional
2VD	Second vertical derivative
3D	Three dimensional
Ag	Silver
AK	Alaska
Al	Aluminium
Amu	Atomic mass unit
Ar	Argon
AS	Analytical signal
As	Arsenic
Au	Gold
Ba	Barium
B.C.	British Columbia
Br	Bromine
BSE	Back scatter electron
Ca	Calcium
CA-TIMS	Chemical Abrasion - Thermal Ionization Mass Spectrometry
Ce	Cerium
Co	Cobalt
CL	Cathodoluminescence
cm	Centimetre
Cr	Chromium
Cs	Caesium
csv	Comma separated value
D_n	Deformation phase, numeric subscript indicates relative age
DEM	Digital elevation model
dxf	Digital exchange format
EDS	Energy dispersive spectrometer
Eu	Europium
F_n	Fold, numeric subscript indicates relative age
F	Fluorine
FCT	Fish Canyon Tuff
FFT	Fast fourier transform
g/t	Grams per tonne
Ga	Billion years
Ge	Germanium
GIS	Global information systems
GPS	Global positioning system
GSC	Geological Survey of Canada
GSCH	Graphitic schist
H	Hydrogen
Hf	Hafnium

ID-TIMS	Isotope dilution thermal ionization mass spectrometry
IGRF	International geomagnetic reference field
INAA	Instrumental neutron activation analysis
Ir	Iridium
jgw	Georeferenced file associated with .jpeg files
K	Potassium
KHQ	Keno Hill Quartzite
Km	Kilometre
L_n	Lineation, numeric subscript indicates relative age
L_{ncr}	Crenulation lineation, numeric subscript indicates relative age
L_{nint}	Intersection lineation, numeric subscript indicates relative age
L_{nstr}	Stretching lineation, numeric subscript indicates relative age
La	Lanthanum
Lu	Lutetium
m	metre
M	Million
Ma	Million years
Masl	Metres above sea level
mE	Metres East
mm	Millimetres
mN	Metres North
Mo	Molybdenum
MSWD	Mean squared weighted deviation
Na	Sodium
Nd	Neodymium
Ni	Nickel
NRMT	Northern Rocky Mountains Trench
nT	Nanotesla
NTS	National Topographic System
N.W.T.	Northwest Territory
O	Oxygen
Oz/t	Ounces per ton
Pb	Lead
pg	Picogram
ppb	Parts per billion
ppl	Plane-polarised light
ppm	Parts per million
Pr	Praseodymium
P-T	Pressure-temperature
QTZT	Quartzite
Rb	Rubidium
RBF	Radial basis function
RC	Reverse circulation
RMF	Residual magnetic field
RTF	Residual total field

RTP	Reduced-to-pole
S_n	Foliation, numeric subscript indicates relative age
Sb	Antimony
Sc	Scandium
SCH	Schist
Se	Selenium
SEDEX	Sedimentary exhalative
SEM	Scanning Electron Microscopy
Si	Silicon
Sm	Samarium
Sn	Tin
Sr	Stronium
SSCH	Sericite schist
Ta	Tatalum
Tb	Terbium
TCR	Taylor Creek rhyolite
Th	Thorium
THEM	Time-domain Helicopter ElectroMagnetic
THG	Total horizontal gradient
TMI	Total magnetic intensity
TPS	Tombstone Plutonic Suite
TYC	Treadwell-Yukon Company
U	Uranium
UBC	University of British Columbia
UKHM	United Keno Hill Mines
UNB	University of New Brunswick
USGS	United States Geological Survey
UTM	Universal Transverse Mercator
W	Tungsten
Wt. %	Weight percent
Xpl	Cross-polarised light
XRD	X-Ray diffraction
XRF	X-Ray fluorescence
Yb	Ytterbium
YGS	Yukon Geological Survey
YK	Yukon
Zn	Zinc
Zr	Zirconium
µm	Micrometre

1. Introduction

The Ag-Pb-Zn Keno Hill mining district of the Yukon Territory, Canada is an historic mining region that has been actively mined for close to 100 years. The district is known for its exceptionally high-grade, vein-hosted, fault-controlled ore (Cathro, 2006). The majority of the Keno Hill mining district is currently being explored and developed by Alexco Resource Corp (hereafter, Alexco). Between 1913 and 1990 the camp produced in excess of 6 million kilograms of silver (at an average grade of 1,373 grams per tonne), 300,000 tonnes of lead (at an average grade of 6.7 %), and 195,000 tonnes of zinc (at an average grade of 4.1 %; Cathro, 2006; Table 1.1). Over this period the Keno Hill mining district was the second largest producer of silver in Canada, and one of the richest lead-zinc vein-type deposits in the world (Cathro, 2006).

The district is located within, and is dominated by, rocks of the western Selwyn Basin including polydeformed, metamorphosed and imbricated basinal sedimentary rocks that accumulated along the Neoproterozoic – Paleozoic continental margin of the ancestral North American plate (Murphy, 1997; Fingler, 2005; Figure 1.1), plus Triassic metagabbroic and metadioritic rocks (Murphy, 1997). The district comprises several fault-controlled, vein-type base metal deposits that are typically hosted in the Mississippian age Keno Hill Quartzite (Lynch, 1989a, b).

Table 1.1: Keno Hill Camp. Total recorded production - 1913 to 1990 (listed in order of decreasing Ag ounces (Modified after Cathro, 2006).

	Recovered Grades								
MINE	**Tonnes**	**Ag oz/t**	**Pb %**	**Zn %**	**Ag ounces**	**Pb pounds**	**Zn pounds**	**Ag/Pb**	**Pb/Zn**
Hector-Calumet	2,721,288	35.4	7.5	6.1	96,219,690	406,912,502	334,570,797	4.7	1.2
Elsa	491,009	61.4	4.9	1.4	30,158,040	47,708,019	13,484,869	12.6	3.5
Husky	429,367	41.7	3.9	0.4	17,889,418	33,290,002	3,309,284	10.7	10.1
Sadie-Ladue	244,330	52.1	6.5	4.5	12,725,633	31,923,607	22,029,310	8	1.4
Keno	283,762	44.4	10.7	3.7	12,602,298	60,549,038	21,189,428	4.2	2.9
Lucky Queen	123,590	89.2	7	2.7	11,019,368	17,223,250	6,653,462	12.8	2.6
Silver King	207,618	53	7.7	0.8	10,995,915	31,917,957	3,510,383	6.9	9.1
No Cash	166,530	29.8	3.6	1.9	4,969,107	11,912,346	6,188,199	8.3	1.9
Galkeno	167,063	27.2	5.2	2.7	4,544,142	17,437,410	8,999,204	5.2	1.9
Bermingham	186,266	20.3	4.2	0.6	3,777,932	15,575,525	2,157,714	4.9	7.2
Bellekeno	40,502	42.6	9.8	2.3	1,724,371	7,966,619	1,828,776	4.3	4.4
Black Cap	48,576	27.4	1.6	0.3	1,331,131	1,560,359	269,402	17.1	5.8
Onek	95,290	13.6	5.5	3.4	1,299,333	10,456,254	6,452,107	2.5	1.6
Ruby	40,652	25.2	3	1.3	1,024,141	2,420,577	1,022,818	8.5	2.4
Shamrock	5,336	180.3	37.6	0.3	962,396	4,013,179	36,523	4.8	109.9
Comstock	22,863	39.7	10.7	3.8	907,176	4,891,434	1,719,131	3.7	2.8
Dixie	23,872	20.2	3.8	5.1	481,942	1,813,155	2,455,694	5.3	0.7
Husky SW	10,461	39.6	0.3	0.1	414,261	56,193	17,300	147.4	3.2
Townsite	18,570	16.4	4.3	2	305,423	1,583,393	730,014	3.9	2.2
Mt. Keno (Runer)	1,588	139.3	17.7		221,152	561,770		7.9	
Miller (UN & Dragon)	9,390	15.1	2.2	0.7	141,358	419,702	139,638	6.7	3
Flame & Moth	1,590	18.3	1.1	0.9	29,120	35,363	28,895	16.5	1.2
Elsa Mill Tailings	1,884	14.4	3	0.8	27,216	112,462	29,423	4.8	3.8
Others*	1,752	3021.4	555.4	1.4	265,037	1,088,604	4340	86.3	388.8
TOTAL (Imperial)	**5,343,088**	**40.1**	**6.7**	**4.1**	**214,035,599**	**711,428,720**	**436,826,711**	**6**	**1.6**
Total (Metric)	**4,847,164 tonnes**	**1,373 g/t**	**6.70%**	**4.10%**	**6,657,234.9 kilograms**	**322,698.4 tonnes**	**198,141.1 tonnes**		

* Combined totals of all other deposits with 1,000 tonnes recovered

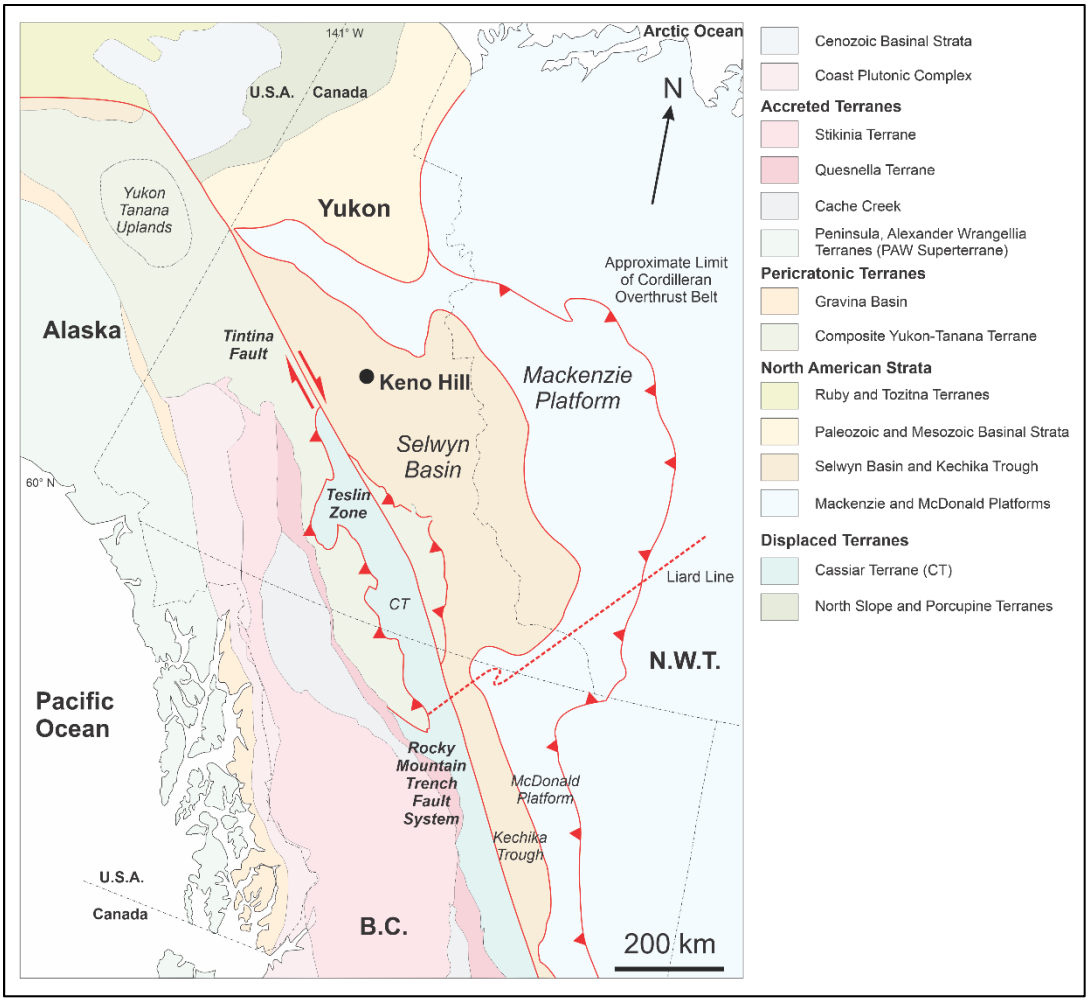

Figure 1.1: Regional geology of the northern Cordillera in Yukon, British Columbia, and eastern Alaska (Modified after Mair et al., 2006)

1.1 Rationale

Structural geometry is well recognised as an important control on many aspects of precious and base metal lode deposits (Robert et al., 1994; Table 1.2). In deformed terranes, such as the Keno Hill district, structures control the shape, orientation, and location of mineralized zones and ore deposits.

Despite the long history of mining activities in the Keno Hill district, no dedicated structural geological analyses have been completed prior to this thesis. Discussions on the structural geology of the district have most often formed minor parts of district-scale studies examining vein paragenesis (Kania, 1926; Zajac, 1957; Hantelmann, 2013), mineralogy (Aho, 1949), vein geochemistry and zonation (Tessari, 1979; Lynch, 1989a; b, Lynch et al., 1990), lithogeochemistry (Gleeson and Boyle, 1980), and stratigraphy (Boyle, 1965; McOnie and Read, 2007), or are incorporated into regional-scale studies (e.g. Tempelman-Kluit, 1966; Murphy, 1997; Roots, 1997; Stephens, 2003; Mair et al., 2006). This thesis provides a comprehensive and substantially more definitive study of the district-scale structural history and the local to regional-scale controls on Ag-Pb-Zn mineralisation, combined with elucidation of how the district accords with current models of Cordilleran tectonics.

Table 1.2: The main factors influencing the geometry of precious and base metal lode deposits (modified after Robert et al., 1994).

Factor	Effects
Stress/Strain Regime	• Controls orientation and kinematics of shear zones and veins • Variations in stress ratio imposes deviations from 2D deformation
Strength Anisotropy	• Influences localization of shear zones and veins, as well as their reactivation • Induces local refraction of stress axes, causing deviations from regional patterns • Influences complexity of shear zone and vein networks
History of Deposit	• Dictates the degree of structural overprinting and modification of original shape and orientation • Influences the complexity of vein networks.

1.2 Objectives and Scope of Work

The objectives of this thesis can be broadly assigned to two themes reflecting scale. The first theme comprises characterization of the district-scale structural history of the Keno Hill area, and the second theme aims to understand how structures observed at the deposit- and district-scale relate to regional-scale structures and tectonism in the northern Cordillera. To complete these objectives, key questions were posed:

- What are the deposit- to district-scale structural characteristics within the Keno Hill district?
- What were the district-scale structural controls on Ag-Pb-Zn mineralisation, and can an understanding of these controls be used to define areas for exploration within the district?
- What was the timing of Ag-Pb-Zn mineralisation at Keno Hill, and how does this correlate with regional deformation, magmatism, and metamorphism?
- How does deformation at Keno Hill correlate with current models of Cordilleran tectonics?
- Are there identifiable regional-scale structural controls on Ag-Pb-Zn mineralisation at Keno Hill and if so, do these controls indicate the presence of currently under-explored areas that are be prospective for precious and base metals?

A multidisciplinary approach was used to answer the aforementioned questions. At the deposit- to district-scale, detailed structural mapping, drill-core logging, and analysis of collected structural data was completed at numerous open pit and underground deposits (Figure 1.2) and outcrop exposures within the Keno Hill district to understand the structural, stratigraphic, and intrusive relationships and geometry of deposit-scale structures. Geochemical analyses were acquired on primarily, but not exclusively, intrusive rocks. Geochronological analyses were completed on intrusive and fault-related rocks to establish the timing of fault movement, hydrothermal alteration, and associated Ag-Pb-Zn mineralisation. At the district-scale, 2D interpretation and analysis of remote sensing datasets and 3D modelling of subsurface data were used to define the district-scale fault architecture, and to define areas of within-district exploration potential. At the regional-scale, 2D interpretation and analysis of remote sensing data and palinspastic fault restoration was used to define the regional-scale controls on Ag-Pb-Zn mineralisation at Keno Hill, to correlate the structures at Keno Hill with other major deposits or districts within the Cordillera, and to identify any under-explored areas that may correlate with Keno Hill.

This thesis focusses on the structural history and structural controls on Ag-Pb-Zn mineralisation at Keno Hill, and its relationship to current models of Cordilleran tectonics, however, it should be noted that the author has completed numerous additional studies throughout the northern Cordillera in British Columbia, Yukon, Alaska. These include base and precious metal projects in rocks of the Selwyn Basin or their equivalent

in Alaska, and rocks of the Yukon-Tanana Terrane. Details of the projects are proprietary, and as such will not be directly discussed in this thesis; however, the knowledge gained from these studies was essential in placing the Keno Hill deposits within the regional structural and tectonic context.

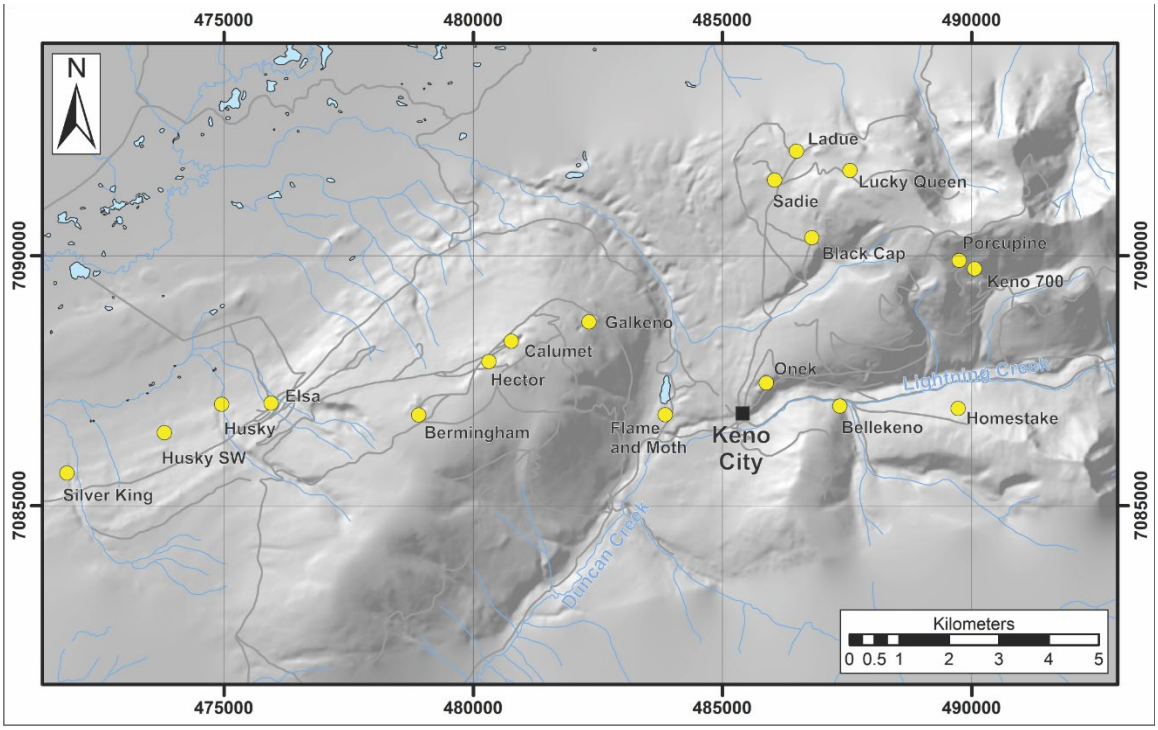

Figure 1.2: Locations of selected mines and deposits in the Keno Hill district overlain on five metre resolution digital elevation model.

1.3 Significance

The work presented in this thesis builds and expands upon studies by numerous authors over the last century. The understanding of the structural history of the Keno Hill district has changed overtime. Boyle (1965) suggested that rocks within the district formed a

"simple homoclinal succession" with "no extensive overturning of strata, or recumbent folding". Tempelman-Kluit (1966) recognised abundant deformation and stratigraphic repetition of Mesozoic units in the Tombstone area but suggested that the Mayo district (just west of Keno Hill) lacked large-scale thrusts and major faults. Lynch (1989a) proposed a two-phase model of deformation comprising early "thrust and nappe" formation, followed by a "transcurrent shear" phase associated with base metal mineralisation, while Murphy (1997) also noted the additional presence of post-mineralisation cross-cutting faults. The work presented here represents the first highly detailed structural analysis of the Keno Hill district and defines the structural history for the Keno Hill district as comprising early ductile to brittle-ductile progressive deformation, syn-mineralisation brittle deformation, and post-mineralisation brittle deformation.

Previous work has linked Ag-Pb-Zn mineralisation to the emplacement of the Tombstone intrusive suite (e.g., Murphy, 1997) and in particular the Roop Lakes stock (Lynch et al., 1990). K-Ar geochronological work by Tessari (1979) suggested that Ag-Pb-Zn mineralisation occurred at circa 87Ma. New geochronology ages presented here indicate that mineralisation took place between 81 and 78 Ma and is likely unrelated to emplacement of the Tombstone Intrusive Suite; however, the heat source for the mineralizing fluids remains unclear.

Additionally, this research develops the first interpretation of regional structural controls on Ag-Pb-Zn mineralisation within the Keno Hill district. The work shows that at the

regional-scale the Keno Hill district is located within a previously undescribed left-stepping, releasing bend within a major syn-mineralisation, sinistral strike-ship fault system. This observation has significant implications for regional exploration (Chapter 7.3.1). Importantly, the major sinistral strike-slip fault system associated with Ag-Pb-Zn mineralisation at Keno Hill is shown to be continuous with a similar major structural zone in Alaska that hosts the Fort Knox deposit. This suggests a structural, albeit not temporal, link between two world-class deposits. The author proposes that the major fault network that links the Keno Hill and Fort Knox deposits may be the upper crustal expression of a long-lived basement structure that may be of Proterozoic age. This observation draws similarities between the Keno Hill and Fort Knox deposits and numerous other major or world class precious and base metal deposits in the northern Cordillera that are similarly situated above or proximal to major Proterozoic basement fault zones.

1.4 Thesis Structure

The thesis is presented in a traditional format to provide a coherent and systematic account of the research. Chapters 1 to 3 include largely introductory material including the significance of the work, the geological setting of the Keno Hill district, and techniques used to acquire the data. Chapters 4 to 6 present the results of the data acquisition and analysis, and chapters 7 and 8 comprise discussion and conclusions. A series of appendices are provided as separate digital files that includes additional

supporting information on techniques used in the thesis, all collected data, and maps and interpretations created during the course of the research in a GIS environment.

Chapter 2 presents a literature review to detail the current understanding of the geological setting for the Selwyn Basin and Keno Hill district. The literature review briefly summarises the current tectonic models and ongoing controversies related to northern Cordilleran tectonics. An understanding of the models and controversies is essential for a discussion on placing Ag-Pb-Zn mineralisation within the regional context. The literature review compiles data and ideas from published articles and theses, historic assessment reports, historic memoranda, and unpublished reports supplied to the author by Alexco.

Chapter 3 summarises the available data and data acquisition techniques used in the preparation of this thesis. Additional information on specific analytical techniques and methodologies can be found in Appendix A.

Chapter 4 details the lithological characteristics, and the temporal and geometric, stratigraphic and intrusive relationships present in the Keno Hill district. Descriptions in this chapter are largely based on the author's own observations; however, where applicable these are augmented by observations of previous workers. All observations by previous workers are cited. Descriptions of collected sample data are available in Appendix B, and geochemical data are available in Appendix C.

Chapter 5 presents the results and analysis of structural data collected in the field and during 2D and 3D desktop analysis of subsurface and remote sensing datasets. All field data were collected by the author or the author's field assistants during three field seasons from September to December 2008; June to August 2009; and May to July 2010, a combined period of approximately 10 months. All analyses of field data, remote sensing data, and subsurface data were completed by the author. All collected structural data can be found in Appendix D. Deposit-scale maps, district- to regional-scale interpretations of remote sensing data, and 3D models created during the course of the research are available in Appendix E.

Chapter 6 presents the results and analysis of geochronological sampling and analysis by the $^{40}Ar/^{39}Ar$ and U-Pb methods. Samples were collected by the author during field work. Analysis by the $^{40}Ar/^{39}Ar$ method was carried out at Queen's University, and analysis by the U-Pb CA-TIMS method was completed at the University of British Columbia. Interpretation of the results was completed by the author. Supporting geochronological data can be found in Appendix F.

Chapters 7 and 8 present the discussions and conclusions of the research, respectively. The discussion includes comparing the results of the authors study to the work of previous authors to understand the regional context and significance of observations by the author.

1.5 Location and Access

The Keno Hill district is located approximately 350 km NE of Whitehorse, YK (460 km by road), 55 km east of Mayo, YK (the nearest large municipality and administrative centre), 80 km south of the Yukon and Mackenzie river watersheds, and approximately 300 km south of the arctic circle (Figure 1.3). The mining district broadly comprises Keno Hill, Galena Hill, and Sourdough Hill within NTS map sheets 105M/13, 14, and 15. Keno City, a small community located approximately central to the mining district is located at UTM Zone 8V 495080 mE, 7087000 mN (63° 54' 33" N, 135° 18' 10" W).

Elevation in the mining district ranges from approximately 525 metres above sea level along the South McQuesten River, to approximately 1975 metres above sea level at the summit of Keno Hill. The topography is characterised by moderate to gently sloping terrain, except on the steep to subvertical northern slopes of Keno Hill and Sourdough Hill. Dense vegetation comprising alder, poplar, birch, and spruce, along with several species of shrub is common in the low-lying areas, and alpine tundra occurs at higher elevations (Simpson et al., 2007).

Several small to large open pits and trenches exist within the district where rock exposure approaches 100 %. Elsewhere, *in situ* rock exposure is commonly less than 5 % and as such the majority of work was completed within the historic open pit developments. One underground deposit, the Bellekeno deposit, was accessible; at the time of study the rock

mass conditions in the Bellekeno deposit required only screen and bolt infrastructure (no shotcrete was observed) and provided 100 % rock exposure.

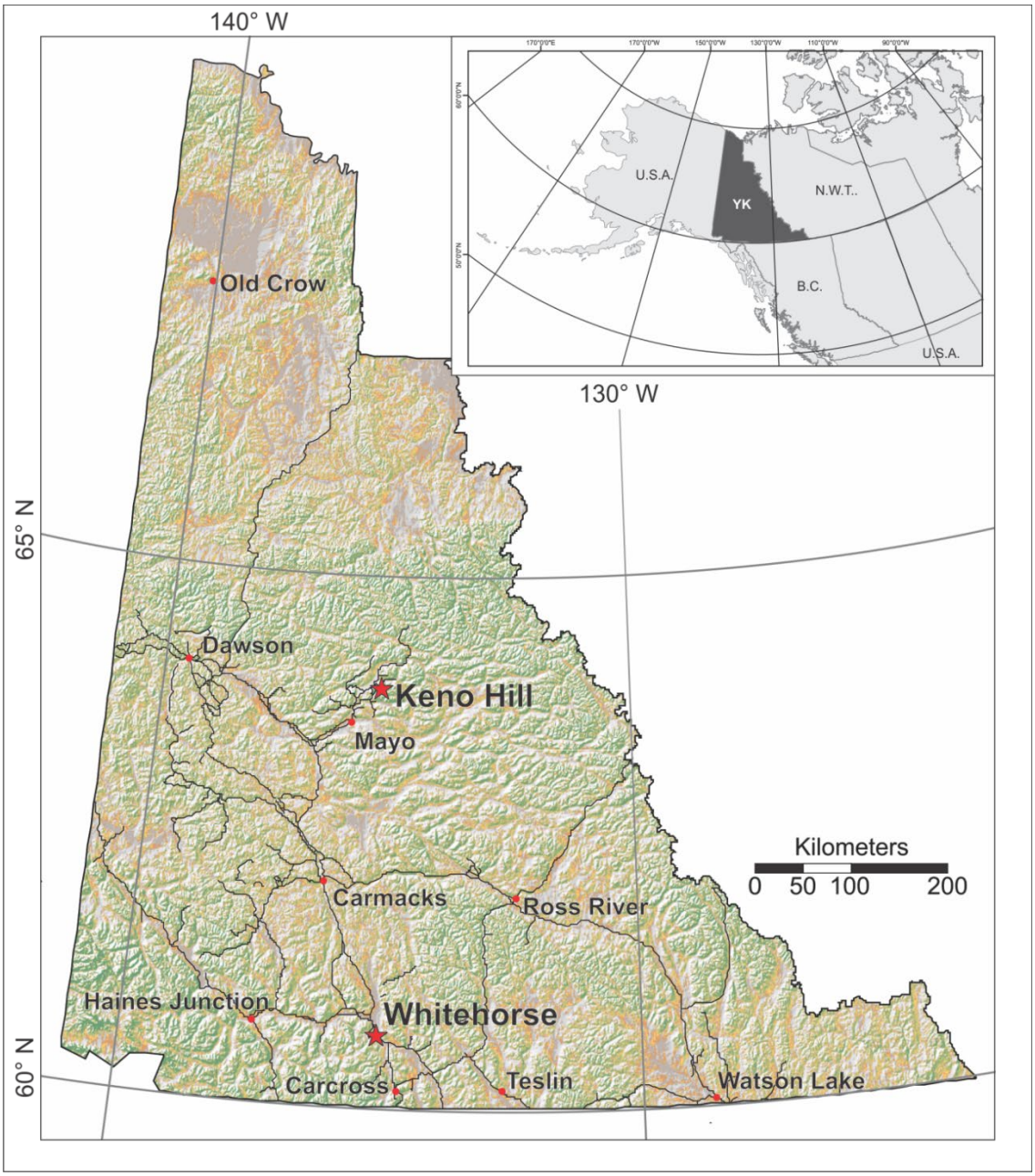

Figure 1.3: Shaded relief image of the Yukon showing location of Keno Hill, selected municipalities, and the major road network. Inset map of NW North America.

2. Geological Setting

This chapter describes and discusses the tectonic, structural, and stratigraphic evolution of the northern Cordillera and the Keno Hill district's setting within that framework. The Keno Hill district is located in and is dominated by sedimentary rocks of the Selwyn Basin (Figure 2.1; Lynch, 1989a; b; Murphy and Roots, 1992). Sedimentation within the Keno Hill district ranged from the Late Proterozoic through to at least the Mississippian (Murphy, 1997; Gordey, 2013); magmatism and deformation are occurred during the Mesozoic. This chapter will focus on the geological setting of the region throughout the Phanerozoic. A brief discussion of the tectonic evolution of the North American Cordillera and the tectonic evolution of terranes present in Yukon, more specifically the development of the Selwyn Basin, is followed by a synopsis of the stratigraphy and structural geology of the Keno Hill district.

2.1 Tectonic Assembly of the North American Cordillera

The North American Cordilleran orogen was constructed along the western margin (present-day coordinates) of the Laurentian craton, the ancestral Precambrian core of the North American continent (Nelson et al., 2013), and extends for 8,000 km from Alaska in the north to Guatemala and Honduras in the south, with a width of 650–1,600 km (King, 1987).

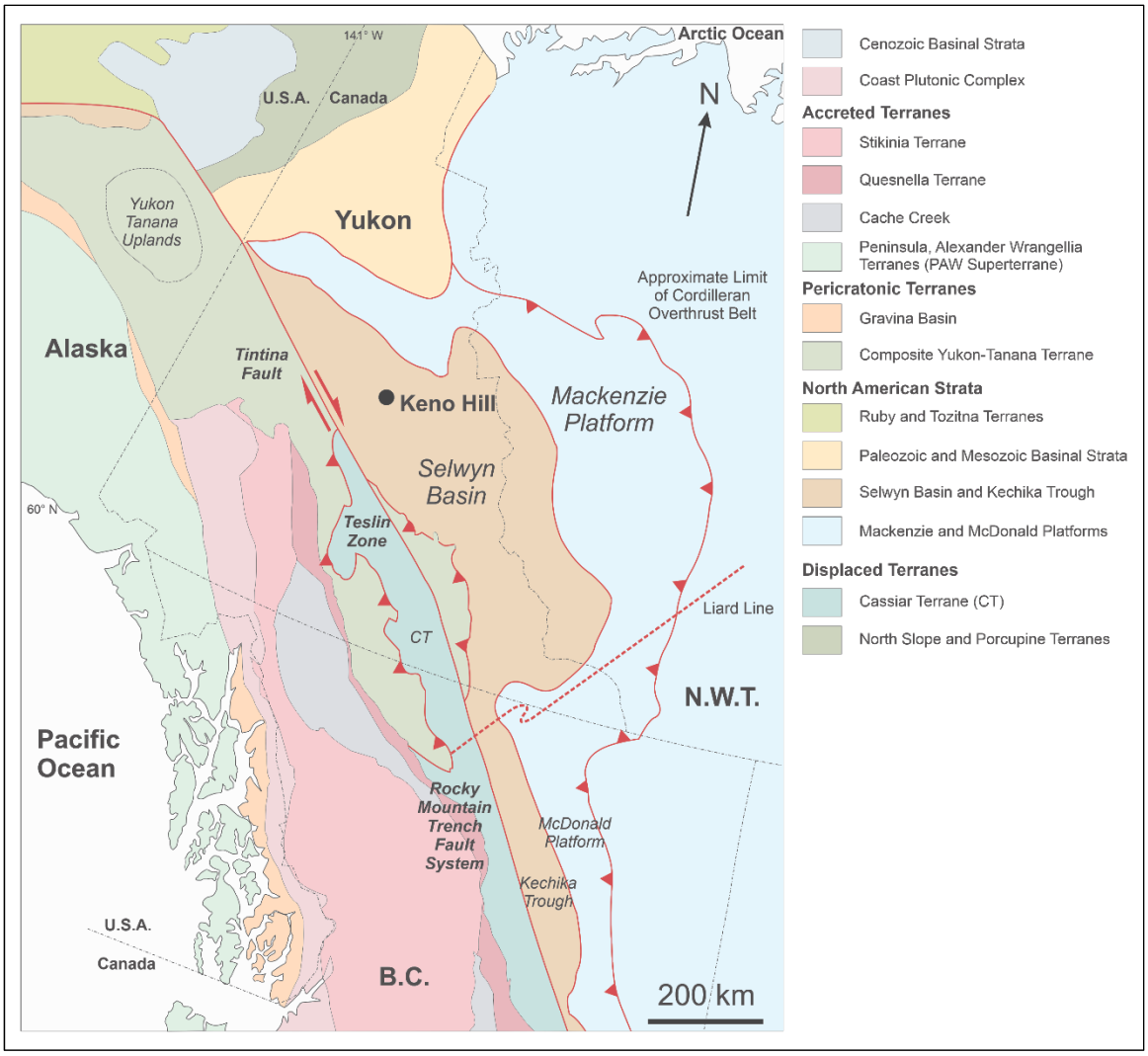

Figure 2.1: Regional geology of the northern Cordillera in the Yukon Territory, British Columbia, and eastern Alaska. Modified from Mair et al. (2006).

The Cordillera is an accretionary orogen where deformation, metamorphism, and crustal growth accompanied continued subduction and accretion, rather than a process ending in continent-continent collision (Cawood et al., 2009; Nelson et al., 2013). The Cordillera is a segment of the Circum-Pacific orogenic belt where subduction of oceanic lithosphere has been underway since the initiation of the breakup of Pangea in the Triassic (Figure 2.2; Dickinson, 2004). Initial inboard propagation of magmatic arcs along the western

margin of Laurentia (ca. 400–360 Ma) coincided with the final closing of the Iapetus Ocean (van Staal, 2007), while the Middle Jurassic and younger crustal thickening event and associated arc accretion was coeval with opening of the Atlantic Ocean (Figure 2.3). Thus, a megacycle driven by major changes in continental plate motion can account for the broadest aspects of Cordilleran tectonic history (Nelson et al., 2013).

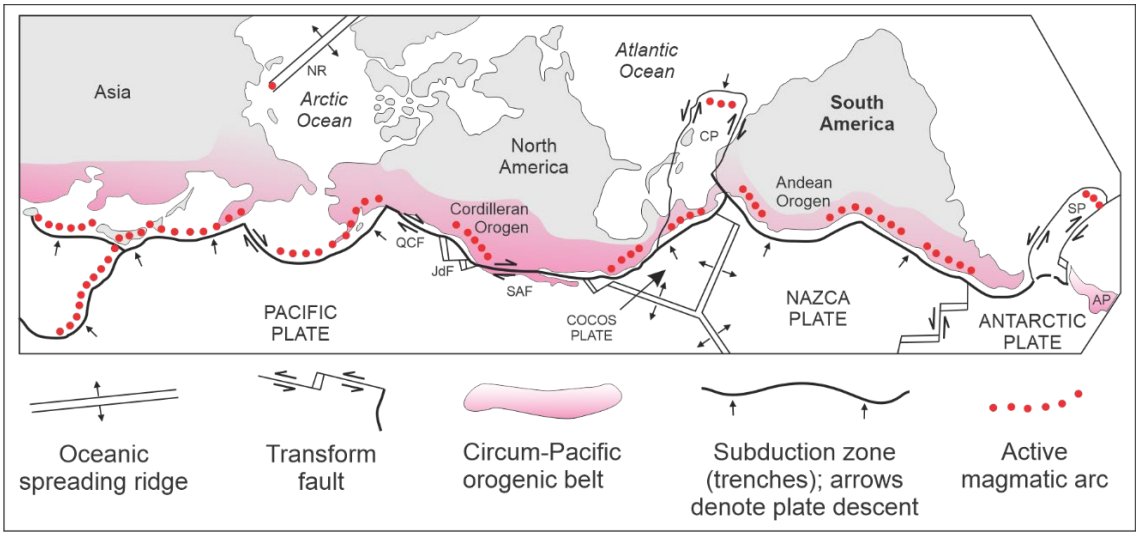

Figure 2.2: Position of the Cordilleran orogen of western North America along the Circum-Pacific orogenic belt.

Mercator projection with pole at 25° N Latitude, 15° E Longitude. AP, Antarctic Peninsula; CP, Caribbean plate; JdF, Juan de Fuca plate; NR, Nansen Ridge (northern extremity of Atlantic spreading system); QCF, Queen Charlotte Fault; SAF, San Andreas Fault; SP, Scotia plate. Modified from Dickinson (2004).

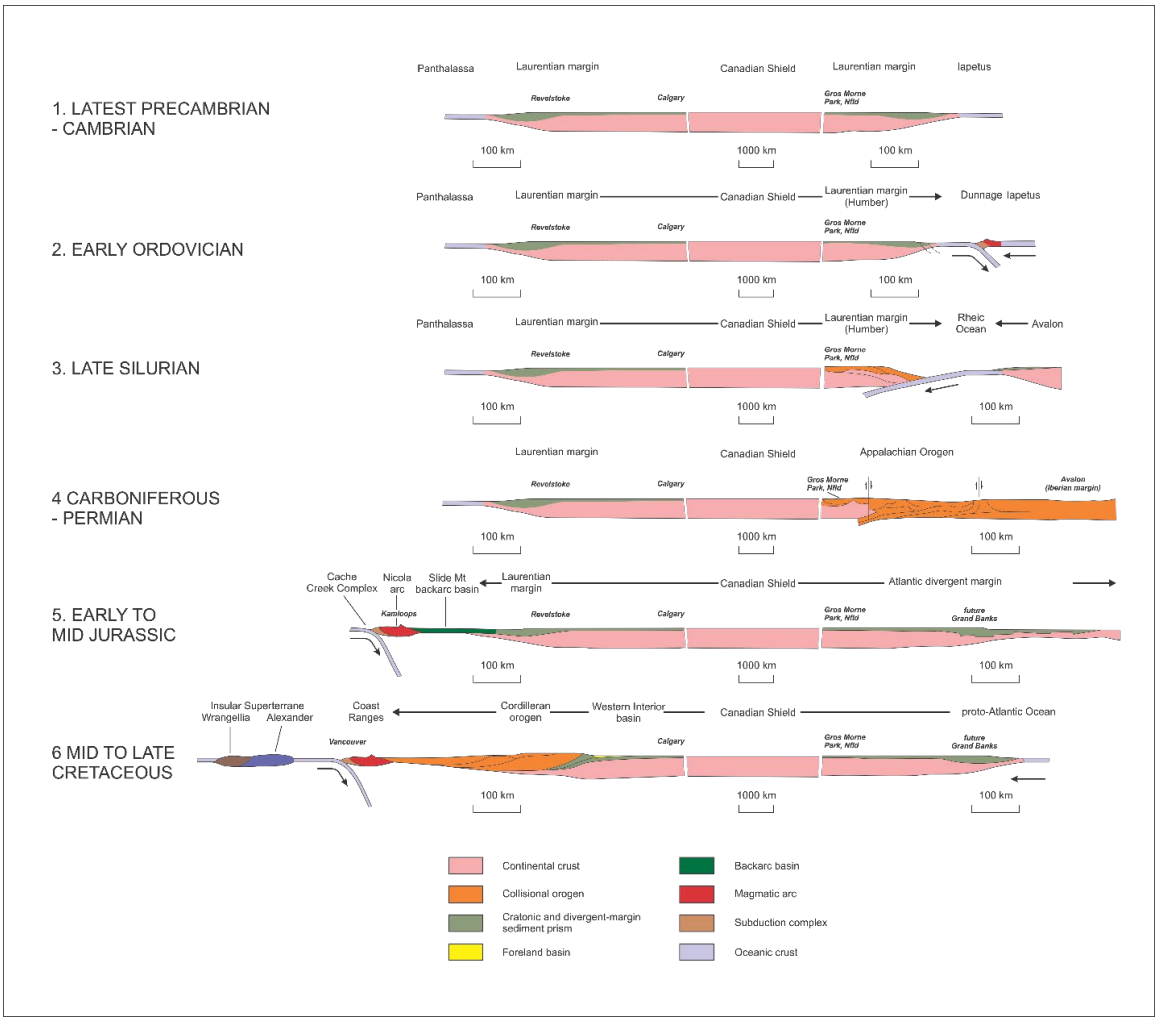

Figure 2.3: Sequential east-west cross-sections through Canada, summarising the changes in the plate-tectonic regime during the Phanerozoic. Modified from Miall and Blakey (2019).

The complex and protracted Phanerozoic tectonic evolution of the northern Cordillera is recorded mainly in orogenic collages that consist of tectonostratigraphic terranes composed of fragments of igneous arcs, accretionary-wedge, and subduction-zone complexes, passive continental margins, and cratons. These are overlapped by continental-margin-arc and sedimentary-basin assemblages (Figure 2.4; Nokleberg et al., 2000; Dickinson, 2004). The history comprises Paleozoic extensional tectonics followed

by Late Triassic to Paleocene compressional tectonics. A brief period of Late Paleocene-Eocene crustal transtension throughout the southern portion of the northern Cordillera subsequently gave way to processes concentrated mainly near the present plate margin (Nelson et al., 2013). For further detail the reader is directed to Dickinson's (2004) and Nelson et al.'s (2013) studies.

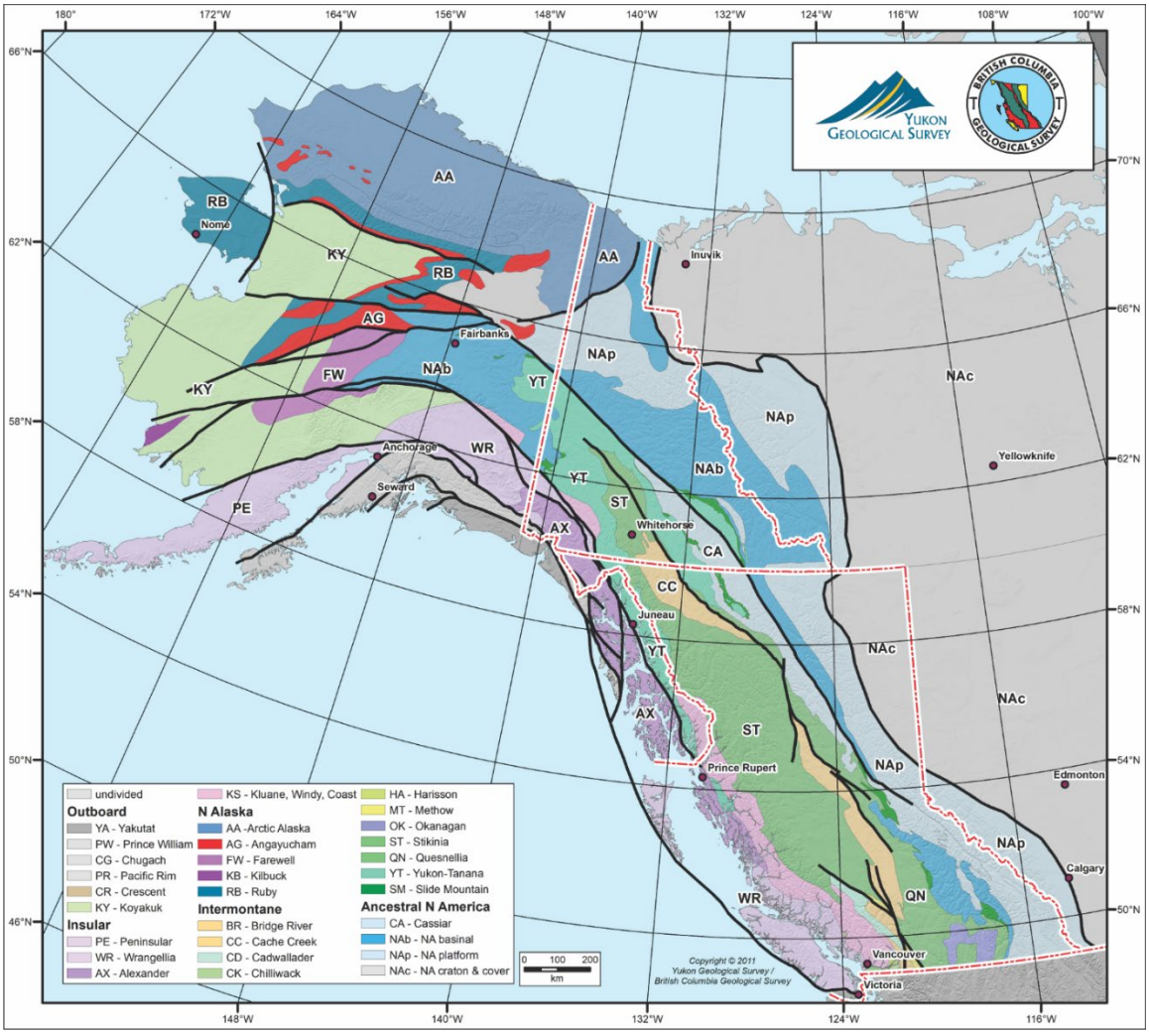

Figure 2.4: Map showing framework of terranes in the northern Cordillera. Modified from Colpron and Nelson (2011).

2.1.1 Tectonic Realms

Nelson et al. (2013) defined a series of four paleogeographic realms within the northern Cordillera that are based on the region of origin and sets of related terranes (Figure 2.5). The four realms and their characteristics as defined by Nelson et al. (2013) are:

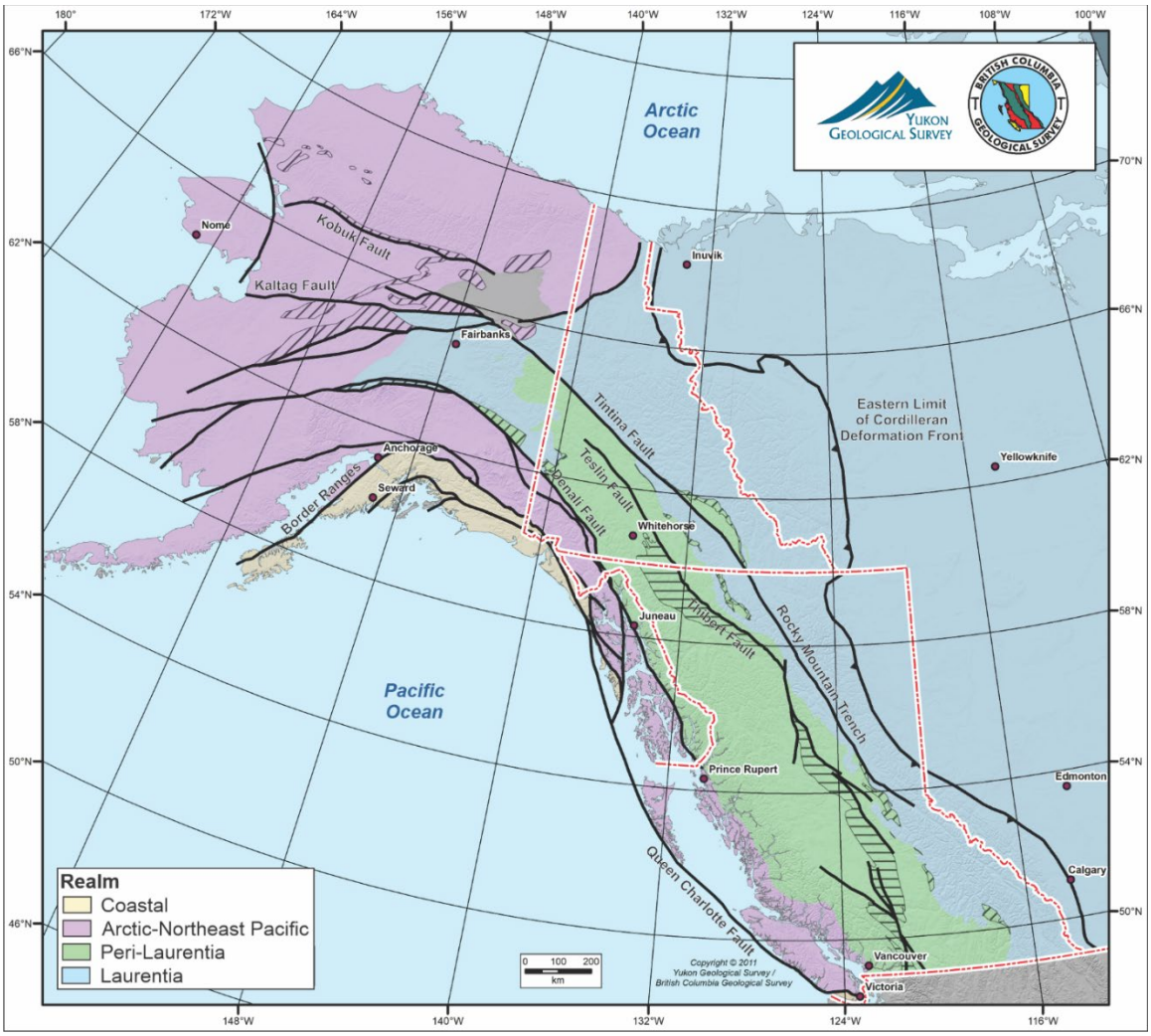

Figure 2.5: Map showing framework of tectonic realms in the northern Cordillera. Modified from Colpron and Nelson (2011).

1. The Laurentian realm refers to the western (present coordinates) margin of Laurentia and the overlying strata deposited onto the margin (Figure 2.5). The Paleozoic architecture includes long-lived, generally shallow-water platforms (e.g., Mackenzie, McDonald, Bow, and McEvoy), and deep-water basins (e.g., Selwyn, Kechika, and Richardson; NAb on Figure 2.4).
2. The peri-Laurentian realm comprises marginal arc, basin, and pericratonic and fore-arc accretionary complexes that evolved proximal to the western Laurentian margin (Figure 2.5). Terranes in this realm include the Slide Mountain, Yukon-Tanana, Stikinia, Cache Creek, and Bridge River allochthonous terranes (Figure 2.4). The Slide Mountain terrane is an oceanic assemblage with stratigraphic associations with both Laurentia (Klepacki and Wheeler, 1985) and the Yukon-Tanana terrane (Murphy et al., 2006) that defines the boundary between the Laurentian and peri-Laurentian realms. The Cache Creek and Bridge River terranes represent accretionary complexes that bounded the peri-Laurentian arc terranes on their oceanward margins.
3. The Arctic-Northeast Pacific realm includes pre-Devonian and younger terranes of Baltican, Caledonian, and/or Siberian affinity that originated in the present circum-Arctic region (Figure 2.5). Terranes in this realm include, but are not limited to, the early Neoproterozoic to Cretaceous Arctic Alaska terrane (Moore et al., 1994), the regionally variable and composite Alexander terrane, the Wrangellia, and the Peninsular terranes (Figure 2.4). The Insular superterrane comprises Paleozoic arc assemblages and overlying Devonian to Permian limestone of the Alexander terrane (Butler et al., 1997), and a largely post-

Carboniferous succession of Permian arc volcanic rocks, Triassic basalt and overlying Upper Triassic limestone of the Wrangellia terrane (Jones et al., 1977). Together terranes of the Arctic-Northeast realm show evidence of a linked tectonic history from the Proterozoic through to the Cretaceous.

4. The Coastal realm comprises upper Mesozoic and Cenozoic accretionary prisms that originated near the eastern margin of the Pacific basin, along or near the Cordilleran margin (Figure 2.5). Terranes in this realm include Paleocene to Eocene seamounts of the Crescent terrane and accretionary complexes filled with sediment shed from the developing Cordillera (Figure 2.4).

2.1.2 Late Proterozoic to Late Triassic Cordilleran (Passive Margin) Tectonics

Between the Late Proterozoic and Early Mississippian, major periods of rifting occurred along the ancestral northwestern American margin (Nokleberg et al., 2000). As such, prior to the Late Devonian (Dickinson, 2004) or Mississippian (Miall and Blakey, 2019), the western continental margin of North America was either a divergent (passive) margin facing the paleo-Pacific (Panthalassa) Ocean or a backarc basin. (Figure 2.3; Miall and Blakey, 2019).

During the Ediacaran, break-up of the Rodinia supercontinent occurred, and is recorded in three depositional grand-cycles within the upper Windermere Supergroup of the northern Cordillera (Narbonne and Aitken, 1995; Dalrymple and Narbonne, 1996; Turner et al., 2011). The break-up of Rodinia was likely coeval with deposition of coarse,

siliciclastic rocks of the Hyland Group into the Selwyn basin (Gordey and Anderson, 1993; Colpron et al., 2013).

The extension-related processes associated with continental break-up changed to subduction-related processes in the Devonian, with eastward subduction of oceanic crust initiating the development of peri-Laurentian magmatic arcs along the length of the North American Cordillera. During the late Devonian to Permian, backarc extension (Figure 2.6) led to opening of the Slide Mountain Ocean and oceanward migration of the peri-Laurentian Yukon-Tanana, Quesnellia, and Stikinia arcs (Colpron et al., 2007; Nelson et al., 2013).

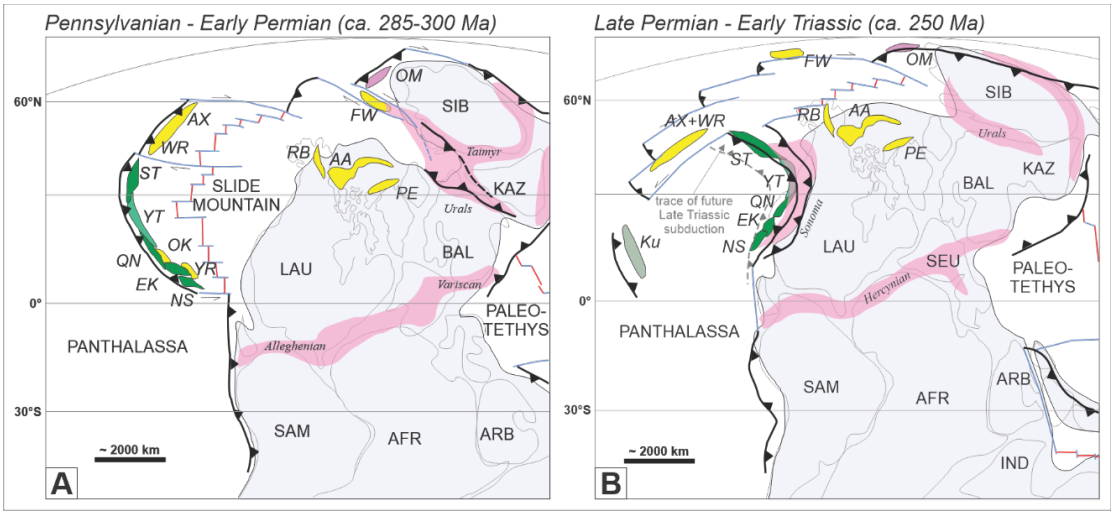

Figure 2.6: Paleogeographic reconstruction of A) Late Paleozoic (Pennsylvanian to Early Permian), and B) end Paleozoic (Late Permian to Early Triassic).

Terrane abbreviations: AA, Arctic Alaska; AX, Alexander; EK, Eastern Klamaths; FW, Farewell; Ku, Kutcho Arc; NS, Northern Sierras; OK, Okanagan; OM, Omulevka; PE, Pearya; QN, Quesnellia; RB, Ruby; ST, Stikinia; WR, Wrangellia; YR, Yreka; YT, Yukon-Tanana. Continent abbreviations: AFR, Africa; ARB, Arabia; BAL, Baltica; IND, India; KAZ, Kazakhstan; LAU, Laurentia; SAM, South America; SEU, Southern Europe; SIB, Siberia. Modified from Nelson et al. (2013).

In Canada, the continental margin remained passive until the Late Triassic. During this period, the Canadian portion of the continental margin accumulated craton-derived shallow to deep marine deposits in numerous basins including the Selwyn Basin (Miall, 2019; Miall and Blakey, 2019).

Closure of the Slide Mountain Ocean occurred in the Triassic. Final closure of the ocean was completed by the end of the Triassic and initiated accretion of the Yukon-Tanana and Quesnellia terranes to the continental margin (Figure 2.6 and Figure 2.7; Nelson et al., 2013).

2.1.3 Late Triassic to Middle Cretaceous Cordilleran (Terrane Accretion) Tectonics

From about the Late Triassic through the mid-Cretaceous, a succession of island arcs and tectonically paired subduction zones formed near the continental margin. These included the Yukon-Tanana, Stikinia, and Quesnellia arcs, and the Peninsula-Alexander-Wrangellia composite terrane. Oblique convergence between the arcs and the continental margin initiated in the mid-Jurassic and resulted in fragmentation, and displacement of formerly continuous arcs (Figure 2.7 and Figure 2.8). These fragments were subsequently accreted to the continental margin and resulted in substantial growth of the North American continent (Nokleberg et al., 2000).

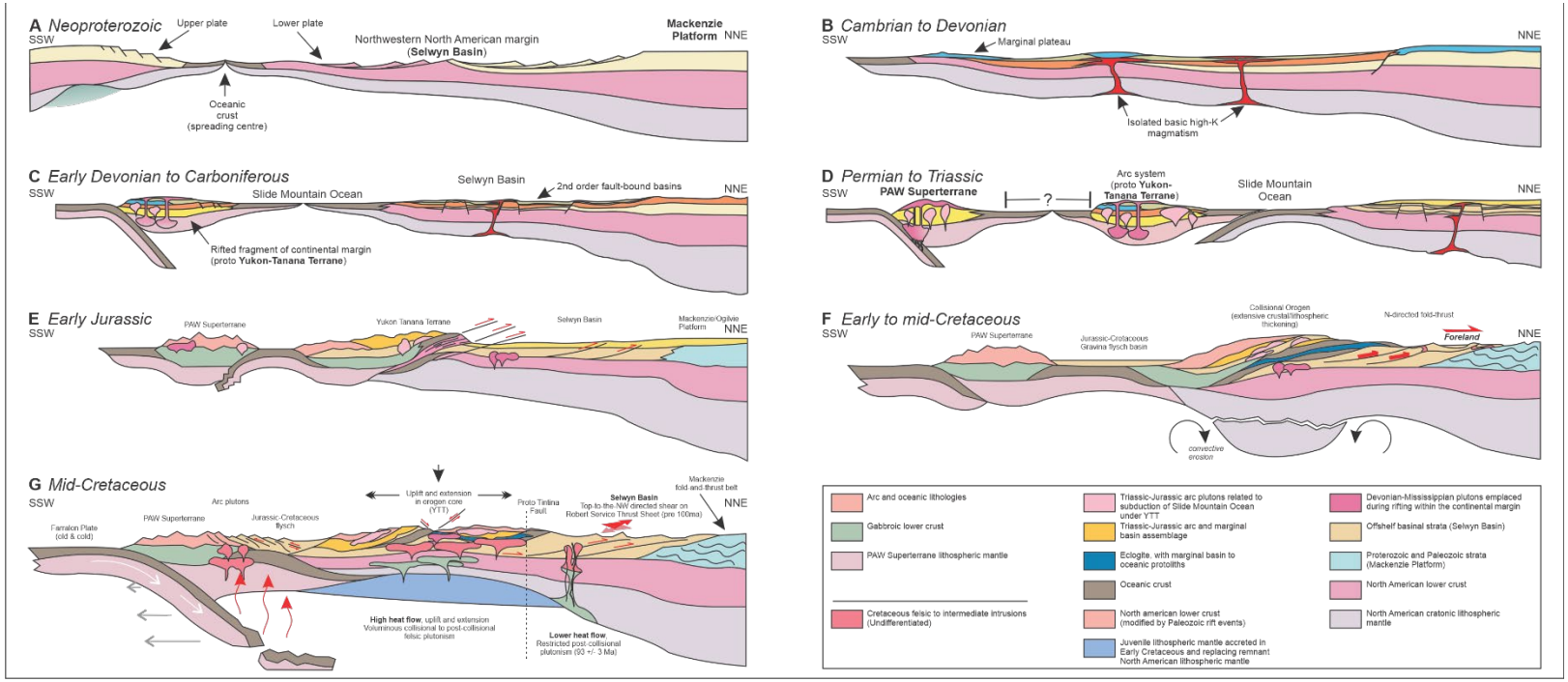

Figure 2.7: Schematic cross sections across the northern Cordilleran orogen (approximately through the west-central Yukon) illustrating the development of the Cordilleran margin. Modified after Mair et al. (2006).

A: The epicratonic Selwyn Basin formed in a divergent-margin setting that resulted from rifting at 760–730 Ma (Ross et al., 1995; Colpron et al., 2002). B: Early Paleozoic to the Early Devonian deposition of thin carbonate and shale units into Selwyn Basin implies quiet and periodically anoxic conditions in a basin isolated from an open ocean. C: Early Devonian to Early Mississippian backarc rifting initiated opening of the Slide Mountain Ocean (Piercey et al., 2003). D: Late Triassic to Early Jurassic closure of the Slide Mountain Ocean by west-dipping subduction led to the collision of the Yukon-Tanana terrane with the continental margin (Hansen, 1990; Creaser et al., 1999; Nelson and Friedman, 2004). E: Early Jurassic onset of collision and over-thrusting of oceanic and arc components over the continental margin. F: Late Jurassic to Early Cretaceous thrusting of Yukon-Tanana terrane over the continental margin resulted in broadly north-directed thrusting of Selwyn Basin strata. G: Uplift and extension in the core of the orogen (Yukon-Tanana terrane uplands) followed substantial crustal thickening and loading. The extension in the orogen core was coeval with the waning stages of thrust-fault–related deformation in Selwyn Basin.

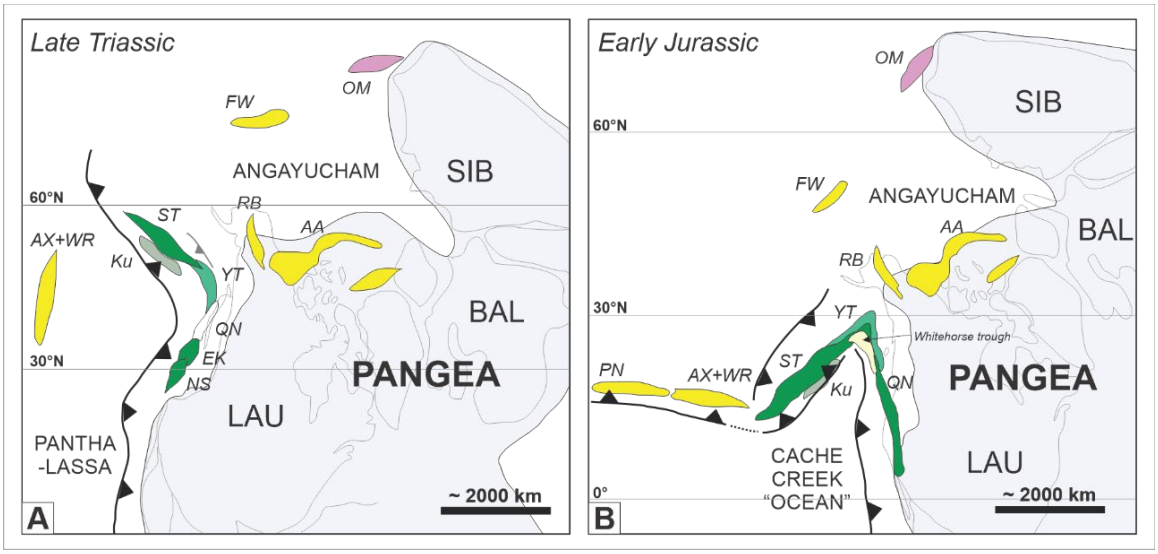

Figure 2.8: Paleogeographic reconstructions of the; A) Late Triassic and B) Early Jurassic during exhumation of the Yukon-Tanana terrane.

Terrane abbreviations: AA, Arctic Alaska; AX, Alexander; EK, Eastern Klamaths; FW, Farewell; Ku, Kutcho; NS, Northern Sierras; OM, Omulevka; PN, Peninsula; QN, Quesnellia; RB, Ruby; ST, Stikinia; WR, Wrangellia; YT, Yukon-Tanana. Continent abbreviations: BAL, Baltica; LAU, Laurentia; SIB, Siberia. Modified from Nelson et al. (2013).

The Middle Jurassic to middle Cretaceous was characterised by the subduction of oceanic crust along the continental margin, punctuated by the arrival of intraoceanic arcs subducting seafloor down to the west, rather than the east (Godfrey and Dilek, 2000, Ingersoll, 2000, Dickinson, 2001; 2004). In Canada, closure of the Cache Creek Ocean led to collision of the Quesnellia, Stikinia, and Yukon-Tanana terranes with the continental margin (Figure 2.9; Mihalynuk et al., 1994) with obduction occurring circa 172 Ma (U-Pb zircon and $^{40}Ar/^{39}Ar$; Mihalynuk et al., 2004).

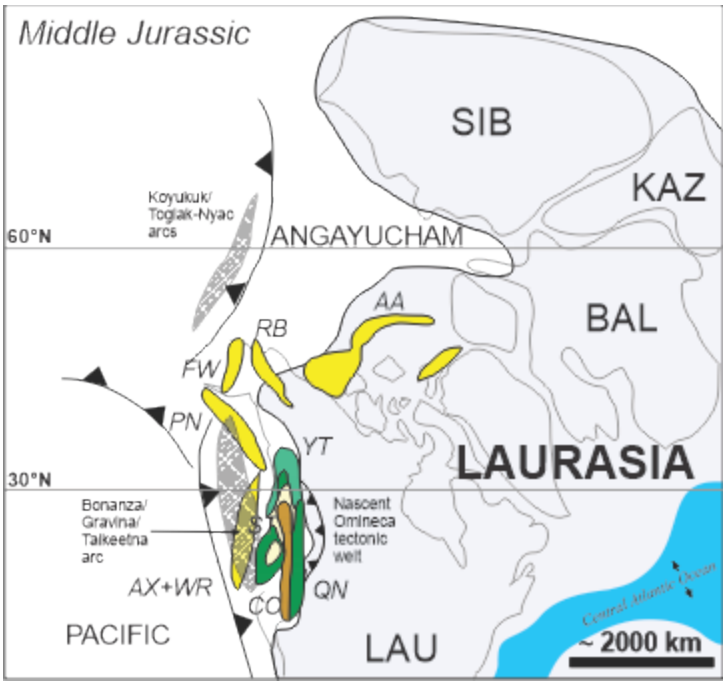

Figure 2.9: Paleogeographic reconstruction of the Middle Jurassic.

Terrane abbreviations: AA, Arctic Alaska; AX, Alexander; CC, Cache Creek; FW, Farewell; PN, Peninsula; QN, Quesnellia; RB, Ruby; ST, Stikinia; WR, Wrangellia; YT, Yukon-Tanana. Continent abbreviations: BAL, Baltica; KAZ, Kazakhstan; LAU, Laurentia; SIB, Siberia. Modified from Nelson et al. (2013).

Middle Jurassic accretion fundamentally changed the emerging Canadian Cordillera from a set of loosely connected arc and pericratonic terranes to a single, progressively thickening transpressional/transtensional orogen, within which crustal-scale detachments and transcurrent faults were increasingly linked (Evenchick et al., 2007; Nelson et al., 2013). Following accretion of the Stikinia and Quesnellia terranes, the Insular superterrane initiated docking with the continental margin in Middle to early Late Jurassic (Figure 2.9; Dickinson, 2004; Nelson et al., 2013). The timing of closure between the Insular and peri-Laurentian terranes varies considerably along strike, with initial accretion of the Wrangellia terrane occurring in the Middle Jurassic (Bajocian) in

the Blue Mountains of Oregon (Follo, 1992; White et al., 1992), and in the Late Jurassic (Kimmeridgian) in southwestern Alaska (Clift et al., 2005). The diachronous timing may suggest initial convergence was a promontory-promontory collision.

Early to middle-Cretaceous heterogeneous strain across the northern Cordillera produced varying regional structural styles (Nelson et al., 2013):

- Coast belt and Skeena fold belt: sinistral transpression;
- Omineca belt and Rocky Mountain foreland fold and thrust belt: east-vergent, linked ductile and brittle compressive deformation;
- Eastern Intermontane region: dextral transpression; and
- Selwyn basin and Yukon-Tanana uplands: NW-vergent, orogen-parallel ductile deformation, thrusting, and extension.

Initiation of large, orogen-parallel dextral faults occurred in the Intermontane region between 115 and 95 Ma, including the Teslin Cassiar and Teslin-Thibert-Kutcho faults. These faults are associated with Early Cretaceous syn-kinematic and late-kinematic plutons (Johnston, 1999; Gabrielse et al., 2006; Figure 2.10 and Figure 2.11) that include the metallogenically important Tombstone/Tungsten and Fairbanks suites (Mair et al., 2006; Nelson et al., 2013).

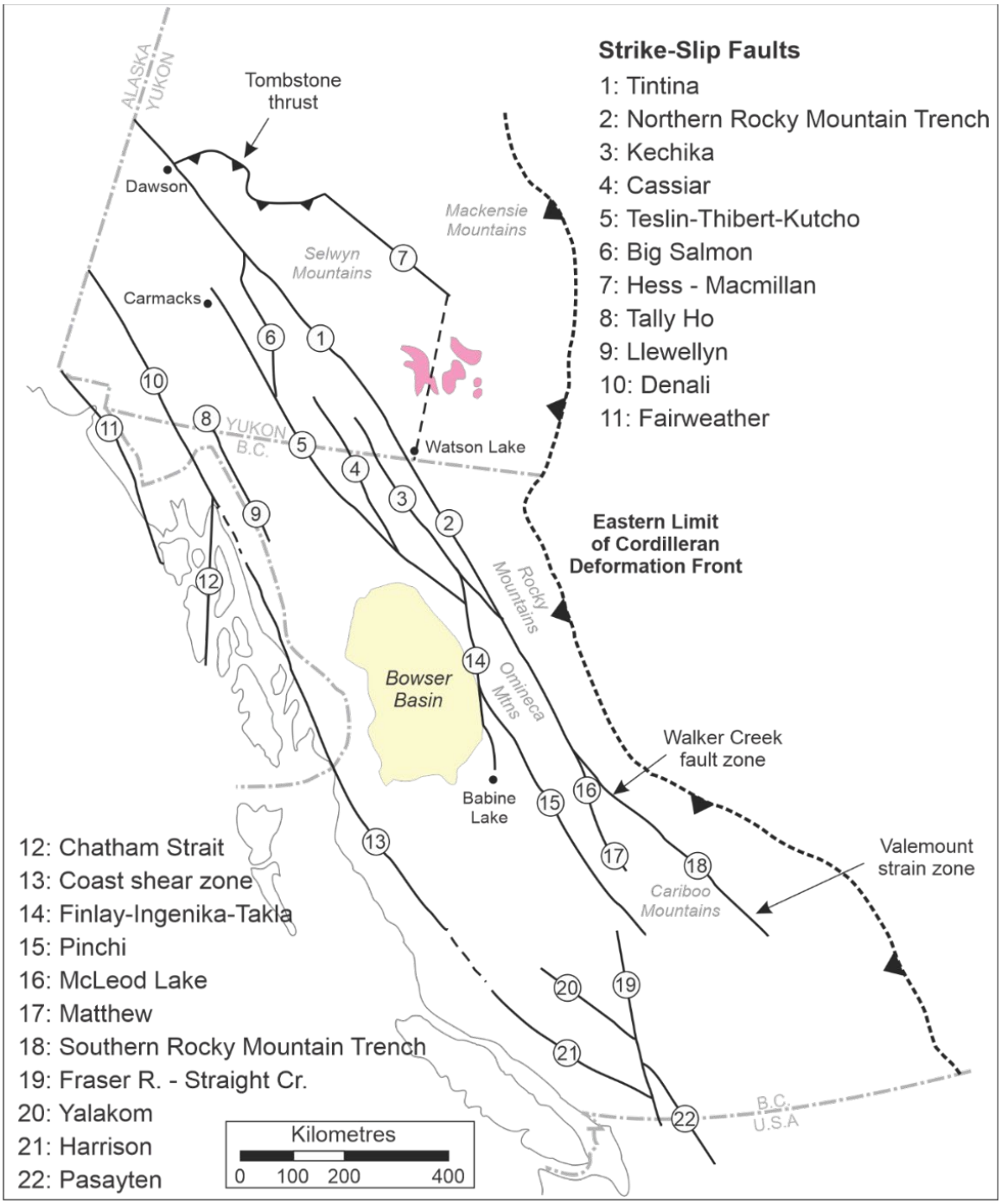

Figure 2.10: Distribution of regional, orogen-parallel, strike-slip faults in the Canadian Cordillera.

Pink areas NE of the Tintina Fault in southeastern Yukon and southwestern Northwest Territories are mid-Cretaceous plutons. Dashed line in the same area represents the trend of a late Early Cretaceous extensional core zone linking strike-slip faults in northern British Columbia and southern Yukon with the Hess-Macmillan fault system. Modified from Gabrielse et al. (2006)

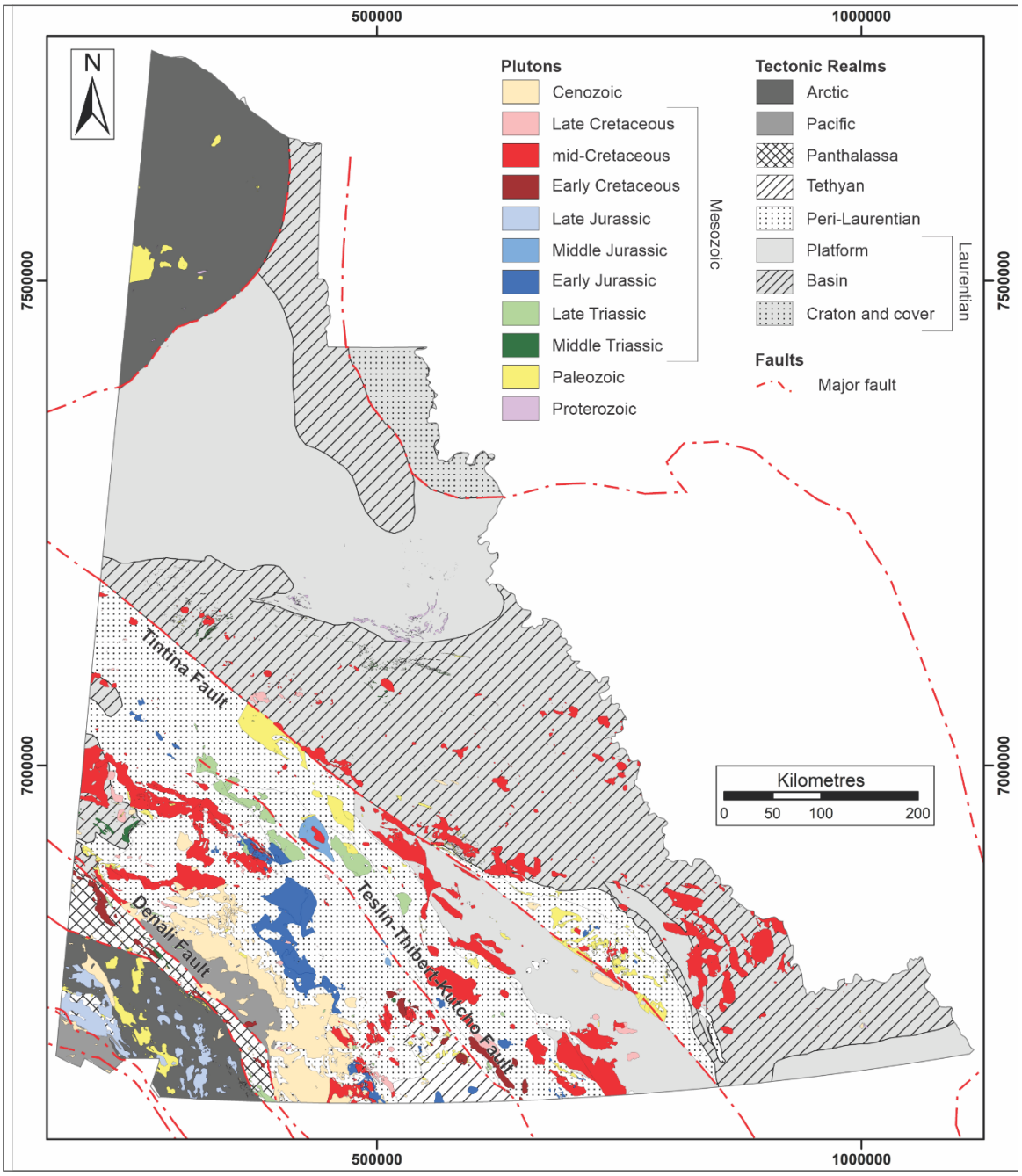

Figure 2.11: Map of Yukon showing distribution of plutons by age, with a focus on Mesozoic plutons.

Pluton age and location data from Colpron et al. (2016) Yukon bedrock geology map and associated database. Maximum age column in database was used to define ages of plutons. Terrane data from Colpron and Nelson (2011).

2.1.4 Late Cretaceous to Eocene Tectonics – The Baja BC Controversy

The Late Cretaceous to the end of Eocene tectonic evolution of the northern Cordillera is the source of some controversy. During the middle to Late Cretaceous, motion of oceanic plates west of the Cordillera was northward and included a large component of orogen-parallel dextral displacement (Engebretson et al., 1985; Johnston et al., 1996b; Johnston, 1999). Major plate reconfiguration occurred in the NE Pacific Ocean between the Paleocene and Eocene, with the Kula, Farallon, and Resurrection plates subducting beneath the North American margin by the Cenozoic (Haeussler et al., 2003). During this period the Cordilleran magmatic arc stepped oceanward, extensive Late Cretaceous plutonism formed the major Cordilleran batholith belt along the arc axis (Dickinson, 2004), and braided sets of post-accretionary, orogen-parallel, mainly dextral strike-slip faults were formed including, but not limited to the Tintina, Denali (Figure 2.10), and Queen Charlotte faults. The debate arises from the amount of northward translation that occurred along these faults and has been termed the Baja BC controversy (Irving, 1985).

The Baja BC hypothesis asserts that outboard terranes of the Cordillera (i.e. the Insular and Intermontane terranes) underwent post-mid Cretaceous northward translation of up to 4,000 km with respect to the continental interior, and is largely derived from interpretations of paleomagnetic data (Beck and Noson, 1972; Beck et al., 1981; Bogue et al., 1995; Wynne et al., 1995; 1998; Irving et al., 1996; Ward et al., 1997; Butler et al., 2001; Haskin et al., 2003; Housen et al., 2003; Bogue and Grommé, 2004; Kim and Kodama, 2004; Enkin, 2006; Enkin et al., 2006b; Rusmore et al., 2013). Alternatively, geological, geophysical, and rare paleomagnetic studies suggest that cumulative dextral

offset along Cretaceous to Eocene, orogen-parallel fault is approximately 1000 km (Butler et el., 2001), and has been calculated at 860 km by Gabrielse et al. (2006). This hypothesis is refered to here as the moderate translation model.

At Keno Hill, district-scale deformation associated with dextral strike-slip fault movement and northward translation of the outboard terranes is relatively minor; however, an understanding of the two competing regional models is important to correlate Ag-Pb-Zn mineralisation at Keno Hill with economic mineralisation elsewhere in the Cordillera. While evidence for both models is compelling, regional interpretations presented in this thesis support the moderate translation model. For balance, brief synopses of both models are presented below.

Baja BC Hypothesis

Paleomagnetic studies since the early 1970s indicate that during the middle Cretaceous, the western edge of northern North America was situated alongside California and northern Mexico (Housen and Beck, 1999) and that post-mid-Cretaceous, between about 90 and 60 Ma (e.g. Irving, 1985; Irving et al., 1996; Enkin, 2006), the Insular and pericratonic terranes migrated northward with respect to the continental interior over distances ranging in estimate from 1,000 to 4,000 km (Beck and Noson, 1972; Beck et al., 1981; Bogue et al., 1995; Wynne et al., 1995; 1998; Irving et al., 1996; Ward et al., 1997; Butler et al., 2001; Haskin et al., 2003; Housen et al., 2003; Bogue and Grommé, 2004; Kim and Kodama, 2004; Enkin, 2006; Enkin et al., 2006b; Rusmore et al., 2013). A selection of estimated northward displacements of the outboard terranes as defined by

paleomagnetic studies are outlined in Table 2.1. The data shown in Table 2.1 do not comprise an exhaustive list of all published data but are a brief synopsis showing the ranges of displacement estimated from paleomagnetic data. While not all reported paleomagnetic data supports the Baja B.C. hypothesis (e.g., Butler et al., 2001; Haskin et al., 2003; McCausland et al., 2005), in general the data indicate northward displacement of at least 1,500 km.

In addition to paleomagnetic data, detrital zircon data from the Nanaimo Group (Guest et al., 2015) and paleobotanical data from the Winthrop Formation in the Tyaughton-Methow Basin, southern B.C. (Miller et al., 2006) have been used to support the Baja BC hypothesis. With regard to the detrital zircon data, it should be noted that small populations of Archean and Early Proterozoic zircons in the Cretaceous Queen Charlotte, Nanaimo, and Methow basins of the Insular Terrane are considered to have been derived from the Canadian Shield, and as such indicate deposition in northern latitudes, and are incompatible with the Baja B.C. hypothesis (Mahoney et al., 1999).

Table 2.1: Summary of estimated northward displacement of outboard terranes based on paleomagnetic data, listed in chronological order of publication date.

Author	Displacement	Terrane/Suite/Group	Location	Compatible with Baja B.C.?
Rusmore et al. (2013)	1700 km	Coast Plutonic Complex	Western B.C.	✓
Enkin et al. (2006b)	Multi-stage "yo-yo" translation.	Silverquick – Powell succession, Tyaughton-Methow Basin, Stikinia Terrane, Intermontane	Southern B.C.	✓
McCausland et al. (2005)	360 ± 575 km	Swede Dome stock, Yukon Tanana Terrane	Central Yukon	✗
Bogue and Grommé (2004)	2350 km	Duke Island Complex, Insular Terrane	Alaska	✓
Kim and Kodama (2004)	1600 km	Nanaimo Group	Vancouver Island	✓
Haskin et al. (2003)	1050 ± 450 km	Spences Bridge Group, Tyaughton-Methow Basin, Coast Belt.	Southern B.C.	✗
Butler et al. (2001)	~ 1000 km	Duke Island complex and MacColl Ridge Formation, Silverquick – Powell succession, Nanaimo Group, Mt Stuart Batholith	Alaska and Washington, USA; southern B.C.	✗
Wynne et al. (1998)	1900 ± 700 km	Carmacks Volcanic Group	South and central Yukon	✓
Cowan et al. (1997)	3000 km	Mt Stuart Batholith, Mt Tatlow, Tyaughton Basin, Duke Island Complex; Spences Bridge Group, Carmacks volcanics; MacColl Ridge Formation	Alaska and Washington, USA; Vancouver Island, northern and southern B.C.	✓
Ward et al. (1997)	No displacement stated, but suggests equivalent latitude to present day Baja, California	Nanaimo Group	Vancouver Island	✓
Irving et al. (1996)	2000 to 4000 km	Coast Domain: Nicolai Formation, Karmutsen Formation, Hound Island volcanics, Duke Island complex, MacColl Ridge Formation, Silverquick-Powell Creek succession, Mt Stuart batholith	Alaska and Washington, USA; Vancouver Island and southern B.C.	✓
Irving et al. (1996)	1000 to 2000 km	Interior Domain: Carmacks Volcanic Group, Spences Bridge Group	Southern B.C.; south and central Yukon	✓
Johnston et al. (1996b)	1900 km	Carmacks Volcanic Group	South and central Yukon	✓
Bogue et al. (1995)	3000 ± 1300 km	Duke Island Complex	Alaska	✓
Irving et al. (1995)	1100 ± 600	Spences Bridge Group, Tyaughton-Methow Basin, Coast Belt	Southern B.C.	✓
Wynne et al. (1995)	3000 ± 500 km	Silverquick – Powell succession, Tyaughton-Methow Basin, Stikinia Terrane, Intermontane	Southern B.C.	✓
Beck (1991)	> 1000 km		Baja and southern California	✓
Chamberlain and Lambert (1985)	1500 km	Malton Gneiss complex, southern B.C.	Southern B.C.	✓
Irving (1985)	2400 km	Spuzzum and Porteau plutons, Coast Plutonic Complex	Southern B.C.	✓
Beck and Noson (1972)	2500 to 3500 km	Mt Stuart Batholith,	Washington, USA	✓

Paleomagnetic data have commonly been interpreted to indicate solely northward migration of the outboard terranes, whereby the Insular Terrane migrated 1,000 to 2,000

km before docking with the Intermontane Terrane, after which the amalgamated terranes migrated another 1,000 to 2,000 km north (e.g., Irving et al., 1996). Mahoney et al. (2001), Enkin (2006), and Enkin et al. (2006b) have suggested that the Intermontane and the Insular terranes were amalgamated by the Albian (latest Early Cretaceous) and then travelled south together to the latitude of the Baja Peninsula in the early Late Cretaceous, and subsequently migrated north again to their approximate present position by the Eocene (Riddell, 2011). Mahoney et al. (2001) consider the large magnitude of this suggested multi-stage "yo-yo" translation to be geologically unreasonable within the current understanding of Late Cretaceous terrane displacements and oceanic plate trajectories, and suggest their results may be the result of: 1) differential compaction between packages; 2) the initial dip of the strata; 3) the reliability of the Late Cretaceous reference pole; 4) concordance of problematic paleomagnetic data with the Late Cretaceous Long Normal SuperChron; 5) a rapid polar wander episode in the Late Cretaceous; or 6) inaccuracies in the hot-spot reference frame and incomplete understanding of ocean plate trajectories.

The results of various paleomagnetic studies suggest that most northward displacement took place along structures located east of the Selwyn Basin (Johnston, 1999; Enkin et al., 2006a), however, faults along which such large displacements occurred have not been identified (Kerr, 1995; Mahoney et al., 1999; Nelson et al., 2013; Hildebrand, 2015). Johnston (1999) suggested that syn-kinematic intrusions, adjacent to middle Cretaceous faults may have accommodated more than 400 km of dextral displacement, however

Johnston (1999) also notes that structures along which the displacement occurred have not been identified and suitable syn-kinematic intrusions are rare.

Despite the wealth of data, numerous authors have questioned the validity of much of the paleomagnetic data. Butler et al. (2001) and Nelson et al., (2013) suggest numerous factors that may have artificially shallowed the magnetic inclination and produced errors in interpretations. These include

- Pre-magnetisation folding in the Duke Island ultramafic complex (Bogue et al., 1995);
- Authigenic magnetite in the Silverquick – Powell Creek succession (Wynne et al., 1995);
- Deformation and chemical remagnetisation by alteration and compaction in the Nanaimo Group (Ward et al., 1997);
- A complex and disputed magnetic history in the Mount Stuart batholith (Beck et al., 1981); and
- Paleohorizontal direction derived from columnar joints and lahar flows in the Carmacks Group, neither of which are reliable paleohorizontal indicators (Enkin et al., 2006a).

Butler et al. (2001) suggested that interpretation of large magnitude displacements is the result of "sparse and piecewise application of paleomagnetism and supporting geologic and geochemical methods to an orogen which experienced complex deformation and from which supracrustal rocks have largely been removed". Nelson et al. (2013) state that abundant geological data in the Intermontane region preclude large-scale transport of

terranes north of the Denali Fault, and that NE of the Tintina Fault well-documented geological relationships within the continental margin preclude the existence of faults that could have accommodated the additional 1,500 km of displacement implied by the Carmacks poles.

Moderate Translation Model

Geological mapping and geophysical studies do not support such large estimates of northward transport. Rather, these suggest a cumulative dextral offset along Cretaceous to Eocene, orogen-parallel faults of 860 km with respect to the North American craton (Gabrielse et al., 2006). Approximately 430 km of dextral offset was accommodated by the Tintina Fault (Figure 2.12; Gabrielse et al., 2006), and 300 – 400 km of dextral offset was accommodated by the Denali Fault (Eisbacher, 1976; Lowey, 1998).

The 430 km of dextral offset along the Tintina Fault calculated by Gabrielse et al. (2006) was determined from the correlation of 8 geological elements NE of the fault, with their counterparts on the opposite side of the fault in either eastern Alaska or elsewhere in Yukon (Table 2.2; Figure 2.12). This calculation is supported by 3D inversion and interpretation of gravity data applied to the crustal architecture of the northern Cordillera by Hayward (2019). The gravity data show low-density zones associated with middle to Late Cretaceous granitic intrusions, and Neoproterozoic and Cretaceous sedimentary rocks. The depth extent of low-density zones defines a shallow to moderately NE-dipping surface that is interpreted to be a pre-Eocene décollement, which is dextrally displaced by approximately 430 km across the Tintina Fault (Hayward, 2019).

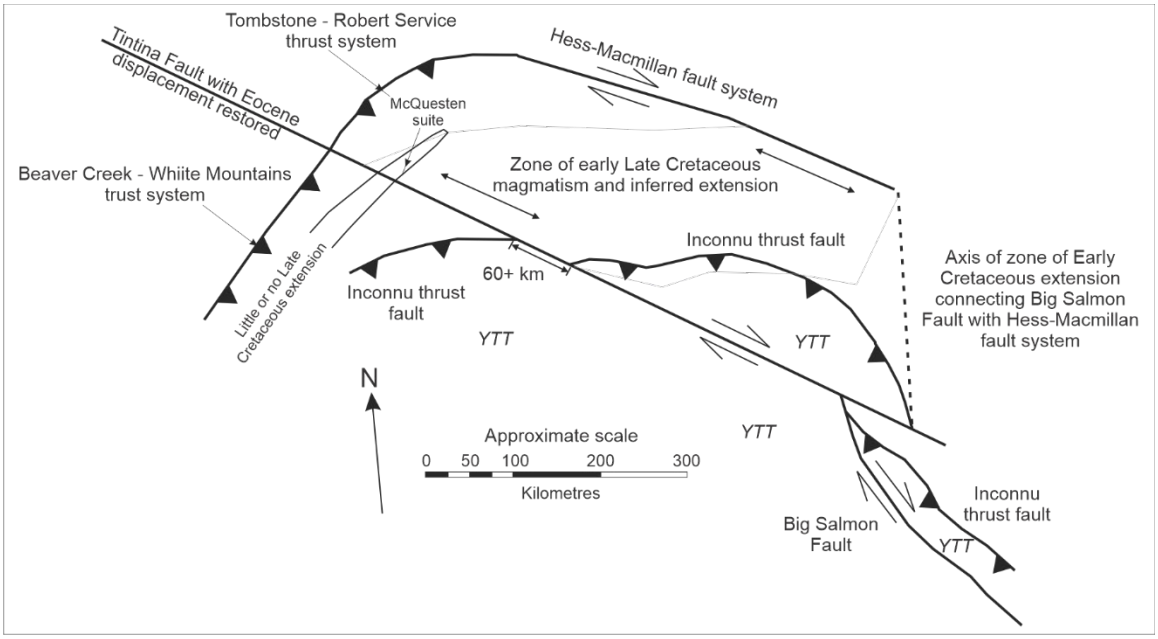

Figure 2.12: Schematic map of the northern Cordillera during the Late Cretaceous showing palinspastic restoration of 430 km of dextral strike-slip movement along the Tintina Fault. Extension during magmatism in Selwyn basin NE of the Tintina Fault accounts for an additional 60 km of offset of Inconnu thrust fault. YTT = Yukon-Tanana terrane. Modified from Gabrielse et al. (2006).

In addition to consistent geological relationships, limited paleomagnetic and detrital zircon data also support the model of moderate northward transport (Mahoney et al., 1999). Butler et al. (2001) interpreted discordant paleomagnetic results from plutonic rocks in the Coast Mountain belt near Prince Rupert, B.C. to be "consistent with a Cretaceous paleogeography that limits post-mid-Cretaceous northward motion to ~1000 km". McCausland et al. (2005) retrieved paleomagnetic results from the Swede Dome stock (coeval with Carmacks volcanism) in the Yukon Tanana Terrane that indicate northward translation of 360 ± 575 km.

Table 2.2: Correlative geological elements offset by the Tintina Fault summarised from Gabrielse et al. (2006) and references therein.

NE of the Tintina Fault		SW of the Tintina Fault
Early Cretaceous Tombstone and Robert Service thrust faults; Mississippian KHQ and Triassic metamafic sills.	→	Beaver Creek and White Mountain thrust faults; Mississippian Globe Quartzite and Triassic metamafic sills.
Upper boundary of the Tombstone strain zone SE of Dawson.	→	Gradual metamorphic transition of less deformed Wickersham grit to highly deformed Fairbanks schist north of Fairbanks.
Early Cretaceous, Au-associated, Tombstone plutonic suite.	→	Unnamed belt of Au-associated late Early to early Late Cretaceous metaluminous plutons extending from near Fairbanks to the Tintina Fault.
Inconnu thrust fault which juxtaposes the North American continental margin sequence with rocks of the Slide Mountain and Yukon-Tanana terranes.	→	Unnamed structure that separates rocks of the Slide Mountain and Yukon-Tanana terranes from the North American continental margin sequence near Eagle, Alaska.
Slide Mountain Terrane blueschist and eclogite assemblage with limestone, lower Permian basalt, variegated chert, and serpentinised ultramafic rock coupled with Triassic, post-orogenic conglomerate, and mid-Paleozoic carbonaceous clastic rocks.	→	Belt of blueschist, lower Permian basalt, chert, ultramafic rock, middle Permian limestone, and undated clastic rocks.
Lower Paleozoic rocks of the McEvoy platform.	→	Northern end of the Cassiar platform where rocks of are identical to the McEvoy platform.
Southern end of a zone of Early Cretaceous extension and plutonism inferred to be a transfer zone kinematically linking the Hess-Macmillan Fault to strike slip faults on opposite side of the Tintina Fault (e.g., Big Salmon Fault).	→	Early Cretaceous Big Salmon Fault.
Late Cretaceous McQuesten plutonic suite.	→	Unnamed belt of southwestward-trending Late Cretaceous Sn-bearing peraluminous granitic plutons.

2.2 Geology of the Selwyn Basin

The Selwyn Basin covers an area of approximately 700 km in length by 200 km width across central Yukon and southwestern Northwest Territories (Figure 2.13). It forms part of an area between the North America craton to the east, and the Tintina Fault to the west is an area characterised by a complex array of Paleozoic basins and arches (Miall, 2019). Platform strata overlie the innermost part of the Cordilleran belt and are separated from the peri-Laurentian accreted terranes by Neoproterozoic to Mesozoic slope, basin, and shelf facies strata including rocks of the Selwyn Basin (Mair et al., 2006).

The Selwyn Basin comprises a Proterozoic to Paleozoic miogeoclinal slope-to-basin succession of clastic and carbonaceous sedimentary rocks deposited in an epicratonic rift basin off the ancestral North American continental margin (Gabrielse, 1967; Abbott et al., 1986; Gabrielse and Yorath, 1991; Gordey and Anderson, 1993; Mair et al., 2006). The sedimentary sequence is intruded by numerous Cambrian, Triassic, and middle to Upper Cretaceous mafic to felsic intrusive rocks.

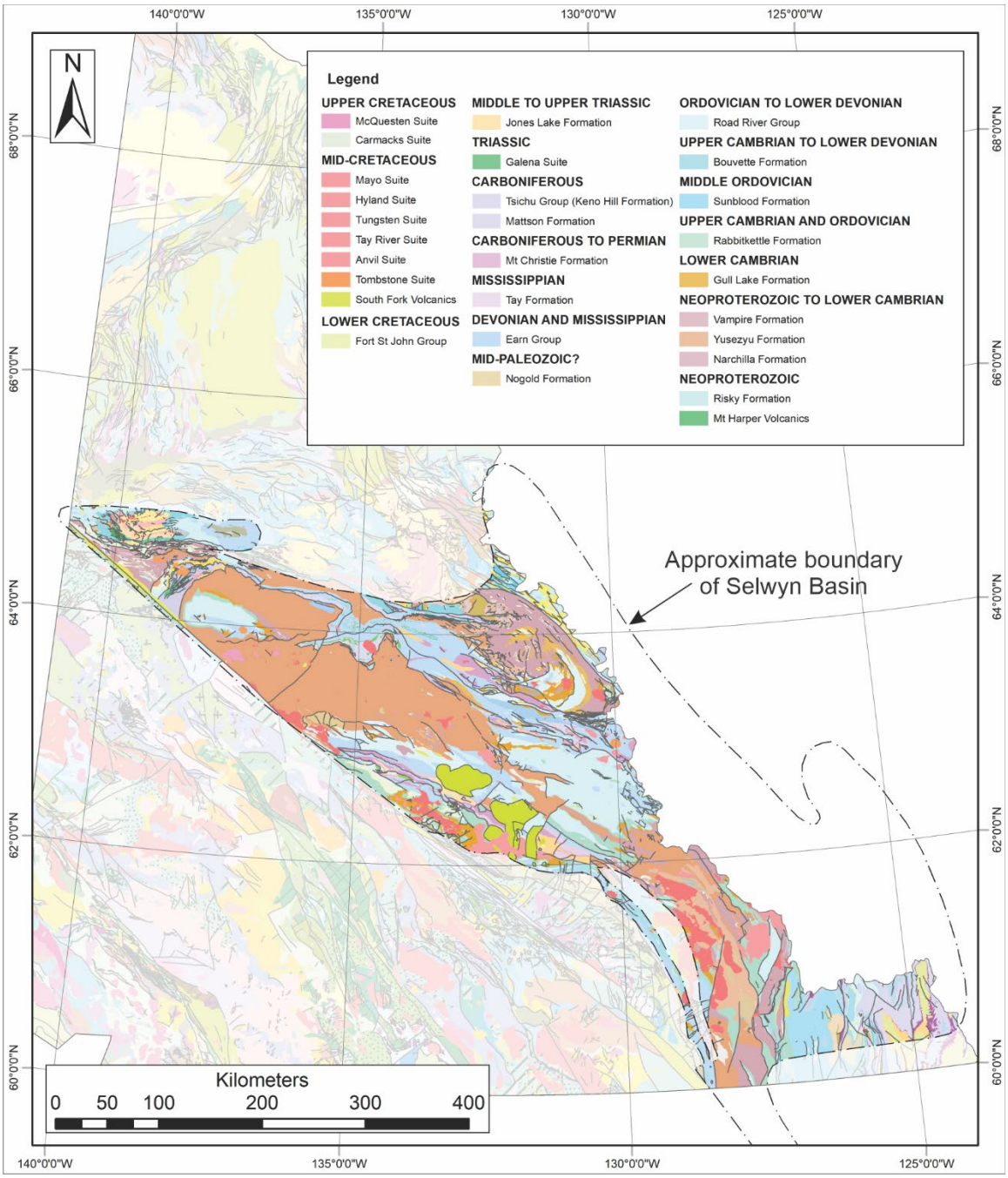

Figure 2.13: Simplified geological map of Yukon highlighting the bedrock geology of the Selwyn Basin and selected lithological units.

Bedrock geology data from Colpron et al. (2016); Approximate boundary of the Selwyn Basin from Fernandes et al. (2017).

To the north the basin is bound by the Dawson Fault. To the NE and east, the basinal successions merge on to Proterozoic clastic, carbonate, and volcanic rocks of the Mackenzie platform. To the south, the Selwyn Basin narrows in plan view across the Liard Line, a Paleoproterozoic to Neoproterozoic basement transfer fault (Figure 2.1; Hansen et al., 1993; Cecile et al., 1997; Lund, 2008); and a thin sliver of coeval basinal strata, the Kechika Trough continues south into British Columbia for approximately 500 km (McClay et al., 1989). To the SW the Selwyn Basin is juxtaposed against the peri-cratonal Yukon-Tanana Terrane and relatively high-standing Cassiar and McEvoy platforms along the Tintina Fault (Nelson et al., 2013).

2.2.1 Metasedimentary Rocks

Gordey (2013) states that the strata of the Selwyn Basin can be subdivided into four main groups. These include:

1. Neoproterozoic to Lower Cambrian turbiditic sandstone and shale of the Hyland Group (Figure 2.13; Fritz et al., 1983; 1991; Gordey and Anderson, 1993); Lower Cambrian shale of the Gull Lake Formation (Figure 2.13; Gordey and Anderson, 1993; Murphy, 1997); Late Cambrian to Early Ordovician laminated, siliceous limestone, and siltstone of the Rabbitkettle Formation (Figure 2.13; Gordey and Anderson, 1993; Murphy, 1997); and Early Ordovician to Early Devonian carbonaceous shale, chert and dolomitic mudstone of the Road River Group (Figure 2.13; Gordey and Anderson, 1993; Murphy, 1997). These represent a relatively deep-water assemblage with a minimum aggregate thickness of

approximately 3,000 m (Gordey, 2013) that was flanked to the SW (present co-ordinates) by shallow water Silurian to Devonian carbonate and clastic rocks of the McEvoy Platform (Gordey, 2013).

2. Devonian to Mississippian turbiditic quartz-chert sandstone and chert-pebble conglomerate of the Earn Group, separated from Hyland Group rocks by a regional unconformity (Figure 2.13). The Earn Group was deposited in submarine fan complexes and is characterised by complex internal stratigraphy with internal unconformities and extreme changes in lithology, thickness, and facies (Abbott et al., 1986; Garzione et al., 1997; Mair et al., 2006). The Earn Group may have an aggregate thickness of 1,200 metres (Gordey, 2013).
3. Mississippian to Triassic mixed carbonate and siliciclastic rocks (Figure 2.13) interpreted to have been deposited on a shallow marine shelf. The aggregate thickness for this sequence is approximately 1,700 m (Gordey, 2013).
4. Rare occurrences of Early Cretaceous deep marine, chert-bearing clastic strata with an aggregate thickness of 120 m (Gordey, 2013).

Neoproterozoic to Early Cambrian Rocks

Variably deformed, gritty quartz sandstone, shale, maroon argillite, chloritic schist, and carbonate rocks of the Hyland Group underlie most of the Selwyn Basin (Gordey and Anderson, 1993; Murphy, 1997; Mair et al., 2006). The Hyland Group is interpreted as a broad turbidite fan and represents the slope-to-basin facies equivalent of the uppermost Windermere strata of the Mackenzie Platform (Ross, 1991; Mair et al., 2006). The age of

Hyland Group strata is constrained by trace fossil analysis to the latest Neoproterozoic to Early Cambrian (Fritz et al., 1983, 1991; Gordey and Anderson, 1993).

The Hyland Group comprises two main lithostratigraphic formations: the Yusezyu and Narchilla formations (Roots, 1997; Figure 2.13). The Yusezyu Formation is the oldest unit exposed in the basin and comprises a monotonous succession of variably deformed fine- to coarse-grained metaclastic rocks including phyllite and metasandstone (psammite) with less common grit, quartzite, minor limestone, chlorite schist, and rare conglomerate lenses (Murphy, 1997; Roots, 1997). Primitive trace fossils in the formation from the Nahanni area indicate a Late Proterozoic age for the Yusezyu Formation (Fritz et al., 1983, 1991; Gordey and Anderson, 1993). Murphy (1997) defines a highly deformed equivalent of the Yusezyu Formation in the Tombstone Strain Zone where metaclastic rocks have been overprinted by a shear fabric that was the product of thrust-associated deformation. Within the Tombstone Strain Zone, Yusezyu Formation rocks are characterised by prominently foliated and lineated quartzofeldspathic and micaceous psammite, cream to pale green muscovite ± chlorite quartz schist and phyllite, clear and blue quartz grain gritty schist and metagrit, and rare marble (Murphy, 1997; McOnie and Read, 2009) that overthrusts the Mississippian Keno Hill Quartzite (KHQ; Murphy, 1997). Roots (1997) noted that no primary depositional features remain in the rocks within the Tombstone Strain Zone, however the mineral variations define compositional layers which reflect, and perhaps accentuate, compositional differences in primary bedding, and that changes in the structural fabric clearly follow the original

bedding contacts. The northern boundary of the Hyland Group is the surface trace of the Robert Service Thrust where it structurally overlies the KHQ (Murphy, 1997).

The Yusezyu Formation is overlain sharply and conformably by the Narchilla Formation, or unconformably by lower to upper Paleozoic rocks (Gordey, 2013). The Narchilla Formation is similar to the Yusezyu Formation with slate, argillite, phyllite and minor sandstone common, but also comprises green-grey and purple-grey phyllite (Roots, 1997; Murphy, 1997). At its type section, the Narchilla Formation has a Late Proterozoic to Early Cambrian age (Gordey and Anderson, 1993).

Regionally the Hyland Group is overlain to the south by an 800 m thick succession of Cambrian to Middle Devonian basinal strata that includes the lower to middle Cambrian shale-dominated Gull Lake Formation, lower Cambrian to Lower Ordovician limestone and siltstone of the Rabbitkettle Formation, and Lower Ordovician to Upper Devonian shale-dominated, fine-grained clastic strata of the Road River Group (Gordey and Anderson, 1993; Murphy, 1997; Mair et al., 2006).

Devonian to Mississippian Rocks

Across the Selwyn Basin, Earn Group rocks (Figure 2.13) are broadly characterised by dark grey to black shale (phyllite) with lesser amounts of chert, siltstone, sandstone, limestone, bedded barite, chlorite-mica phyllite, and chert pebble conglomerate that represent submarine fan and channel-related facies (Murphy, 1997; Gordey, 2013). At its

type locality in the Glenlyon area, the Earn Group comprises four units (Campbell, 1967):

- Dark grey to black chert, argillite, quartzite, and grit of the lower unit (unit 10 of Campbell, 1967);
- Massive chert-pebble conglomerate of the Crystal Peak Formation (unit 11 of Campbell, 1967);
- Dark grey to black limestone of the Kalzas Formation (unit 12 of Campbell, 1967); and
- Chert, quartzite, argillite, and minor limestone of the uppermost unit (unit 13 of Campbell, 1967).

The Earn Group contains Early Mississippian to possibly Pennsylvanian fossils at its type locality, while fossils from the Nahani and Niddery areas indicate an Early Devonian to Late Devonian age. Gordey (2013) indicates that age of deposition for the Earn Group ranges from probable Ordovician to Silurian (unit 10 of Campbell, 1967), through the Devonian to Mississippian for the Crystal Peak Formation, and early Mississippian for the Kalzas Formation, to Carboniferous to Permian or even Triassic for unit 13 of Campbell (1967).

Mississippian to Triassic Rocks

Stratigraphically above the Earn Group are a series of Mississippian to Triassic clastic shelf assemblages that represent uniform shelf sedimentation with relatively low clastic input (Gordey, 2013). These assemblages include fine-grained clastic and minor

carbonate strata of the Mississippian Tay Formation, chert and shale of the lower Permian Mount Christie Formation, clastic and carbonate strata of the Middle to Upper Triassic Jones Lake Formation, and massive, thick-bedded, and fine-grained orthoquartzite of the KHQ (Gordey, 2013).

The KHQ extends for approximately 220 km along the northern edge of the Selwyn Basin west from the Keno Hill district to the Tombstone River region (Tempelman-Kluit, 1970; Mortensen and Thompson, 1990; Gordey and Anderson, 1993). At its type locality in the Keno Hill district, quartzite horizons vary from thick to thin-bedded and are intercalated with phyllite and schist.

The KHQ unit is correlated with Mississippian quartz-rich clastic rocks of the Tsichu Group in the Nahanni and Niddery lake areas (Figure 2.13; Murphy, 1997), and the Mississippian Globe quartzite in Alaska (Weber et al., 1992). Blusson (1978) correlated the KHQ with Alaskan rocks that are similarly intruded by metadiorite sills, and as such suggested a late Paleozoic age for the formation. Conodont ages from KHQ strata in the Dawson area have yielded Viséan-Namurian (Mississippian) ages (Mortensen and Thompson, 1990; Orchard, 1991). U-Pb (zircon) dates from felsic metavolcanic rocks associated with the KHQ NE of the study area have yielded a broad Late Devonian to Early Mississippian age (Abbott and Turner, 1990; Murphy, 1997; Roots, 1997).

Within the Tombstone Strain Zone, KHQ rocks are more highly deformed than elsewhere in the basin. Outside of the Tombstone Strain Zone, numerous authors have observed

primary sedimentary structures within the KHQ including cross-bedding (Tempelman-Kluit, 1966) and bedding laminations (Lynch, 1989a). Within the Tombstone Strain Zone, Roots (1997) noted that the KHQ is well-foliated and lineated, and that stratigraphic details, including contacts, have been obliterated.

Protoliths of the KHQ were likely sandstone and black shale (Roots, 1997) that were deposited in a variably energetic, shallow marine, to locally non-marine environment (Tempelman-Kluit, 1970). Tempelman-Kluit (1970) suggested that the homogeneity of the thick quartzite intervals reflect constant conditions of deposition and uniformly sized source material deposited on a gently dipping paleoslope. However, detrital zircons recovered from the KHQ yield a variety of ages, and as such indicate a heterogeneous source with multiple sedimentary cycles (Roots, 1997 and references therein). Numerous discrete lithological packages were identified within the KHQ by Otto (2010) within the Keno Hill area. It was noted that facies changes defining the packages were not typically predictable with thick schistose sections locally giving way to equally thick, layer parallel, quartzite dominant sections. Otto (2010) interpreted this facies distribution to be indicative of terrigenous deposition by turbidites in a marginal flysch basin.

2.2.2 Intrusive rocks

Two sets of foliated intrusions were described by Murphy (1997) in the McQuesten River region. A set of small, fine- to medium-grained, rarely porphyritic, quartz-feldspar-chlorite-biotite rocks intrude the Narchilla Formation as dykes and sills and are not

documented above the Narchilla Formation. These are considered to be feeders for a mafic metavolcanic member of the immediately overlying Gull Lake Formation (Gordey, 2013).

A set of foliated mafic metaigneous intrusions intrude Phanerozoic sedimentary strata between Keno Hill and the Tombstone range with a strike length of over 200 km (Mortensen and Thompson, 1990) and commonly intrude the Earn Group and KHQ. These intrusive rocks are of hornblende-plagioclase dioritic to gabbroic composition (Murphy, 1997), and are strongly chlorite altered. In the Ogilvie mountain range this suite of mafic intrusions has been dated at 232.2 +1.5/-1.2 Ma (U-Pb baddeleyite) giving an early Late Triassic (Carnian) emplacement age (Mortensen and Thompson, 1990). While Triassic magmatism is well documented in the accreted terranes outboard of the North American continental margin, it is rare within cratonic strata, such as the Selwyn Basin (Mortensen and Thompson, 1990). In the Keno Hill area, foliated mafic metaigneous intrusions form dismembered, strongly boudinaged lenses of varying size, but can reach thicknesses in excess of 100 m and can be traced over several kilometres.

Unfoliated felsic to intermediate intrusions occur throughout the Selwyn Basin (Figure 2.14) and can be subdivided into five broad suites:

1) The 115 – 96 Ma Anvil-Hyland-Cassiar belt (Hart et al., 2004a; Heffernan, 2004 Rasmussen, 2013);
2) The 98 – 94 Ma Tungsten suite (Gordey and Anderson, 1993; Hart et al., 2004a, b);

3) The 98-93 Ma Mayo suite (Murphy, 1997; Hart et al., 2004a, b; Rasmussen, 2013);
4) The 94 – 90 Ma Tombstone suite (Murphy, 1997; Hart et al., 2004a, b; Rasmussen, 2013); and
5) The 64 – 67 Ma McQuesten Suite (Murphy, 1997; Rasmussen, 2013).

The Anvil-Hyland-Cassiar belt comprises the Anvil (114 – 98 Ma; Hart et al., 2004a; Rasmussen, 2013), Hyland River (106 – 96 Ma; Hart et al., 2004a; Heffernan, 2004), and Cassiar (115 – 100 Ma; Hart et al., 2004a; Rasmussen, 2013) plutonic suites that intruded Neoproterozoic and Paleozoic rocks of the Selwyn Basin and displaced Cassiar Terrane (Figure 2.14; Pigage and Anderson, 1985; Driver et al., 2000; Heffernan and Mortensen, 2000; Hart et al., 2004a). These suites intruded along a belt greater than 900 km long towards the south and west of the Selwyn Basin. The belt is dominated by variably porphyritic, peraluminous to slightly peraluminous biotite granite and granodiorite, with local muscovite-bearing phases (Hart et al., 2004a). The Anvil suite is associated with the Anvil mining district that comprises a NW-trending belt of SEDEX Zn-Pb-Ag deposits (e.g., the Vangorda deposit; McClay, 1991; Brown and McClay, 1994), whereas the Cassiar suite is associated with tungsten ± molybdenum skarns and veins, with distal Ag-Pb-Zn veins (Hart et al., 2004a).

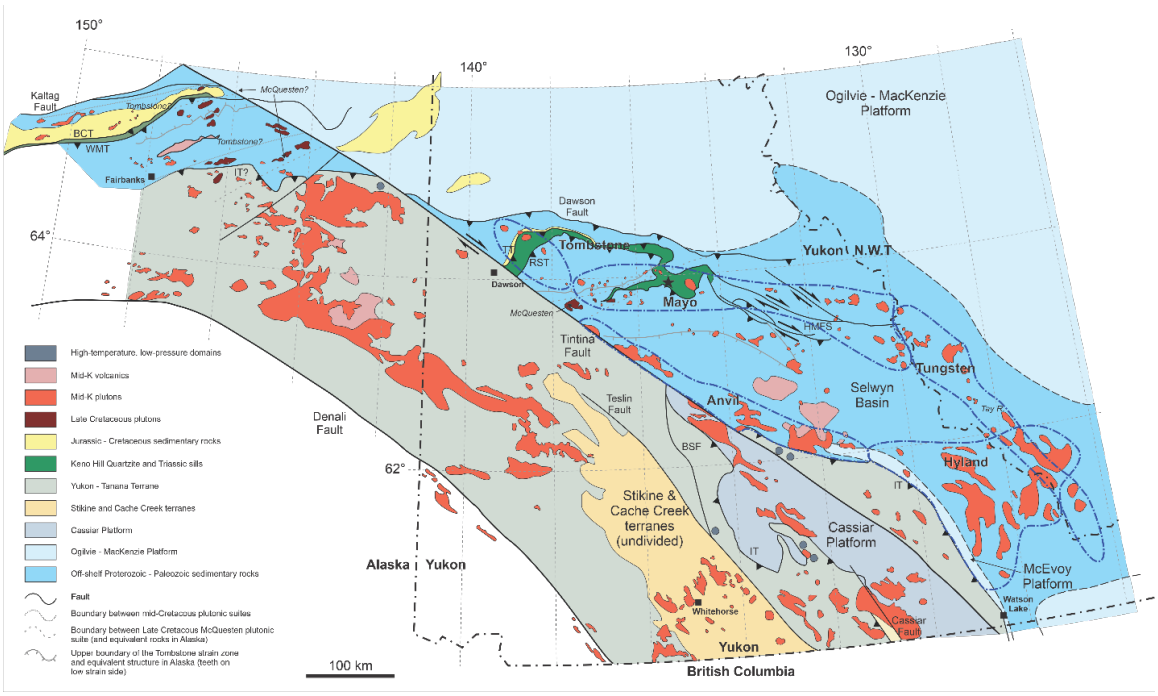

Figure 2.14: Simplified geological map of Yukon and eastern Alaska illustrating the geological features on opposite sides of the Tintina Fault and the distribution of Cretaceous-age intrusions.

Abbreviations: Yukon: HMFS = Hess-Macmillan Fault system; IT = Inconnu thrust Fault; RST = Robert Service thrust Fault; TT = Tombstone thrust Fault. Alaska: BCT = Beaver Creek thrust Fault; WMT = White Mountains thrust Fault. Modified after Gabrielse et al. (2006) and Hart et al. (2004a)

The Tombstone, Tungsten, and Mayo suite plutons (Figure 2.14) were emplaced in a post-collisional extensional regime at circa 93 ± 3 Ma (Mair et al., 2006; Tupper and Bennett, 2010) and have commonly been amalgamated into the Tombstone-Tungsten belt (e.g., Mortensen et al., 2000; Mair et al., 2006). The Tungsten suite forms a 300 km long NW-trending belt near the eastern margin of the Selwyn Basin. The suite is dominated by leucocratic biotite granite, monzogranite, and quartz monzonite (Hart et al., 2004a). This suite is associated with the world-class scheelite skarn deposits at Mactung and Cantung, and with sub-economic copper and gold, and local zinc and tin enrichments (Hart et al., 2004a).

The Mayo suite comprises approximately 100 small (1-20 km^2) plutons along a 400 km long belt across central Yukon (Hart et al., 2004a, b). Pluton lithology comprises porphyritic to coarse-grained leucocratic quartz monzonite, with rare granodiorite and biotite granite (Murphy, 1997; Hart et al., 2004a). Intrusion-hosted gold deposits at Dublin Gulch and Scheelite Dome are associated with Mayo suite plutonism (Murphy, 1997; Hart et al., 2000). Lynch et al. (1990) associated Ag-Pb-Zn mineralisation at Keno Hill with Mayo suite plutonism.

The Tombstone suite are the most widespread intrusions in the northern Selwyn Basin and occur at all stratigraphic and structural levels (Murphy, 1997). The suite is correlated with the Livengood suite in Alaska (Figure 2.14; Hart et al., 2004b) and after reconstruction of post-Tombstone magmatism movement along the Tintina Fault (moderate translation model), the Tombstone-Livengood belt forms a narrow, 300 km long, east- to NE-trending belt of quartz-alkalic plutons. The suites comprise biotite-hornblende ± pyroxene monzonite and syenite, with minor quartz monzonite, monzodiorite, and monzogabbro (Hart et al., 2004a). Murphy (1997) suggested that a lack of observed textural variability in the intrusions suggests that they crystallised at similar shallow crustal levels. The Tombstone suite is associated with the Brewery Creek gold deposit in Yukon.

The McQuesten suite defines a short, ENE-trending belt between the Tintina Fault and Sunshine Creek in the northern Selwyn Basin. The intrusions comprise biotite ±

muscovite granite, monzogranite, and diorite however more felsic and mafic compositions have been recognised (Murphy, 1997; Kingston, 2009; Kingston et al., 2010). The McQuesten suite has been correlated with dykes of similar composition and age at the Rau occurrence in the Selwyn Basin (Kingston, 2009).

2.2.3 Structure and Tectonics

Selwyn Basin strata form a strongly deformed and thrust faulted package between the Mackenzie fold and thrust belt and the peri-Laurentian accreted terranes. Jurassic and Cretaceous over-thrusting of the Yukon-Tanana Terrane over the continental margin initiated the development of thin-skinned, north-directed thrust sheets within the western Selwyn Basin (Mair et al., 2006) including, from north to south, the Dawson, Tombstone, Robert Service, Tay River and Twopete thrust sheets (Mair et al., 2006; Gordey, 2013). During this time, basinal facies of the Selwyn Basin were juxtaposed against platformal successions of the Mackenzie Platform along the east-trending Dawson thrust fault (Mair et al., 2006). The Dawson thrust fault is the structurally lowest of three major, low-angle, approximately east-striking faults in the northern Selwyn basin (Figure 2.15). Prior to Jurassic-Cretaceous deformation, the Dawson thrust was a major basin bounding, presumably normal fault that had existed since at least the Neoproterozoic and influenced sedimentation and magmatism (Abbott, 1997).

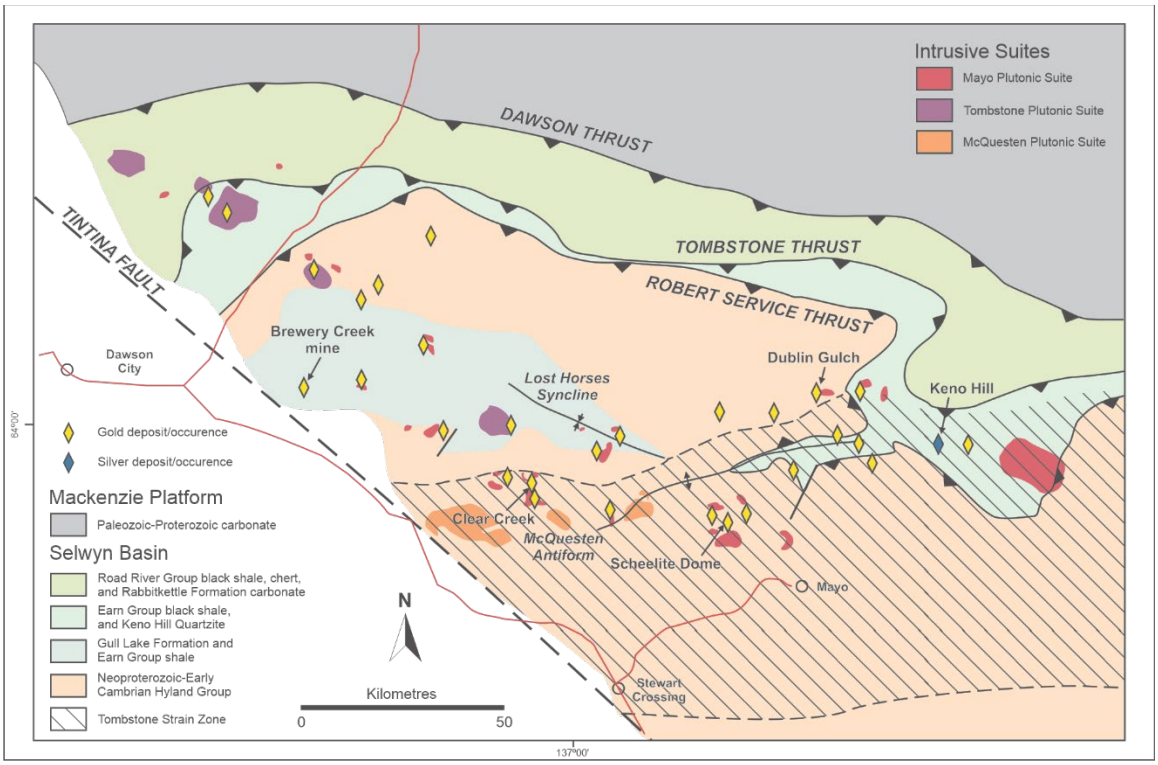

Figure 2.15: Simplified geological map of the northern Selwyn Basin showing locations of the Dawson, Tombstone, and Robert Service thrusts, the Tombstone High Strain Zone, and gold and silver occurrences. Modified after Hart (2007).

Structurally above the Dawson Thrust are the Tombstone and Robert Service thrusts (Figure 2.15), which together account for more than 100 km of displacement (Murphy, 1997; Mair et al., 2006). Displacement across the Twopete and Tay River thrusts in the Tay River area is between 15 and 35 km (Gordey, 2013).

At its western extent, the Tombstone Thrust juxtaposes the Mississippian KHQ above Jurassic-age schist and juxtaposes progressively older strata to the east (Mair et al., 2006). The Robert Service Thrust juxtaposes Upper Proterozoic Hyland Group rocks onto the KHQ and undifferentiated Upper Paleozoic to Triassic strata (Figure 2.16; Murphy, 1997; Mair et al., 2006). Mair et al. (2006) suggest that the lack of pre-Hyland Group

rocks near the base of the Robert Service Thrust implies that the fault tracks into a detachment within the lower Hyland Group.

The regional metamorphic grade in the Robert Service and Tombstone thrust sheets reaches lower to middle greenschist facies. This is coincident with an increase in strain that is termed the Tombstone Strain Zone and encompasses the Keno Hill mining district (Murphy, 1997).

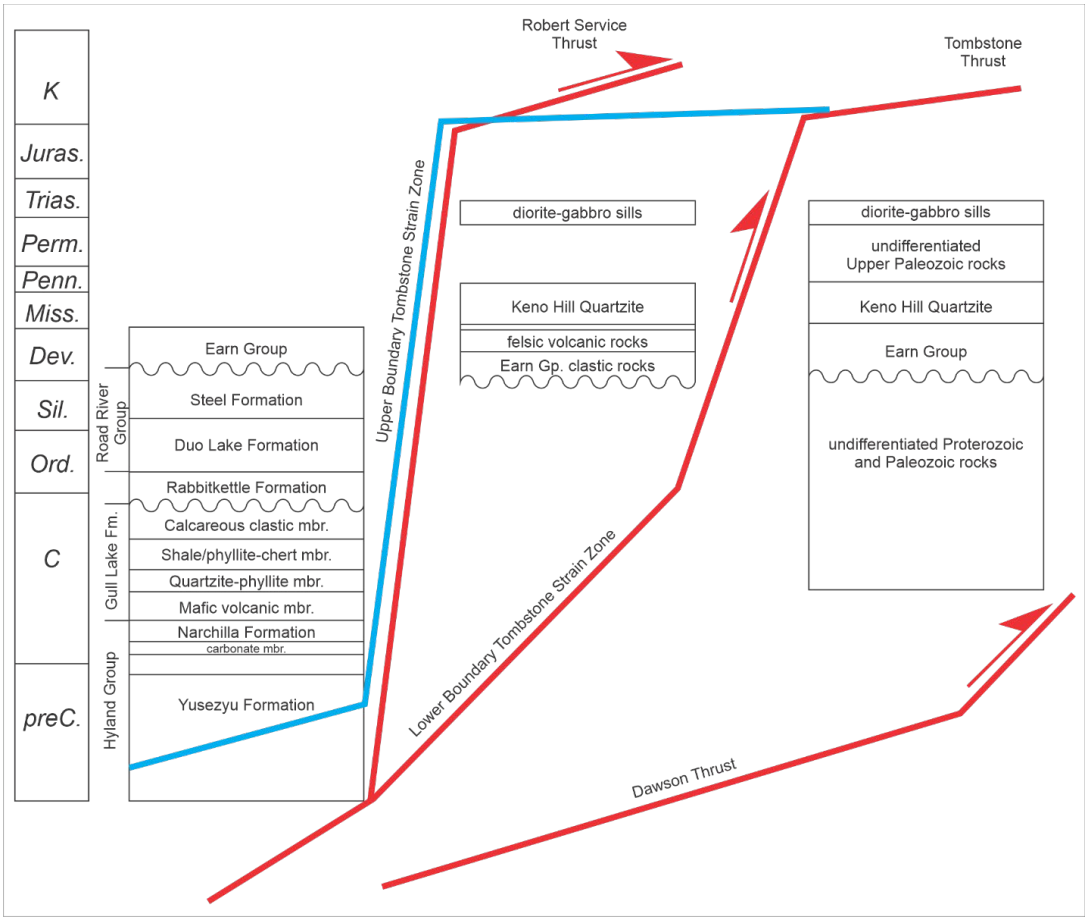

Figure 2.16: Stratigraphic units of the McQuesten River region and their relationship with regional structures and intrusive episodes. Modified from Murphy (1997).

The cessation of ductile deformation in the lower Robert Service thrust sheet occurred between 100.5 ± 0.4 Ma and 104.6 ± 2.0 Ma ($^{40}Ar/^{39}Ar$ muscovite; Mair et al., 2006), and coincided with north-south directed shortening in the Yukon Tanana uplands, uplift and extension of the orogen core, and dextral transtension that produced orogen-parallel, NW-striking, dextral strike-slip faults (Mair et al., 2006; Sánchez et al., 2013; 2014; M. Grimshaw, personal communication, September 04, 2020).

2.3 Geology of the Keno Hill District

The Keno Hill district is located within the Tombstone Strain Zone and is structurally bound above and below by the regionally extensive Robert Service and Tombstone thrust faults, respectively (Figure 2.15 and Figure 2.16). The stratigraphic sequence (Figure 2.16 and Figure 2.17) is strongly deformed and comprises Upper Proterozoic, metaclastic rocks of the Yusezyu Formation (unit P_Y^T of Murphy (1997)) that overthrust Middle Devonian to Mississippian phyllite of the Earn Group (Abbott, 1990; Murphy, 1997) and the Mississippian (Viséan – Namurian) KHQ (Mortensen and Thompson, 1990; Orchard, 1991). In general, the KHQ is situated structurally above rocks of the Earn Group, but in the east of the district, regional-scale mapping suggests that the Earn Group and KHQ are thrust or fold imbricated (Figure 2.17; Murphy, 1997; Alexco, 2021). The stratigraphic sequence is commonly intruded by Triassic (Mortensen and Thompson, 1990), foliated, mafic metaigneous intrusions; middle-Cretaceous, nonfoliated, felsic dykes; and rare, likely post-middle Cretaceous lamprophyre dykes (Murphy, 1997).

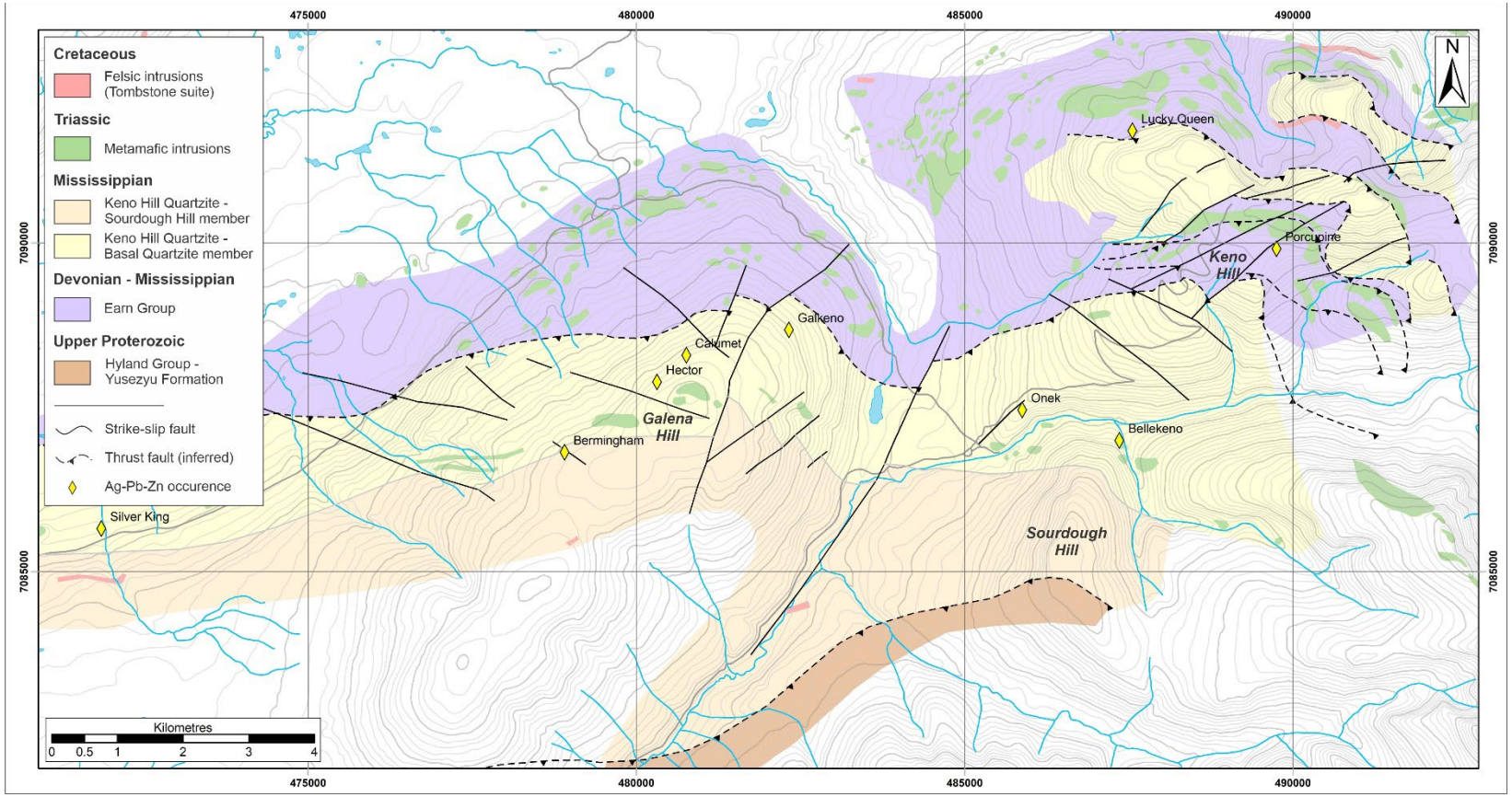

Figure 2.17: Simplified geological map of the Keno Hill district. Modified after Boyle (1965), Murphy (1997), and Alexco (2021).

2.3.1 Metasedimentary Rocks

Upper Proterozoic Rocks – Yusezyu Formation

Within the Keno Hill district, the Hyland Group is composed of prominently foliated and lineated quartzofeldspathic and micaceous psammite (Murphy, 1997) and cream to pale green muscovite ± chlorite quartz schist, clear and blue quartz grain gritty schist and metagrit, and rare marble (McOnie and Read, 2009) of the Yusezyu Formation.

Yusezyu Formation rocks have been variably termed the upper schist unit (Boyle, 1965; Poole, 1965; Green, 1971) or the Grit Unit/Division (Gabrielse et al., 1973; Gleeson and Boyle, 1980; Lynch, 1989a). Whereas the Yusezyu Formation extends well south of the area (Murphy, 1997), within the district the unit is spatially restricted to the extreme southern portion of the district with rare outcrops on the southern flanks of Galena Hill and Sourdough Hill.

Paleozoic Rocks – Earn Group and KHQ

Earn Group rocks broadly comprise a deep marine assemblage of dark grey to black shale, with subordinate chert, siltstone, sandstone, limestone, bedded barite, baritic limestone, chlorite-muscovite phyllite, and chert-pebble conglomerate (Murphy, 1997). Within in the district, the Earn Group has been subdivided into two members: the grey schist and the chlorite ± sericite schist (Murphy, 1997; McOnie and Read, 2009).

The grey schist (unit DM_{EP}^{T} of Murphy (1997)) consists of non-calcareous to locally calcareous grey graphitic schist (phyllite) with local grey, phyllitic limestone lenses, and sporadic lenses of siltstone of thinly laminated quartzite or quartzofeldspathic metasandstone (Murphy, 1997; McOnie and Read, 2009). The chlorite ± sericite schist (unit DM_{EV}^{T} of Murphy (1997)) is considered to be a felsic metavolcanic rock and occurs near the top of the Earn Group and near the base of the KHQ (Murphy, 1997). The chlorite ± sericite schist unit has been traced for over 120 km to the east, into weakly foliated to massive quartz-feldspar porphyritic rocks by Murphy and Roots (1992) and Roots (1997).

Earn Group rocks were formerly termed the "Lower Schist" (Boyle, 1965), and were mapped as underlying the lower part of the northern flank of Galena Hill, and much of the northern flank of Keno Hill, as far south as the Porcupine deposit (Figure 2.17; Murphy, 1997). Poulton and Tempelman-Kluit (1982) reported a Jurassic age fossil assemblage for a similar unit in the Dawson region; however, Abbott (1990) suggested a Devonian – Mississippian age for the Earn Group. The unit is truncated at the base by the Tombstone Thrust (Murphy, 1997).

Structurally overlying or imbricated with the Earn Group is the KHQ. The KHQ has been described as comprising massive to foliated and lineated, medium to dark grey graphitic quartzite containing variable amounts of graphite, muscovite, chlorite, tourmaline, carbonate, and detrital zircon; phyllitic quartzite; and grey, locally carbonaceous phyllite (Murphy, 1997; Cathro, 2006). The type locality for the KHQ is the Keno Hill mining

district where it has been mapped for a strike length of greater than 30 km and up to 6 km width (McOnie and Read, 2009; Figure 2.17)

The long history of study, exploration, and production in the district has led to numerous naming conventions applied to the KHQ. The variations in naming conventions are typically a result of differences in the scale at which the unit was mapped; however, they in part reflect progressive revisions in the interpreted age of deposition of the KHQ. Boyle (1965) termed a section through the Hector-Calumet mine the "Central Quartzite Formation" and identified 7 discrete divisions that ranged in thickness from approximately 30 to 240 m. These included the Silver King Member, the Hector-Calumet member, the Galkeno member, and four unnamed divisions that ranged in composition from sericite schist, graphitic schist and phyllite, interbedded schist and quartzite, to thick-bedded quartzite (Figure 2.18).

McOnie and Read (2009) subdivided the KHQ into two members (the Basal Quartzite and Sourdough Hill members). They attempted to correlate highly strained rocks within the district to the stratigraphy defined by Tempelman-Kluit (1970) in the less deformed and unmetamorphosed rocks in the Tombstone River - Upper Klondike River areas (Figure 2.18).

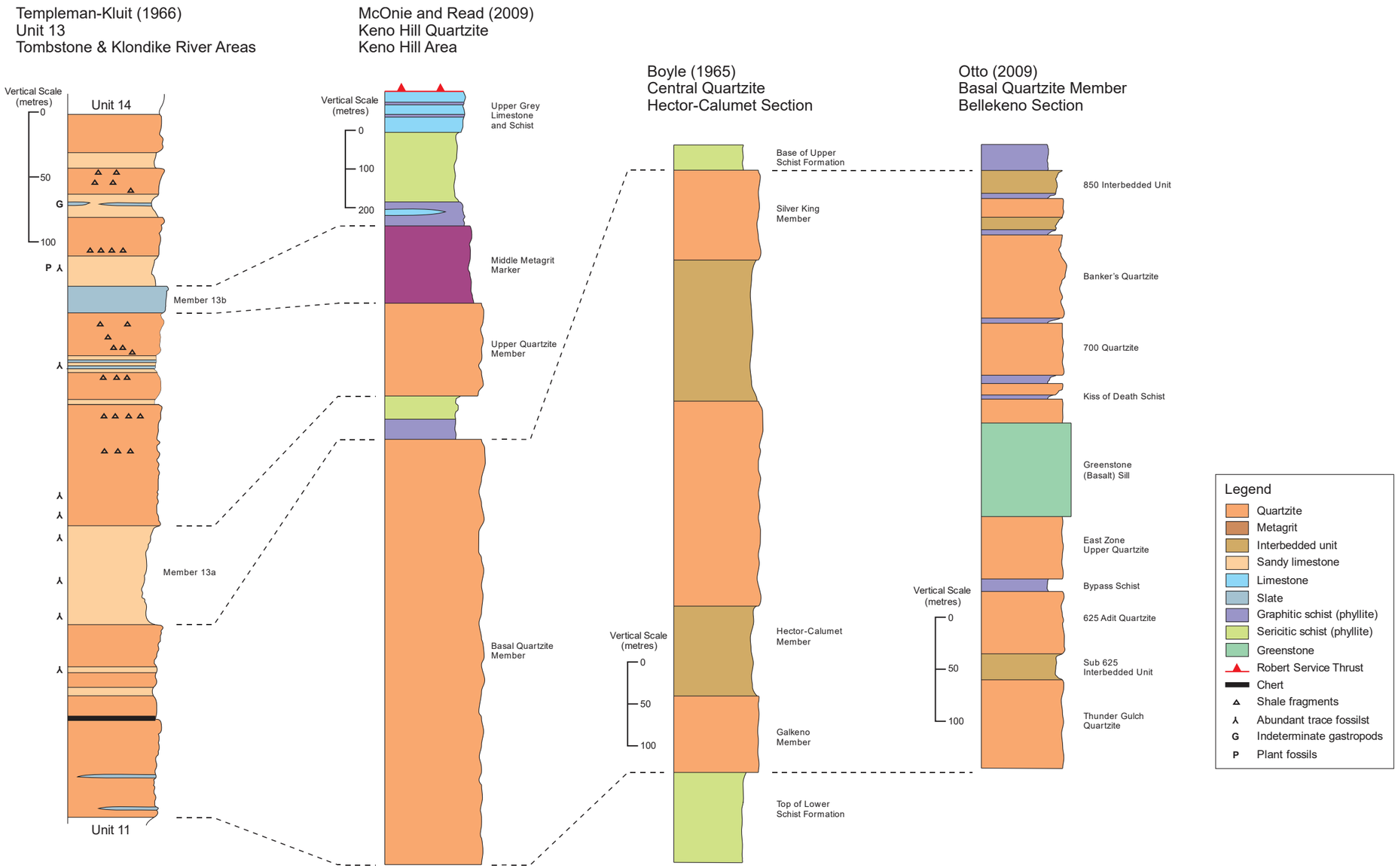

Figure 2.1: Comparison and correlation of stratigraphic logs for the KHQ from various localities compiled from data of Boyle (1965), Tempelman-Kluit (1966), McOnie and Read (2009), and Otto (2010).

The Basal Quartzite member (equivalent to the Central Quartzite Formation of Boyle (1965) is widely recognised as an important host to Ag-Pb-Zn mineralisation (Boyle, 1965; McOnie and Read, 2009). McOnie and Read (2009) noted that the upper part of the Basal Quartzite member contained up to 30% carbonaceous schist and is more calcareous than the lower part of the member. Otto's (2010) detailed structural and stratigraphic analysis of a greater than 500 m thick section of the Bellekeno underground workings identified 18 individual units of varying thickness within what is presumably the Basal Quartzite (Figure 2.18).

The Sourdough Hill member (McOnie and Read, 2009) is dominated by graphitic schist and minor quartzite and is structurally located between the underlying Basal Quartzite member and the overlying Robert Service Thrust. The member includes numerous discrete marker units. McOnie and Read (2009) observed two distinct graphitic and sericite schist units (the "Graphitic Schist Marker" and "Sericitic Schist Marker", respectively) towards the base of the member that they correlated with unit 13a of Tempelman-Kluit (1970; Figure 2.18), and a "Middle Grit Marker" that is correlated with unit 13b of Tempelman-Kluit (1970). Towards the top of the member are schist (phyllite) and limestone packages that were previously assigned to the "Upper Schist" unit and considered to be of equivalent age to the Earn Group (e.g., Boyle, 1965), and subsequently were considered to be part of the structurally overthrust Precambrian Yusezyu Formation (Murphy, 1997). McOnie and Read (2009) consider these packages to be the uppermost units of the Sourdough Hill member.

Extensive imbricate thrusting and isoclinal folding, and internal facies transitions, mean that the thickness of the KHQ is difficult to determine within the study area (e.g., Green and McTaggart, 1960; Boyle, 1965; Abbott, 1990; Murphy, 1997; Roots, 1997; Otto, 2010). Boyle (1965) measured a 900 m thick section on Galena Hill; Lynch (1989a; b) suggested that the structural thickness of the KHQ was approximately 1000 m; and Murphy (1997) suggested that approximately 2 km of quartzite occurs between the top of the Earn Group and the Robert Service Thrust. McOnie and Read (2009) recorded a thickness for the Basal Quartzite member in boreholes of up to 295 m but indicated that the thickness in cross-section may be up to 1100 m on the limb of an isoclinal fold (Figure 2.18). They suggested that whereas folding might have increased the thickness of the unit, the unit may have been thicker than the measured 150 m (Tempelman-Kluit, 1970) in the Tombstone area.

2.3.2 Intrusive Rocks

Foliated and lineated metamafic intrusive rocks (greenstone) are common within the KHQ and underlying Earn Group. At the district-scale, metamafic sills commonly weather with a high relief to the surrounding rocks to form small hills in the valleys and cliff sections on mountain flanks. In section they commonly form large lensoid structures that are easily identifiable from distance with thicknesses in the 10's of meters (Figure 2.19). Individual bodies range in thickness from less that one metre to greater than 100 metres, and McOnie and Read (2009) suggest that even thicker sills may be present towards the base of the northern flank of Keno Hill. Sills are commonly aphyric, and of

gabbro or plagioclase diorite composition (Murphy, 1997). Thicker sills may have a blocky core, with foliated margins becoming chloritic phyllite. Thin sills are foliated throughout.

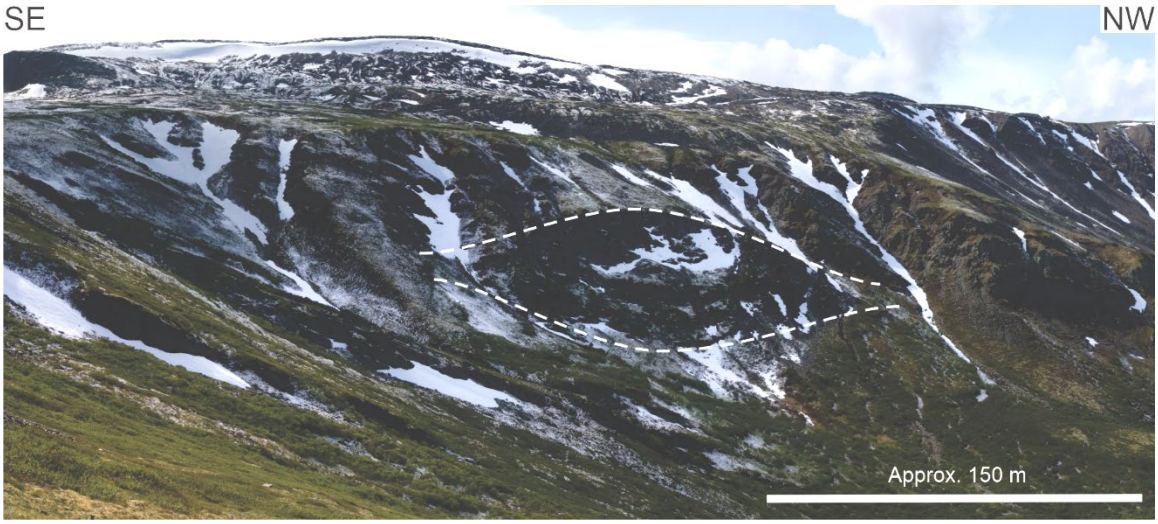

Figure 2.19: Photograph of macro-scale boudinage of greenstone unit on north flank of Keno Hill. Photograph looking SW from UTM 490325 mE, 7091887 mN.

Boyle (1965) and Lynch (1986) proposed that the Keno Hill metamafic intrusions form an important host for Ag mineralisation. This suggestion was not corroborated by the author, but anecdotal evidence suggests that greenstone-hosted Ag-Pb-Zn mineralisation may be present north and northeast of Keno Hill where greenstones intrude Earn Group rocks, and at depth within the Eagle deposit on the southern flank of Galena Hill (D. Tupper personal, communication, July 25, 2009).

Sporadic, small, nonfoliated, intrusive bodies have been mapped across the Keno Hill district that are of mid-Cretaceous age, and typically assigned to the Tombstone

magmatic suite (e.g., Murphy, 1997; Tupper and Bennett, 2010). The intrusions are metre-scale felsic (granitic) dykes with porphyritic to aplitic textures. A buff-weathered rhyolite sill in Galena Creek, towards the western end of the district was mapped by Boyle (1965) and McTaggart (1960) as having a five kilometre long strike length. Only one, approximately 10 metre wide felsic dyke was observed by the author on the north flank of Galena Hill and its length was not established.

Rare lamprophyre dykes are present in the Keno Hill district. Dykes are unaltered, medium-grained, biotite- to phlogopite-rich mafic intrusion with a few percent of poikiolitic biotite phenocrysts set in a feldspar-rich groundmass (McOnie and Read, 2009). The timing of lamprophyre emplacement is uncertain. Boyle (1965) indicates that at the Formo property a lamprophyre dyke intruded after regional greenschist-grade metamorphism and is sinistrally offset by the Ag-Pb-Zn-mineralised Formo vein. However, Murphy (1997) suggests that regionally middle-Cretaceous Tombstone intrusions are locally cut by biotite-rich lamprophyre dykes. Murphy (1997) suggests that the spatial relationship between Tombstone intrusions and lamprophyre dyke may indicate that they are part of the same intrusive suite.

2.3.3 Structure

The model for the structural evolution of the Keno Hill district has changed significantly since Boyle's (1965) assertion that rocks within the district formed a "simple homoclinal succession" with "no extensive overturning of strata, or recumbent folding". Subsequent

studies have identified abundant deformation in the district including early fold and thrust development, and later shearing associated with base metal mineralisation (Tempelman-Kluit,1966; Lynch, 1989a). Murphy and Héon (1995) and Murphy (1997) defined the Tombstone Strain Zone (Figure 2.15) and established a polyphase deformation history for the area including the presence of post-mineralisation cross-cutting faults. The work presented in this thesis builds upon the work of Murphy (1997) and proposes a three-phase structural history for the Keno Hill district (Figure 2.20). This comprises an early phase of progressive ductile to brittle-ductile deformation (defined herein as D_1), followed by brittle deformation associated with Ag-Pb-Zn mineralisation (defined herein as D_2), and a final phase of post-mineralisation brittle deformation (defined herein as D_3).

Early deformation (D_1) was controlled by the development of the Robert Service and Tombstone thrust sheets and northward translation of strata along the Tombstone and Robert Service thrusts between 160 – 130 Ma, (Murphy, 1997) with cessation by 100 Ma (Mair et al., 2006). Within the district, early deformation is characterised by fold and thrust and foliation development (Figure 2.21), foliation-parallel displacement, obliteration of primary sedimentary fabrics, and foliation-subparallel, barren quartz veining. Early deformation is responsible for the district-wide lower to middle greenschist grade metamorphism (Murphy, 1997).

	Event Relative Age	Event Descripton	Absolute Age Constraint
Magmatism		McQuesten Suite Intrusions *Medium- to coarse-grained potassium feldspar, biotite ± muscovite, grantie and quartz monzonite (Murphy 1997)*	64 - 67 Ma (U-Pb zircon, monazite) Murphy (1997)
Deformation/ Mineralization	D_3 (Local)	Dextral strike slip fault development. *Faults trend NNW and offset D_2 mineralized faults.*	
	D_2 (Local)	Sinistral strike-slip fault development. *Minor, late stage, antithetic dextral strike-slip faults and associated open folded to warped strata (F_2).* *Associated with the Ag-Pb-Zn mineralisation.*	Mineralization: 87 ± 3 Ma (K-Ar whole rock) Sinclair et al. (1980)
Magmatism		Tombstone Suite Intrusions *Clay and carbonate altered, medium- to coarse grained, porphyritic aplite and granite.*	93.6 ± 1.4 Ma (U-Pb zircon) Tupper and Bennet (2010)
Deformation/ Metamorphism	D_1	N to NW translation of strata along Tombstone and Robert Service thrusts. *Two phases of sub-coaxial isoclinal folds developed (F_{1a-b}), with associated S_1 and S_2 fabric formation.* *Associated with greenschist-grade metamorphism.*	Cessation of D_1 by 100 - 104 Ma ($^{40}Ar/^{39}$ Ar muscovite) Mair et al. (2006)
Magmatism		Triassic mafic sill emplacement. *Magnesian Na-Ca amphibole-pyroxene-quartz-plagioclase, variably foliated, porphyritic to rarely aphanitic, coarse- to fine-grained, tabular to lensoid, gabbro and diorite intrusions concordant with the regional $S_{0\text{-}1a\text{-}1b}$ foliation.*	232.2 +1.5/-1.2 Ma (U-Pb baddeleyite) Mortensen and Thompson (1990)
Basin Development/ Sedimentation		Mississippian Earn Group sedimentation. *Graphitic schist with minor quartzite, limestone, and sericite schist (Upper Schist).* *Grey to light grey, massive quartzite unit with minor interbedded graphitic, sericitic and chlorite schist, and grey phyllite (Keno Hill Quartzite).* *Dark grey - black phyllite with intercalated quartzite and carbonaceous schist (Lower Schist).*	Keno Hill Quartzite: Visean - Namurian (conodont) Mortensen and Thompson (1990); Orchard (1991)
		Precambrian Hyland Group sedimentation. *Fine- to coarse-grained sandstones (locally termed grits) and sericite schist.*	

Figure 2.20: Summary of depositional, deformational, and intrusive events in the Keno Hill district.

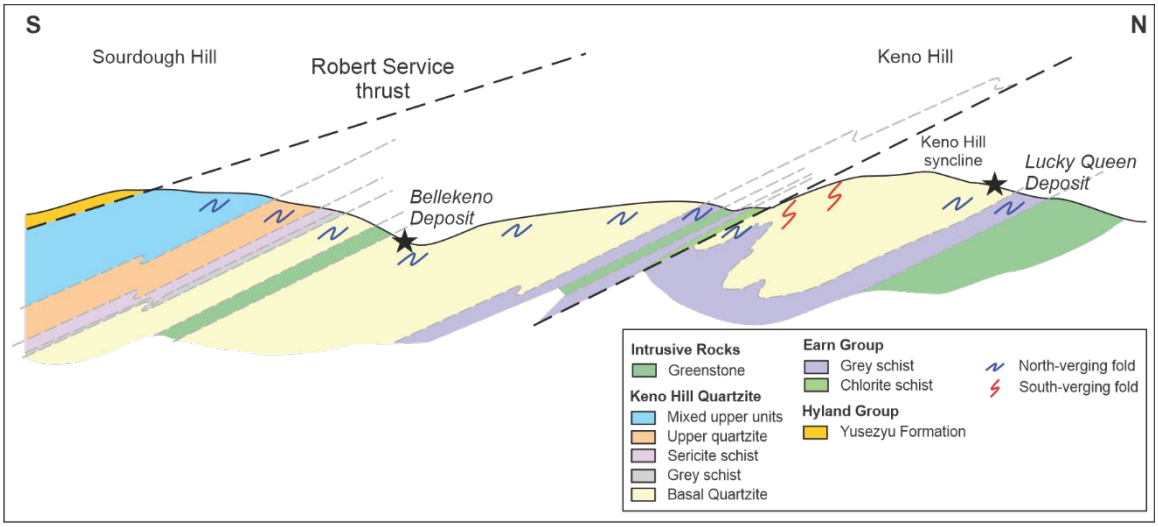

Figure 2.21: Schematic cross-section through Sourdough and Keno Hill. Not to scale. Modified from McOnie and Read (2009).

Syn-Ag-Pb-Zn-mineralisation deformation (D_2) is characterized by brittle, ENE-trending, sinistral strike-slip faults, linked by NE-trending sinistral-normal faults, with minor, late stage, antithetic, N-trending, dextral strike-slip faults, and associated open folded to warped strata. Boyle (1965) described syn-mineralisation vein-faults as "brittle displacement zones that exhibit complex variations in style along their length". Boyle (1965) suggested that Ag-Pb-Zn-mineralisation occurred along discontinuous networks of NE-trending "longitudinal" vein-faults, and that displacement was transferred to other "longitudinal" vein-faults along N-trending "transverse" faults. The work here will show that, while absolute displacement during D_2 was probably small, the bulk of displacement took place along ENE-trending, strike-slip faults, that were linked by subordinate, oblique-slip NE-trending faults that hosted the bulk of base-metal mineralisation. This thesis will show that mineralisation at Keno Hill developed in a regional-scale, left-stepping (releasing) bend of a major, ENE-trending, possibly translithospheric (TLF),

fault system. This thesis proposes that while the TLF may have originated early in the history of the Cordillera (possibly prior to basin development). Syn-Ag-Pb-Zn-mineralisation reactivation of the TLF during D_2 fault development may have occurred in response to coeval uplift and extension of the orogen core in the accreted Yukon Tanana Terrane.

The final phase of deformation defined in this thesis (D_3) is characterised by post-Ag-Pb-Zn mineralisation, NNW-trending dextral strike-slip faults that offset mineralised structures. These structures are subparallel to, and show the same kinematics as the Tintina Fault (e.g., Roddick, 1967; Gabrielse, 1985; Gabrielse et al, 2006).

3. Methodology

This chapter briefly outlines the available data, and data acquisition and analytical techniques used during the course of this thesis. The methodologies, basis, and rationale for the techniques, are discussed in greater detail in Appendix A. Included are discussions of field data acquisition, sample collection, statistical analysis of data, techniques for two- and three-dimensional analysis of surface, subsurface, and remotely sensed data, and laboratory techniques including optical, geochemical, and geochronological analytical techniques.

The study area for this thesis is broadly defined by Alexco's mining claims, which cover an area of 233.5 km^2 (Figure 3.1). The majority of data collection took place within this boundary; however, localities were visited outside of Alexco's claim boundaries. Verbal permission was gained from the claim holders prior to visiting and studying the additional localities.

3.1 Field Data Collection

Field data were collected over a combined period of approximately 10 months that comprised three field seasons; these were September to December 2008; June to August 2009; and May to July 2010. Field data collection comprised surface and subsurface litho-structural mapping of selected localities throughout study area, and borehole logging of selected, representative core samples (Appendix A.1).

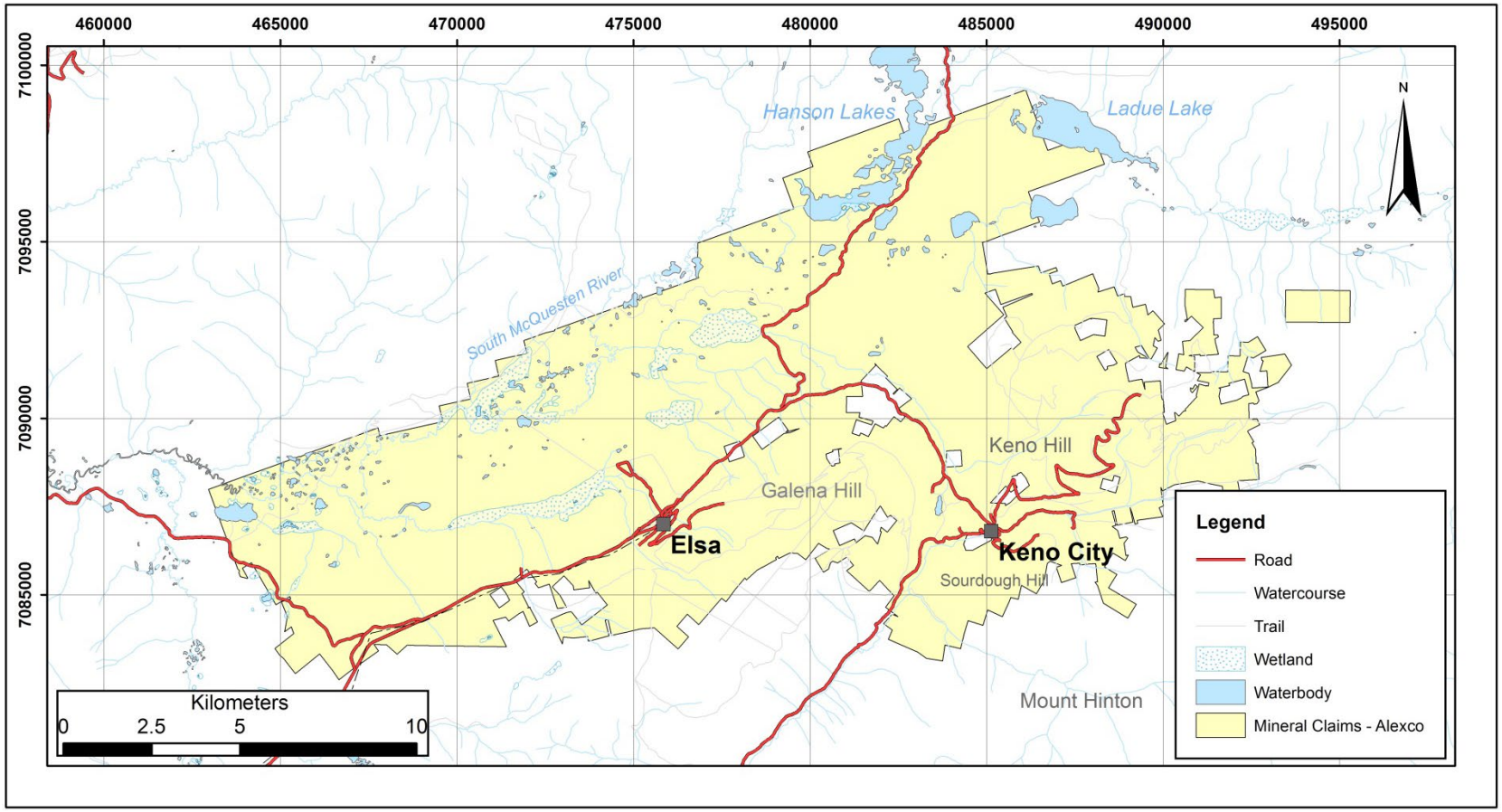

Figure 3.1: Map showing study area defined by limit of mining leases currently held by Alexco (data obtained from http://mapservices.gov.yk.ca/GeoYukon, January 26, 2016).

8693 individual *in situ* structural measurements were collected (Appendix B), and 226 rocks samples were collected that comprised 83 samples selected *in situ* from surface localities, 29 samples collected from the active Bellekeno underground workings, and 113 samples collected from drill core (Appendix C). Structural measurements were recorded using standard mapping techniques and locations of structural measurements and sample collection sites were recorded using a handheld Garmin GPS receiver in the NAD83 UTM Zone 8N datum. The locations of underground measurements were recorded by measuring the distance and direction from marked survey points on drift walls (Appendix A.1).

Planar structural elements were recorded as dip/dip direction (subsequently converted to dip/strike in Microsoft Excel^{TM}). Linear structural elements were recorded as plunge/azimuth, or where necessary trend/rake. Unless stated otherwise, all measurements stated in this thesis are given as dip/strike or plunge/azimuth.

Typically, albeit not exclusively, surficial mapping was focussed on areas of known Ag-Pb-Zn mineralisation, including historic open pit mines and trenches in the study area. Open pits in the area typically exhibit rock exposure that approaches 100% exposure. Elsewhere exposure is limited and commonly less than 1%. In addition to the surficial areas, the Bellekeno underground workings were studied (Figure 3.2).

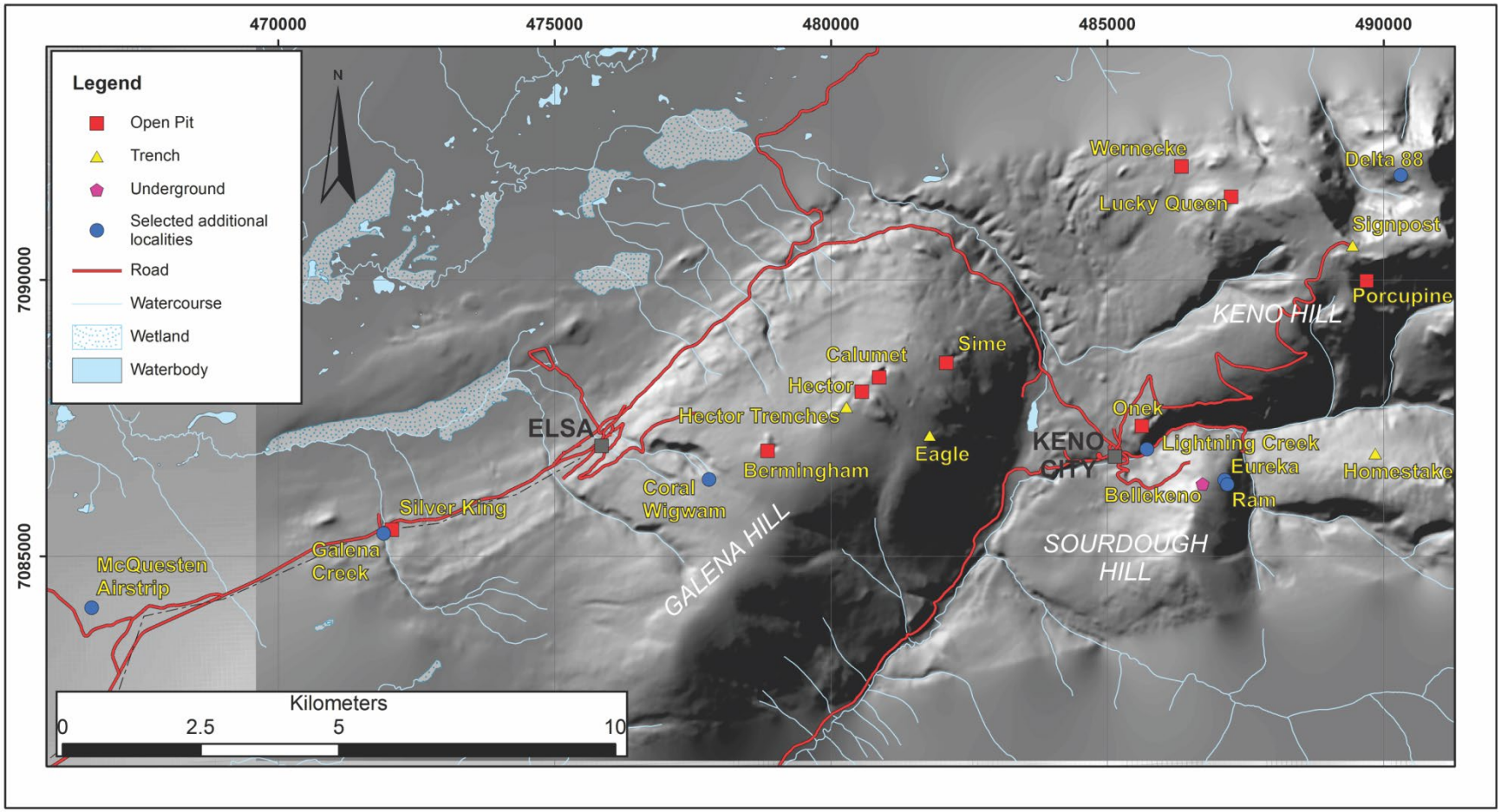

Figure 3.2: Map of the Keno Hill district showing selected locations for data collection overlaid on digital elevation model (DEM).

Concurrent with the field data collection for this project, Alexco conducted a litho-stratigraphic mapping program across the study area, the details of which have been used to augment the observations and measurements collected for this thesis. The litho-stratigraphic mapping program was conducted by Al McOnie and Dr. Peter Read (McOnie and Read, 2009).

Mapping of open pit and trench developments comprised the systematic measurement of structural, lithological, and alteration data from accessible pit or trench walls. Mapping was completed at 1:200 or 1:500 scale and was completed on nine open pit mines (five on Galena Hill, and four on Keno Hill), four trenches (two on Galena Hill, one on Sourdough Hill, and one on Keno Hill), and numerous additional localities (Figure 3.2; Appendix D). Localities included:

- Open pits
    - Galena Hill
        - Silver King/Silver King East
        - Bermingham /Bermingham West
        - Hector
        - Calumet
        - Sime
    - Keno Hill
        - Onek
        - Porcupine
        - Lucky Queen
        - Wernecke
- Trenches
    - Galena Hill
        - Hector trenches
        - Eagle (claim holder at the time of visit was Mega Silver Inc.);

    - Sourdough Hill
        - Homestake (claim holder at the time of the visit was Mr. Mathias Bindig)
    - Keno Hill
        - Signpost

Additional localities visited included (but are not limited to):

- Eureka/Ram deposit;
- Lightning Creek (claim holder at the time of the visit was Mr. Mathias Bindig);
- Galena Creek;
- Delta 88;
- Ram;
- Various additional localities on Galena Hill and Keno Hill; and
- East decline access drive, and the 750-1 crosscut of the Bellekeno underground workings

Drill core from 40 boreholes was analysed (Table 3.1). The boreholes were collared within 15 separate deposits within the study area (Figure 3.3). Analysis of drill core comprised systematic logging and photographing of lithological and alteration variations, observations on mineralogy and mineralisation, and structures present within in the analysed intervals. None of boreholes analysed were oriented, and as such only the alpha angles (α) of planar features were recorded.

Table 3.1: Collar locations and initial orientations of logged boreholes. All values rounded to nearest whole number; collar co-ordinate datum is NAD83 UTM Zone 8N.

Prospect	Hole ID	Easting (mE)	Northing (mN)	Elevation (m)	Initial Azimuth (°)	Initial Dip (°)	Max Depth (m)	Reference on Figure 3.3
Bellekeno	BKUD09-0153	486558	7086161	979	138	30	105	Bk1
	BKUD09-0158	486705	7086364	993	181	55	55	Bk2
	BKUD09-0160	486599	7086185	984	125	45	61	Bk3
	K-06-0035	486817	7086142	1353	308	60	412	Bk4
	K-07-0096	487223	7086699	1167	308	66	322	Bk5
	K-07-0099	487222	7086700	1165	295	55	270	Bk6
	K-07-0105	487059	7086326	1284	285	72	600	Bk7
	K-07-0109	487057	7086326	1284	125	65	350	Bk8
	K-08-0127	487540	7086408	1101	276	5	405	Bk9
	K-08-0128	487540	7086416	1104	285	15	377	Bk10
	K-09-0184	486889	7086333	1312	303	60	280	Bk11
	K-09-0187	487170	7086810	1143	266	87	223	Bk12
Elsa	K-07-0071	475427	7086772	836	310	50	279	Et1
Hector Calumet	K-08-0176	481070	7087759	1397	348	67	643	Hc1
	K-08-0179	479589	7087349	1318	321	67	142	Hc2
Husky and Husky SW	K-06-0008	474636	7086617	794	330	55	305	Hu1
	K-06-0039	473875	7086388	762	320.5	65	213	Hu2
	K-07-0110	474038	7086059	811	325	60	612	Hu3
Keno 700	K-08-0165	489550	7090168	1654	295	60	250	K71
Leo	K-08-0131	470872	7086175	685	320	50	140	Le1
	K-08-0133	470952	7086153	688	320	55	216	Le2
Lucky Queen	K-08-0170	487458	7091222	1593	305	60	300	Lq1
	K-08-0172	487679	7091338	1596	310	50	280	Lq2
	K-09-0206	487628	7091329	1593	322	57	252	Lq3
Onek	K-07-0120	485887	7087367	1058	350	50	250	On1
	K-07-0125	485978	7087523	1087	303	60	161	On2
	K-08-0152	485726	7087230	1041	011	63	221	On3
Ram	K-09-0192	487101	7086293	1277	070	54	116	Ra1
Ruby	K-06-0029	479065	7087086	1306	315	60	200	Rb1
Runer	K-09-0198	487734	7087637	1140	102	51	275	Rn1
Shamrock	K-06-0024	488604	7090727	1616	310	50	76	Sm1
Silver King and Silver King East	K-06-0003	472052	7085247	817	330	60	457	Sm1
	K-06-0007	472151	7085324	811	317	59	365	Sk2
	K-07-0051	472979	7085722	784	340	60	250	Sk3
	K-07-0058	472860	7085738	782	360	55	250	Sk4
Tick	K-07-0062	474838	7086285	860	319	50	251	Tk1
	K-07-0080	475067	7086504	857	355	50	245	Tk2
Townsite	K-07-0085	479834	7087638	1311	323	52	290	Tn1
	K-07-0111	480234	7088119	1305	323	60	222	Tn2

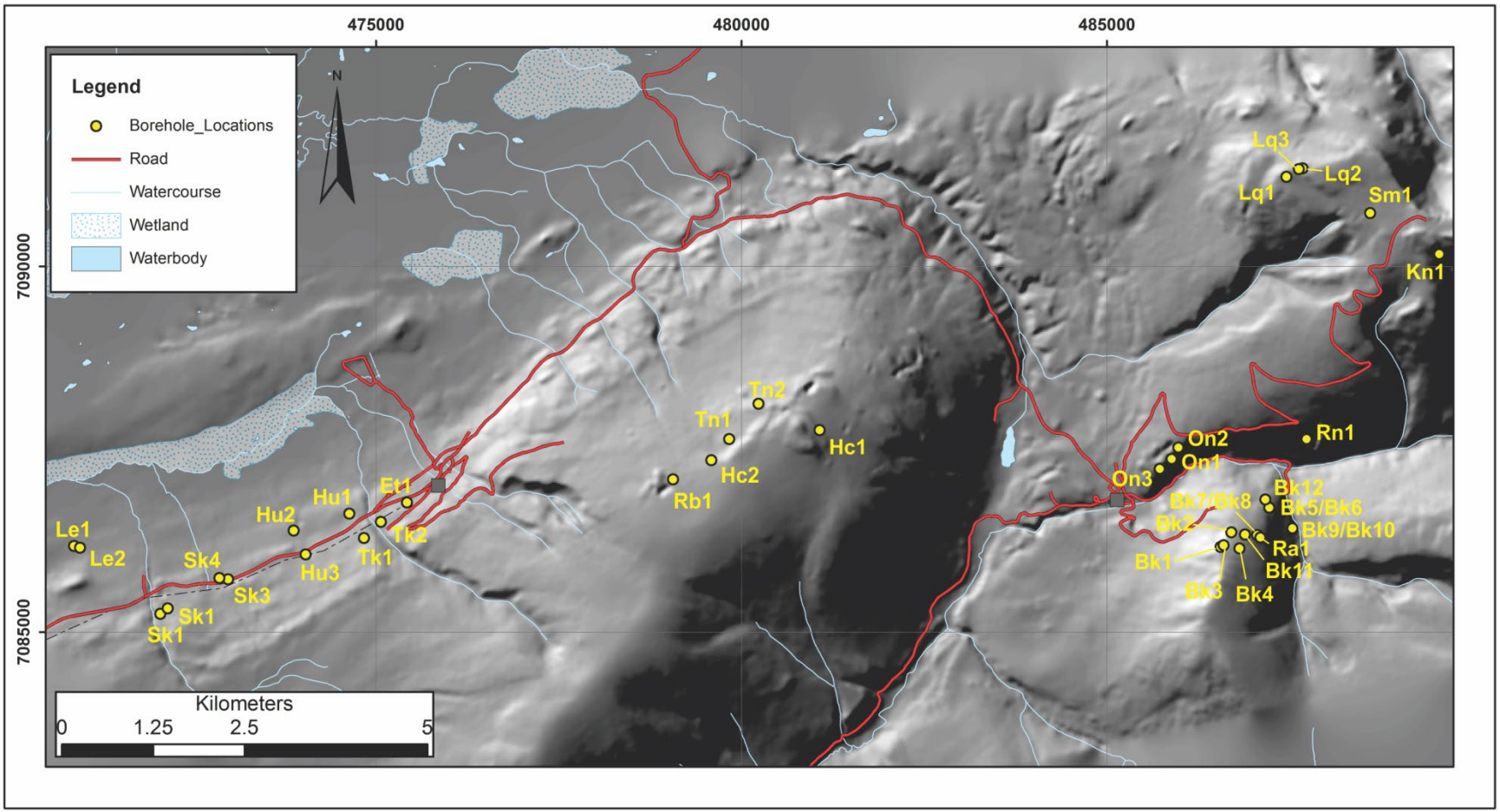

Figure 3.3: Collar locations of logged boreholes overlaid on digital elevation model. Reference numbers refer to Table 3.1.

3.1.1 Statistical Analysis of Field Data

Statistical analysis of field data was completed using Pangaea Scientific's Spheristat™ stereographic projection software to assess trends in the data. Pangaea Scientific's MyFault™ software or FaultKin™ 8.1. For fault stress analysis faults within each data set would be assigned a weighting of 1 to 4, based on observable fault width and length, and a confidence value of 1 to 4, based on the confidence placed in the slip vector orientation. If a fault displayed a clear offset or deflection of marker horizons or structures, or had consistently well developed and uniformly oriented slickensides/slickenlines and associated steps the fault was assigned a confidence value of 4, while a fault with weakly developed slickensides/slickenlines would be assigned a confidence value of 1. For the shortening and extension direction calculations, where a fault surface showed multiple, contradictory slip vector orientations, the fault would be considered to have experienced multiple discrete slip events and as such would be entered into the calculation as two discrete faults, with confidence values applied to each set of slip vectors.

3.2 Additional Available Data

In addition to data directly collected by the author, numerous data packages were supplied by Alexco and the Yukon Geological Survey (YGS). These included historic borehole data (up to 2010), assessment reports, remote sensing data (including geophysical data), regional, and deposit scale maps, and historic level plans. Below is a

summary of data supplied to the author throughout the course of the study. A complete list of available data is presented in Appendix A.2:

- Borehole database current to May 2010 containing data for 18,611 boreholes;
    - Data for 629 boreholes drilled by Alexco between 2006 and May 2010;
    - Data for 17,982 boreholes drilled prior to 2006.
- Remote sensing data;
    - Airborne magnetic geophysical data and accompanying report acquired by Alexco in 2006 (McPhar, 2006). The data has 200-metre line spacing flight lines, gridded with 60 metre cells.
    - SkyTEM airborne magnetic, electromagnetic, resistivity, and elevation data acquired by Monster Mining Corporation in 2011 and supplied to the author by Metallic Minerals Corporation in 2017. The data has 100-metre line spacing flight lines, gridded with 30 metre cells:
    - Regional airborne magnetic and gravity geophysical data obtained from the YGS covering the Yukon, British Columbia, and Alaska (Oneschuk et al., 2019; Miles and Oneschuk, 2016; Jobin et al., 2017)
    - High resolution aerial orthophotographs (Booysen et al., 2021) covering the Keno Hill district and derived 5 metre resolution topographic data
- Historic level plans, cross-sections, and interpreted 3D wireframes for faults, veins, and lithological contact (as .dxf files) for numerous deposits.
- District to regional-scale bedrock geology maps supplied by Alexco and the YGS.
- Numerous assessment reports and internal reports supplied to the author by Alexco.

3.3 Two-dimensional (2D) Analysis

Structural lineament interpretations focus on defining the distribution of structures in a given area, including the tectono-stratigraphic geometry (form line mapping), fault and shear zones (subdivided by age, order, and kinematics), and folds (subdivided by age). Structural lineament interpretations provide the structural and temporal framework within which to understand the distribution of mineralization within the area.

During this project, a district-scale structural lineament analysis was completed on two, combined, proprietary airborne magnetic datasets that were acquired by Alexco and Metallic Minerals Corporation (Metallic Minerals), and a digital elevation dataset acquired by Alexco (Figure 3.4). In addition, a regional lineament interpretation was conducted on an airborne dataset obtained from the YGS (Appendix D). Information on the acquisition of the remote sensing datasets is available in Appendix A.3.

The 2D structural lineament study of the Keno Hill area was conducted to identify the location and orientation of potential individual faults and shears, or fault and shear zones, and to evaluate their relative timing relationships within the context of the local and regional geological setting (Appendix D). The aim of the interpretation was to identify, deduce, and resolve the structural geometries present in the imagery. This provides a structural and temporal framework within which to understand the distribution of Ag-Pb-Zn mineralization in the Keno Hill area, and outlines areas of structural complexity that are key target areas for Ag-Pb-Zn mineralization (Siddorn et al., 2020).

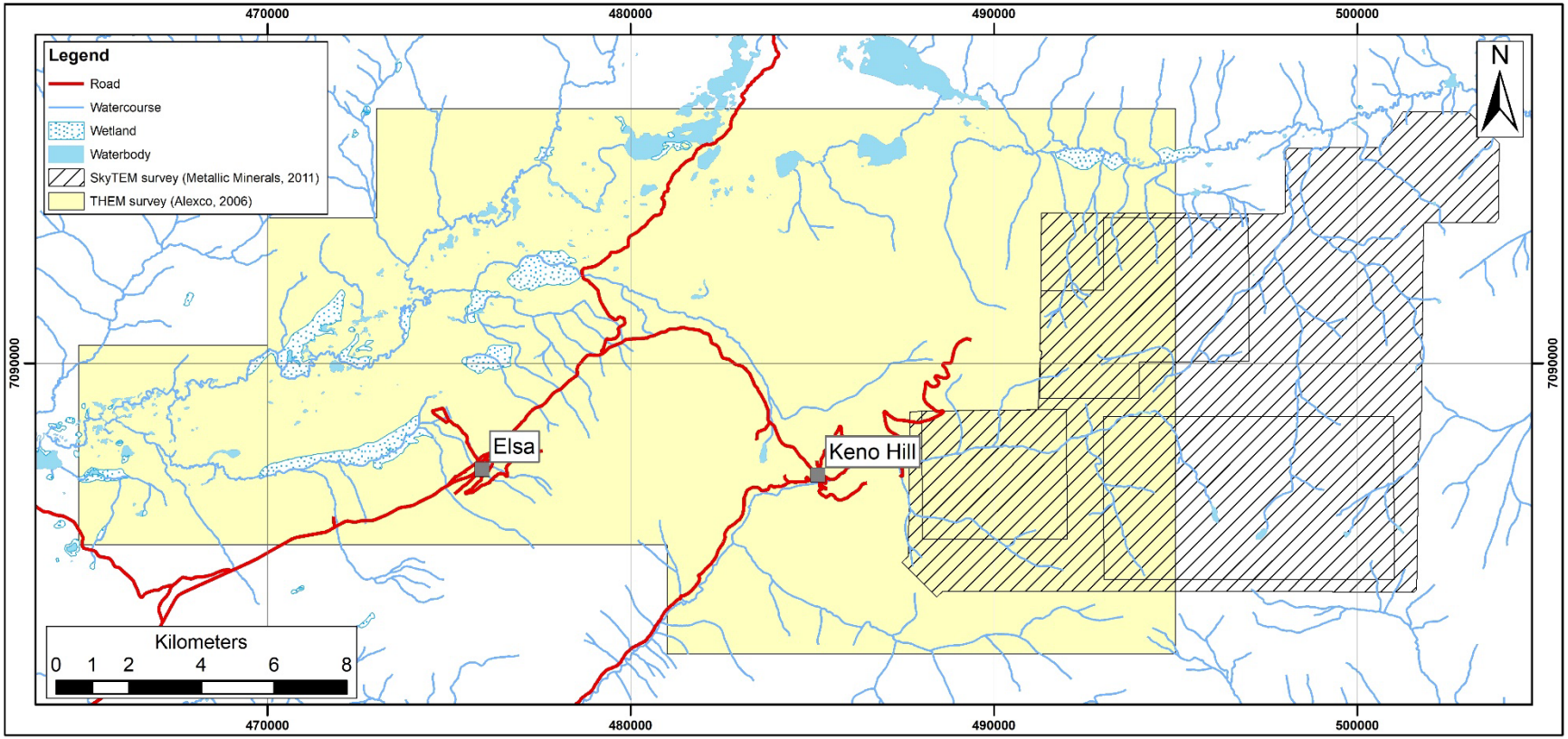

Figure 3.4: Map showing limits of the Alexco's 2006 helicopter magnetic and THEM survey and Metallic Mineral's 2011 SkyTEM survey.

The airborne magnetic data sets supplied by Alexco and Metallic Minerals were of varying vintage, and had varying flight line directions, flight line spacing, and acquisition height. As such, prior to the district-scale interpretation the datasets were compiled and levelled by Ronacher-McKenzie Geoscience, on behalf of the author (Figure 3.5). The variations in flight line spacing and acquisition height mean that there are variations in resolution of the magnetic data across the area. In general, the SkyTEM data to the east of the area (supplied by Metallic Minerals) has a line spacing of 100 metres, and as such is of higher resolution than the THEM data (200 metre line spacing, supplied by Alexco) to the west of the area. To ensure no scale bias was introduced, the district-scale interpretation was completed at a scale of 1:25,000; this was the best usable scale for the lowest resolution dataset.

The regional interpretation was completed on a single, magnetic compilation dataset. The compilation includes relatively high-resolution airborne surveys (250 to 500 metre line spacing); however, for the area of interest the line spacing for the survey is relatively coarse (800 m). As such the regional interpretation was completed at a scale of 1:250,000.

Interpretations were based on the first vertical derivative (1VD; Figure 3.5) and tilt derivative maps, and on digital elevation (DEM; Figure 3.6) data. The interpretations follow the methodology outlined by Siddorn et al. (2020). Details on post-processing and preparation of the data completed by the author are available in Appendix A.4.

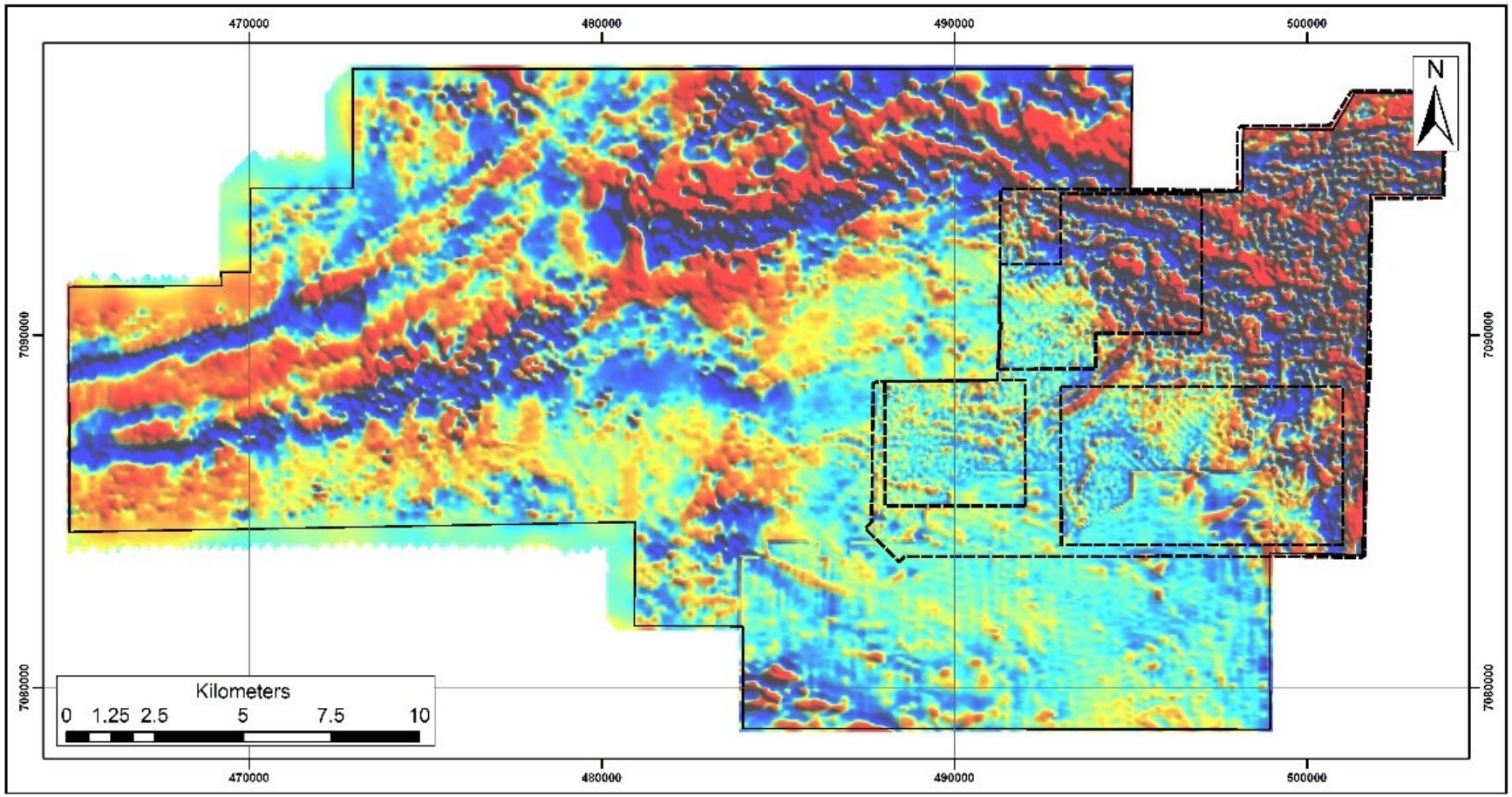

Figure 3.5: Levelled 1VD data used for 2D interpretation of airborne magnetic data. Dashed lines indicate data supplied by Metallic Minerals.

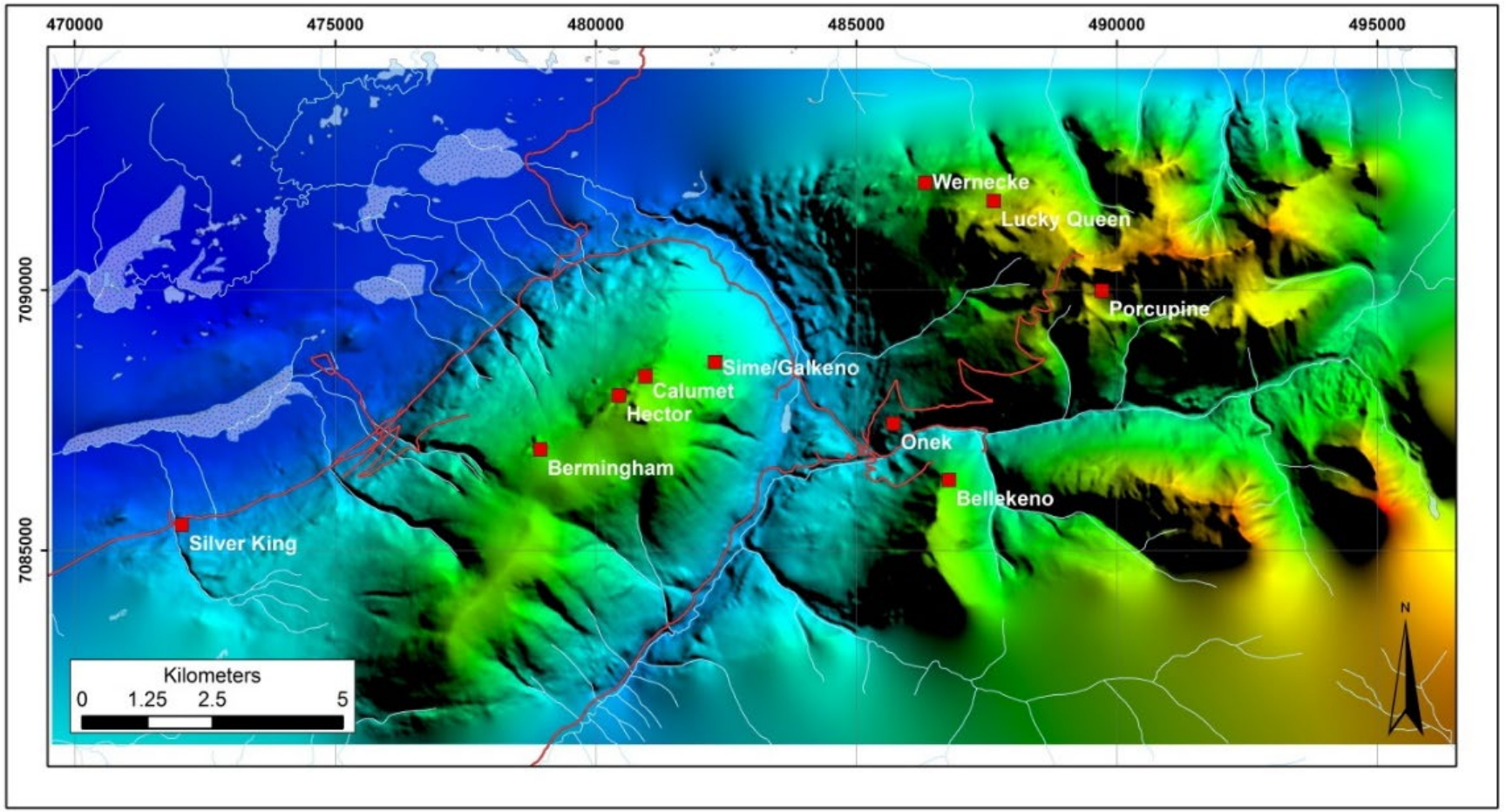

Figure 3.6: Shaded-relief image of DEM data

Each identified lineament was classified in an attribute table in ArcGIS™. The description of the attribute fields used is included in (Appendix A.5). Metadata for the interpretation is provided in Appendix D within a series of ArcGIS™ map packages and provides information on fault order, fault length, fault strike, and interpreted fault age. Faults were classified by age and order based on the criteria outlined in Table 3.2. The interpretation followed a process that is outlined below with additional details present in Appendix A.5:

1. **Interpretation of Magnetic Data:**
    a. **Formline Mapping:** Form lines trace the geometry of stratigraphy and tectonic fabrics within volcanic and metasedimentary rocks or the internal fabric (foliation) within intrusive rocks. Discontinuities between form lines, particularly stratigraphic form lines (e.g., intersecting form lines) highlight structures (faults, folds), unconformities, or intrusive contacts.

    b. **Fault and Shear Zone Mapping:** A structural base layer was drawn using the 1VD data representing all faults regardless of interpreted age, style (e.g., brittle versus ductile), or kinematics.

    c. **Assessment of Age Relationships:** Relative age and cross-cutting relationships were defined between different families of structures. At this stage the potential for fault reactivation is taken into consideration, whereby interpreted older structures may have been reactivated during

later deformation phases and thus appear to offset faults of a younger interpreted age.

d. **Estimation of Structure Scale:** An estimation of fault/shear zone order (i.e., 1st, 2nd, 3rd order) was attributed. This process identifies the locations of major structures verses subsidiary structures. The classification of fault/shear zone order is defined in Table 3.2. Lineament lengths were calculated using a simple geometrical calculation of the total length of the polyline in ArcGIS™.

2. **Statistical Analysis of Lineament Trends:** An analysis of lineament trends is an essential part of the structural lineament interpretation, as it allows the interpreter to identify different sets of structures and to relate those sets to the known structural history of the area. Lineament orientations (strike) were calculated using ET EasyCalculate 10, an add-in extension to ArcGIS™. Rose diagrams showing the frequency of occurrence of lineament orientations were produced in Spheristat™, with frequencies divided into 5° bins. Lineament lengths were used as a weight factor for computing rose diagrams.

3. **Calculation of Lineament Density:** Lineament density calculations provide insight into areas of increased structural complexity that may be associated with areas of increased fluid flow and elevated mineralisation. The lineament

density analysis was conducted using the ArcGIS™ Analysis and Spatial Analyst toolsets (details are provided in Appendix A.5).

Table 3.2: Fault definitions, characteristics, and kinematics

Fault Age	Fault Order	Geophysical Signature	Characteristics	Kinematics
D_1	1	Short, to moderate length, typically wide magnetic low, defining a single fault or fault segment.	Major, linear to curvilinear faults. Offset or truncated by D_2 and D_3 faults.	Reverse
	2	Typically, short length, moderate to narrow width, subtle magnetic low, defining a single fault or fault segment.	Linear to curvilinear faults. Offset or truncated by D_2 and D_3 faults.	Reverse
	3	Short length, narrow, subtle magnetic low, defining a single fault or fault segment.	Minor curvilinear faults. Offset or truncated by D_3 and D_3 faults. Rarely folded about an east-west fold axis.	Reverse
D_2	1	Linear, segmented, wide magnetic low, defining a single fault or fault segment.	Major, ENE-, to NNE-trending, linear faults. Truncate or offset D_1 faults. Offset or truncated by D_3 faults.	Sinistral-Normal
	2	Linear, to curvilinear, moderate length, moderate width magnetic low, defining a single fault or fault segment. May form sigmoidal faults linking 1st order D_2 faults.	Moderate, ENE-, to NNE-trending, linear to curvilinear faults. Truncate or offset D_1 faults. Offset or truncated by D_3 faults.	Sinistral-Normal
	3	Typically, short, linear to curvilinear, narrow, rarely subtle, magnetic low, defining a single fault or fault segment. May form sigmoidal faults linking 1st and 2nd order D_2 faults.	Minor, ENE-, to NNE-trending, linear to curvilinear faults. Truncate or offset D_1 faults. Offset or truncated by D_3 faults.	Sinistral-Normal
D_3	1	Long, linear, typically wide magnetic low defining a single through-going fault that truncates and offsets magnetic high anomalies oblique to the fault.	Major, linear, NW-trending faults. Truncates or offsets D_1 and D_2 faults.	Dextral-Normal
	2	Moderate to sporadically long, moderate to narrow width, commonly subtle magnetic low that defines a single fault that truncates and offsets magnetic high anomalies oblique to the fault.	Moderate linear, NW-trending faults. Truncates or offsets D_1 and D_2 faults. Forms a network with 1st order D_3 faults	Dextral-Normal
	3	Short to moderate length, narrow, subtle magnetic low that defines a single fault that truncates and offsets magnetic high anomalies oblique to the fault.	Minor, linear, NW-trending faults. Truncates or offsets D_1 and D_2 faults. May link between 1st and 2nd order D_3 faults	Dextral-Normal

3.4 Three-dimensional (3D) Analysis

Three dimensional (3D) analysis of subsurface data, including borehole data, surface and sub-surface *in situ* measurements, and magnetic data was completed for the Keno Hill area to determine and visualise the 3D structural architecture and its relationship to Ag-Pb-Zn mineralisation (Appendix D). The analysis was completed in Leapfrog GeoTM 3.0 software. Further details of the data preparation, methodology, and functions used are provided in Appendix A.6.

Due to the large amount of data contained within the database, it was impractical to model the entire Keno Hill area as a single entity. The available borehole data was subdivided into discrete domains based on the geographic location of the data, and on mineralisation trends observed during field investigations and within the borehole data (Figure 3.7). The quantity and quality of available data varies significantly throughout the district. As such, while 3D modelling of Ag grade was completed on each of the domains, detailed fault and vein modelling was only completed for the Galena summit domain. This area contained the largest amount of reliable data for the district.

The 3D modelling was an iterative process, whereby if a modelled element (e.g., a fault, vein domain, or mineralisation grade shell) was modified then all other elements were evaluated subsequent to the modification and adjusted accordingly. Methodologies employed in the 3D modelling included:

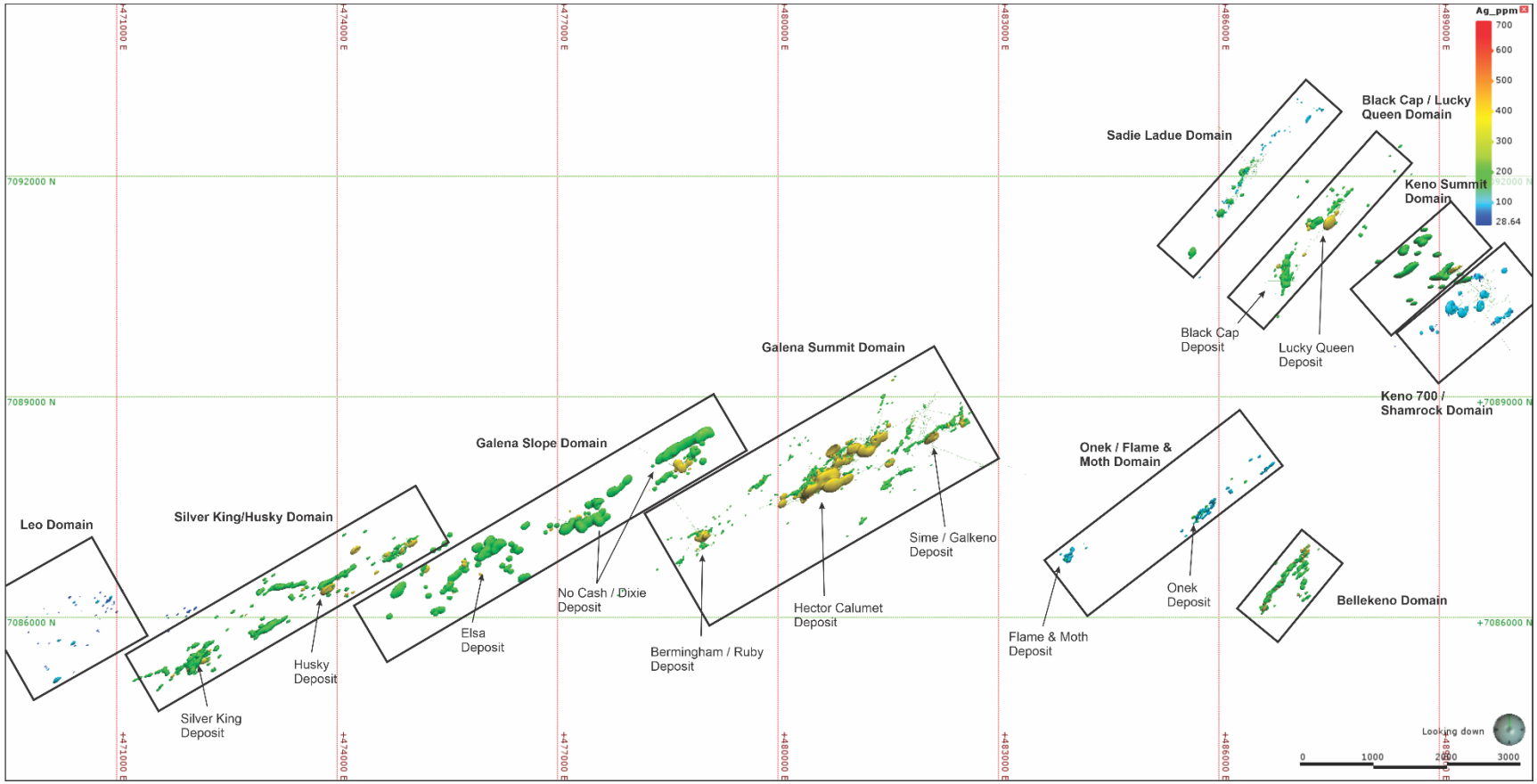

Figure 3.7: Map showing locations of mineralised domains

Ag-Pb-Zn Grade Modelling

Initial, isotropic grade modelling was completed for each of the major economic elements present within the Keno Hill District (i.e., Ag, Pb, and Zn) to assess overall mineralised trends in the district. Subsequent anisotropic modelling iterations were refined using structural trends based on geological knowledge of the district. Ag grade was modelled at the "unrestricted" domain-scale, and subsequently exclusively within modelled veins.

Fault and Vein Modelling

Faults and veins were modelled for the Galena summit mineralised domain. Ag-Pb-Zn-mineralised veins were modelled as 3D volumes and late, post-mineralisation faults were modelled as 2D surfaces. Data used to model faults and veins included:

- Borehole assay data;
- Borehole lithological data including the locations of logged faults;
- Geotechnical logs;
- Core photographs;
- Direct observations of faults in outcrop by the author and previous workers;
- Surface and subsurface lineaments identified during the 2D data interpretation;
- .dxf files of subsurface infrastructure. All drifts and ramps were available; however, no stope data was supplied; and
- Historic level plans, digitised by the author (Figure 3.8).

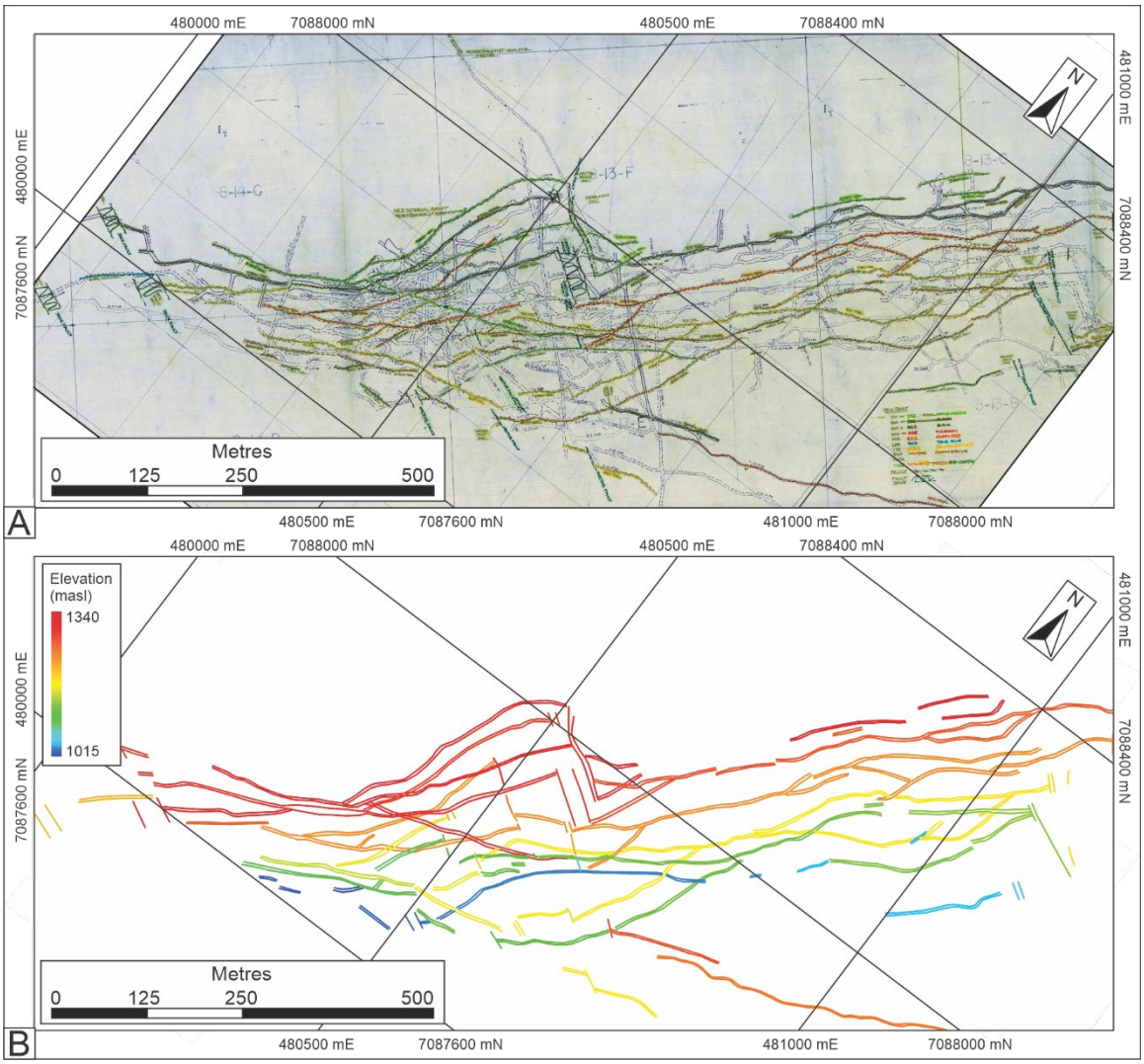

Figure 3.8: Georeferenced scan of composite level plan (A) and digitized faults and vein in the Hector and Calumet deposits. Original composite level plan was produced by United Keno Hill Mines (UKHM; date unknown) and supplied to the author by Alexco in November 2008.

3.5 Laboratory Analytical Techniques

During the field investigations 226 samples were collected. Of the 226 collected samples, 93 polished thin sections and 34 polished slabs were prepared for further petrographic and geochemical analysis (Appendix E). In addition, 6 whole rock samples were selected

for U-Pb and $^{40}Ar/^{39}Ar$ analysis (Appendix F). The following section outlines the procedures employed for each analytical technique; further details are available in Appendix A.7.

3.5.1 Optical and Scanning Electron Microscopy

Polished thin sections were prepared at the University of New Brunswick (UNB) and were analysed using a binocular optical microscope. Samples were analysed under plane polarised light, cross-polarised light, and reflected light. Selected samples were scanned at various scales using a Zeiss Axio Imager A1m microscope, and images were stitched together to produce high-resolution photomicrographs using Zeiss AxioVision™ software.

Samples were analysed for mineralogy, structural fabrics and textures, and additional areas of interest within polished thin sections were identified for further analysis by scanning electron microscope (SEM). The polished thin sections selected for SEM-EDS analysis were assessed under a binocular microscope, areas of interest were marked, and the sections were carbon coated.

A total of eight thin sections were analysed by SEM (Figure 3.9; Appendix C). Six samples were analysed using a JEOL JSM6400 Digital SEM, equipped with Geller dPict digital image acquisition software, and an EDAX (Genesis) Energy Dispersive X-ray Analyzer at UNB's Microscopy and Microanalysis Facility (MMF). Four samples were

analysed using a Hitachi SU-70 Field Emission Gun (FEG) SEM at UNB's Planetary and Space Science Centre (PASSC) including two samples that had previously been analysed using the JEOL 6400 SEM.

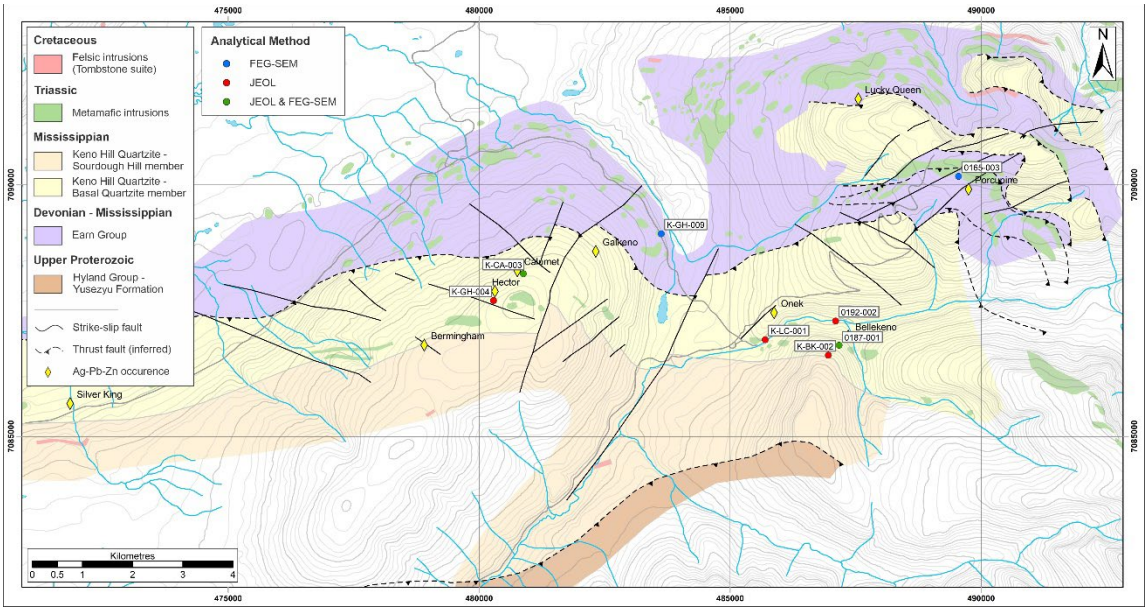

Figure 3.9: Simplified geological map of the Keno Hill district showing sample locations for analysis by SEM. Base map modified from Murphy (1997).

3.5.2 Geochemical Analysis

Forty one field and drill core samples were selected for geochemical analysis (Figure 3.10; Appendix E). Geochemical analytical techniques included instrumental neutron activation analysis (INAA; 40 samples), X-ray diffraction (XRD; 21 samples), and X-ray Fluorescence Spectrometry (XRF; 40 samples).

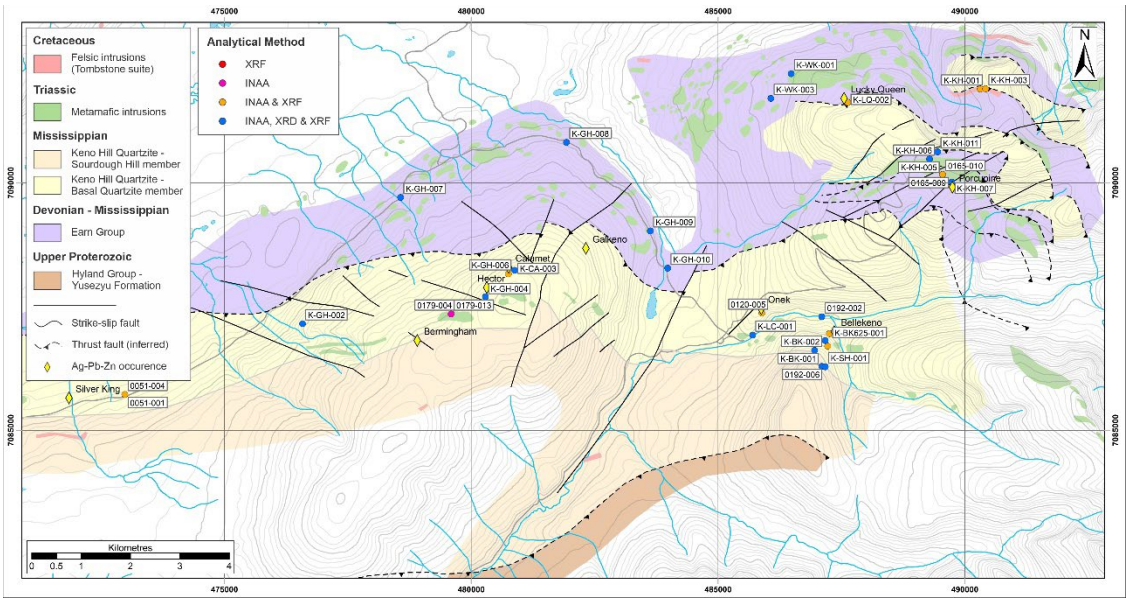

Figure 3.10: Simplified geological map of the Keno Hill district showing sample locations for analysis by INAA, XRD, and XRF. Base map modified from Murphy (1997).

Thirty-four samples of variably deformed greenstone were analysed by the Instrumental Neutron Activation analysis (INAA), X-ray Diffractometry (XRD), and X-ray Fluorescence spectrometry (XRF) methods (Appendix E). Of the 34 samples, 16 were collected from surface exposures that had minimal to no veins present. Samples were cut using a rock saw to remove any surface weathering. Three samples were collected from the 600 level of the Bellekeno underground workings, and 15 samples were collected from drill core.

Seven additional samples were analysed by the XRF and/or INAA; five samples of felsic intrusive rocks from the north flank of Keno Hill (samples K-KH-001 and K-KH-003) and the McQuesten Airstrip locality west of the main study area (samples K-McQ-001, K-McQ-002, and K-McQ-003), one sample of a lamprophyre dyke from the summit of

Galena Hill (sample K-GH-006), and one sample of sericite schist drill core collared near the summit of Galena Hill (sample 0179-004).

Pulps of the selected samples were prepared at the University of New Brunswick; the samples were crushed in a jaw crusher and pulped in a soft iron swing mill with less than 0.1 wt. Fe contamination. XRF (X-ray Fluorescence Spectrometry) analysis was conducted on pressed pellet samples at Memorial University Newfoundland, INAA (instrumental neutron activation analysis) was performed by Activation Laboratories Inc. (ActLabs), and XRD analysis was performed at the University of New Brunswick.

The XRD analysis was conducted on a Bruker D8 Advance. The XRF analysis was conducted on a Bruker S8 Tiger sequential wavelength-dispersive x-ray spectrometer, with an argon/methane flow proportional counter and a scintillation counter. The pressed powder sample preparation allowed for less than a 1 ppm detection limit for selected samples (TERRA, 2019). The XRF analysis produced concentration data for 30 major element oxides and minor elements.

3.6 Geochronology

Six samples were selected for geochronological analysis (Appendix F). Five whole rock samples were selected for $^{40}Ar/^{39}Ar$ analysis, one whole rock sample was selected for U-Pb CA-TIMS (Chemical Abrasion - Thermal Ionization Mass Spectrometry) analysis.

The $^{40}Ar/^{39}Ar$ analysis was completed at Queen's University and the U-Pb CA-TIMS analysis was completed at the University of British Columbia.

3.6.1 $^{40}Ar/^{39}Ar$ Analytical Methodology

Samples for the $^{40}Ar/^{39}Ar$ analysis were collected at (Ag)Pb-Zn-mineralised vein selvages in drill core and from the 750-1 crosscut in the Bellekeno underground mine (samples 0187-005, U0160-009, and K-BX-007), and in strongly sericite-altered rocks within the fault damage zone associated with the Onek vein in an attempt to determine the timing of mineralization and hydrothermal alteration. The details for procedure used for the $^{40}Ar/^{39}Ar$ analysis were provided by D. Archibald (personal communication, February 10, 2012) and available in Appendix A.7.3.

3.6.2 U-Pb Analysis

Igneous suites in the study area comprise greenschist facies metamorphosed, variably foliated gabbro and diorite sills, and rare unfoliated granitic to aplitic dykes. Optical and SEM microscopic analysis of gabbroic rocks identified rare, small, irregularly formed, metamict zircon crystals and very rare baddeleyite. These samples were not considered suitable for U-Pb analysis (Figure 3.11).

One, in situ outcrop of unfoliated, massive, grey to pink, quartz-biotite-hornblende granite was observed. Polished thin section analysis of a sample from this outcrop (sample K-KH-003) showed the sample contained relatively common euhedral to

subhedral zircons. This sample was selected for U-Pb analysis by the CA-TIMS method at UBC. The details for procedure used for the 40Ar/39Ar analysis were provided by R. Friedman (personal communication, May 25, 2010) and available in Appendix A.7.3.

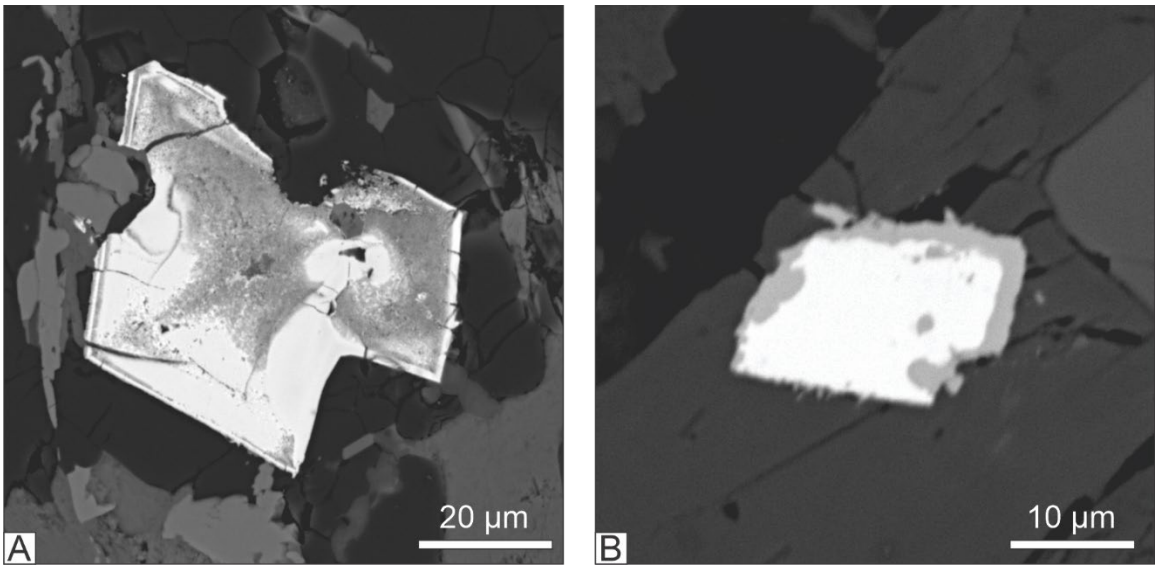

Figure 3.11: SEM-BSE images of metamict zircon grain (A) and baddeleyite grain (B) in metagabbro from the Calumet open pit (sample K-CA-003).

4. Field- and laboratory-based descriptions of lithological units, and associated geometric relationships

This chapter describes the metasedimentary and intrusive rock types and key outcrops observed in the district during field work. Ag-Pb-Zn-mineralisation, and the manifestation of structural elements in the district are in part dependent on lithology, grain size, and unit thickness. To resolve the lithological sequence an understanding of geometric relationships is required. As such, descriptions of the structural characteristics of each unit are made, however, a detailed discussion on the structural geology characteristics is provided in Chapter 5. In addition, descriptions of veins (pre- and syn-Ag-Pb-Zn-mineralisation) are made, and a summary of the results of the greenstone geochemistry study are presented.

Interpretations of the absolute and relative ages of rocks in the Keno Hill district have changed significantly since Boyle's (1965) report and mapping program (see Chapter 2.3). The units described in this chapter follow the stratigraphic sequence outlined by McOnie and Read (2009) (Figure 4.1 and Figure 4.2). The following section shall describe the characteristics of the lithological units in the Keno Hill mining district. The lithological units are described in stratigraphic and intrusive order, from oldest to youngest.

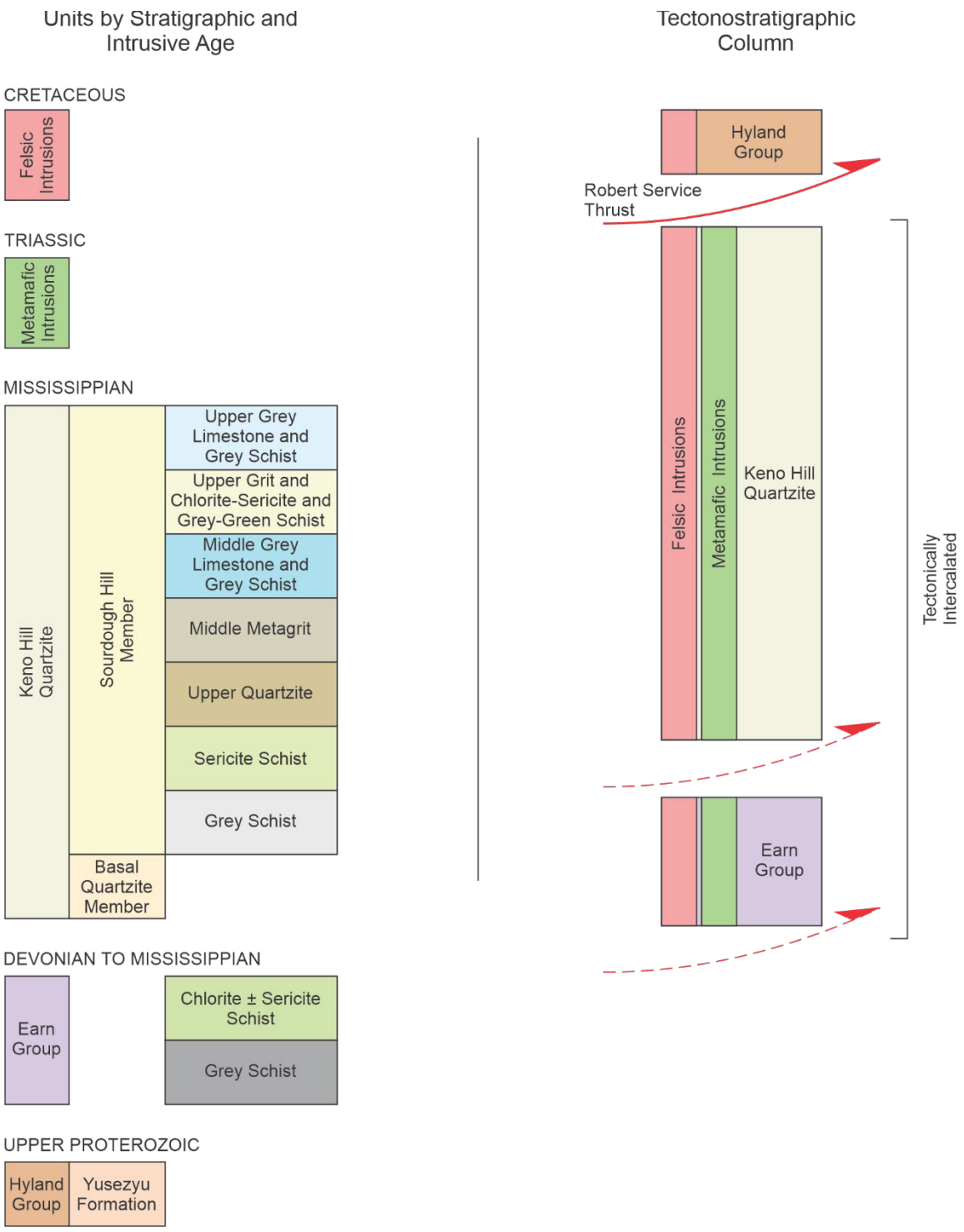

Figure 4.1: Column showing stratigraphic units by age and associated tectonostratigraphic column (modified after McOnie and Read, 2009).

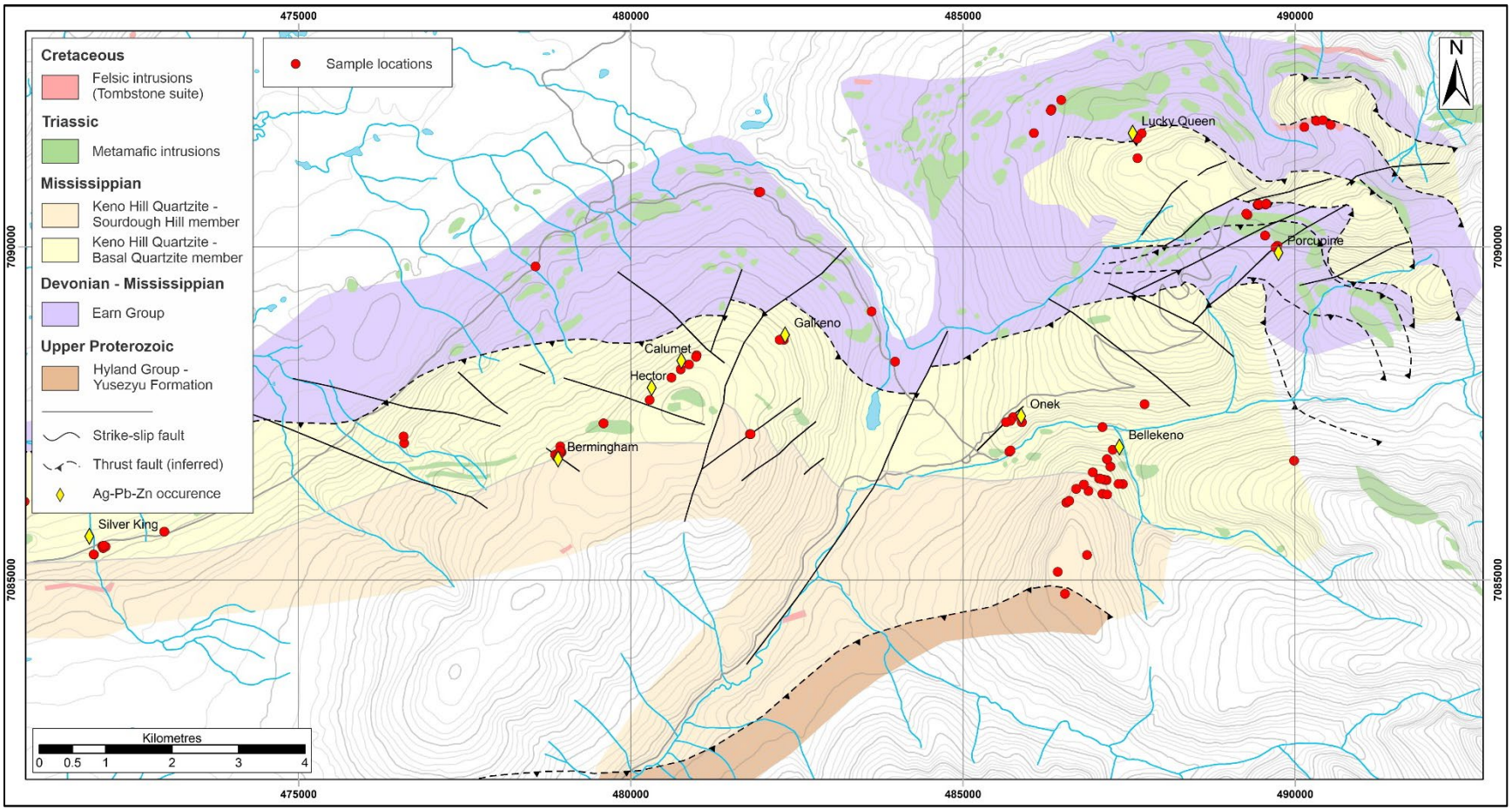

Figure 4.2: Simplified geological map of the Keno Hill district showing sample locations. Base geological data modified after Boyle (1965), Murphy (1997), and Alexco (2021).

4.1 Metasedimentary Units

4.1.1 Yusezyu Formation - Hyland Group

During fieldwork only one outcrop of Yusezyu Formation rock was observed, located near the summit of Sourdough Hill. The outcrop comprised pale grey, weathering to orange - tan coloured, fine-grained, muscovite phyllite. The outcrop contained a strong, south-dipping foliation, and an approximately sub-horizontal, east-west trending intersection lineation. It should be noted that proximal to, and structurally below the location of the observed phyllite, two small outcrops of limestone were observed. Previously these have been assigned to the Yusezyu Formation, however McOnie and Read (2009) consider these to be an upper member of the Keno Hill Quartzite, and as such will be described in a later section.

4.1.2 Earn Group

Grey Schist

Towards the base of the northern flank of Keno Hill, Earn Group rocks are mapped in the vicinity of the Wernecke open pit (Figure 4.2). At this locality, rocks comprise dark grey and weathering to black and sporadically orange graphitic schist. The schist is intercalated with commonly thin, laminated, boudinaged quartzite, and is in fault contact along a steep SE-dipping, NE-striking fault, with massive, to laminated quartzite and lesser graphitic schist that is typical of the basal member of the KHQ. Rocks are

brecciated proximal to the fault and show variable sericite alteration. Siderite with sphalerite and galena sulfidation is common proximal to the fault, with lesser pyrrhotite and bornite, with secondary azurite and malachite also present.

Within the Porcupine and Keno 700 deposits, dark grey to black, weathering to tan phyllite is present in the footwall of the Porcupine Fault (Figure 4.3). Rare layers are weakly calcareous. The phyllite is strongly deformed with two prominent foliations, and open to close, commonly asymmetric, north-verging folds present. Along the ENE-striking, steep SSE-dipping Porcupine Fault, phyllite is in fault contact with a unit of silvery green, weathering to tan sericite schist unit, and a greenstone intrusion. Due to the faulted contact, it is unclear whether the sericite schist is the equivalent of the chlorite ± sericite schist unit of the Earn Group (as suggested by Murphy (2009) and McOnie and Read (2009)), or if it is equivalent to a sericite schist unit that forms a prominent marker horizon within the KHQ. Visually, the sericite schist unit at the Porcupine deposit appears more akin to sericite schist units observed in the Bermingham and Onek deposits, and as such may be assigned to the KHQ.

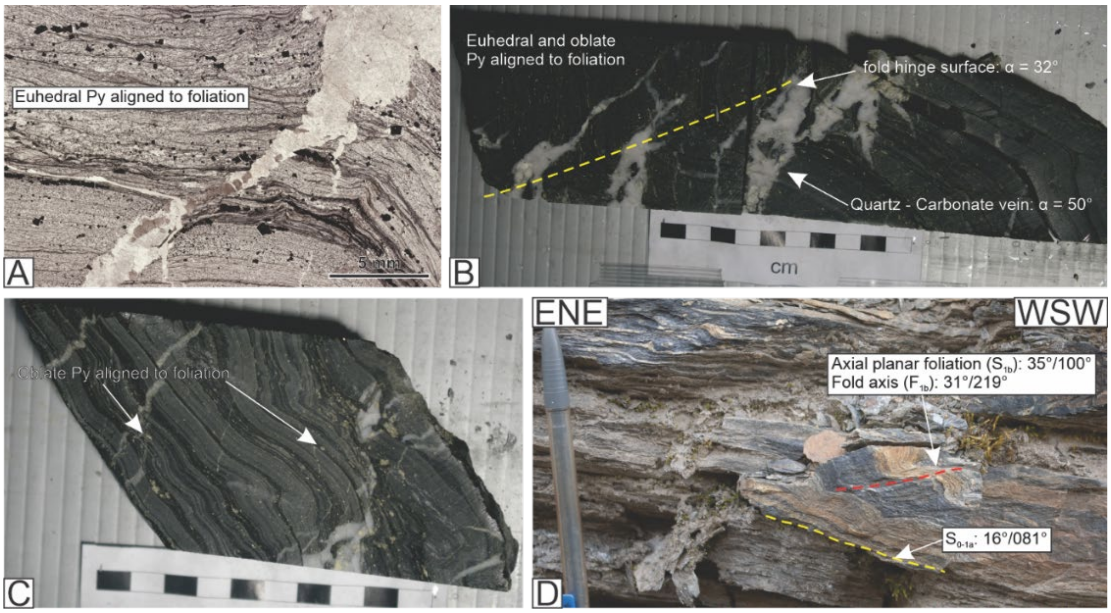

Figure 4.3: Examples of Earn Group "grey schist" rocks in (A) thin section (transmitted light scan), (B and C) drill core, and (D) outcrop.

A: Photomicrograph (ppl) of sample 0165-014 from the Keno 700 deposit (borehole K-08-0165, depth 174.30 m); B: drill core photograph of sample 0165-014 from the Keno 700 deposit (borehole K-08-0165, depth 174.30 m); C: drill core photograph from the Keno 700 deposit (borehole K-08-0165, depth 174.50 m); D: photograph of outcrop at Porcupine deposit showing $S_{0\text{-}1a}$ and S_{1b} foliations (UTM 489740 mE, 7089995 mN).

Chlorite ± Sericite Schist

The chlorite ± sericite schist occurs near the top of the Earn Group and near the base of the Keno Hill Quartzite. It is a silvery green to dark green schist that lacks grit (Figure 4.4) and is considered by Murphy (1997) to be a felsic metavolcanic rock. This unit was observed to outcrop in various localities including at the summit of Keno Hill, where it occurs in the footwall of the No.6 and No.9 veins, along the main highway between Elsa and Keno City, particularly in the valley between Galena and Keno hills, and east of the Wernecke open pit. The unit is strongly deformed at the summit of Keno Hill, where it exhibits a well-developed foliation, and common outcrop- to intrafolial-scale, tight to

isoclinal folds, and C-S fabrics (Figure 4.4A and B). Rare polyclinal folds were also observed. Quartz segregations are abundant, and commonly define isoclinal folds. Chlorite alteration is pervasive but appears strongest proximal to greenstone (metagabbro-metadiorite) intrusions, and hydrothermal sericite is apparent proximal to NNE- to NE-striking faults. At the summit of Keno Hill slivers of chlorite-sericite schist overthrust slivery grey phyllite (grey schist unit) and massive quartzite (KHQ) along numerous small to large-scale thrust faults. A steep strain gradient is apparent when approaching a major thrust fault in the footwall of the No.6 vein.

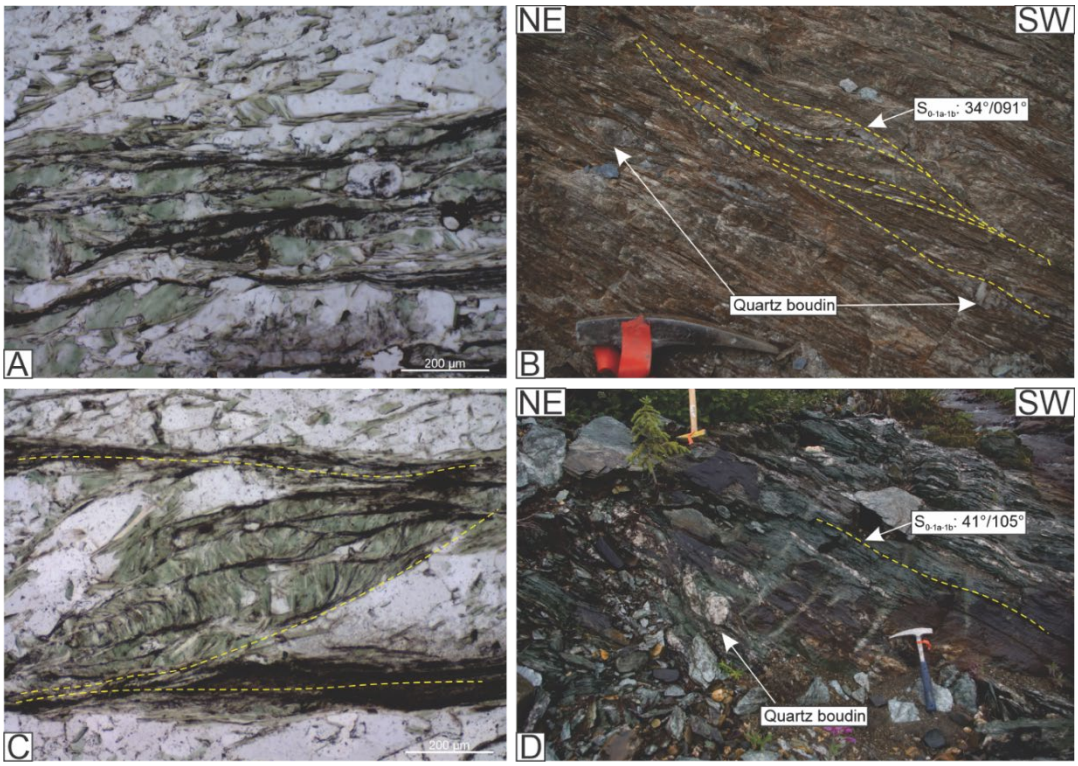

Figure 4.4: Examples of Earn Group "chlorite ± sericite schist" rocks in thin section, and outcrop.

A: Photomicrograph (ppl) of sample K-KH-011 from the summit of Keno Hill (UTM 489448 mE, 7090625 mN); B: photograph of highly strained outcrop at summit of Keno Hill (UTM 489461 mE, 7090629 mN); C: photomicrograph of sample K-GH-010 showing C-S fabric in chlorite ± sericite schist from Keno Elsa Highway near the Galkeno portal (UTM 483979 mE, 7088275 mN); D: photograph of strongly chlorite-altered schist with quartz boudins near the Galkeno portal (UTM 483979 mE, 7088275 mN).

4.1.3 Keno Hill Quartzite

The KHQ is located stratigraphically and structurally above the Devonian to Mississippian Earn Group rocks. In terms of mineralisation, it is the most important unit in the district. The Ag-Pb-Zn-bearing veins in the Keno Hill district crosscut, and are largely contained within, the Mississippian Keno Hill Quartzite unit.

Sensu lato, the KHQ comprises thick packages of massive to foliated quartzite, intercalated with relatively thin schistose units; however, the unit is locally lithologically complex and comprises numerous varying lithologies. Unit thickness and abundance of the various rock types vary laterally and vertically across the district. Rock types present in the KHQ include massive to well-foliated and lineated dark grey to black graphitic quartzite containing variable amounts of graphite, muscovite, and chlorite, phyllitic quartzite; medium to dark grey, locally carbonaceous phyllite; and intercalated graphitic and muscovite schist, and graphitic phyllite. Rare calcareous quartzite and thin limestone units are present towards the top of the unit.

Basal Quartzite Member

The Basal Quartzite member is characterised at the outcrop-scale by the presence of grey to light grey, weathering to orange, massive to rarely laminated, quartzite (Figure 4.5) with varying amounts of interbedded graphite, sericite, and chlorite schist, and grey phyllite.

Figure 4.5: Photograph of massive, grey, homogenous, equigranular quartzite in drill core (borehole BKUD09-0153, depth 68.60 m, Bellekeno deposit).

The thickest observed layers of quartzite were located within the Bermingham, Calumet, and Sime open pits along the summit of Galena Hill, and along Galena Creek proximal to the Silver King open pit (Figure 4.2). At these localities individual layers of quartzite were observed to be up to, or rarely greater than 2 metres in thickness. Folding has resulted in thickening of these layers so that they can appear to be greater than 4 m thick proximal to isoclinal fold hinges (Figure 4.6). Thick (0.4 to 2 metre), massive quartzite layers are fine to medium grained (0.4 to 2.0 millimetre), blocky, fractured, and rarely chlorite altered. They are rarely intercalated with thin (< 1 millimetre) layers of graphitic or sericitic schist.

In polished thin section, the KHQ is a granoblastic fine-grained quartzite composed of equigranular interlocking anhedral quartz with minor discontinuous foliated muscovite and accessory grains of zircon and amphibole. Quartz grains typically have undulatory extinction and sutured grain boundaries with elongated grains displaying preferential orientation. Muscovite layers are commonly internally deformed, and both quartzite and muscovite layers locally contain disseminated euhedral to subhedral pyrite.

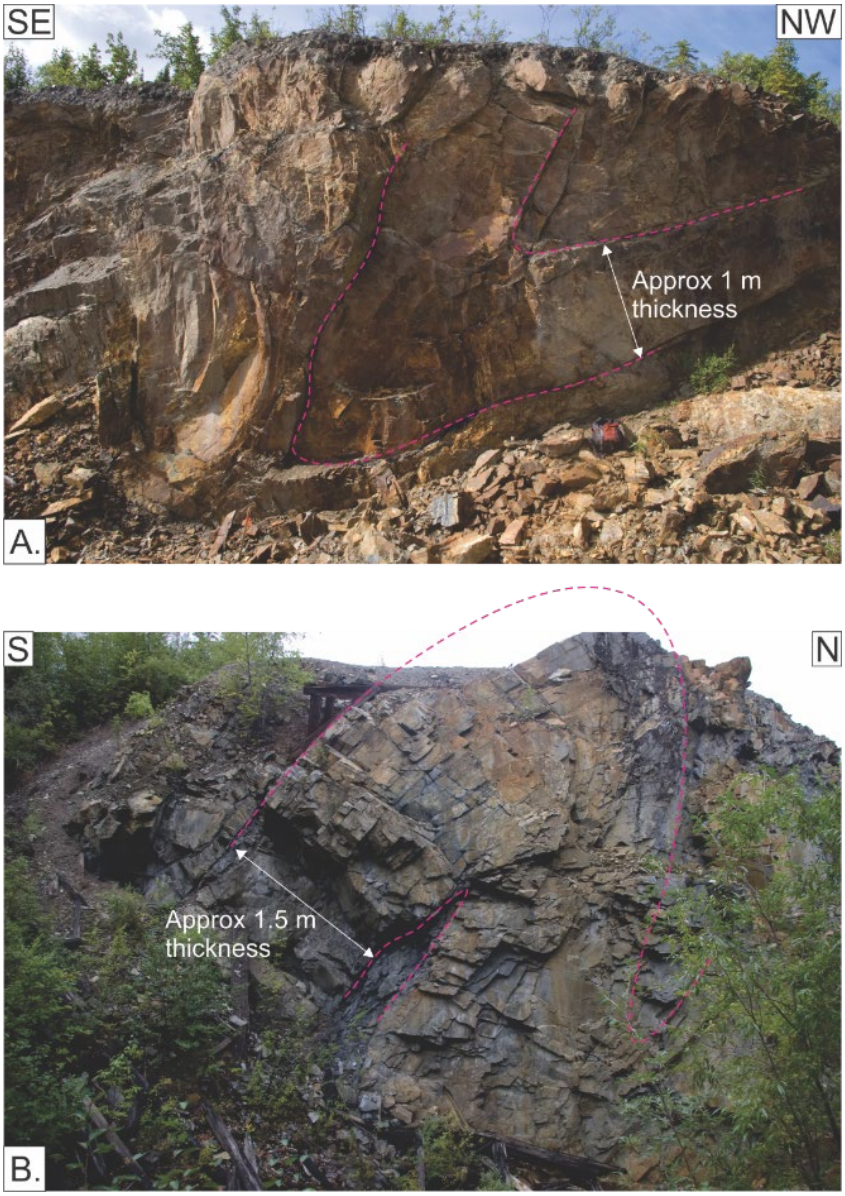

Figure 4.6: Photographs of thick quartzitic units within the Keno Hill Quartzite. Purple dashed line: Fold enveloping surface.

A: Folded, thick quartzite layer in the Bermingham open pit. NAD83 UTM Zone 8N, 478856 mE, 7086911 mN. B: Folded, thick quartzite layer at Galena Creek. NAD83 UTM Zone 8N 471939 mE 7085249 mN.

Vertically, the relative abundances of quartzite and schist vary. Thick, blocky units of quartzite transition in to medium-thick (0.1 to 0.3 metre) layers of quartzite, intercalated

with rare thin (typically 1 to 10 millimetre) schist or phyllite, which in turn transition into thin (5 to 30 millimetre) layers of quartzite with abundant intercalated, commonly graphitic schist (5 to 50 millimetre). The transition between zones of thicker quartzite with low schist content and zones of thinner quartzite with abundant schist is commonly (but not exclusively) sharp, and mineral stretching lineations or rare slickenfibres were commonly observed at the interface. Slickenfibres indicate that layer-parallel slip occurred at transition interfaces (Figure 4.7).

Foliation intensity increases with increasing schist (phyllite) content, and medium to thin layers of quartzite commonly exhibit a pronounced foliation, however as expected foliation intensity is greatest within the schistose units. Tight to isoclinal, rootless folds, and C-S fabrics are common in schistose units, with rare tight to isoclinal, commonly north-verging asymmetric folds observed in thicker quartzite units (Figure 4.8). Tight to isoclinal, and asymmetric folds become increasingly common with reduced quartzite thickness. This indicates that the majority of strain associated with brittle-ductile thrust/fold-related deformation was partitioned into the less competent, more schistose layers. At the Bellekeno deposit, abundant, sporadically rootless, isoclinal folds can be recognised in grey to black schistose layers in the walls of the Bellekeno East decline (Figure 4.9).

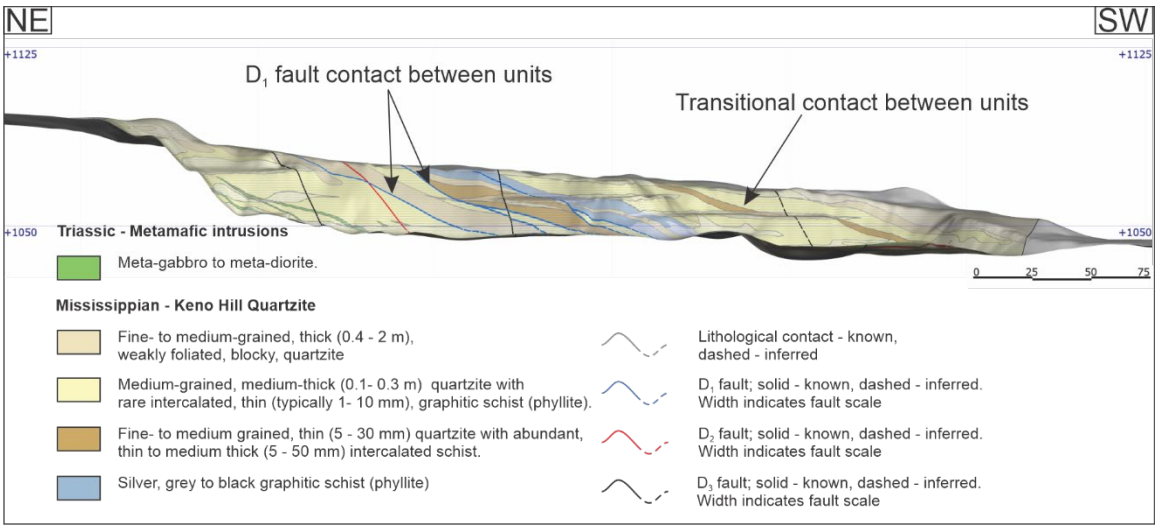

Figure 4.7: Long-section of the SE wall of the Onek open pit. Mapping data collected by the author draped onto topographic data supplied by Alexco.

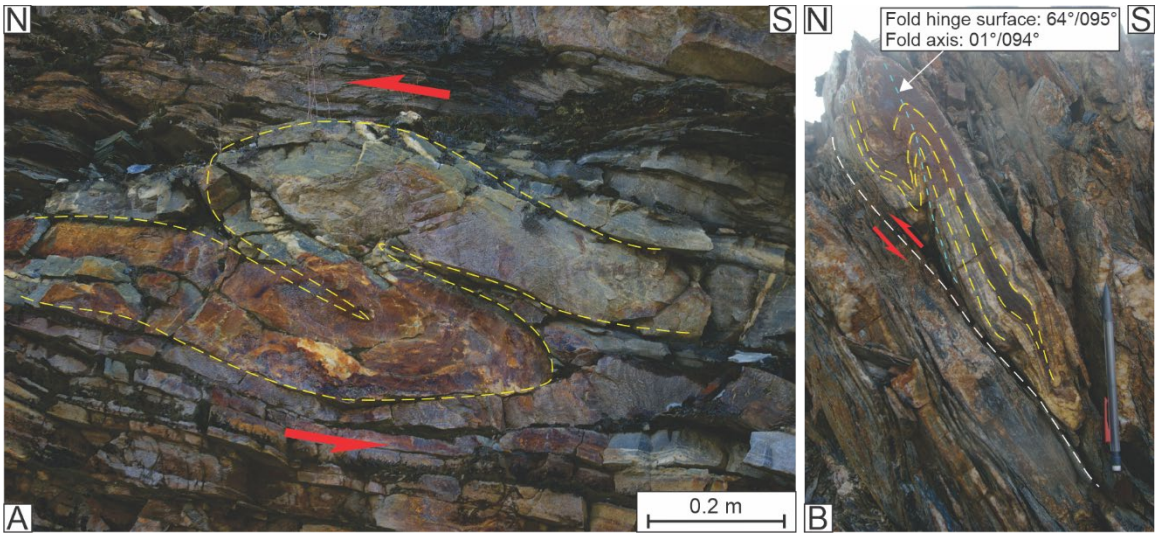

Figure 4.8: Examples of isoclinally folded, thin-layered quartzite intercalated with schist.

A: photograph of recumbent, asymmetric, north-verging, isoclinal fold at the Calumet deposit (UTM 408991 mE, 7088370 mN); B: photograph of upright, asymmetric, north-verging, isoclinal fold proximal to fault zone at the Onek deposit (UTM 485718 mE, 7087395 mN). White dashed line shows trace of fault zone; yellow dashed lines show trace of F_1 fold; blue dashed line shows trace of fold hinge; red arrows indicate transport direction.

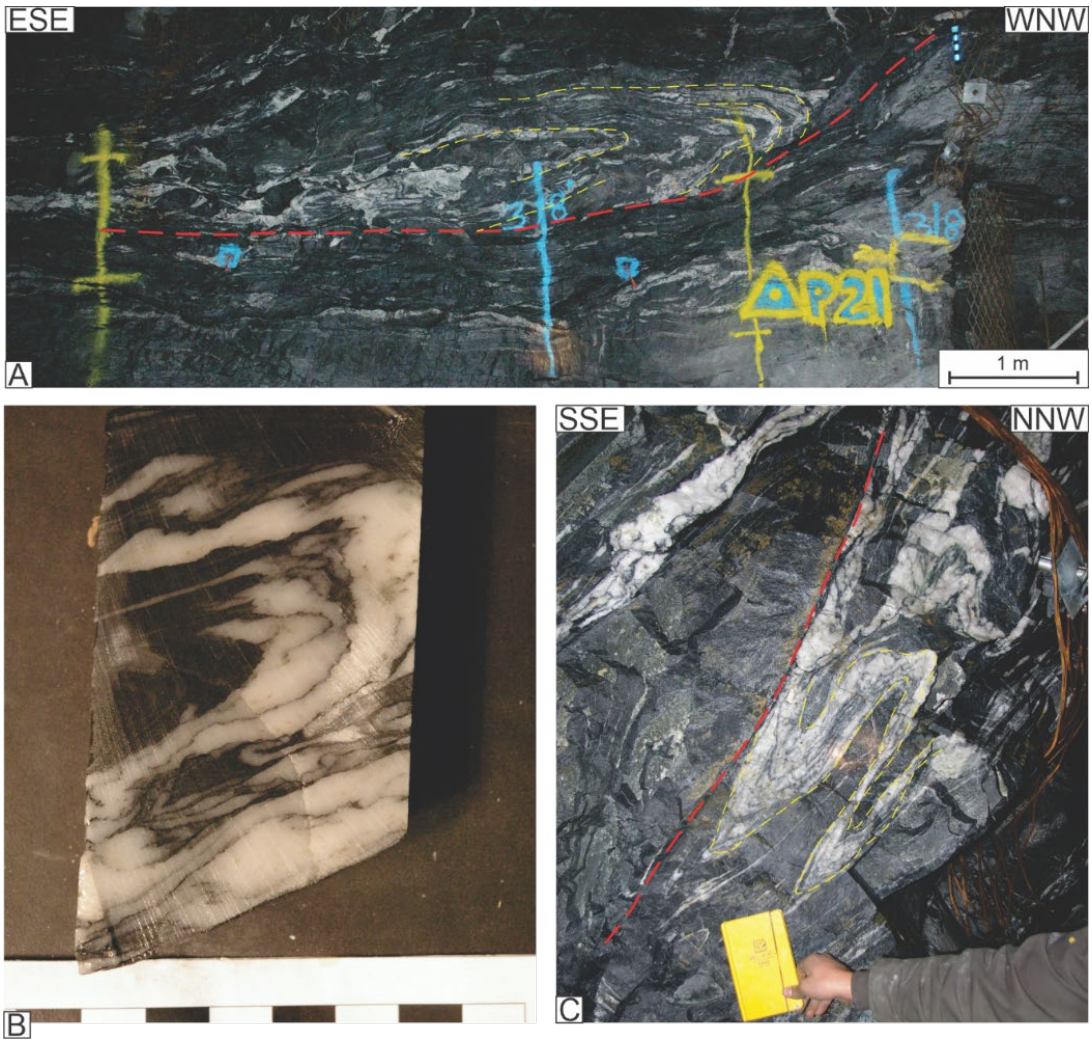

Figure 4.9: Examples of foliation-parallel quartz veins in underground workings and drill core.

A: Photograph of foliation-parallel quartz veins defining large isoclinal fold with lower limb truncated by shear zone in Bellekeno East decline (at survey point P21); B: photograph of isoclinally folded quartz veins in drill core (borehole K-08-0179, depth 70.15 m, Hector Calumet deposit); C: photograph of isoclinally folded quartz veins with upper limb of fold truncated by fault in Bellekeno East decline (10 m west of survey point P17). Red dashed lines show trace of fault/shear zone; yellow dashed lines show trace of F_1 folds.

Sourdough Hill Member

The Sourdough Hill member comprises quartzite-dominated units similar to those described above for the Basal Quartzite member, however, in addition discrete graphitic and sericite schist units are also present. In outcrop, schistose units were observed within the Bermingham and Onek deposits, and the graphitic schist was recorded during underground mapping and in drill core from the Bellekeno deposit, and in the Bermingham and Onek deposits.

The sericite schist is a silver to pale green, weathering to pale green and tan coloured schist, with rare, thin (< 10 millimetre) quartzite layers, and local chlorite alteration (Figure 4.10). The unit was observed in the south wall of the Bermingham open pit (where it has a thickness of greater than 30 metres), southwest of and in the hanging wall of the Onek vein, and possibly southwest of and in the hangingwall of the Porcupine vein (Figure 4.10 to Figure 4.14). Proximal to the Onek vein the unit is hydrothermally altered and has an orange-tan colour. Foliation-parallel boudinaged quartz veins and rare intrafolial arsenopyrite are present, particularly within the Bermingham open pit. The unit is commonly crenulated, warped and/or isoclinally folded, and in the Bermingham open pit the unit displays C-S fabrics.

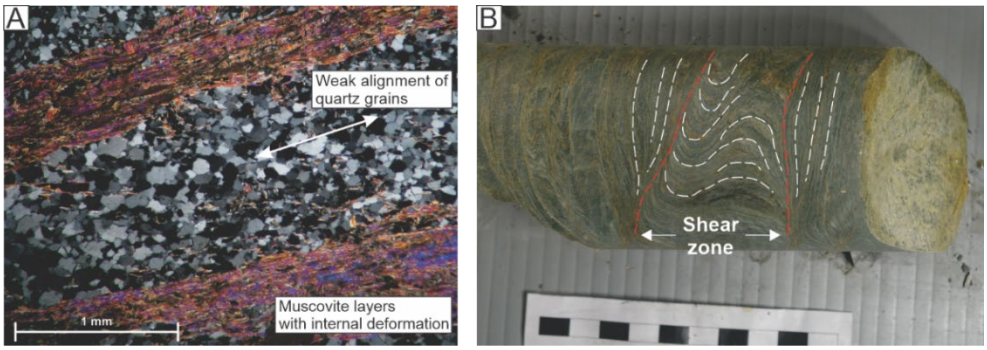

Figure 4.10: Characteristics of sericite schist in A) polished thin section, and B) drill core.

A: photomicrograph sericite schist in sample 0179-009 (borehole K-08-0179, depth 75.10 m, Hector-Calumet deposit); B: photograph of narrow shear zone in drill core (borehole K-07-0120, depth 64.30 m, Onek deposit). White dashed lines show $S_{0\text{-}1b}$ foliation; red dashed lines show trace of D_1 shear zone boundaries.

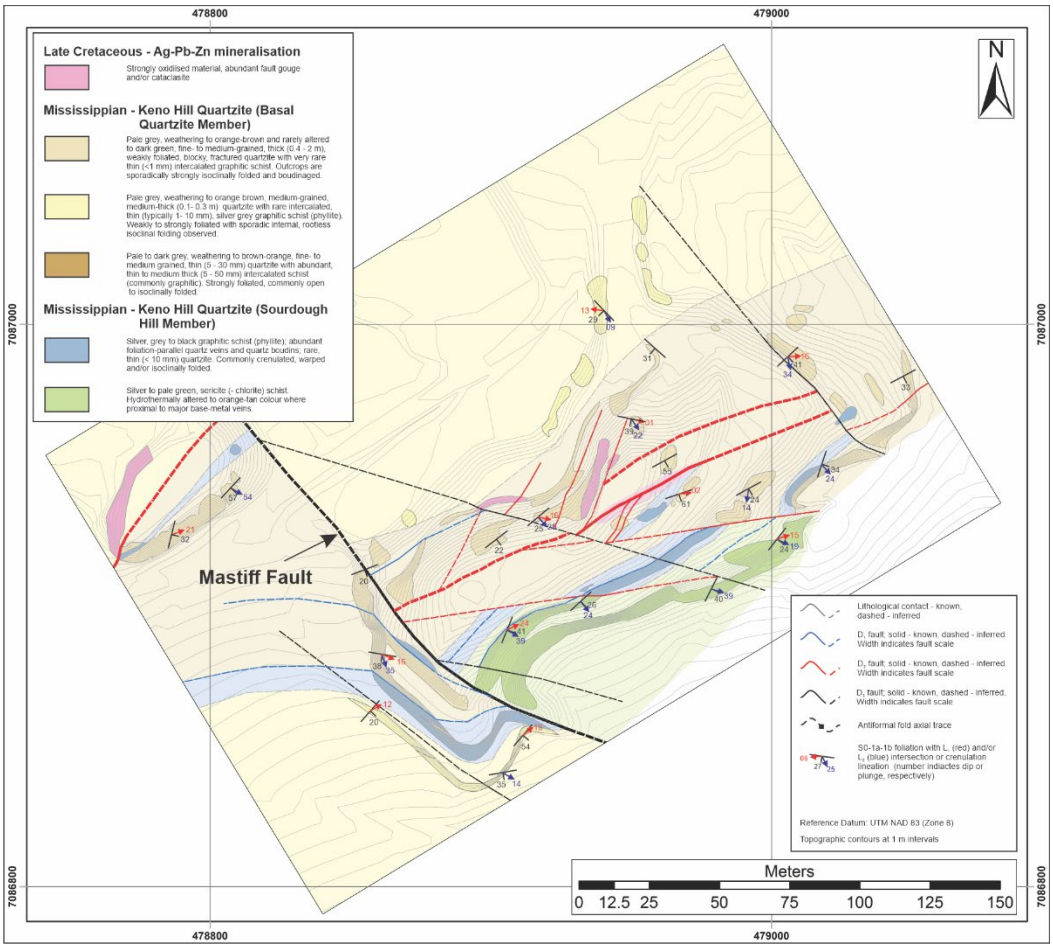

Figure 4.11: Simplified outcrop map and interpretation of the Bermingham deposit.

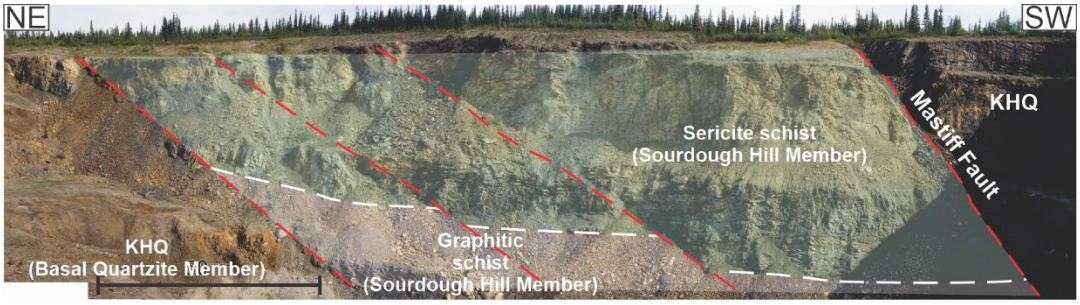

Figure 4.12: Panorama photograph of the SE wall of the Bermingham open pit showing sericite schist overlying graphitic schist (both Earn Group) and in fault contact with the KHQ. Red dashed lines show trace of faults, white dashed lines show approximate contact between sericite and graphitic schist.

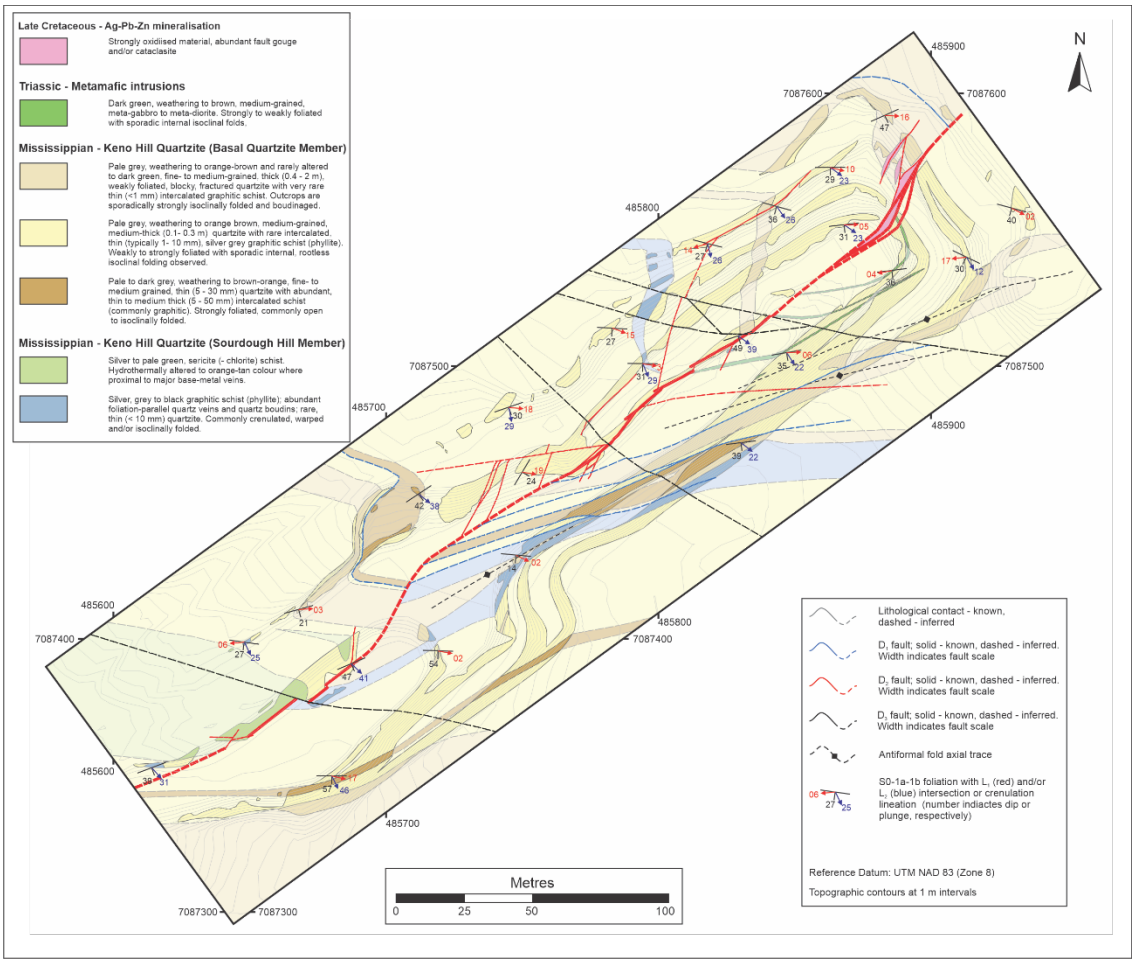

Figure 4.13: Simplified outcrop map and interpretation of the Onek deposit.

While the thickness of the observed sericite schist and its apparent regional extent suggest that this unit can be confidently correlated with McOnie and Read's (2009) sericite schist marker unit, correlation between the graphitic schist units observed by the author and McOnie and Read's (2009) graphitic schist marker unit is less certain. Graphitic schist units observed are silver to grey-black, weathering to orange or black schist (Figure 4.14). Foliation-parallel quartz veins are common, but thin (< 10 millimetre) quartzite layers are very rare. The unit is crenulated, warped, and isoclinally folded, and millimetre- to centimetre-scale chevron folds are commonly present towards the top of the unit and proximal to foliation-parallel slip-surfaces in the Bermingham open pit. Proximal to, and in the footwall of, the late, cross-cutting Mastiff Fault in the Bermingham open pit polyclinal folds are common (Figure 4.14C).

McOnie and Read (2009) indicate that the graphitic schist marker unit stratigraphically occurs directly beneath the sericite schist marker unit. This stratigraphic relationship was observed at the Bermingham deposit (Figure 4.11 and Figure 4.12), however, at the Onek deposit the graphitic schist unit was less than 10 metres thick and in fault contact with quartzite-rich and intercalated quartzite-schist units of the basal quartzite member (Figure 4.7 and Figure 4.13). The fault contact relationship between the graphitic schist and basal quartzite at Onek does not prohibit this mapped unit from being associated with McOnie and Read's (2009) graphitic schist marker unit; however, the association can not be confirmed.

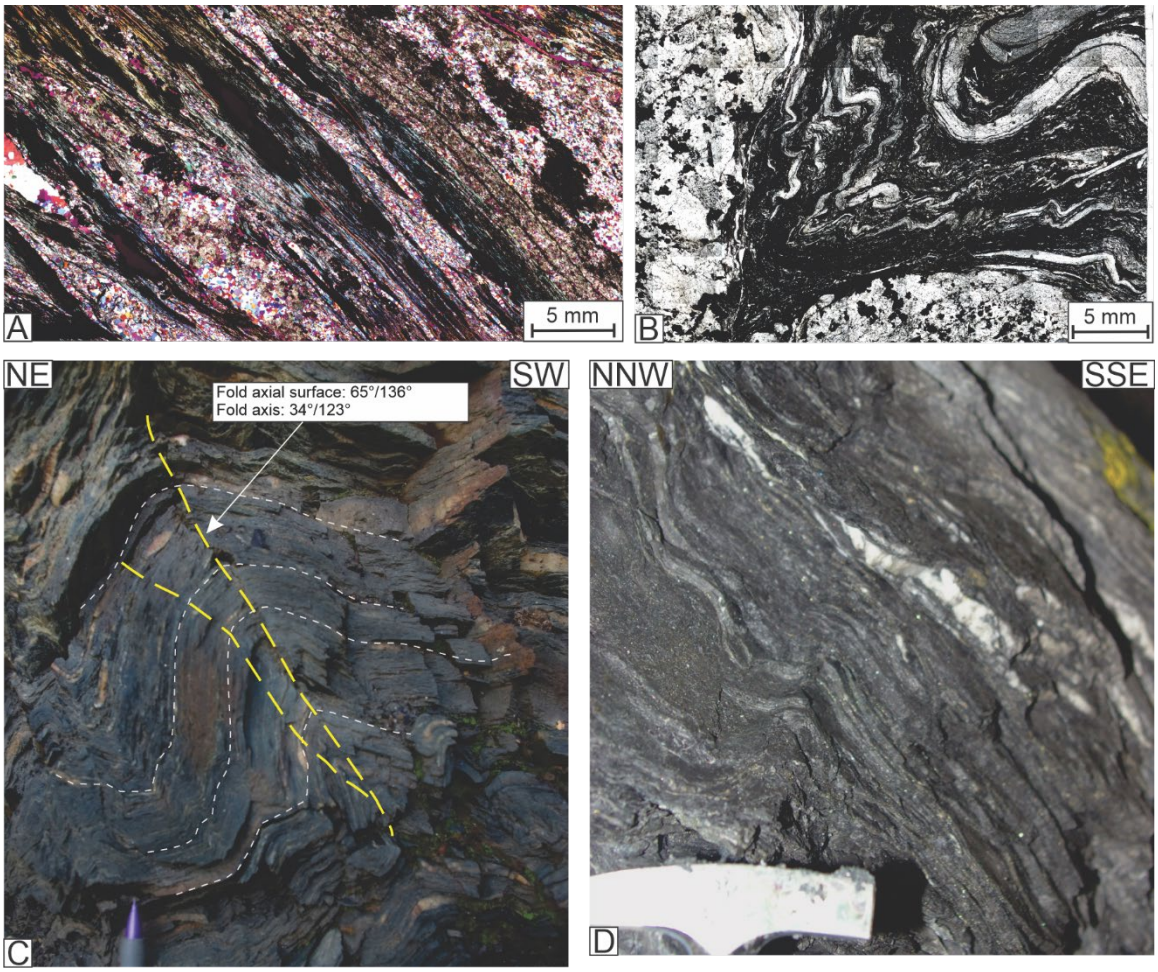

Figure 4.14: Examples of graphitic schist in polished thin section (A and B) and outcrop (C and D).

A: photomicrograph of sub-planar laminated graphitic schist in sample 0120-002 (borehole K-07-0120, depth 93.60 m, Onek deposit); B: photomicrograph of internally folded graphitic schist in contact with relatively undeformed quartzite with abundant sulfides in sample 0179-007 (borehole K-08-0179, depth 67.05 m, Calumet deposit); C: photograph of polyclinal fold in graphitic schist in the Bermingham deposit (UTM 478897mE 7086851mN); D: photograph of graphitic schist in the Bellekeno East decline (at survey point P13).

Numerous additional units assigned to the Sourdough Hill Member were described by McOnie and Read (2009) including various limestone, metagrit, and schist marker units. Due to the narrow scope of work and the focus on known Ag-Pb-Zn bearing veins in the district, none of these were confidently observed during the fieldwork; however, two

small outcrops of crystalline, foliated, pale to dark grey limestone were observed near the summit of Sourdough Hill, and foliated, pale grey, calcareous quartzite and limestone were observed in drill core from the Homestake prospect on Sourdough Hill. These rocks may be associated with either McOnie and Read's (2009) middle grey limestone/grey schist unit, or their upper grey limestone/grey schist unit.

Vein Development in the Keno Hill Quartzite

Vein development in the KHQ can be broadly subdivided into two styles; 1) foliation sub-parallel (concordant) veins, and 2) foliation-oblique (discordant) veins. These are associated with the pre- and syn-Ag-Pb-Zn-mineralisation deformation events, respectively.

Foliation-parallel quartz veins are common throughout both members of the KHQ. They are particularly abundant within schistose and thinner quartzite layers (Figure 4.9) but have also been rarely observed in thicker quartzite units, particularly at the Bermingham and Sime deposits. Foliation-parallel quartz veins are commonly milky white to grey and may define folds.

Foliation-oblique veins are more commonly observed in more competent, quartzite-rich members of the Basal Quartzite, and are rarely observed in schist-dominated layers. Foliation-oblique veins comprise quartz, quartz-carbonate, and carbonate veins, and associated Pb-Zn ± Ag veins. Foliation-oblique veins commonly terminate, or

dramatically thin across the interface between quartzite-dominated and schist-dominated layers, and if observed to cross the transition, veins within in schist-dominated layers become shallower dipping, or foliation-parallel, and may step up through thin, intercalated quartzite layers.

Foliation-oblique veins show extensional textures that are typically best preserved in Pb-Zn ± Ag veins, where sphalerite and galena crystals are commonly euhedral, and can grow to very large sizes (> 50 millimetres; Figure 4.15A and B). Larger Pb-Zn ± Ag veins are commonly brecciated and cemented in carbonate or quartz-carbonate. Rare examples are observed in drill core from the Silver King and Bellekeno deposits where early, foliation oblique quartz-cemented breccias are overprinted by later, extensive, carbonate alteration (Figure 4.15C). Rare quartz veins show comb or crustiform textures (Figure 4.15D and E), and bladed calcite was also observed. In thin section, foliation-oblique brecciated to cataclastic veins comprise angular to subangular, massive to foliated, quartzite clasts with foliation-parallel muscovite layers that may contain trace amounts of disseminated pyrite. Clasts are cemented by carbonate, quartz-carbonate, or quartz. Opaque minerals (either pyrite, or galena) are sporadically present in the cement, and may overgrow the boundary between quartzite clasts and cement, indicating growth during vein propagation (Figure 4.15F).

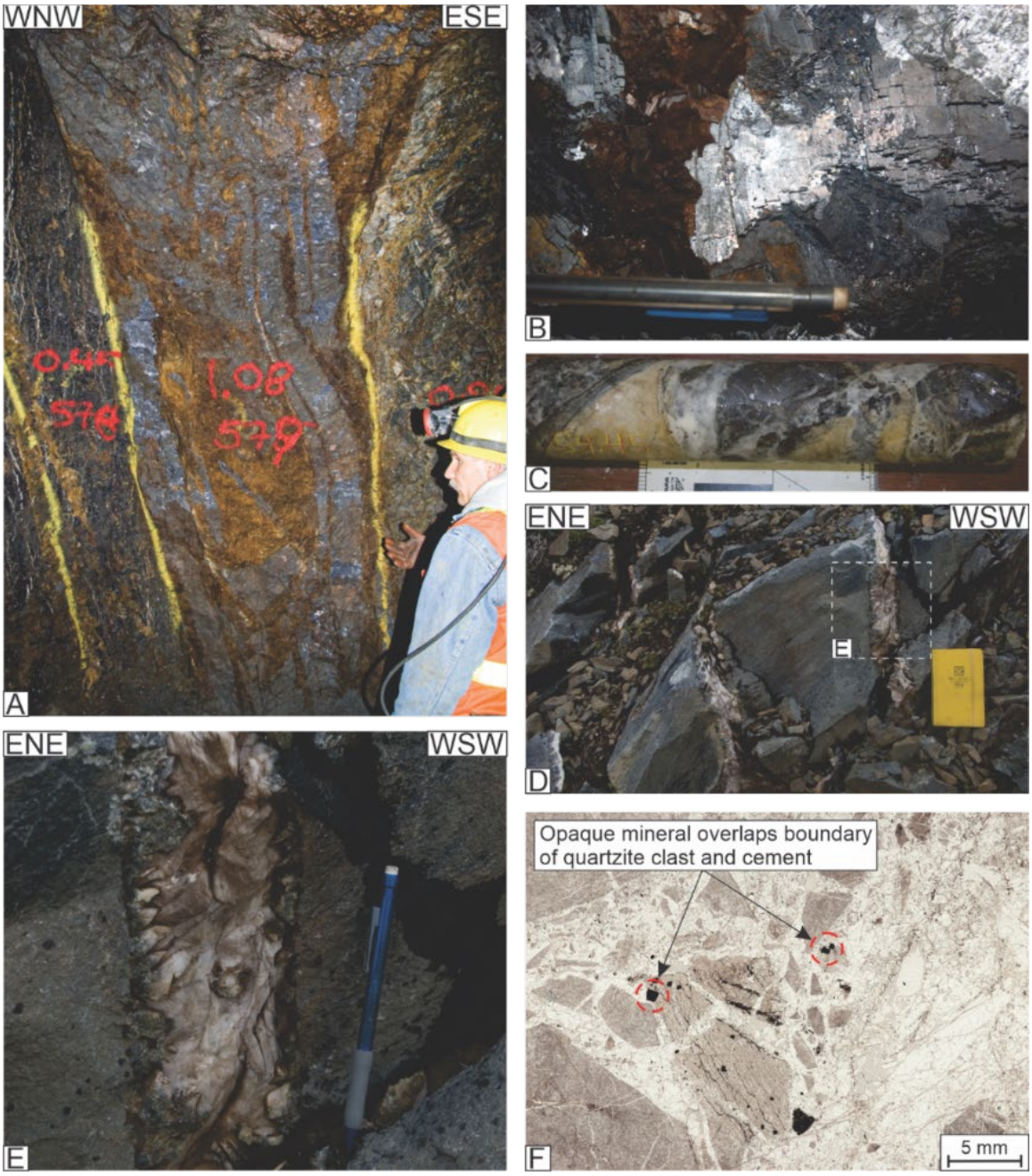

Figure 4.15: Characteristics of foliation-oblique veins.

A: photograph of galena – siderite – sphalerite vein at the 750-1 crosscut in the Bellekeno underground workings; B: photograph of large (up to 2 cm) galena crystals in galena – siderite – sphalerite vein at the 750-1 crosscut in the Bellekeno underground workings; C: photograph of drill core with quartz-supported breccia, overprinted by carbonate (siderite) in quartzite with associated chlorite-sericite alteration and massive galena (borehole BKUD09-0160, depth 54.5 m, Bellekeno deposit, 1187 g/t Ag); D: photograph with inset (E) showing comb texture in quartz veins near the Wernecke deposit (UTM 86480mE, 7092202 mN); F: photomicrograph of sample 0051-009 showing quartz supported breccia with sulfide minerals overlapping clast-cement boundary (borehole K07-0051, depth 183.92m, Silver King East deposit).

4.2 Intrusive Rocks

4.2.1 Metamafic Intrusive Rocks

Boyle (1965) and Lynch (1986) proposed that the Keno Hill mafic intrusions (termed greenstones) form an important host for Ag mineralisation. The location of mineralized veins in the district suggest that greenstone-associated mineralisation is only significant where the sills intrude the less competent rocks of the Earn Group, such as at the Wernecke and Sadie Ladue deposits along the north flank of Keno Hill.

Outcrop and Hand Specimen Descriptions

At the regional scale, mafic sills commonly weather with a high relief to the surrounding rocks to form small hills in the valleys and cliff sections on mountain flanks. In section they commonly form large lensoid structures that are easily identifiable from distance with thicknesses in the 10's of meters (Figure 4.16). Surface exposures are typically blocky, sporadically show a strong fracture cleavage and are dark to pale green, grey, and black weathering to orange, green, and brown (Figure 4.17A). The variation in colour appears to be due, at least in part to, variations in relative feldspar content. Where contacts are not sheared, core samples show a narrow (1 – 3 cm) chilled margin at both the upper and lower contacts. Samples are variably strained with phenocryst alignment evident in most samples (Figure 4.17C).

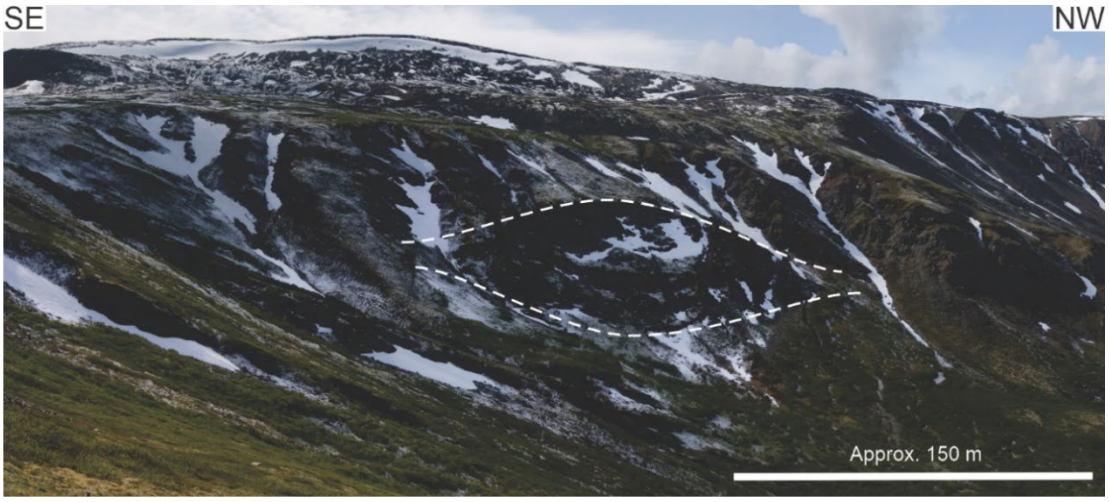

Figure 4.16: Photograph of macro-scale boudinage of greenstone unit on the north flank of Keno Hill. Photograph looking SW from UTM 490325 mE, 7091887 mN.

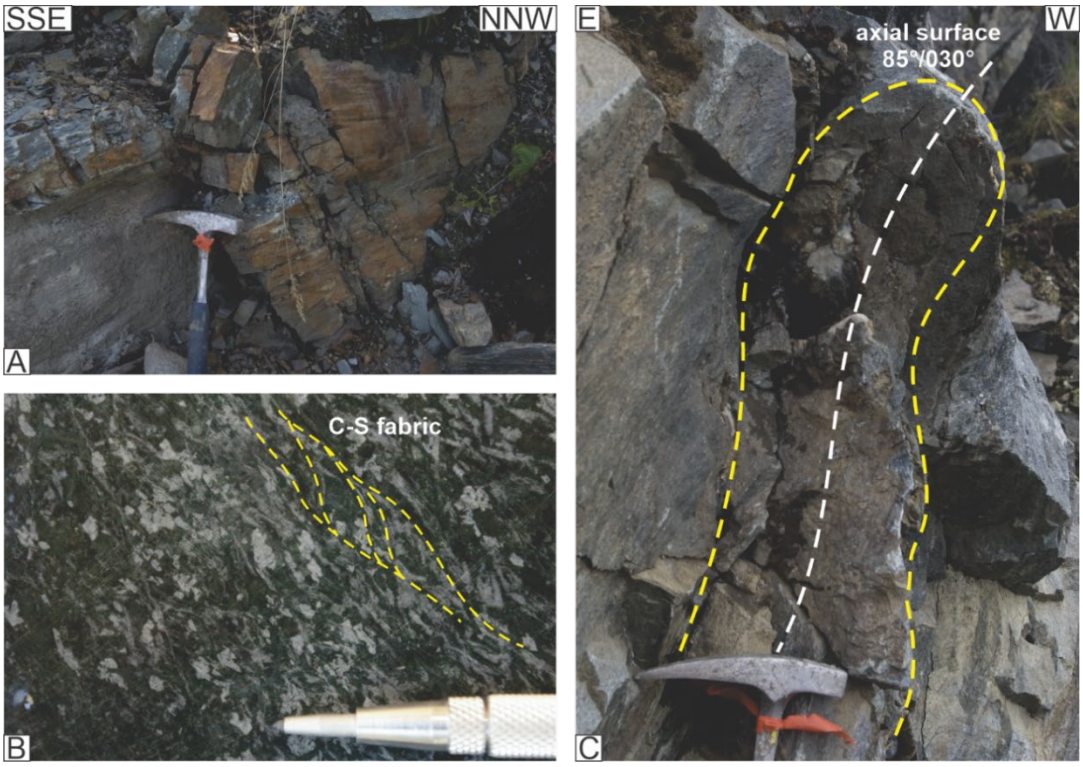

Figure 4.17: Examples of greenstone rocks in outcrop and drill core.

A: photograph of blocky, fractured greenstone near the Ram deposit (UTM 487172 mE, 7086281 mN); B: photograph of foliated greenstone in drill core showing subtle C-S fabric (sample 0165-003, borehole K-08-0165, depth 54.10 m, Keno 700 deposit); C: photograph of upright, isoclinally folded meta-gabbro outcrop east of the Wernecke deposit (UTM 486480 mE, 7092202 mN).

Thirty-four samples of variably deformed greenstone were collected for analysis by X-ray diffraction spectrometry (XRD), X-ray fluorescence spectrometry (XRF), instrumental neutron activation analysis (INAA), and scanning electron microscopy / energy dispersive X-ray spectroscopy (SEM-EDS). The results of the geochemical analyses are available in Appendix E.

Fifteen samples from were collected from drill core, 16 samples from surface exposures, and three samples from the Bellekeno underground workings (Figure 4.18). The samples were collected from seven areas:

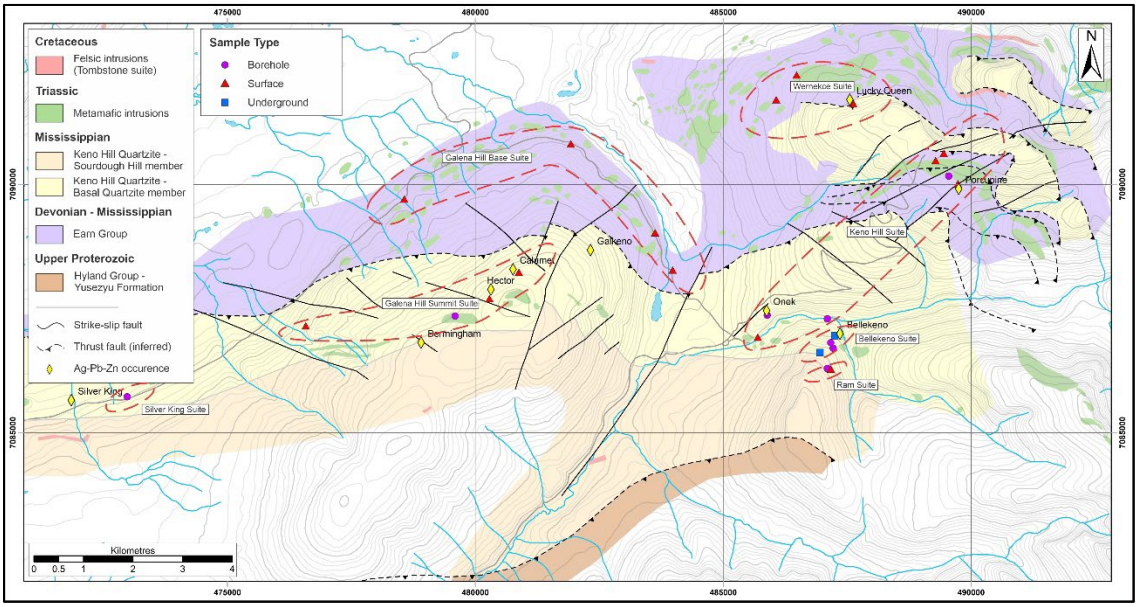

Figure 4.18: Map showing location of greenstone samples collected for geochemical analysis.

Red dashed lines indicate sample suites. Base geological data modified after Boyle (1965), Murphy (1997), and Alexco (2021).

1. **Proximal to the Wernecke deposit (Wernecke suite):** samples are fine to coarse grained, commonly show a mylonitic texture, and have locally, large, up to 2 – 3 m amplitude, upright isoclinally folds (Figure 4.17C). The suite of samples is proximal to a large, mineralised zone and in outcrop show rare siderite, galena, sphalerite, malachite, and azurite mineralisation.
2. **Summit and southern Flank of Keno Hill (Keno Hill suite):** samples range from very fine grained along Lightning Creek (K-LC-001) to coarse grained at the summit of Keno Hill. Samples from the summit of Keno Hill are highly strained and have a mylonitic fabric. Core samples from this suite have rare, 10 mm tremolite crystals, and late-stage quartz-carbonate veins ranging from 2 – 3 mm (typical) up to 20 cm. Pyrite, siderite, and galena mineralisation is observed, but minor. Rare C-S fabrics are developed (Figure 4.17B).
3. **Bellekeno deposit (Bellekeno suite):** samples are typically unfoliated in hand specimen, are fine to coarse grained, and commonly exhibit 0.5 – 1 mm crystals of plagioclase. Rare quartz, sphalerite, siderite, and thin (1 mm) chlorite veins are observed. Chlorite veins can appear to be stylolitic. Rare, up to 2 mm, pyrite crystals are also observed.
4. **Proximal to the Ram prospect (Ram suite):** Three drill core samples were collected at different levels through one sill (samples 0192-001, 0192-002 and 0192-004). Samples are consistently medium grained and show sporadic phenocryst alignment (varying from no alignment to highly strained and foliated). Interleaved 1 – 2 mm quartz-rich layers are present where the samples are strongly folded, with small fold limb terminations indicating shear.

5. **Summit of Galena Hill (Galena Hill Summit suite):** Samples are typically blocky, rarely folded, and show variable fabric development. A fracture cleavage is commonly well developed with rare en echelon quartz veins and ramp and eye structures developed near the Hector prospect.
6. **Base of Galena Hill (Galena Hill Base suite):** Samples are typically blocky, show a strong fracture cleavage, and can be highly strained with rare isoclinal folds evident.
7. **Proximal to the Silver King deposit (Silver King suite):** Samples are medium grained with phenocryst alignment varying from weak to strong. Sample 0051-001 was isoclinally folded and cross-cut by a narrow, foliation-discordant quartz-carbonate vein.

Petrographic and Geochemical Descriptions

Petrographic, XRD (Appendix E), and SEM-EDS analysis of the samples indicate that the primary mineral assemblage of the greenstones was magnesian Na-Ca amphibole (magnesio-hornblende and edenite) (Figure 4.19 and Figure 4.20), pyroxene (proto-enstatite, pyroxmangite, augite, and hypersthene), quartz, and plagioclase. Metamorphism produced abundant chlorite (primarily clinochlore with some nimite), metamorphic amphiboles (typically magnesio-riebeckite, tremolite, and actinolite with minor parvowinchite and kozulite) (Figure 4.19), with minor epidote (Figure 4.20D) and zeolite. Zeolite alteration typically appears only to the west of the district where magnesio-riebeckite is rare and may indicate a shallower depth of burial.

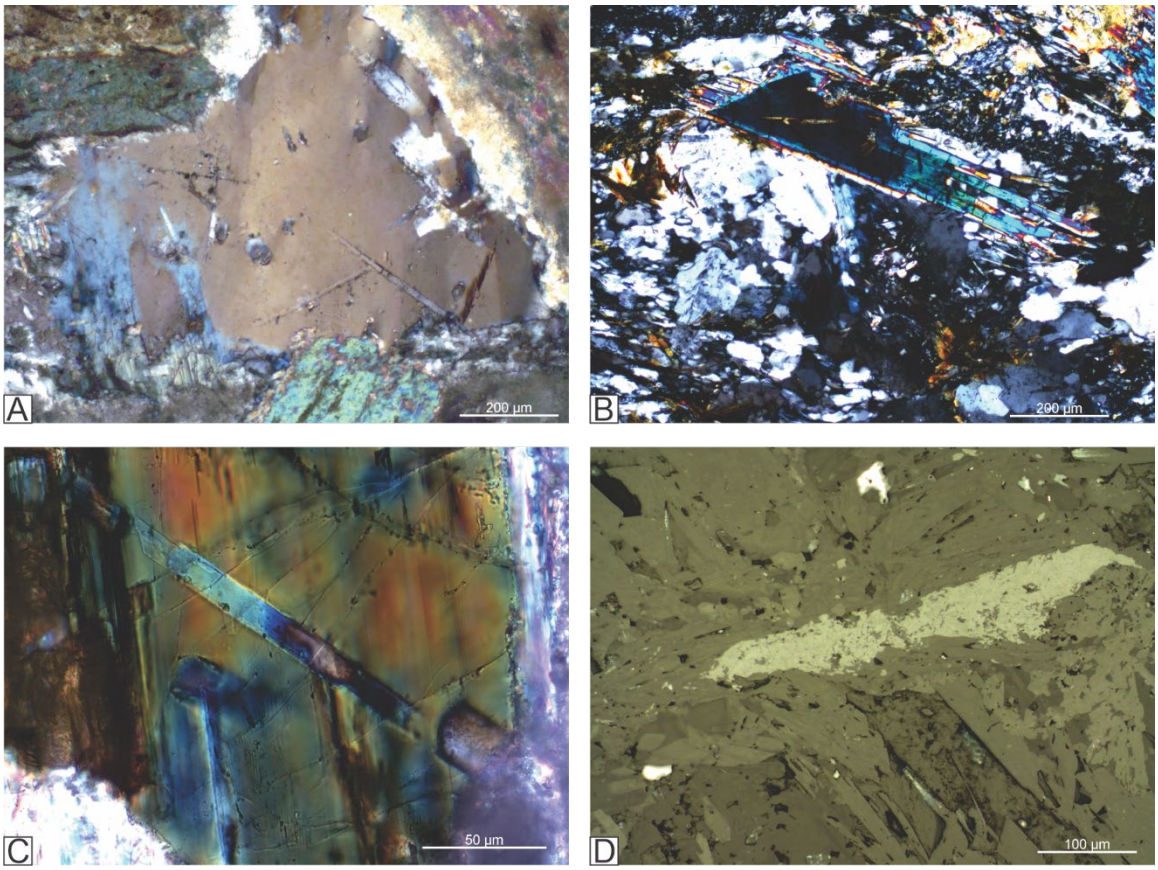

Figure 4.19: Photomicrographs of selected greenstone samples.

A: XPL photomicrograph showing clinochlore overgrowth on quartz with minor apatite inclusions in sample 0187-001 (borehole K-09-0187, depth 14.00 m, Bellekeno deposit); B: XPL photomicrograph showing magnesio-hornblende with metamorphic clinochlore alteration and overgrowth in sample K-CA-003 (UTM 480876 mE, 7088231 mN, Calumet deposit); C: XPL photomicrograph showing magnesio-riebeckite overgrowth on a magmatic magnesio-hornblende in sample K-WK-001 (UTM 486480 mE, 7092202 mN, east of Wernecke deposit); D: RL photomicrograph showing sulfide mineral within the $S_{0\text{-}1a\text{-}1b}$ foliation showing a replacement texture around the rim in sample K-KH-006 (UTM 489285 mE, 7090479 mN, Keno Hill summit).

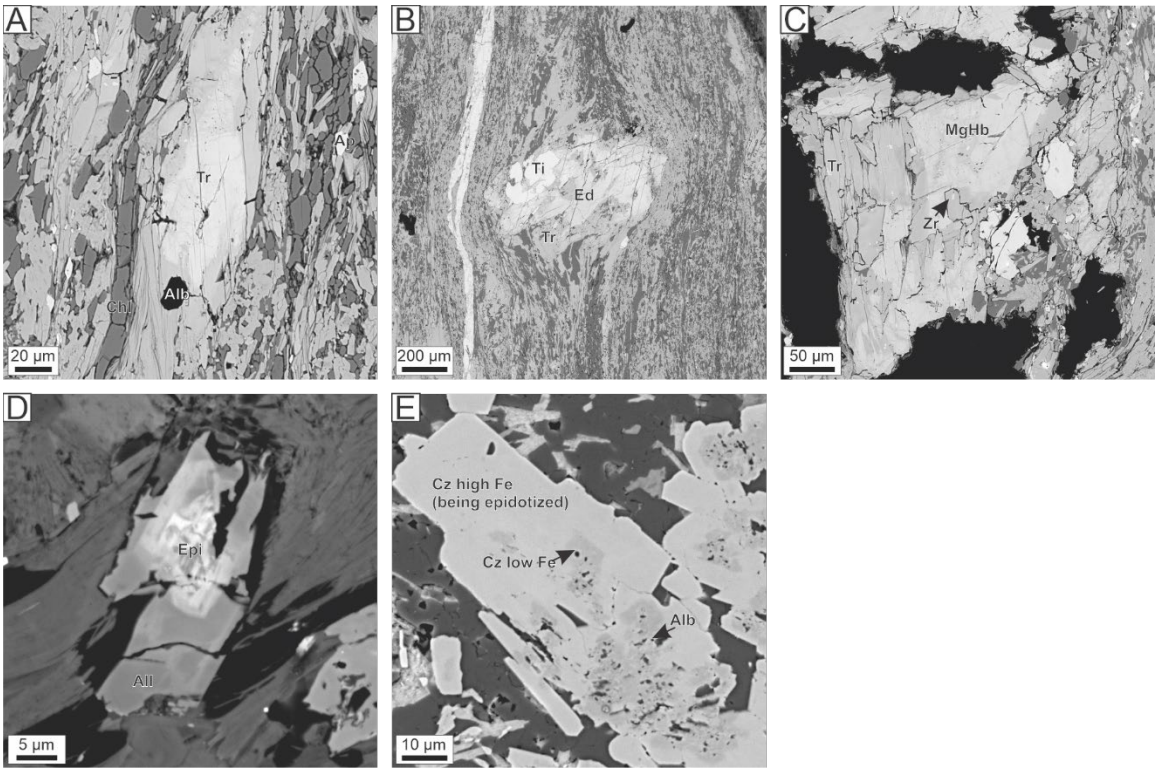

Figure 4.20: SEM-EDS images of greenstone samples.

A: foliation-concordant tremolite and chlorite with albite porphyroblasts (sample K-GH-004, UTM 480285 mE, 7087699 mN, trenches west of Hector deposit); B: primary edenite crystal with metamorphic titanite and tremolite overgrowths (sample K-GH-004, UTM 480285 mE, 7087699 mN, trenches west of Hector deposit); C: primary magnesio-hornblende crystal with metamorphic tremolite overgrowth and minor zircon (sample K-GH-004, UTM 480285 mE, 7087699 mN, trenches west of Hector deposit); D: zoned epidote crystal with REE substitution towards allanite at crystal rim (sample 0192-002, borehole K-09-0192, depth 64.70 m, Ram deposit); E: zoned and epidotized clinozoisite crystal showing increasing Fe content towards the rim and minor albite porphyroblasts (sample K-LC-001, UTM 485697 mE, 7086922 mN, south flank of Keno Hill near Lightning Creek). Alb: albite; All: allanite; Chl: chlorite; Cz: clinozoisite; Ed: edenite; Epi: epidote; Tr: tremolite; Ti: titanite; Zr: zircon.

As expected for a greenschist terrane, petrographic and XRD analysis show that chlorite is abundant in all samples and is commonly aligned with the deformation fabric and/or shear bands. Amphiboles are commonly chloritized, and in rare cases, chlorite can be observed radiating from amphibole rims with no preferred orientation. Chlorite crystals commonly show grey to blue interference colours under cross-polarized light indicating

that the chlorite is commonly Fe rich; this is in agreement with observed Fe content in chlorite by SEM-EDS analysis (Figure 4.19A).

Quartz appears as a major phase in all metagabbroic Bellekeno and Galena Hill summit samples and in samples from the Ram (0192-006), Galena Hill base (K-GH-007 and K-GH-010), and Keno Hill (K-KH-007 and K-KH-011) suites. The abundance of quartz in some samples is attributed to silica alteration and segregation during deformation and metamorphism, and as such is not considered to have been a major constituent of the protolith. The highly sheared and folded samples K-GH-010 and K-KH-011 show abundant quartz with subhedral to euhedral metamorphic overgrowths creating sharp crystal contacts and defining a metamorphic fabric. Elsewhere quartz is commonly seen as very fine-grained crystals that constitute part of the groundmass and rare larger crystals of quartz that consistently show undulose extinction. In sample 0187-001 (Bellekeno suite) porphyroblasts of quartz are commonly overgrown by clinochlore and host apatite inclusions (Figure 4.19A).

Eight varieties of amphibole were identified by XRD and SEM-EDS analysis. Magnesio-hornblende, tremolite, and magnesio-riebeckite are common and form major phases in most samples with parvowinchite (formerly tirodite and (or) manganocummingtonite) occurring as a major phase in samples from the Bellekeno, Ram, and Wernecke suites (0187-001, 0192-001, and K-WK-003, respectively). Amphibole porphyroblasts are commonly pseudomorphed by chlorite with basal sections showing two good cleavages at approximately 120° (Figure 4.19B). Amphiboles show pale green to brown

pleochroism and in places dark brown, non-pleochroic masses are thought to be altered phantoms of amphibole. SEM-EDS analysis indicates that pre-deformation amphiboles typically have magnesio-hornblende or edenite cores that are overgrown by tremolite, actinolite, or rarely magnesio-riebeckite aligned with, and folded by the fabric (e.g., K-KH-006, Keno Hill suite; Figure 4.19 and Figure 4.20). Samples K-CA-003 (Keno Hill suite) and K-WK-001 (Wernecke suite) show magnesio-hornblende crystals that appear to be zoned, syntectonic porphyroblasts with their crystal boundaries curving into alignment with the fabric. Samples K-GH-009 and K-WK-001 (Galena Hill and Wernecke suites, respectively) show small acicular amphiboles aligned with S and C foliations in addition to overgrowing large pre-deformation phenocrysts of magnesio-hornblende.

The occurrence of kozulite and parvowinchite is normally associated with metamorphosed manganese deposits (Deer et al., 1997). Thin 1-2 mm veins and surface alterations with MnO were recorded at several localities across the district and are likely associated with the Ag-Pb-Zn mineralizing event. Samples hosting Mn-rich amphibole tend to be proximal to major ore-hosting structures; this may account for their occurrence in these areas.

Plagioclase feldspar occurs as albite (An 0.2 – 2.4) in nearly all samples and typically occurs as minor phases that may be pseudomorphs of a more calcic plagioclase. Crystals of albite typically occur within the fine-grained groundmass and can be difficult to distinguish, showing rare strong twinning. One sample from the Bellekeno suite (K-BK-

002) contained large plagioclase phenocrysts (now albite) that contained small (< 20 μm) inclusions of acicular amphibole, chlorite, and clinozoisite.

Micas are generally uncommon throughout the samples; however, within highly sheared and folded samples muscovite (e.g., K-KH-011; Keno Hill suite) and annite (e.g., 0192-002; Ram suite) occur as major phases, while illite forms a minor phase in sample K-GH-010 (Galena Hill suite). These phases are exclusively associated with shear band and fabric development.

Petrographic analysis shows that samples contain cubic to hexagonal sulfides (typically galena, pyrite, and sphalerite) associated with shear bands and rarely disseminated throughout (e.g., 0192-002; Ram suite). Alteration haloes around sulfide minerals are common; pyrite crystals are partially oxidized and rarely develop a carbonate rim. Samples from the Keno Hill, Galena Hill, and Ram suites display ductile remobilization of sulfides into shear bands; whereby sulfides have a replacement texture at the rim and are not euhedral suggesting that post-shear band formation, sulfide-bearing fluids utilized the pre-existing fabric in the rock.

SEM-EDS analysis shows abundant metamorphic titanite is commonly aligned with the deformation fabric and in some cases forms a halo around ilmenite crystals. Zircon, apatite, and very rare (< 2 μm) baddeleyite crystals are also observed.

Greenstone Geochemistry Classification

A series of geochemical discrimination plots were produced based on the acquired geochemical data. The data were subdivided into their respective suites (Figure 4.18) to assess the presence of compositional variations based on geographic location and structural level. On this basis the Wernecke, Galena Hill Base, and possibly Silver King suites are considered to be located at a lower structural level than the remaining suites. Two preliminary tests were conducted on all samples to exclude any samples of metasedimentary (Winchester et al., 1980) or cumulate (Pearce, 1996) origin. All samples were within standard limits and as such no samples were omitted from the analysis.

The geochemical discrimination plots show that the samples are generally of sub-alkaline/tholeiitic, metaluminous gabbroic to dioritic composition (Figure 4.21). Analysis of samples based on their structural elevation shows little variation, however in both the R1 vs R2, and AFM diagrams (Figure 4.21appear to show that the Wernecke and Ram suites, and the Silver King and Galena Hill Summit suites present as end members to the system with samples generally becoming increasingly dioritic, with a decreasing Mg# westward, suggesting an evolving magma source from East to West. This trend appears to be more pronounced in the structurally lower samples, than of those in the structurally higher samples.

Pearce and Norry's (1979) Zr vs Zr/Y geotectonic classification plot shows that all points plot in or near the within-plate basalt (WPB) field (Figure 4.22A). Pearce and Cann's (1973) Zr vs Ti diagram shows samples plot in a transitional zone between calc-alkaline

basalt and MORB (Figure 4.22B) with a trend of increasing Zr and Ti westward from Keno Hill towards Galena Hill and the Silver King East deposit.

Mullen's (1983) MnO x 10 – TiO_2 – P_2O_5 x 10 ternary plot shows most samples plotting as island arc tholeiites or more rarely as MORB (Figure 4.22C). A trivariate plot of Zr/4 – Nb x 2 – Y (after Meschede, 1986) plots most samples in a transitional zone between the E-type MORB, within plate tholeiite, and volcanic arc basalt fields (Figure 4.22D).

Pearce and Parkinson's (1993) Yb vs Cr plot shows that the magmatic rocks reflect an increasing degree of partial melting in the source mantle from West to East (Figure 4.22E). Generally, the trend is more pronounced in samples from higher structural levels with the Galena Hill Summit suite showing less partial melting than the Ram suite, while the Keno Hill and Bellekeno suites appear to be transitional. Primitive mantle-normalized multi-element spider diagrams of high field strength elements (HFSE) typically show an E-MORB signature for most samples with slightly elevated Nb and Zr (Figure 4.23).

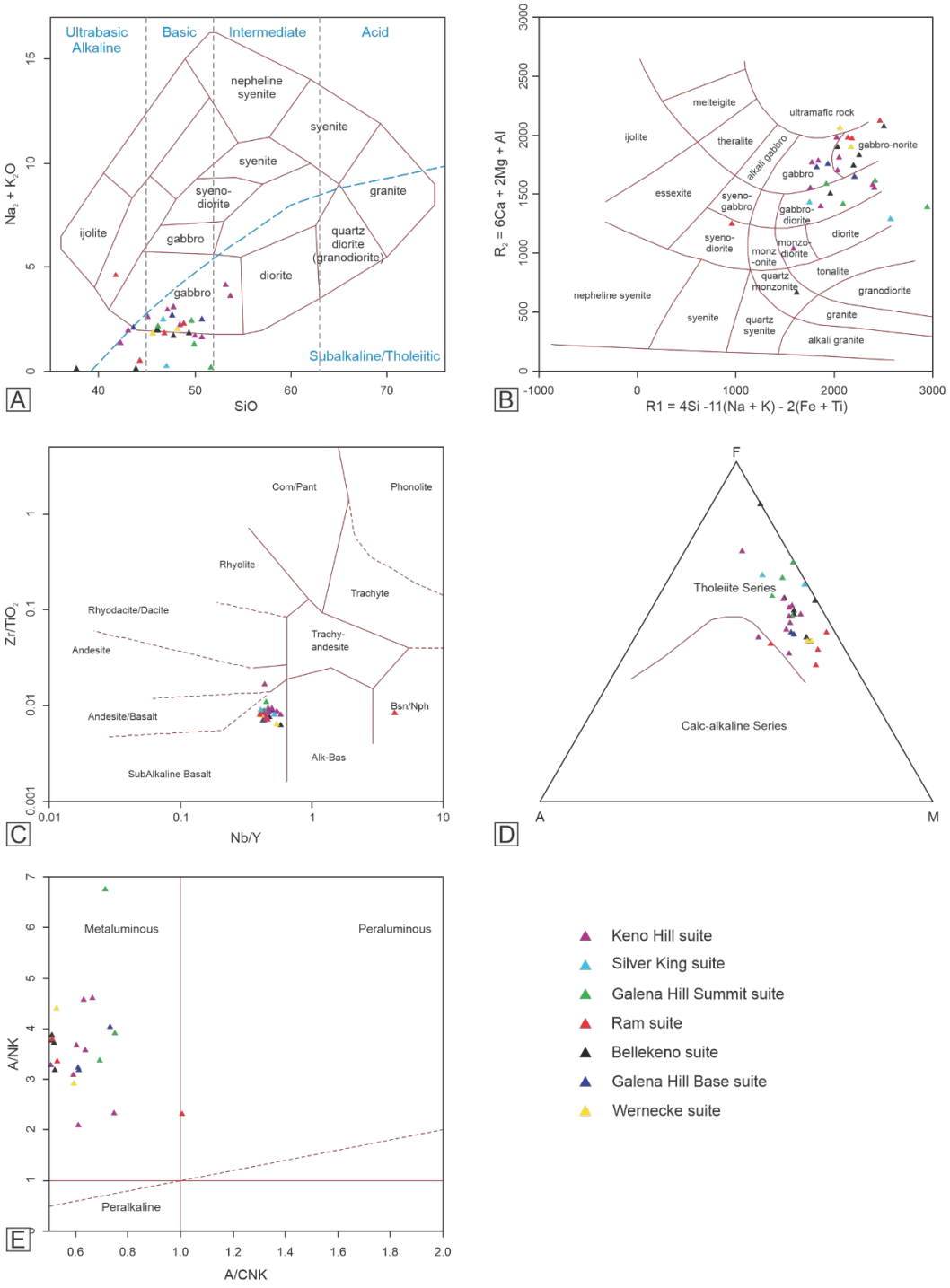

Figure 4.21: Geochemical discrimination plots showing classification of metamafic samples.

A) TAS (total alkali silica) plot showing general tholeiitic composition to samples (after Cox et al., 1979); B) R1 vs R2 plot showing westward fractionation (after De la Roche et al., 1980); C) Nb/Y vs Zr/TiO_2 showing subalkaline compositions to samples (after Winchester and Floyd, 1977); D) AFM diagram showing decreasing Mg# of the source magma westward (after Irvine and Baragar, 1971); E) A/CNK vs A/NK plot showing general metaluminous composition to samples (after Shand, 1943).

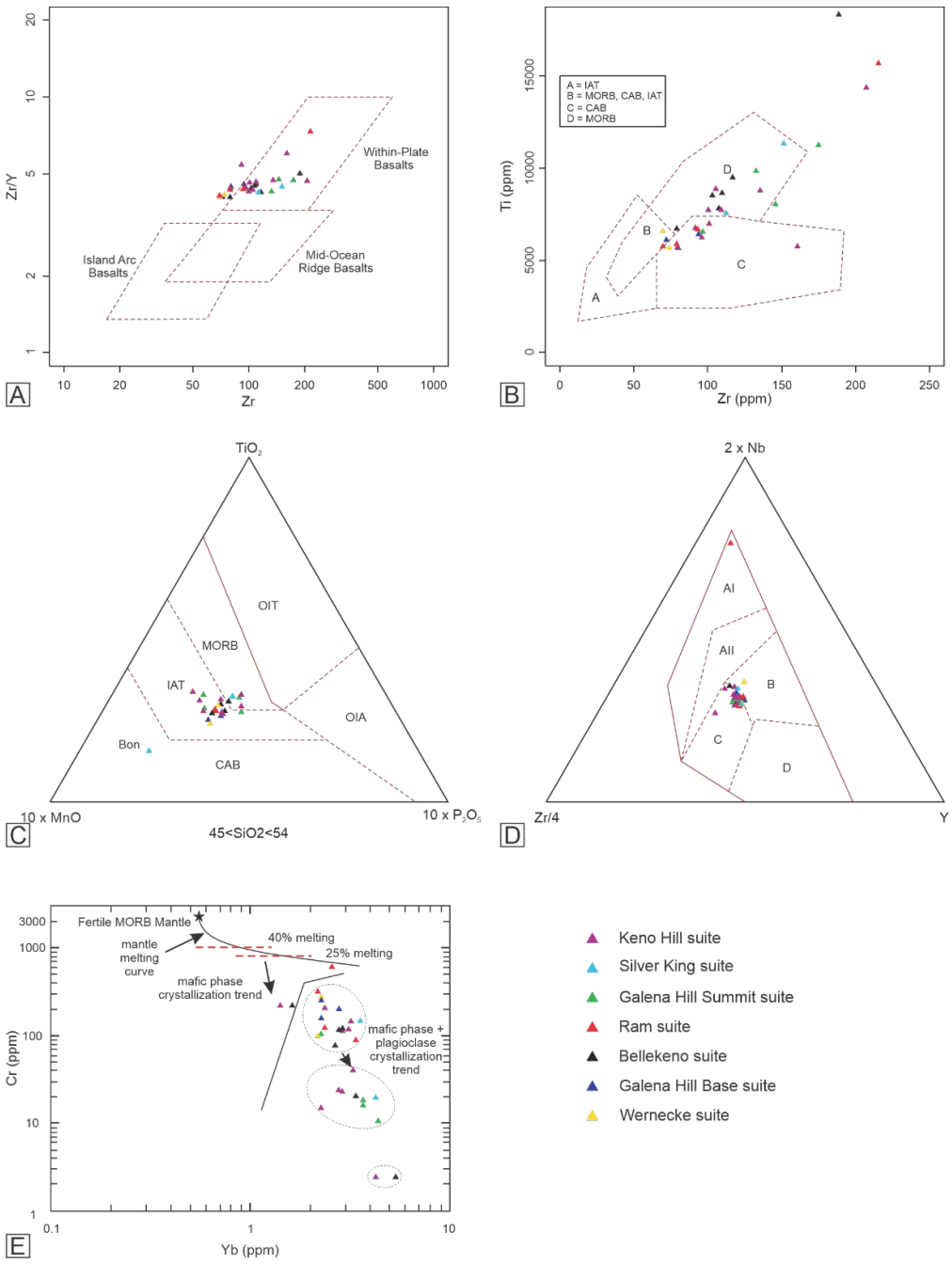

Figure 4.22: Geochemical discrimination plots showing geotectonic classification of metamafic samples.

A) Zr vs Zr/Y plot showing WPB tectonic setting for all samples (after Pearce and Norry, 1979); B) Zr vs Ti plot showing increasing Zr and Ti values westward (after Pearce and Cann, 1973); C) MnO-TiO_2-P_2O_5 ternary plot showing island arc tholeiite classification for most samples (after Mullen, 1983); D) trivariate plot showing transitional E-type MORB – WPB/VAB geotectonic setting for most samples (after Meschede, 1986); E) Yb vs Cr diagram assuming melting in a spinel lherzolite facies (after Pearce and Parkinson, 1993) showing compositional variation between collected samples and decreasing degree of partial melting westward.

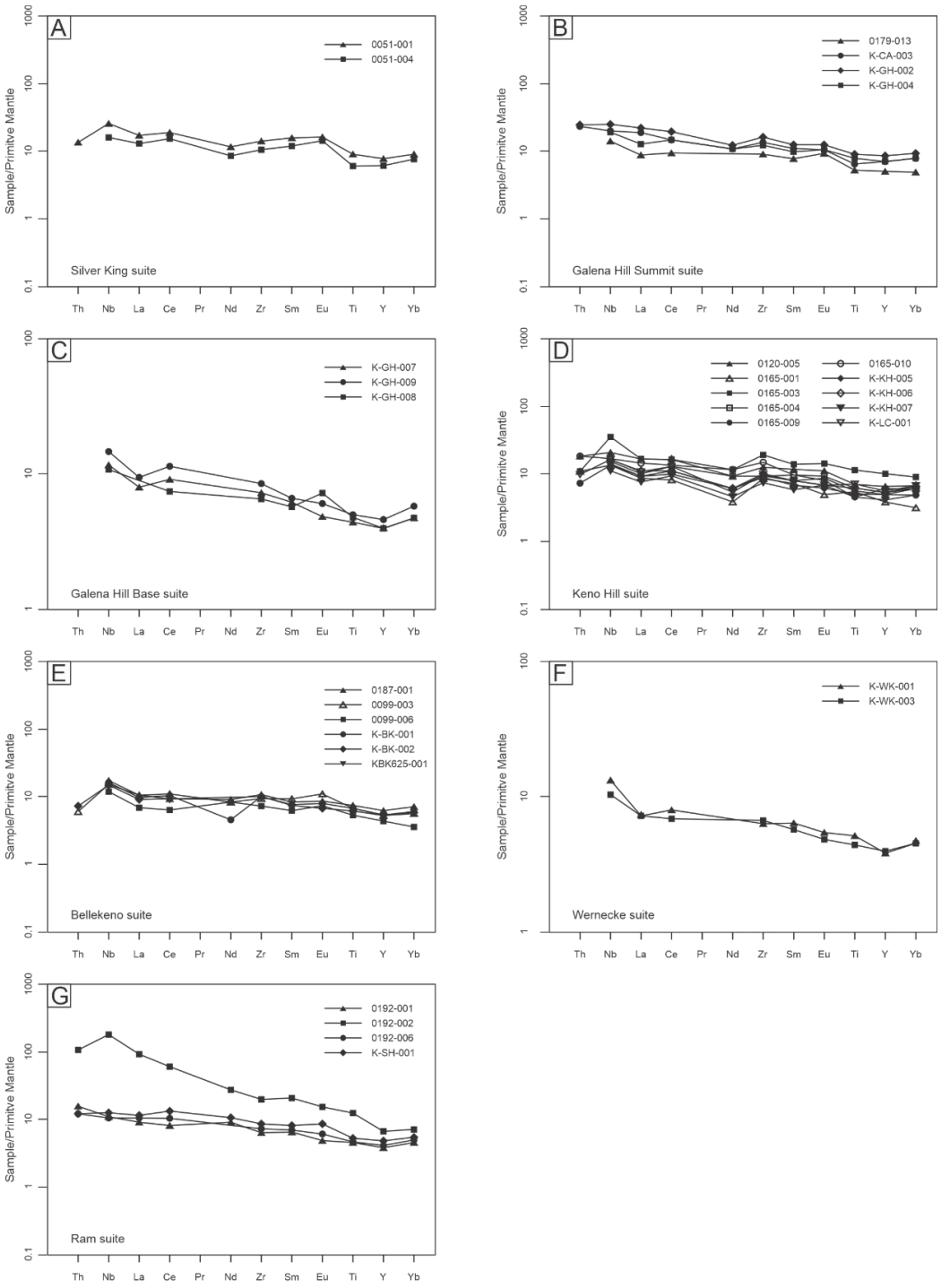

Figure 4.23: Primitive mantle normalized multi-element spider diagrams of high field strength elements (after Swinden, 1996; Sun and McDonough, 1989). Samples tend to show an E-MORB signature.

A) samples from the Silver King East deposit; B) samples from the summit of Galena Hill; C) samples from the base of Galena Hill; D) samples from the summit and southern flank of Keno Hill; E) samples from the Bellekeno deposit; F) samples from the Wernecke deposit; G) samples from the Ram deposit.

4.2.2 Mid-Cretaceous Intrusive Rocks

One outcrop of felsic intrusive rock was observed in the district. This was located on a ridge above and west of Faro Gulch, on the north flank of Keno Hill. The intrusion is highly fractured, and light grey, weathering to pale pink or orange in colour, with a deep red weathered margin (Figure 4.24). The rock is a nonfoliated, massive, gray to pink, quartz-biotite-hornblende granite with two to 20 millimetre phenocrysts of potassium feldspar hosted in a fine- to medium-grained quartz, plagioclase, potassium feldspar, biotite, and hornblende groundmass. Euhedral to subhedral zircon is common and rare, coarse titanite is also observed. The rock intrudes shallow south-dipping, chlorite altered, dark grey to black phyllite and schist of the Earn Group that weathers to pink – orange near the contact. The intrusive contact trends 077°, but no dip could be measured. A sample from this felsic intrusion was collected for U-Pb geochronological analysis, the results of which will be discussed in Chapter 6.3.2

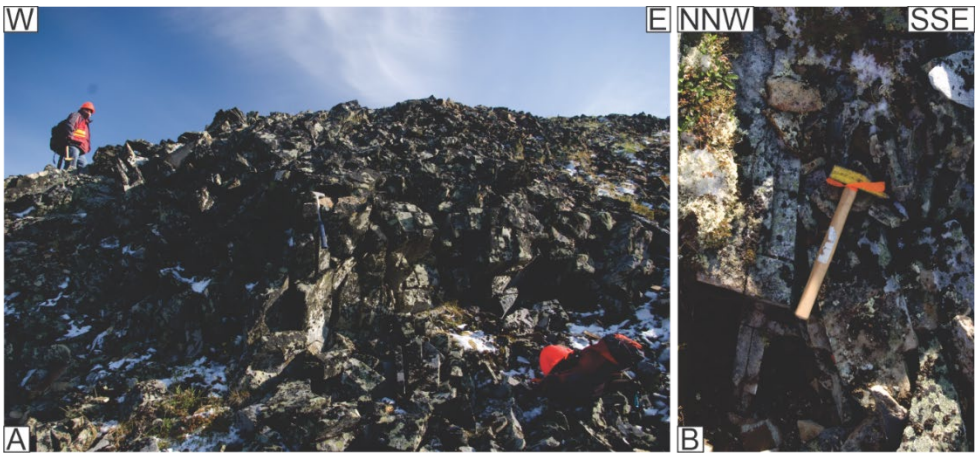

Figure 4.24: Photographs of outcrop of felsic intrusive rock on north flank of Keno Hill (UTM 490420mE, 7091898 mN).

4.2.3 Lamprophyre

The author observed one lamprophye dyke in the SW corner of a small open pit between the Hector and Calumet open pits. The intrusion was a brown, medium-grained, biotite-rich mafic intrusion with biotite phenocrysts set in a feldspar groundmass. The intrusion was 0.3 m wide, steeply ESE-dipping and cross cut the shallow SSW-dipping foliation of the host rock. Strong manganese alteration was observed associated with the dyke. McOnie and Read (2009) reported a similar lamprophyre at the Formo prospect on the north flank of Galena Hill. McOnie and Read (2009) classified the lamprophyre as a minette, however they noted the presence of phlogopite and as such the intrusion may be better defined as an alkali minette (Wooley et al., 1996).

5. Structural Geology of the Keno Hill District

The Keno Hill district has a complex deformational history that has resulted in a complex, but largely predictable structural architecture. The district comprises several fault-controlled, vein-type Ag-Pb-Zn deposits and has experienced at least three discrete episodes of deformation that resulted in extensive fold and fault development, and associated greenschist-grade metamorphism, and subsequent brittle deformation. The three observed deformation events are summarised below and in Table 5.1:

- D_1 pre-Ag-Pb-Zn-mineralisation fold and thrust belt development;
- D_2 sinistral strike-slip to sinistral-normal oblique-slip brittle fault development associated with Ag-Pb-Zn mineralisation, and;
- D_3 post-Ag-Pb-Zn-mineralisation, Cordilleran-scale, dextral-normal oblique-slip fault development.

Ag-Pb-Zn mineralisation in the district is controlled by the complex interplay of D_2 fault geometry and orientation, secondary thickening of host rocks as a result of pre-mineralisation folding, and the mechanical anisotropy between the various lithological units. Ag-Pb-Zn mineralisation is preferentially hosted in thick, competent, quartzite units within the Mississippian Keno Hill Quartzite (KHQ), and to a lesser extent in deformed Triassic greenstone units where they occur within the broad, relatively ductile packages of Earn Group schist.

Table 5.1: Characteristics of deformation events in the Keno Hill district.

Deformation Event	Characteristics	Regional Tectonics	Age
D_1	Two generations of micro- to regional-scale, near coaxial, tight to isoclinal, commonly recumbent, north to NNW verging folding (F_{1a}-F_{1b}). Development of shallowly south- to SSE-dipping S_0-S_2 composite foliation. Development of deposit to regional scale foliation-parallel, north to NNW directed thrust faults. Greenschist-grade metamorphism.	Closure of the Slide Mountain Ocean (Mair et al., 2006). Onset of collision between the Yukon Tanana Terrane and the Laurentian margin. Yukon Tanana terrane overrides the Selwyn Basin (Mair et al., 2006). Associated with north to NW translation of strata along the Tombstone and Robert Service thrust faults (Mair et al., 2006).	Cessation of D_1 deformation by 100 to 104 Ma ($^{40}Ar/^{39}Ar$ muscovite) (Mair et al., 2006).
D_2	NE- to ENE-striking, typically sinistral strike-slip to sinistral-normal oblique-slip faults. Silver-lead-zinc mineralisation (galena, sphalerite, siderite) associated with fault development. Sporadic quartz mineralization with minor associated gold.	Associated tectonics still poorly understood, but possibly associated with the initiation of convergence between the Kula plate and North America (circa 85 Ma), and initiation of the orogen-parallel, dextral strike-slip Proto Tintina Fault (Gabrielse et al., 2006; Mair et al., 2006). Mineralisation possibly associated with emplacement of Tombstone Suite plutons (94 – 84 Ma).	Late Cretaceous. Various dates in the Keno Hill region indicate mineralisation between 82 and 69 Ma (e.g., Sinclair and Tessari, 1980; Hantelmann, 2013).
D_3	Deposit- to regional-scale, NW- to north-striking, dextral strike-slip to dextral-normal oblique-slip faults. Faults offset mineralised faults. Broad, open, to warped, shallow SE- to ESE-plunging fold development (F_3). Rare, tight, chevron to polyclinal fold development in schistose units proximal to D_3 faults.	Orogen-parallel dextral displacement and development of the Tintina Fault Zone (Gabrielse et al., 2006). Continued convergence between the Kula Plate and North America, and associated dextral transpression (Gabrielse et al., 2006).	Cenozoic (Eocene) (Gabrielse et al., 2006).

5.1 Structural Elements of Deformation

This section summarises the structural elements and evidence for the three deformation phases outlined above, from oldest to youngest. The orientations of planar structural elements are written as dip/strike (Canadian Right-Hand Rule), and the orientation of linear structural elements are written as plunge/azimuth.

5.1.1 A Note on Fault Age and Order Nomenclature

Relative fault and fold ages (e.g., D_1, D_2, or D_3; F_{1a}, F_{1b}, F_2, and F_3) were largely determined in the field. Fault ages were determined by local cross-cutting relationships and fold ages by local fold interference patterns. Similarly, a preliminary fault order was commonly assigned to faults or shear zones observed in the field based on fault width, fault products (e.g., gouge, breccia, cataclasite), observed strike length, and effect on local lithological relationships (Appendix B). A critical observation in the characterisation of 1st order faults was that smaller (lower order) faults of the same generation must be observed to splay off or be truncated by the throughgoing first order fault. General criteria for the field characterisation of fault order are given in Table 5.2, however, for both fault/fold ages and fault order the process of classification was iterative; collection of subsequent data sporadically required a reinterpretation of locally observed structures.

Table 5.2: Criteria for field characterisation of fault order.

Fault Age	Fault Order	Field Characteristics
D_1	1	Commonly define major lithological contacts and juxtapose thick sequences of Earn Group rocks against the KHQ, or the KHQ against Hyland Group rocks. Mylonitic texture. High strain gradient approaching structure
	2	May juxtapose different lithologies within a given formation. Limited to no observable strain gradient approaching structure. Slickenlines on fault surface.
	3	Rarely juxtapose different lithologies. Slickenlines on fault or foliation surface.
D_2	1	Through-going fault that can be confidently traced for several hundred metres. Lower order D_2 faults splay off or are truncated by the 1st order fault. Wide (greater than 1 m) fault core comprising gouge, breccia, or cataclasite. ENE-striking and have strike-slip kinematics.
	2	Moderate strike length, and merge with or link between 1st order structures. Variable fault zone widths that range from several metres to a few centimetres and are commonly characterised by breccia or gouge. Variable strikes range from ENE to NNE and kinematics range from strike-slip to dip-slip.
	3	Short strike length. Commonly defined by discrete, narrow faults with widths of less than 1 centimetre. Variable strikes range from ENE to NNE and kinematics range from strike-slip to dip-slip.
D_3	1	Through-going and can be traced for several hundred metres, Commonly well polished, may have fault widths of up to 50 centimetres. Offset markers indicate offset of at least 50 metres.
	2	Limited apparent strike length and may merge with 1st order faults. May be well polished.
	3	Short strike length. Narrow, discrete fault surfaces with evidence of slip (e.g., slickenlines), and offset markers indicating slip of a few centimetres.

It should be noted that the interpretation of the structural architecture is not solely reliant on field observations. Interpretations of the 2D and 3D structural architecture are presented in chapter 5.2 and integration of field and remote sensing observations form a major part of this thesis. It is well known that fault characteristics and products vary along strike, as such, if a structure measured in the field was clearly associated with (location and orientation) a structure observable in remote sensing data, local fault orders may have been adjusted to maintain a coherent structural model. The criteria for the characterisation of fault age and order in airborne magnetic data is given in Table 5.3.

5.1.2 Pre-Ag-Pb-Zn-Mineralisation (D_1)

Structural elements that developed prior to Ag-Pb-Zn-mineralisation (here termed D_1) are indicative of ductile to brittle-ductile tectonics. These elements include, but are not limited to, two generations of near coaxial folding (F_{1a} and F_{1b}), thrust to reverse faults, a composite, transposed foliation ($S_{0\text{-}1a\text{-}1b}$), and associated fabrics. A discussion of whether all structural elements described in this section should be ascribed to the same progressive deformation phase or to discrete phases of deformation is presented at the end of this section; however, statistical analysis of all structural elements described in this section appears to suggest that no significant rotation of the regional stress field occurred during development of the structures and, as such for the purposes of this chapter, they are defined as being associated with a single, progressive deformation event (D_1).

F_1 Fold Characteristics and Geometry

F_{1a} folds were observed along Galena Creek (near the Silver King open pit), within the Sime, Calumet, and Onek open pits in the centre of the district, at the Upper Faith showing in the far east of the area, and in drill core from the Bellekeno deposit. Sporadic evidence for F_{1a} folds is present in thin section. F_{1a} folds were commonly defined in sequences of relatively thin (less than 20 cm) quartzite intercalated with schist; however, one F_{1a} fold was identified in a relatively thick (approximately 50 cm) unit of massive quartzite in the northern pit of the Sime deposit. F_{1a} folds are isoclinal with limbs and axial surfaces folded by F_{1b} folds, and wavelengths, where measurable, range from the millimetre-scale at the Onek open pit, up to approximately one metre at the Sime open pit.

F_{1b} folds are ubiquitous across the district and are observed at the microscale in thin section and up to mesoscale in pit walls or cliff sections. Good examples were observed along Galena Creek, and in the Bermingham, Sime, and Onek open pits. F_{1b} folds are tight to isoclinal, inclined to recumbent, and locally upright proximal to late cross-cutting faults. They are symmetric to asymmetric and north- to NNW-verging. F_{1b} folds were observed within all metasedimentary and metamafic rocks in the district. Within thick packages of quartzite, F_{1b} folds commonly produce mesoscale stratigraphic repetition, however within more schistose units F_{1b} folds may occur as small scale, intrafolial and locally rootless folds. F_{1b} fold axial surfaces are subparallel to the regional foliation and dip shallowly south to SSE. Where measurable, F_{1a} and F_{1b} fold axes are subparallel, and typically plunge shallowly east-west to ENE-WSW (Figure 5.1A and B). However,

towards the far east of Keno Hill, at the Upper Faith showing, deviation between F_{1a} (05°/294°) and F_{1b} (36°/127°) fold axes was observed.

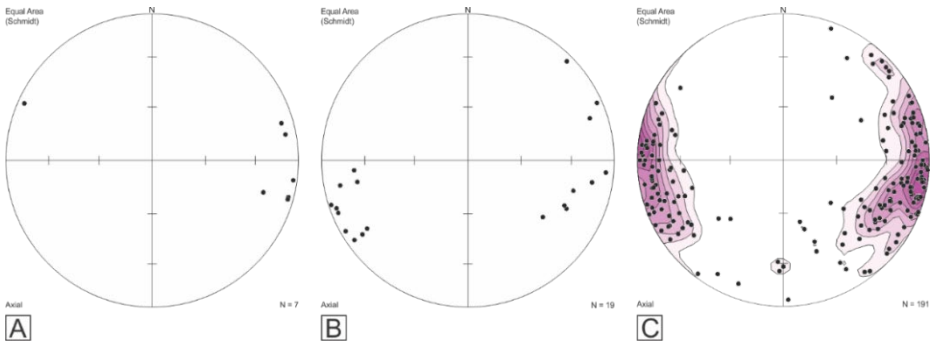

Figure 5.1: Lambert equal area lower hemisphere projections of F_1 fold axes in the Keno Hill district.

A: Measured F_{1a} fold axes (polar data, 7 measurements); B: Measured F_{1b} fold axes (polar data, 19 measurements); C: Density contoured stereographic projection of combined measured F_{1a} and F_{1b} fold axes with undifferentiated F_{1a-b} fold axes; peak density plunges 03°/098° (polar data, 191 measurements, contour intervals 2σ).

Due to the similarity in fold axis orientation and fold shape, differentiation between F_{1a} and F_{1b} is difficult unless F_{1a-b} fold interference patterns are directly observed in outcrop or drill core. Hook-type interference patterns were routinely observed that resemble Ramsay's (1967) type 3 interference pattern, and more closely Thiessen and Means' (1980) type G pattern (Figure 5.2). This suggests that the shortening directions for both the F_{1a} and F_{1b} episodes of folding were effectively equivalent. The lack of variation in regional stress field orientation suggests they should be considered members of the same deformation event.

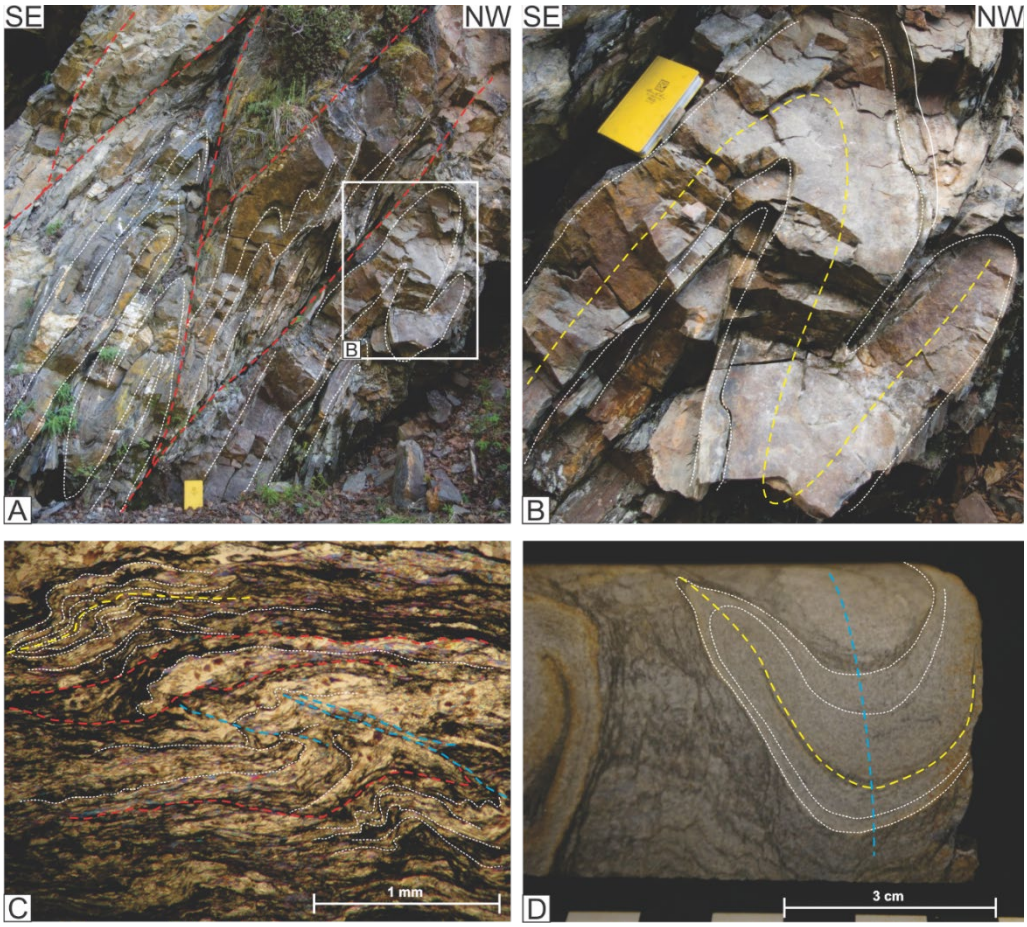

Figure 5.2: F_{1a-b} fold interference patterns.

A: Photograph of F_{1b} folds and D_1 reverse faults along Galena Creek, with inset (B) photograph of F_{1a-b} fold interference pattern (UTM 471013 mE, 7085383 mN). C: Photomicrograph showing F_{1a-b} fold interference pattern in schistose rocks from sample 0179-006 (borehole K-08-0179, depth 66.85 m, Hector-Calumet deposit); D: Photograph of F_{1a-b} fold interference pattern in thinly laminated quartzite and schist from sample 0184-001 (borehole K-09-0184, depth 242.20 m, Bellekeno deposit). White dashed lines show S_0-S_{1b} foliation; yellow dashed lines show trace of F_{1a} fold axial surfaces; blue dashed lines show trace of F_{1b} fold axial surfaces; and red dashed lines show trace of D_1 reverse fault surfaces.

The scale and spatial distribution of F_{1a} folds is poorly constrained; however, their potential impact on focussing Ag-Pb-Zn mineralisation should not be overlooked. It is known that the Basal Quartzite member of the KHQ preferentially hosts Ag-Pb-Zn mineralisation. Large, tight to isoclinal F_{1b} folds in this unit were observed to produce stratigraphic repetition and thicken the Basal Quartzite member proximal to F_{1b} fold

hinges along Galena Creek and in the Bermingham and Sime open pits. As such, if F_{1a} folding is of a larger amplitude and is more spatially common than observed, two overprinting generations of tight to isoclinal folding has the potential to locally quadruple the original thickness of the basal quartzite member, and thus significantly increase the thickness of the potentially mineralised horizon.

D_1 Fabrics and Lineations

A dominant east- to ENE-striking, shallow- to moderate-dipping foliation (here termed S_{1b}) is well-developed throughout the district and is subparallel to F_{1b} fold axial surfaces. The foliation may define compositional variations, but no primary sedimentary structures were observed. A foliation predating the dominant foliation (here termed S_{1a}) was observed locally within the district but is best preserved in thick quartzitic units in the Sime and Bellekeno deposits. The S_{1a} foliation is folded about F_{1b} fold axes and is not associated with compositional variations. The ubiquity of the S_{1b} foliation and its association with compositional variations, coupled with the general sparsity of S_{1a} foliations suggests that the dominant foliation may be considered a composite S_0-S_{1a}-S_{1b}, transposed foliation (Figure 5.3).

While the S_{1a} foliation is rarely directly observed in outcrop, a crenulation lineation (L_{1cr}) may be developed in schistose rocks on the S_{1b} foliation, or about F_{1b} fold hinges in quartzitic rocks. In addition, S_{1a}-S_{1b} intersection lineations (L_{1int}) are commonly observed within schistose rocks and locally within quartzite units (Figure 5.4 and 5.5). The L_{1int}

and L_{1cr} lineations typically plunge shallowly ENE to ESE and WSW to WNW (Figure 5.4). The observed variation in orientation is the result of subsequent, F_2 open folding to warping of the stratigraphy.

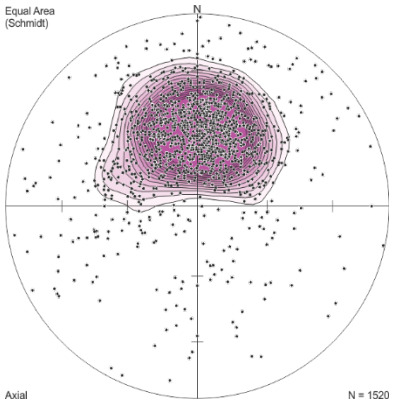

Figure 5.3: Density contoured, Lambert equal area lower hemisphere projection of measured $S_{0\text{-}1a\text{-}1b}$ foliations in the Keno Hill district; peak orientation 31°/096°; polar data, 1520 measurements, contour intervals 2σ.

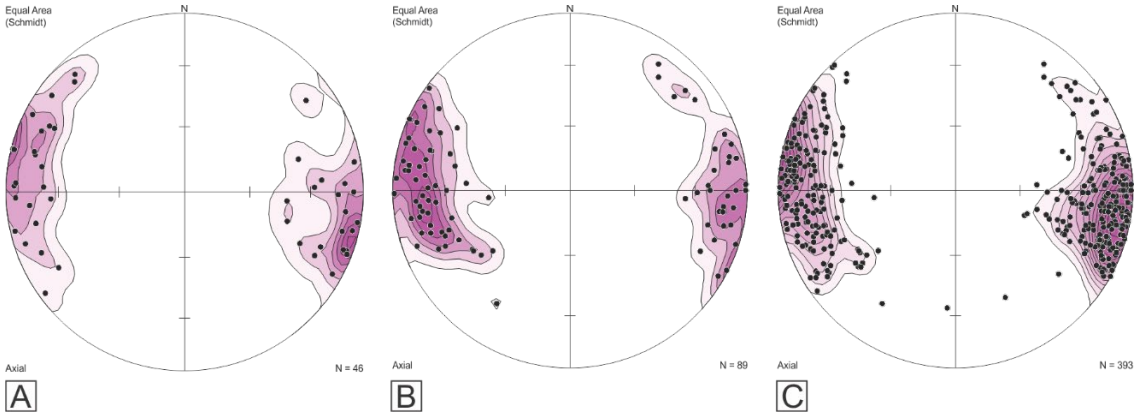

Figure 5.4: Density contoured Lambert equal area lower hemisphere projections of L_1 lineations in the Keno Hill district.

A: Density contoured, measured $S_{1a\text{-}b}$ crenulation lineations (L_{1cr}); peak density plunges 03°/106° (polar data, 46 measurements, contour intervals 2σ); B: Density contoured, measured $S_{1a\text{-}b}$ intersection lineations (L_{1int}); peak density plunges 19°/264° (polar data, 89 measurements, contour intervals 2σ); C: Density contoured, measured undifferentiated $S_{1a\text{-}b}$ lineations (L_1); peak density plunges 06°/100° (polar data, 393 measurements, contour intervals 2σ).

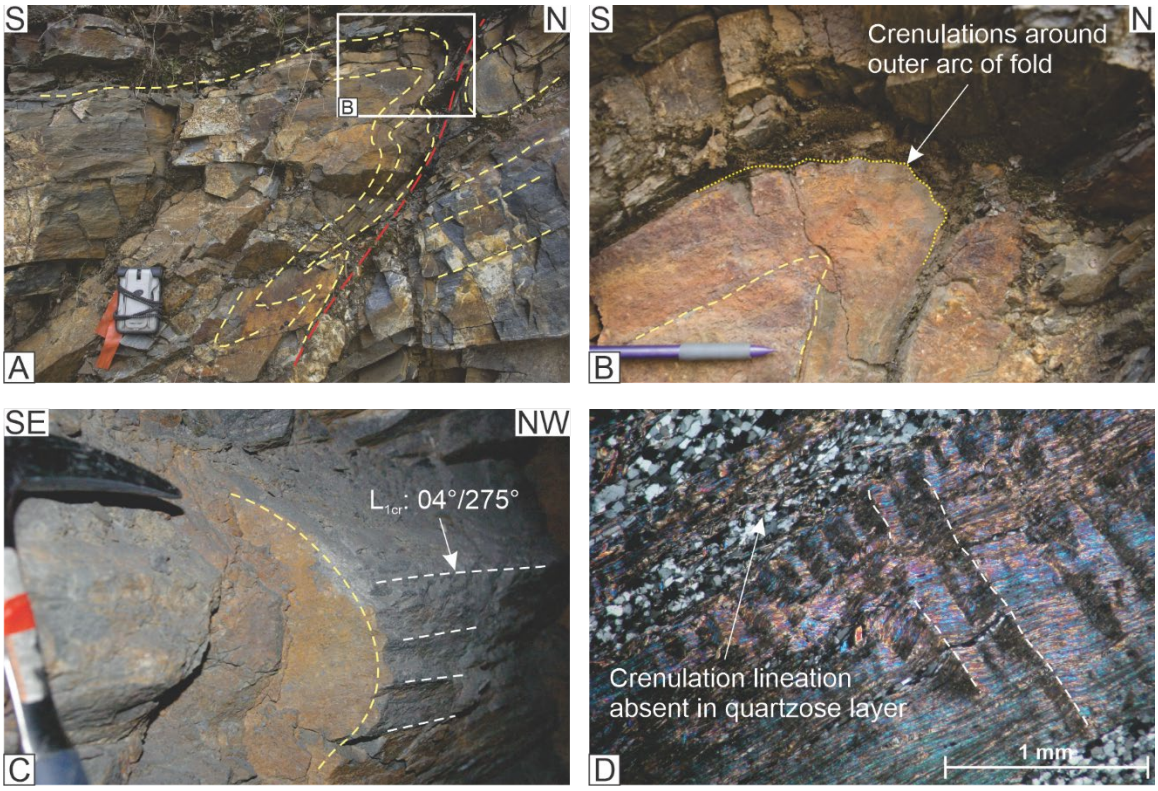

Figure 5.5: Meso- to micro-scale examples of S_{1a-b} crenulation cleavage development across the Keno Hill district.

A: Photograph of F_{1b} fold, with inset (B) photograph of F_{1b} fold nose showing crenulation about fold hinge within the basal quartzite unit in the Bermingham open pit (UTM 471013 mE, 7085383 mN); C: Photograph of F_{1b} fold nose showing shallow west-plunging L_{1cr} lineation about fold hinge in quartzite in the Bellekeno east decline (12 m west of P6 survey point); D: Photomicrograph (XPL) of crenulations within schist in sample 179-009. Note that crenulations are preserved only within micaceous layers, and not within narrow quartzose layers (borehole K-08-0179, depth 75.08 m, Hector-Calumet deposit)

C-S fabrics are observed from micro- to meso-scales with fabrics geometry indicating an approximate north- to NNW-directed displacement orientation that correlates with vergence of asymmetric F_{1b} folds (Figure 5.6). The intersection lineation between C and S fabrics is variable, but commonly plunges shallow ENE to ESE, and correlates with F_1 fold axes, and L_{1int} and L_{1cr} lineations.

Boudinage is observable from the hand specimen-scale within quartz segregations, up to outcrop-scale boudinage of the basal quartzite unit (Figure 5.7). Boudinage may be present at the macro-scale with greenstone lenses that outcrop on scarps on the north flanks of Keno Hill and Mt. Hinton appearing to pinch and swell. Boudins were commonly observed in cross- or oblique-section, and as such measurement of boudin axis is difficult; however, where confidence in the measurement is high boudin axes plunge shallowly east to ESE, and are subparallel to F_1 fold axes, and L_{1int} and L_{1cr} lineations.

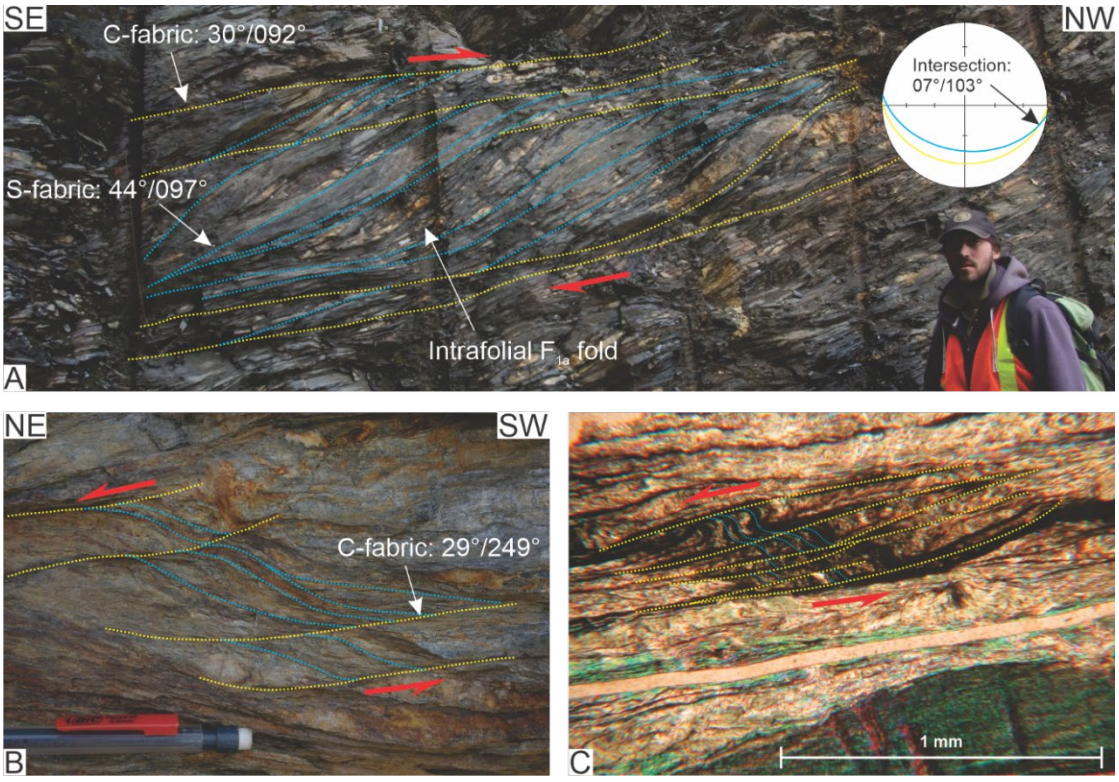

Figure 5.6: Examples of meso- to micro-scale C-S fabric development across the Keno Hill district. C-fabric: yellow dashed lines, S-fabric: blue dashed lines, red arrows: movement direction.

A: Photograph of C-S fabric in schist in the SW wall of the Bermingham open pit with inset lower hemisphere stereoplot showing intersection of C and S fabrics. Intrafolial F_{1a} folds within S-fabric indicates that C-S fabric formation took place during late D_1 (F_{1b}) deformation (UTM 478888 mE, 7086849 mN). B: Photograph of C-S fabric in quartzite in the Onek open pit (UTM 485710 mE, 7087379 mN). C: Photomicrograph of C-S fabric developed in schist from sample 0165-017 (borehole K-08-0165, depth 197.92m, Keno 700 deposit)

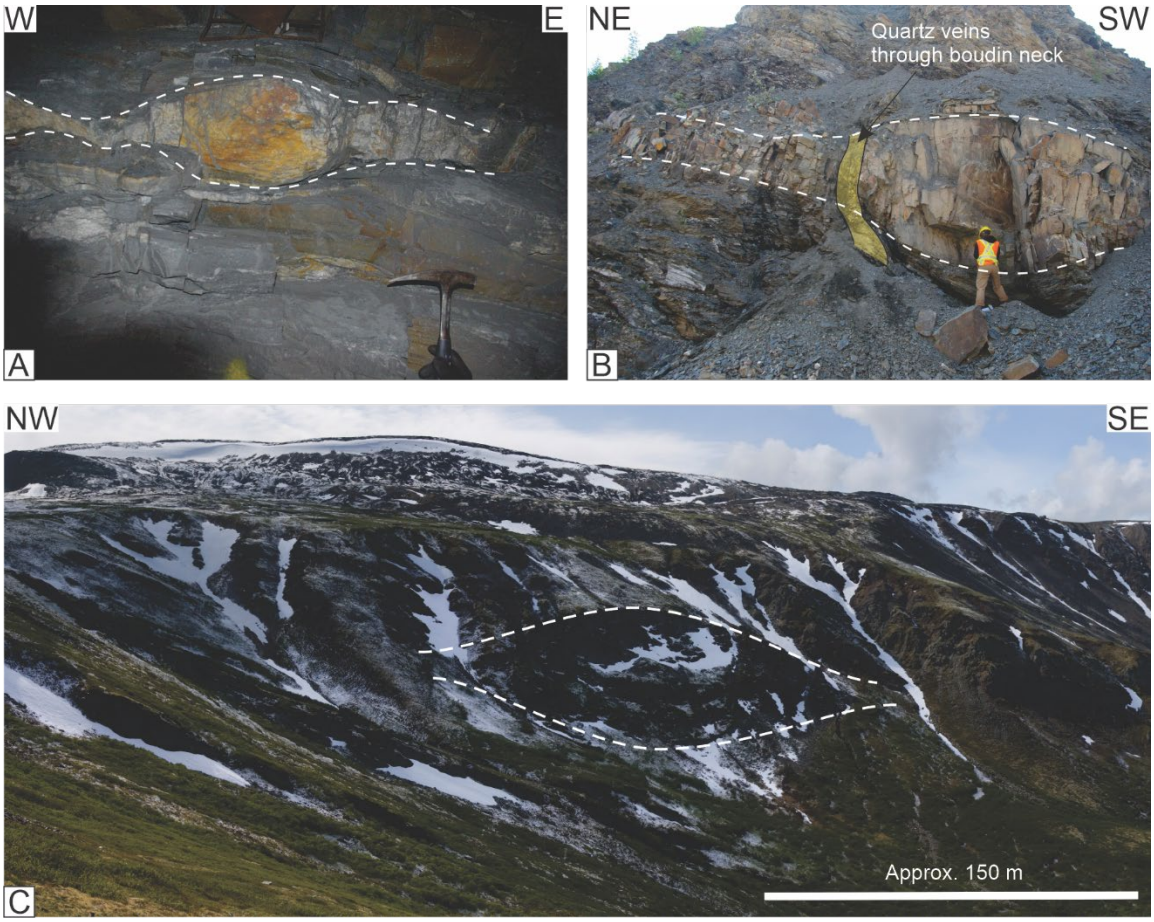

Figure 5.7: Examples of D_1 associated boudin development across the Keno Hill district.

A: Photograph of boudinaged quartzite within intercalated graphitic schist and quartzite; boudin axis 38°/092° (North wall of Bellekeno East Decline, 64 m west of remuck bay); B: Photograph of large quartzite boudin within intercalated graphitic schist and quartzite in the Onek open pit. Abundant quartz veins present at boudin neck. UTM 485748 mE, 7087430 mN; C: Photograph of macro-scale boudinage of greenstone unit in north flank of Keno Hill. Photograph looking SW from UTM 490325 mE, 7091887 mN.

D_1 Veins and Associated Structures

Quartz mineralisation associated with D_1 is commonly represented by quartz veins and segregations that are typically, but not uniformly restricted to schistose layers. Veins are commonly subparallel to the $S_{0\text{-}1a\text{-}1b}$ foliation and may be axial planar to F_{1b} folds, but may also be folded about F_{1b} or rarely F_{1a} fold axes. Veins emplaced in fold hinge

extension fractures were also observed and are associated with outer-arc extension of F_{1b} folds (Figure 5.8), while rotation of quartz veins defines flexural flow along F_{1b} fold limbs. Veins are commonly laminated and boudinaged (with boudin axes subparallel to F_1 fold axes).

Vein boudinage and folding of veins about F_{1b} fold axes suggests that veins were formed prior to or during D_1 deformation. Outer-arc extension veins imply that veins or segregations were formed concurrent with D_1 deformation. F_{1b} fold-axial-planar veins lie in planes close to parallel to the maximum stretching axis for D_1 deformation, and as such may be considered to have formed post-D_1 deformation. However, axial planar veins in tectonites are abundant and well documented in literature (e.g., Edelman, 1973; Ramsay and Huber, 1987; Rosenberg et al., 1995; Davidson et al., 1996; Brown et al., 2004; Craw et al., 2006; Skelton et al., 2015), and can form in response to both progressive and polyphase deformation or during metamorphism as subsolidus or anatectic segregations channeled along fold hinge zones (Druguet, 2019). Druguet (2019) outlined eight settings in which axial planar veins can develop:

- Progressive deformation:
    1. Standard folding mechanisms: tangential longitudinal strain (TLS) is more efficient at producing axial planar veins than flexural flow, however TLS-associated veins are commonly discontinuous and limited to the fold's outer arc;
    2. Complex fracture arrays localised along short limbs of asymmetric folds;

3. Vein-related folds: complex flanking folds develop as a result of vein rotation, and fold may not match with regional fold orientations;
4. High strain and transposition of early veins: coplanarity of veins with folds is achieved after transposition; accompanied by boudinage or internal foliation in veins;
5. High strain and late veins axial planar to foliations: an axial planar foliation is already developed and controls the orientation of late-tectonic veins. Veins record little deformation relative to the host rock.

- Polyphase deformation:
  6. Veins predate folding: veins form as extensional veins at a high angle to the foliation and may be stretched into coplanarity with fold axial surfaces during subsequent folding;
  7. Veins post-date folding: veins are injected along a pre-existing foliation.
- Anatectic or subsolidus channeling of veins
  8. Veins channeled toward fold hinge zone by ductile deformation ± fluid melt/buoyancy

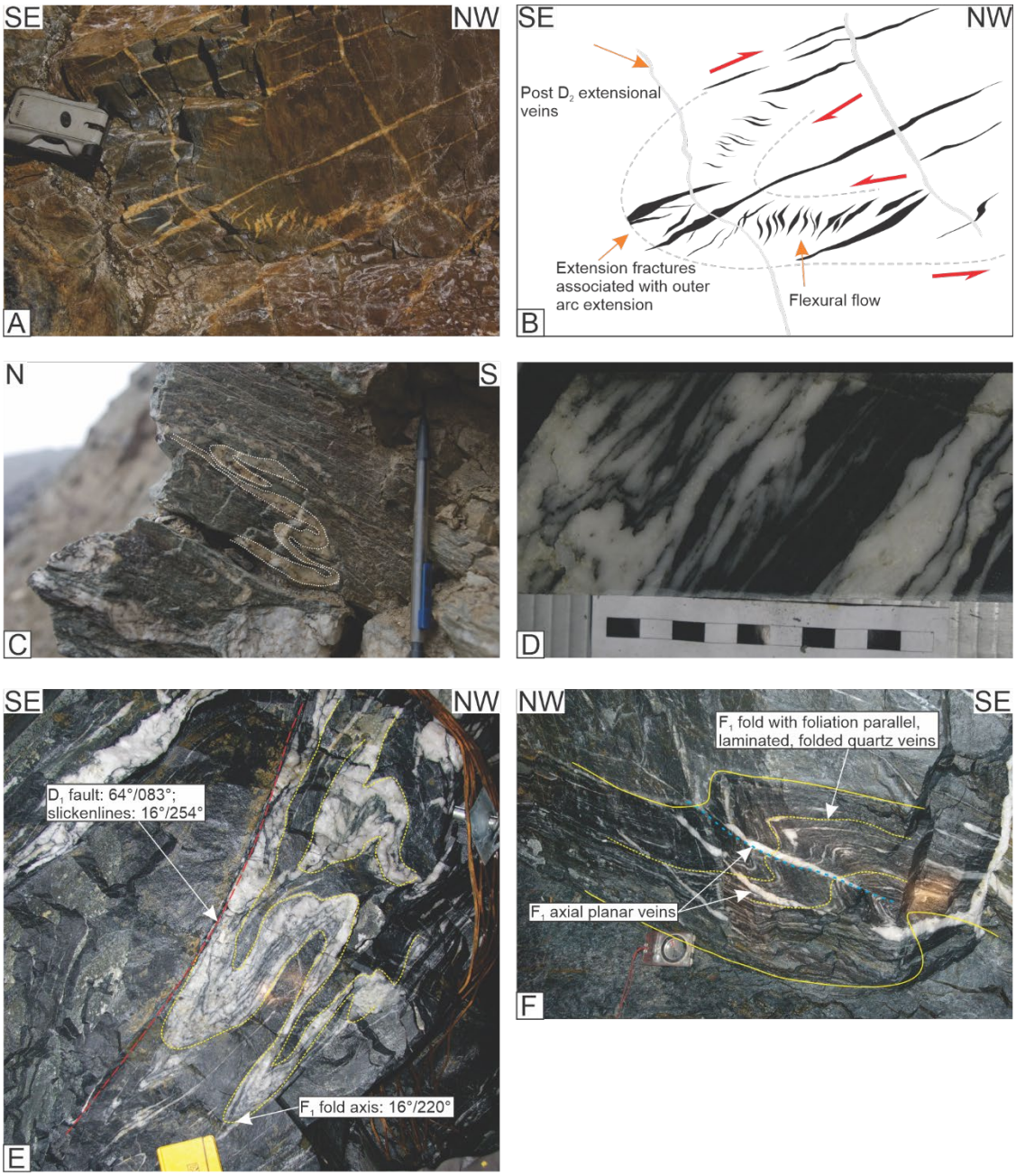

Figure 5.8: Examples of D_1 associated quartz veins across the Keno Hill district.

A: Photograph of F_1 fold in quartzite in the Bermingham open pit. Fold axis parallel quartz veins are visible at fold hinge and at lithological contacts; rotated quartz veins are apparent in limbs of fold (UTM 478861 mE, 7086885 mN); B: Interpretation of photograph A showing fold axis parallel veins associated with outer arc extension and flexural slip along lithological contacts, and flexural flow in fold limbs (UTM 478861 mE, 7086885 mN); C: Photograph of isoclinally (F_1) folded quartz vein in chlorite-mica schist at the Signpost locality (489454 mE, 7090627 mN); D: Photograph of foliation-parallel quartz veins in drill core (borehole K-08-0165, depth 197.92m, Keno 700 deposit); E: Photograph of D_1 fault parallel to (and truncating) laminated, folded quartz veins, Bellekeno East Decline; F: F_1 fold with foliation parallel, laminated quartz cut by F1 axial planar veins, Bellekeno East Decline.

The characteristics of foliation-parallel veins suggest that quartz segregation or injection took place throughout the D_1 deformation phase. Using Druguet's (2019) classification pre-Ag-Pb-Zn-mineralisation veins can be characterised as follows:

- Type 4 (pre- to early-D_1 deformation): Laminated, boudinaged, $S_{0\text{-}1a\text{-}1b}$ foliation-parallel veins are common, particularly within schistose units, and may rotate about F_{1b} fold hinges (e.g., Figure 5.8C to F). These are considered to be early veins, possibly associated with formation of F_{1a} folds. Rare quartz veins were observed to rotate about F_{1a} fold axes and as such veining or quartz segregation may have predated F_{1a} fold development. A lack of extensional textures within veins means that these veins are classed as type 4 veins rather than type 6.
- Type 1 (syn- to late-D_1 deformation): Outer arc extensional veins associated with TLS and rotated veins associated with flexural flow in F_{1b} fold limbs are considered to have formed during F_{1b} fold development (e.g., Figure 5.8A and B).
- Type 5 or type 7 (late-D_1 deformation): relatively undeformed, F_{1b} axial planar veins. Veins are coplanar with foliation-parallel or foliation-oblique thrust or reverse faults (e.g., Figure 5.8A, B, and F).

D_1 Strain Partitioning, Faults and Shear Zones

D_1 strain is strongly partitioned between more siliceous and more micaceous units with graphitic to chlorite-mica schist, and sericite schist accommodating the bulk of strain. Strain partitioning is characterised by strong alignment of mica grains parallel to the

foliation. Strain partitioning was observed from the micro- to meso-scale (Figure 5.9). Euhedral pyrite is commonly associated with the more graphitic schist units and is especially within Earn Group rocks. Pyrite crystals show solid body rotation, with sigma strain shadows in outcrop indicating north-directed shortening, similar to vergence directions for F_{1b} folds (Figure 5.10).

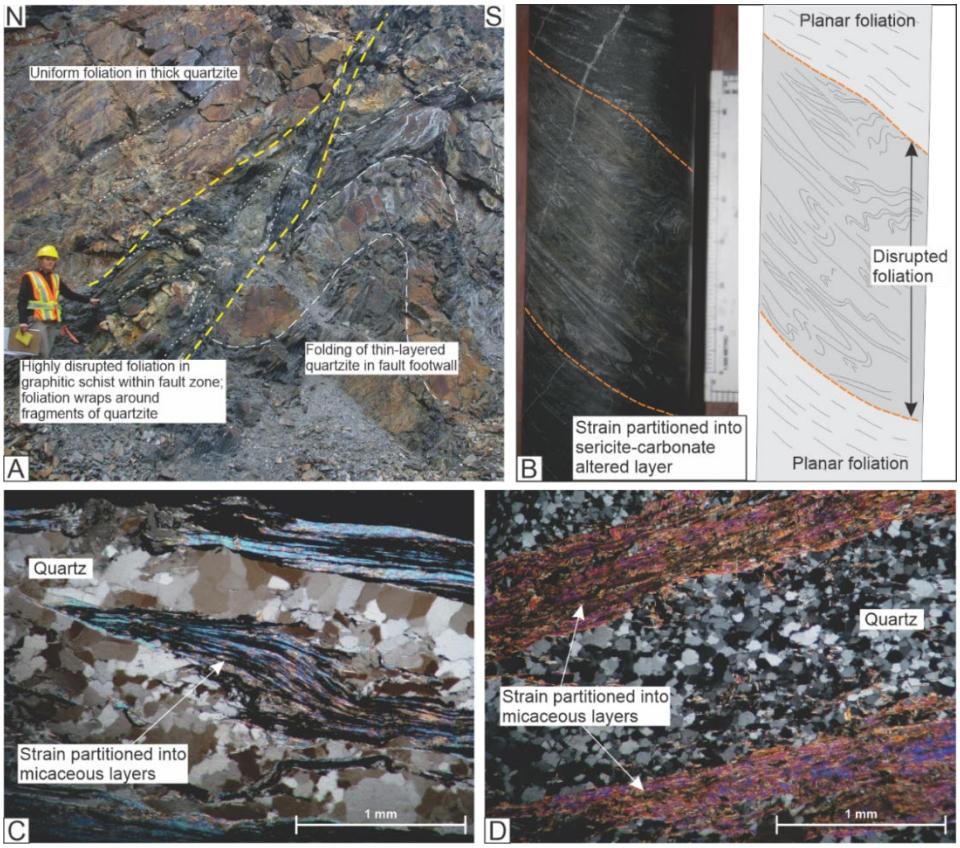

Figure 5.9: Examples of meso- to micro-scale strain partitioning associated with D_1 deformation.

A: Photograph of D_1 fault zone in the north pit of the Sime workings showing strain partitioned into graphitic schist (UTM 482380 mE, 7088713 mN); B: Photograph (left) and photograph interpretation (right) of strain partitioned into sericite and carbonate altered layer within greenstone (borehole K-09-0192, depth 64.72 m, Bellekeno deposit); C: Photomicrograph (XPL) of strain partitioned into micaceous layers in schistose unit (borehole K-08-0179, depth 56.88 m Hector Calumet deposit, sample 0179-002; D: Photomicrograph (XPL) of strain partitioned into micaceous layer in sericitic schist unit (Borehole K-08-0179, depth 75.08 m Hector Calumet deposit, sample 0179-009).

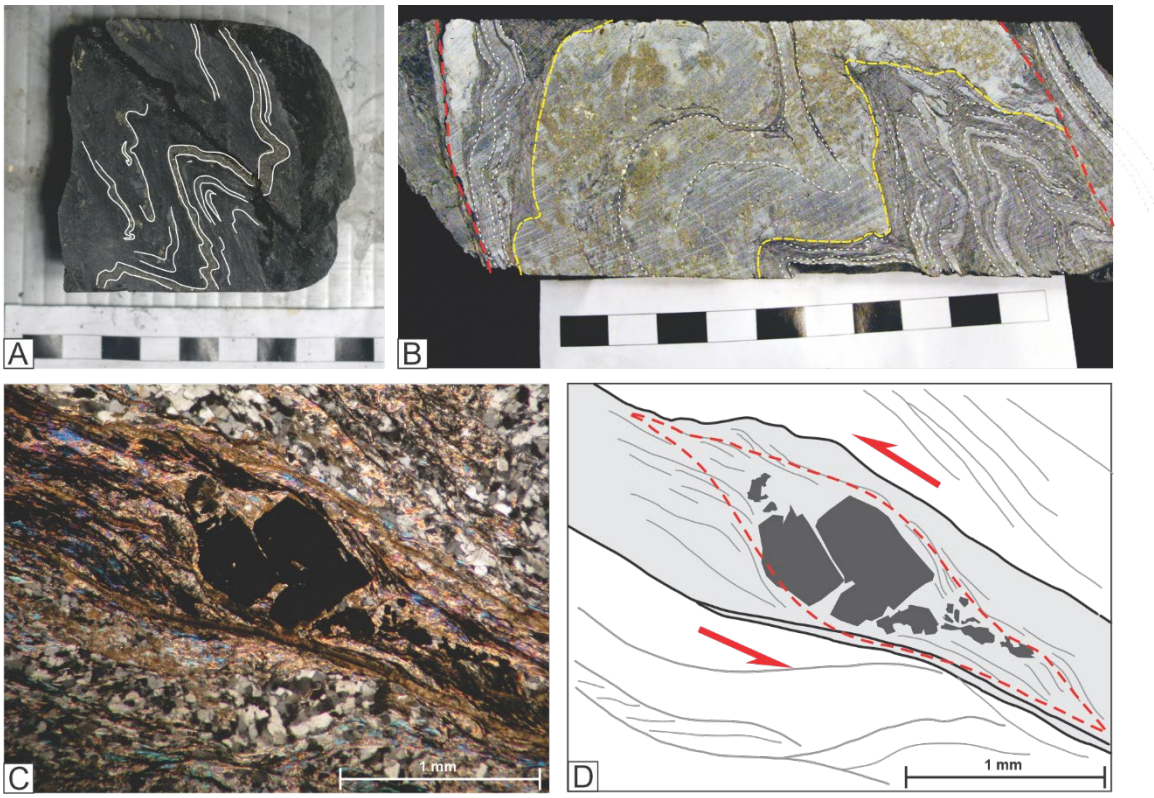

Figure 5.10: Examples of pre- to syn-D_1 pyrite sulfidation.

A: Photograph of F_1 folded (M-folded) layer with abundant pyrite within graphitic schist (Borehole K-07-0120, depth 148.06 m, Onek deposit); B: Photograph of F_1 folded and D_1 faulted intercalated quartzite and schist. Pyrite mineralisation is largely confined to the quartzite layer (Borehole K-08-0179, depth 66.80 m, Hector Calumet deposit sample 0179-005); C and D: Photomicrograph (XPL) (C) and interpretation (D) showing rotation of pyrite within S_1 foliation. (Borehole K-08-0179, depth 66.80 m Hector Calumet deposit, sample 0179-005).

D_1 faults and shear zones are subparallel to $S_{0\text{-}1a\text{-}1b}$, and dip shallowly SSE. Large, D_1 fault surfaces show slickensides that have slickenlines with a commonly moderate to shallow SE to SW plunge, and steps that indicate thrusting towards the NE to NW (Figure 5.11A). Slickensides showing evidence of NE- to NW-directed slip are present on most $S_{0\text{-}1a\text{-}1b}$ foliation surfaces, particularly where the foliation is coincident with a change in lithology. Fault zones are commonly narrow and may be limited to the width of the interface between lithological units. However, wider fault zones were observed in the

north pit of the Sime deposit, where a > 4 metre wide package of disrupted graphitic schist with dismembered, folded layers of quartzite separates thick sequences of blocky quartzite along the long, moderate to shallow, south-dipping long limb of a major N-verging F_{1b} fold; in the south walls of the Calumet and Onek deposits where schist-dominated fault zones are subparallel or slightly steeper-dipping than the regional foliation and juxtapose thick quartzite against intercalated quartzite and schist. In the western corner of the Bermingham pit, a foliation subparallel fault appears to truncate the short limb of a N-verging fold in thick quartzite. Slickensides are associated with most D_1 slip surfaces, indicating that fault movement was largely brittle. However, within the trenches at the summit of Keno Hill (Signpost locality), a steep strain gradient was observed within a chlorite-mica schist unit that was marked by NNW-verging intrafolial folds, a distinct increase in intensity of the schistose foliation down-section and mylonitisation that was coincident with an abrupt change in lithology to quartzite down-section. This may define the location of a major D_1 shear zone.

Inversion of fault and striae data using FaultKin^{TM} software (Marrett and Allmendinger, 1990; Allmendinger et al., 2012) indicates that D_1 shortening occurred along a shallow north- to NNW-plunging axis (Figure 5.11B and C). Note the P-axis (pressure) and T-axis (tension) may not exactly equate to the $\sigma 1$ and $\sigma 3$ principal stress directions for D_1 unless the fault planes and their conjugates were planes of maximum shear stress or minimum confining strength (Allmendinger et al., 1989). It should also be noted that locally slickensides show steps that indicate approximately south-directed extension. This may be indicative of a period of stress relaxation and post-orogenic collapse following

north- to NNW-directed D_1 shortening. District- to regional-scale thrust faults are generally rare, with thrusting and shortening typically accommodated by small-scale $S_{0\text{-}1a\text{-}1b}$ -parallel slip at the interface between thin to thick quartzitic units and schistose units.

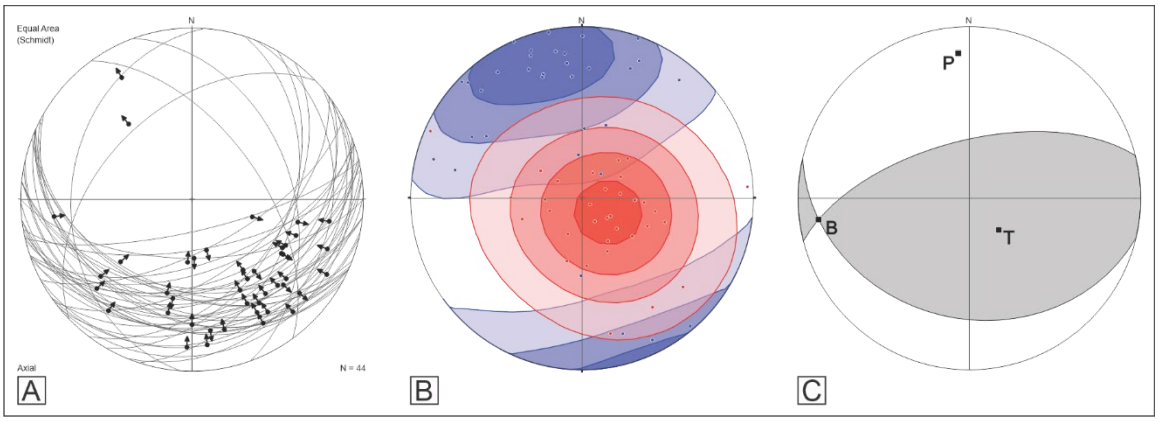

Figure 5.11: Lambert equal area projections of D_1 fault measurements and associated inversions using FaultKin™ software (Marrett and Allmendinger, 1990; Allmendinger et al., 2012).

A: Measured D_1 faults (great circles; polar data, 44 measurements) with slickenline measurements (dots), and hanging wall slip direction (arrows); B: Shortening axes (blue dots) with Kamb contours of shortening axes (blue contours), and extension axes (red dots) with Kamb contours of extension axes (red contours); C: Kinematic axes overlain on P T dihedra plot calculated with Linked Bingham statistics in FaultKin™ software (Allmendinger et al., 2012) for D_1 faults (P: shortening axis, T: extensional axis, B: intersection of nodal planes).

D_1-Associated Joints

At the meso-scale, joints rotate about $F_{1a\text{-}b}$ fold axes, which is particularly evident in the Onek open pit. A large number of joint orientations were measured across the district (total count 3709); however, analysing joint populations associated exclusively with D_1 deformation is problematic. The subsequent D_2 and D_3 deformation events are considered to have occurred in a dominantly or exclusively upper crustal, brittle regime, and as such the majority of measured joints are considered to be associated with post-D_1 deformation.

An attempt was made to assess the populations of D_1-associated joints using the Spheristat^{TM} software's subtract density peak function. The theory behind this process was that by systematically removing density peaks of joints that are likely associated with syn- and post-mineralisation, it should be possible to assess the populations of joints associated with pre-mineralisation deformation.

Joint measurements were subdivided by geographic location into two domains: 1) joints measured on or to the west of Galena Hill, and 2) joints measured on Keno Hill and Sourdough Hill. The joint measurements were plotted and contoured on a Lambert equal area stereographic projection. The principal stress orientations for the D_2 and D_3 deformation phases are discussed later in this thesis; however, it should be noted here that the interpreted shortening direction for D_2 was broadly NNE to SSW oriented and subhorizontal, and the interpreted shortening direction for D_3 was approximately north-south oriented and subhorizontal. Density peaks were subtracted that were steep to subvertical-dipping and NE (i.e., subparallel to D_2 shortening) or north-south (i.e., subparallel to D_3 shortening) trending. In addition, peaks were removed that were subparallel to the typical measured orientations of D_2 and D_3 faults. Three iterations of density peak subtraction were completed on the joint datasets for both geographic domains (Figure 5.12).

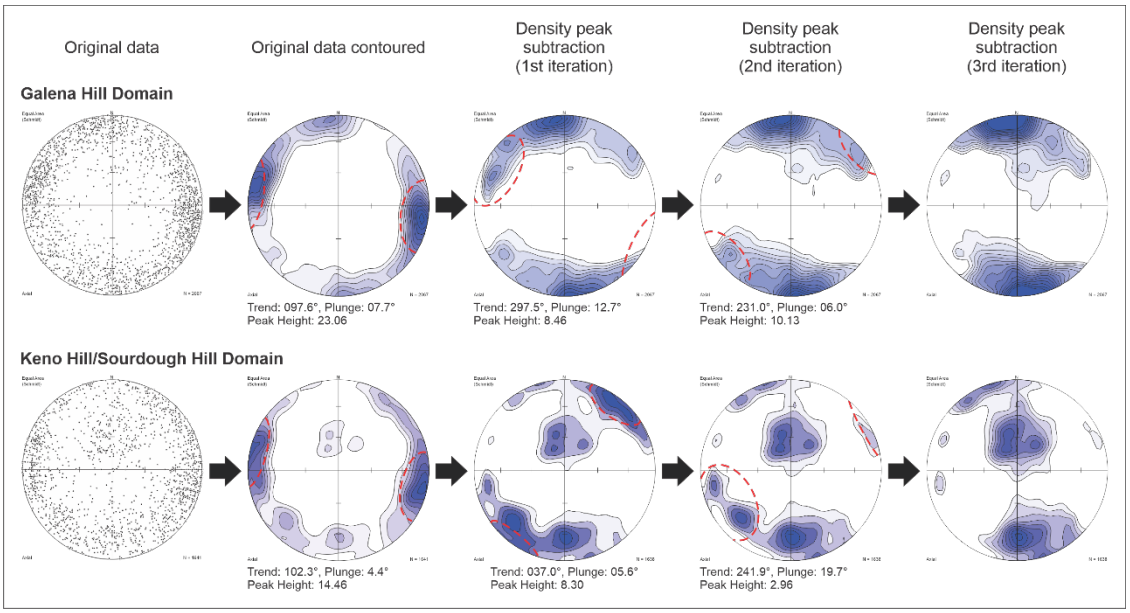

Figure 5.12: Density peak subtraction methodology for analysis of potentially D_1-associated joints in the Galena Hill and Keno Hill/Sourdough Hill areas.

The results of the density peak subtraction process show that both geographic domains contain a set or sets of approximately east-west-trending, subvertical to steep south-dipping and moderate to steep north-dipping joints (Figure 5.13). It is not clear what phase of deformation is responsible for the generation of these joints sets. Given that the shortening direction for D_1 is considered to be north-south to NNW to SSE (Figure 5.11), the orientation of the joint set is misaligned with the extension direction. It is possible that this joint set formed as shear joints (i.e., Mode II or III fractures) related to D_2 deformation; however, closely spaced, steep-dipping east-west trending joints have been observed at the Onek deposit that are spatially associated with D_1 boudin necks (Figure 5.14). As such it is possible that these sets of joints may have formed in response to stretching in the limbs of F_1 folds during D_1 deformation.

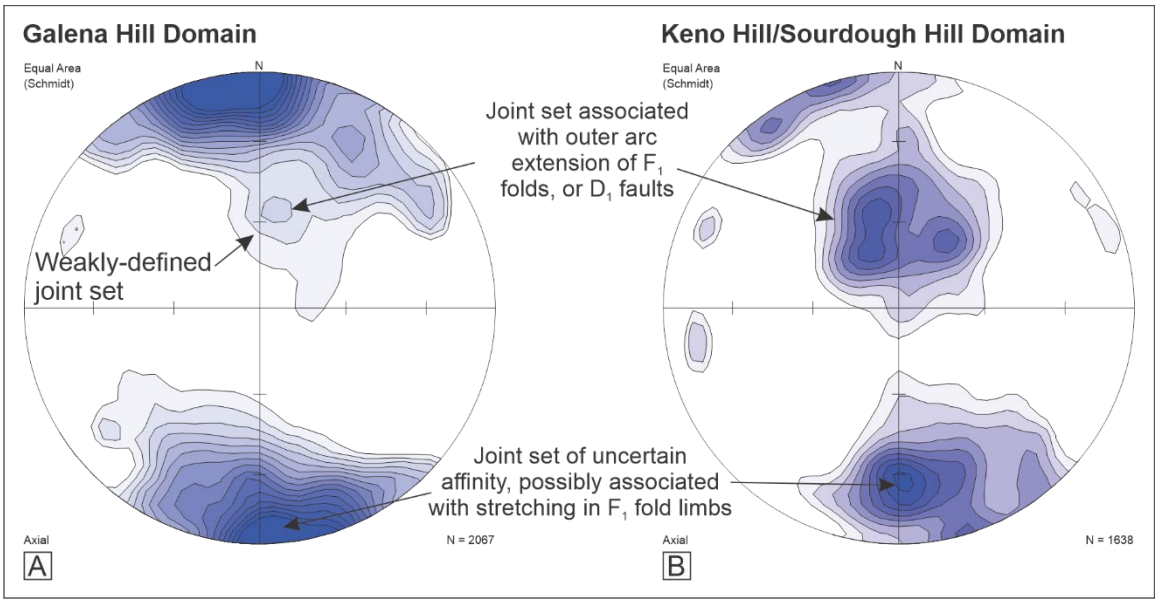

Figure 5.13: Density peak subtracted, contoured, Lambert equal area projections of joint data for the (A) Galena Hill and (B) Keno Hill/Sourdough Hill areas showing results of density peak subtraction process to analyse potential D_1-associated joints.

A second set of joints is observed that is moderate to shallow SSE- to SSW-dipping (Figure 5.13). At the regional-scale this set of joints is subparallel to the $S_{0\text{-}1a\text{-}1b}$ foliation, D_1 faults and to F_1 fold axial surfaces. Variation in joint-dip in outcrop shows that joints associate with this population represent longitudinal or radial joints that formed around the outer arc of F_1 folds during D_1 deformation. This set of joints is well developed in the Keno Hill/Sourdough Hill domain but is less well developed towards the west in the Galena Hill domain (Figure 5.13). The reason for the variation in development of outer arc joints between domains is not immediately clear, however one potential explanation is described below. At the mesoscopic scale the structural elements of D_1-associated deformation appear broadly consistent across the study area. However, district-scale stratigraphic mapping by McOnie and Read (2009) indicates the presence of a major D_1 thrust fault, and possible major F_1 fold axis near the summit of Keno Hill (Figure 2.21).

Stratigraphic repetition of the Earn Group and KHQ on the northern flank of Keno Hill and the occurrence of mylonite at the signpost locality appears to corroborate this interpretation. Similar stratigraphic repetition has not been documented on Galena Hill. As such Galena Hill may be located on the long limb of a major F_1 fold, and distal to major D_1 faults, thereby reducing the opportunity for development of F_1 fold-radial joints.

F_1 fold-radial joints, and approximately east-west striking, subvertical to steep-dipping joints associated with boudin necks were documented in outcrop in the Onek open pit (Figure 5.14B to D). A subset of the measured joints was analysed from a section within the hanging wall of the Onek vein (Figure 5.14A). While joints associated with syn- and post-mineralisation deformation were also observed in this section, the results of the analysis show a similar statistical distribution to the results for the Keno Hill/Sourdough Hill domain following density peak subtraction (Figure 5.13B and Figure 5.14E).

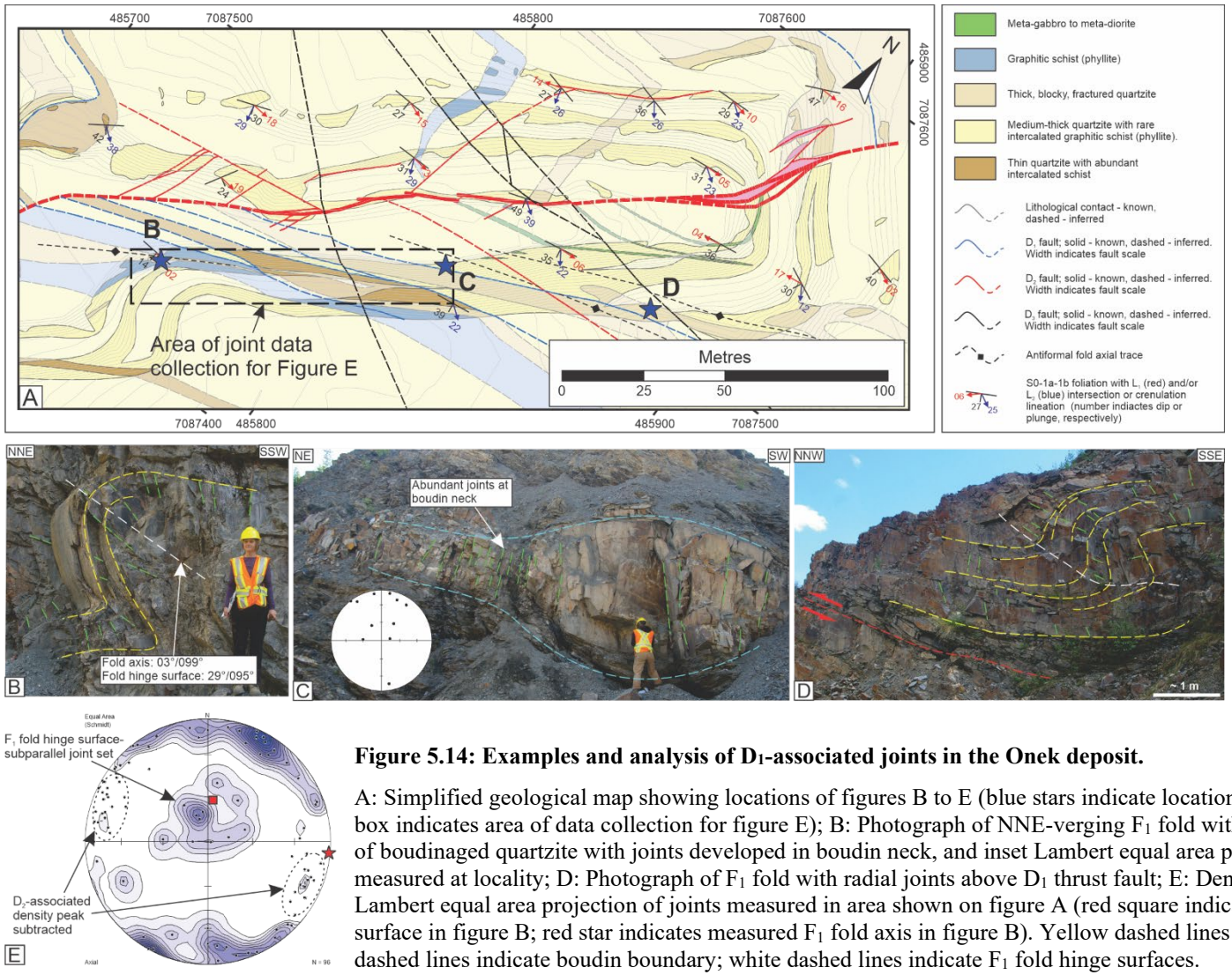

Figure 5.14: Examples and analysis of D_1-associated joints in the Onek deposit.

A: Simplified geological map showing locations of figures B to E (blue stars indicate locations of figures B to D; dashed box indicates area of data collection for figure E); B: Photograph of NNE-verging F_1 fold with radial joints; C: Photograph of boudinaged quartzite with joints developed in boudin neck, and inset Lambert equal area projection of poles to joints measured at locality; D: Photograph of F_1 fold with radial joints above D_1 thrust fault; E: Density subtracted, contoured, Lambert equal area projection of joints measured in area shown on figure A (red square indicates measured F_1 fold hinge surface in figure B; red star indicates measured F_1 fold axis in figure B). Yellow dashed lines indicate fold geometry; blue dashed lines indicate boudin boundary; white dashed lines indicate F_1 fold hinge surfaces.

Progressive or polyphase deformation?

D_1 deformation is associated with lower to middle greenschist-facies metamorphism (Mair et al., 2006) and its associated moderate temperatures and depths, typically 300–450 °C and 2–5 kilobars (Spear, 1993; Feenstra and Franz, 2015). Elements of both ductile and brittle deformation were observed and assigned to the D_1 deformation phase. Ductile deformation is characterised by C-S fabrics, sigma strain shadows on pyrite crystals, sporadic mylonitic fabrics, flexural flow on fold limbs, ubiquitous isoclinal and more rare rootless folds, and F_{1a}-F_{1b} fold interference patterns. Evidence for brittle deformation and (or) a high strain rate during deformation is comprised of the abundance of D_1 faults and their associated stepped slickensides, the rotation of joints about the F_{1a-b} fold axis, outer arc extension and associated quartz veining at fold hinges, and the strong and predictable partitioning of strain into the more incompetent schistose rocks.

Several of the structural elements described above, in particular the two generations of folding, can be the product of both progressive (e.g. Turner and Weiss, 1963; Whitten, 1966; Ghosh, 1993; Alsop and Holdsworth, 2002; Grasemann et al., 2004; Jones et al., 2004; Carreras et al., 2005; Fossen et al., 2013; Carreras and Druguet, 2019) and polyphase deformation (e.g. Ramsay, 1962; Ghosh and Ramberg 1968; Grujic, 1993; Ghosh et al., 1993, 1995; Ghosh and Sengupta, 1996; Grujic et al., 2002; Laurent et al., 2016). Park (1969) states that "the division of orogenic structural sequences into three or four well-defined phases carries the implication that orogenic deformation is episodic (or spasmodic) in character, consisting of a small number of relatively short-lived and

widely-felt compressional events which are clearly separated from each other, rather than a continuous and progressive response to a long-applied compression, perhaps varying in intensity in place and time". Furthermore, Fossen et al. (2019) state that for a deformation phase to be defined, its structural expression should be identified and mapped at a regional scale (at least hundreds of square kilometers). Given the size of the field study area, and the general sparsity of structures unequivocally associated with F_{1a} fold formation, the author is reluctant to assign the F_{1a} folding event a discrete deformation nomenclature.

Fossen et al. (2019) state that "the term progressive deformation refers to a period of continuous (non-stop) deformation during which composite structures such as overprinting cleavages, refolded folds, and folds and fabrics, typically with significant variation in style and orientation, may form" and that "the overall stress orientation is, by definition, constant for a single deformation phase". Kinematics (transport directions, sense of shear) represent an important aspect of deformation, and structures that fit into a coherent kinematic framework may have formed during the same deformation (Fossen et al., 2019). F_{1a} and F_{1b} fold axes, boudin axes, L_{1cr} and L_{1int} lineations, and the intersection of S and C fabrics are broadly coaxial, and near perpendicular to slip vectors from slickenfibres, vergence of F_{1b} folds, sigma strain shadows, and movement direction of C-S fabrics. This suggests that all structural elements are kinematically compatible and formed within the same regional stress regime, albeit possibly at different structural elevations. The lack of sudden changes in regional shortening direction for all these elements suggests D_1 deformation was progressive rather than polyphase.

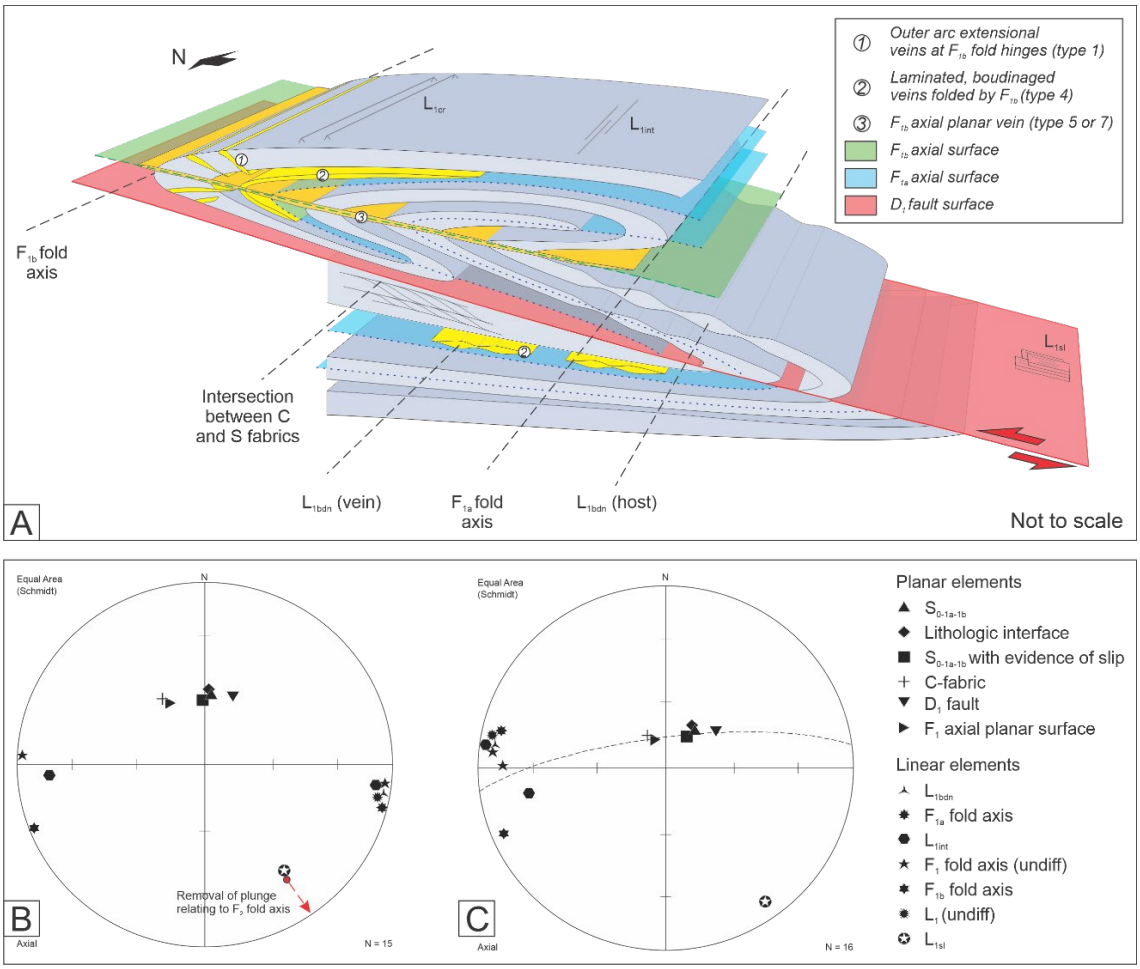

Figure 5.15: Geometric relationships between planar and linear, D_1 associated, structural elements.

A: Schematic diagram showing hook-type F_{1a}-F_{1b} fold interference pattern offset along a D_1 fault. All linear elements are approximately subparallel, except for slickenlines associated with fault movement. Planar elements include the approximately coplanar D_1 fault and F_{1b} fold axial surface, and the F_{1a} fold axial surface, which is folded by F_{1b}. Outer arc extensional veins; folded, laminated, boudinaged veins; and F_1 axial planar veins are also shown.

B: Lambert equal area projections of average orientations linear and planar, D_1 associated structural elements as measured in the field. Average orientations were derived from the centre point of density contoured maxima for each element. Note that where two maxima were calculated for a given element, both centre points were plotted.

C: Lambert equal area projections of average orientations linear and planar, D_1 associated structural elements rotated to remove the plunge of F_2 folding/warping. Overall, linear elements produce a shallow west to WSW-plunging cluster, whereas planar elements become shallower dipping and broadly E-striking. Great circle represents the π-girdle for planar elements; the girdle has a dip/strike of 78°/263° and a pole of 12°/173°.

The evidence for syn-D_1 joint development presented above suggests that either D_1 deformation and associated metamorphism occurred at a shallow depth of burial with a high strain rate, or that D_1 deformation, including the formation of F_{1a} and F_{1b} folds, and the transposed $S_{0\text{-}1a\text{-}1b}$ foliation records the progressive exhumation of rocks from deep to shallow structural levels. Where $F_{1a\text{-}b}$ fold interference patterns are observed, radial joints appear more closely related associated to F_{1b} folds than to F_{1a} folds. This may be a function of scale and lithology, with F_{1b} commonly producing larger folds, including folds of relatively thick packages of brittle quartzitic units. However, this may also suggest that D_1 deformation did not exclusively take place a high structural level with a high strain rate, but that D_1 deformation initiated at a relatively low structural level with moderate temperatures and pressures and its associated ductile deformation elements including F_{1a} folds, and that deformation subsequently progressed to higher, brittle-ductile structural levels that permitted the development of brittle fault characteristics, extensional joints, and extensional veins about F_{1b} fold hinges.

Three vein styles were observed that were correlated with D_1 deformation (Figure 5.8 and Figure 5.15). These included (pre- or early syn-deformation) foliation-parallel veins that may be folded by F_{1b}, or more rarely F_{1a} folds (Type 4 of Druguet (2019)); syn-deformation outer-arc extension (TLS) and flexural flow veins (Type 1 of Druguet (2019)); and late deformation, relatively undeformed, F_{1b} axial planar veins (Types 5 or 7 of Druguet (2019)). Vein types 1, 4, and 5 are all considered to have been emplaced in a progressive deformation regime, whereas type 7 may be emplaced during polyphase deformation.

The kinematic compatibility and lack of variation in shortening direction for all structural elements, the association of brittle extensional joints with the later F_{1b} phase of folding, and the presence of Type 1, 4, and possibly 5 veins all suggest that D_1 deformation was progressive. As a caveat, the study area was relatively small, and while F_{1a} and F_{1b} folds are commonly coaxial, some deviation between fold axes was observed towards the far east of the study area. To the authors knowledge, this thesis represents the first documentation of the earlier F_{1a} phase of folding anywhere in the Tombstone Strain Zone, and as such the development of F_{1a} folds may have been spatially limited. If this apparent spatial restriction is real, that means that under Fossen et al.'s (2019) criteria, F_{1a} folds cannot be assigned to a discrete phase of deformation, and that therefore deformation was progressive.

5.1.3 Syn-Ag-Pb-Zn-Mineralisation (D_2)

D_2 deformation is characterised by brittle deformation and the emplacement of Ag-Pb-Zn mineralised veins. The principal structural elements associated with D_2 comprise sinistral strike-slip to sinistral-normal oblique-slip faults and a broad warping of the $S_{0\text{-}1a\text{-}1b}$ composite foliation.

D_2 Fault Characteristics

D_2 faults were active coevally with Ag-Pb-Zn vein emplacement and are present in all open pits across the district, and in the Bellekeno underground workings. D_2 faults show a bimodal distribution with ENE-striking, steep to moderate, SSE-dipping, and NE-

striking, steep to moderate SE-dipping faults common (Figure 5.16). Locally, NNE- and north-striking D_2 faults were also observed, such as in the north pit of the Sime deposit. D_2 faults are highly oblique to the regional S_0-S_{1a}-S_{1b} foliation and D_1 faults/shear zones, and offset lithological units and D_1 faults/shear zones with a sinistral strike-slip to sinistral-normal oblique-slip movement sense. D_2 faults are in turn dextrally offset by later, SE-striking (D_3) faults.

D_2 faults and fault zones vary from narrow (1 to 2 centimetres), discrete surfaces of short strike length to greater than 8 metres wide (e.g., in the Calumet pit and the Bellekeno 750-1 crosscut) where they are associated with Pb (galena) and Zn (sphalerite) ± carbonate (siderite) and Ag mineralised veins, fault gouge, and local breccia or cataclasite (Figure 5.17 and Figure 5.18), and rarely pseudotachylyte. The longest D_2 faults are ENE-striking (Figure 5.16C) and can be tracked continuously in outcrop for up to 600 metres (e.g., the No.6 fault and associated vein at the summit of Keno Hill. In remote sensing data ENE-striking faults can be traced for several kilometres with individual fault segments reaching greater than five kilometres (discussed in chapter 5.2.1). These faults are considered to be first order structures based on their length and width in both field observations and remote sensing data sets, and their commonly throughgoing geometry. Second and third order D_2 faults typically strike NE (Figure 5.16D) and splay off first order faults, with lengths that range from tens to hundreds of metres (in both field observations and remote sensing data sets). Second and third order D_2 faults are rarely greater than one kilometre in length in remote sensing data sets.

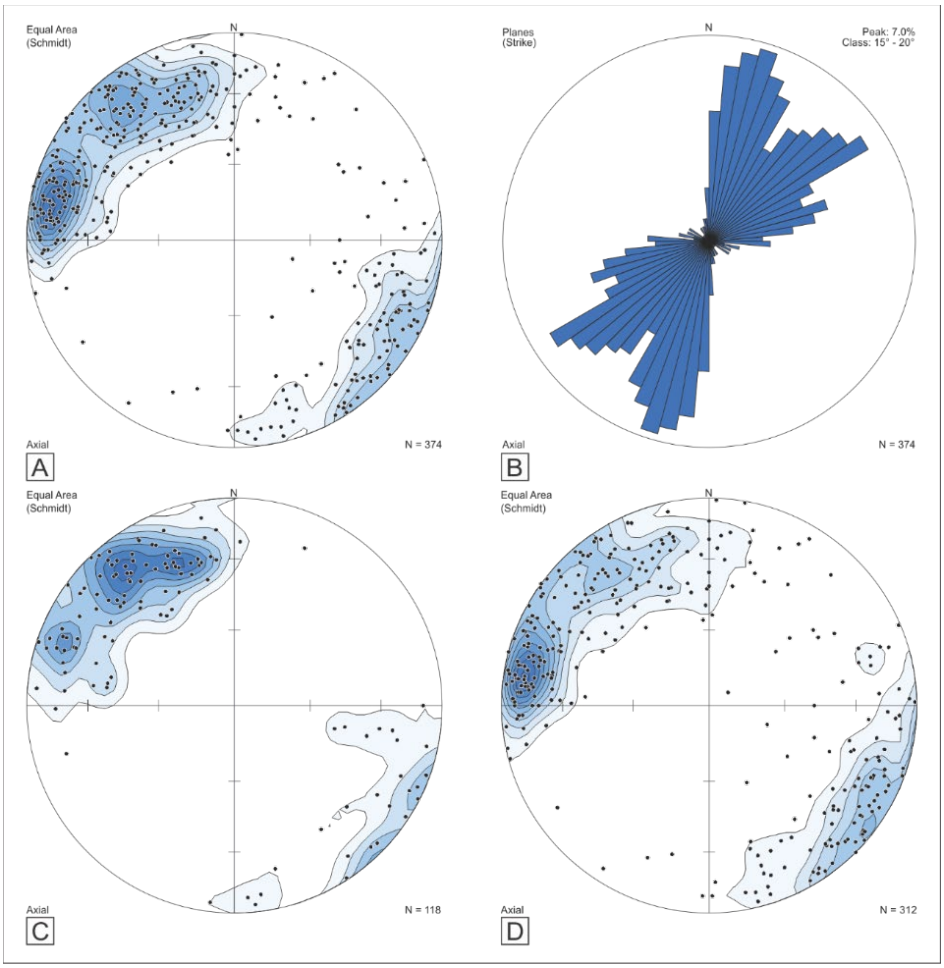

Figure 5.16: Lambert equal area lower hemisphere projections and rose diagram of D_2 faults in the Keno Hill district.

A: Density contoured, all measured D_2 faults; peak densities oriented 73°/051° and 75°/014° (polar data, 374 measurements, contour intervals 2σ); B: Unweighted rose diagram of all measured D_2 faults showing bimodal distribution of fault strike with peaks at 010° – 020° and 055° to 060°. 374 measurements; C: Density contoured, measured first order D_2 faults; peak densities oriented 72°/051° and 71°/065° (polar data, 118 measurements, contour intervals 2σ); D: Density contoured, measured second, third, and undefined order D_2 faults; peak density oriented 75°/009° (polar data, 312 measurements, contour intervals 2σ).

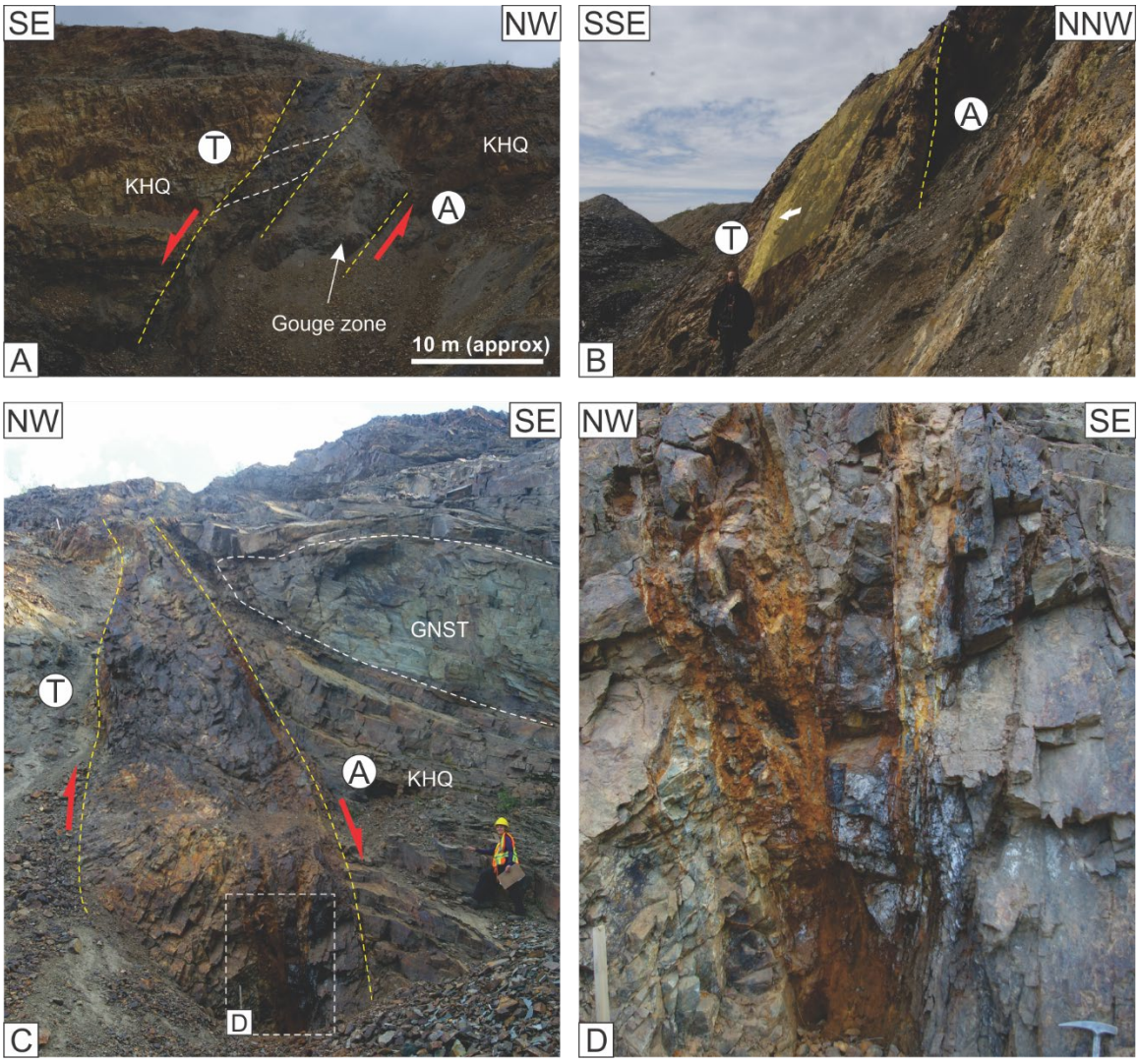

Figure 5.17: Examples of major D_2, Pb-Zn ± Ag mineralised veins in pits and trenches within the Keno Hill district.

A: Photograph of the main vein/fault oriented 54°/059° at the SW end of the Calumet open pit. Yellow dashed lines indicate location of faults within fault zone, white dashed line indicates cataclastic fabric (UTM 480863mE, 7088285mN); B: Photograph of No.6 vein oriented 62°/079°, with slickenline (L_{2sl}) oriented 05°/255° in trench at the summit of Keno Hill. Yellow features indicate fault surfaces, white arrow indicates slickenline (UTM 489470mE, 7090649mN); C: Photograph of the main vein oriented 67°/072° with inset showing location of figure D in the Onek open pit (UTM 485886mE, 7087549mN); D: Close up photograph of main vein showing strongly oxidised gouge and narrow galena veins in the Onek open pit (UTM: 485886mE, 7087549mN).

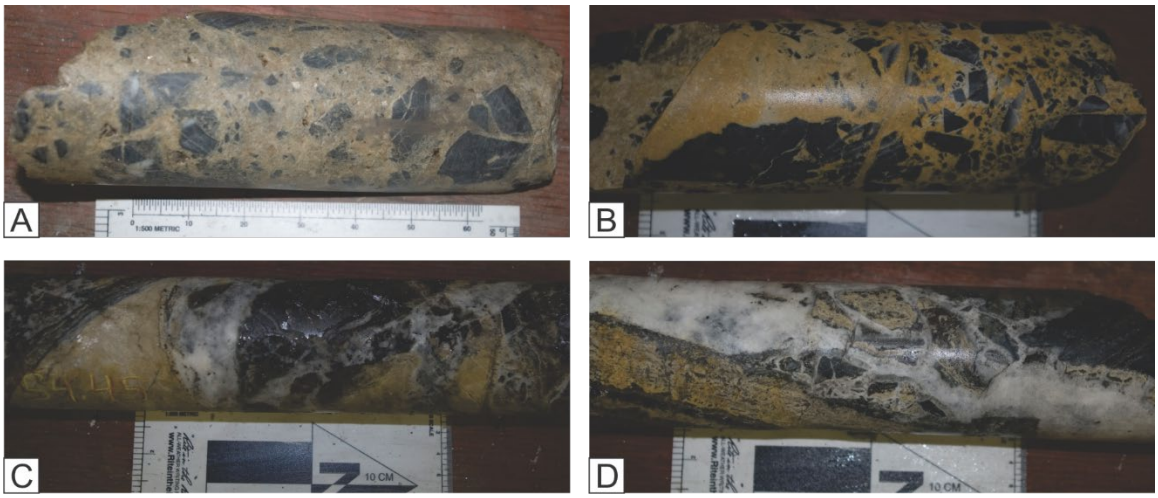

Figure 5.18: Photographs showing examples of fault breccia associated with D_2 fault in the Bellekeno deposit.

A: Quartz and siderite supported breccia with sphalerite and pyrite stringers. No assays available for interval but is at the margin of an approximately two metre wide zone with 3228 g/t Ag. Borehole BKUD09-0158, depth 35.3 metres; B: Quartz and overprinting siderite supported breccia. Siderite and sphalerite are vuggy in places. No assays available for interval, but is at margin of an approximately four metre wide zone with 2352 g/t Ag. Borehole K-09-0187, depth 198.0 metres; C: Quartz- and siderite-supported breccia in quartzite with associated chlorite-sericite alteration and massive galena. 1187 g/t Ag, borehole BKUD09-0160, depth 54.5 metres; D: Quartz- and siderite- supported breccia in quartzite with associated chlorite-sericite alteration and massive galena. 1187 g/t Ag, borehole BKUD09-0160, depth 54.7 metres.

Slickenlines (L_{2sl}) and slickenfibres with associated steps are common on D_2 faults and allow for assessment of fault kinematics (Figure 5.19). First order, ENE-striking faults commonly display shallow ENE- to WSW-plunging slickenlines (L_{2sl}), and steps on fault surfaces indicate sinistral strike-slip movement. Second order, NE-striking faults commonly display moderate- to steep-plunging lineations (L_{2sl} or L_{2g}), with steps that indicate normal dip-slip to sinistral-normal oblique-slip kinematics.

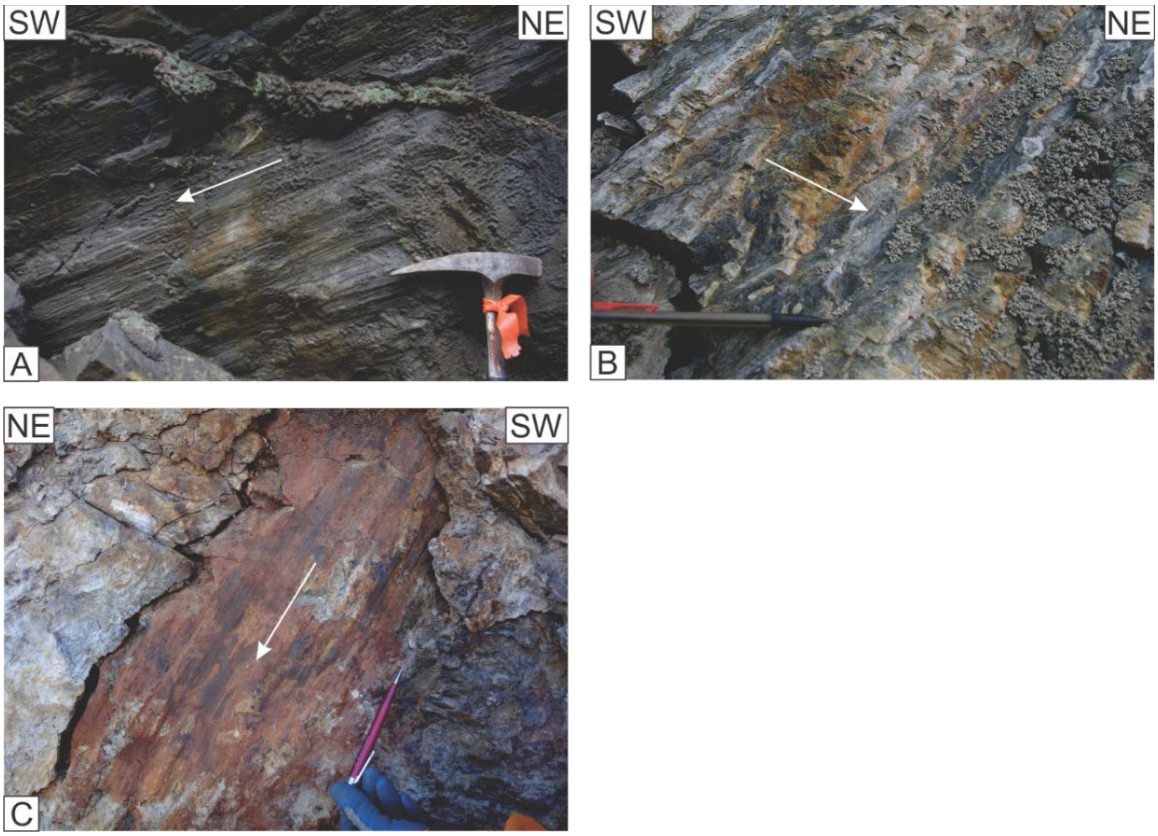

Figure 5.19: Examples of slickenlines, slickenfibres, and associated steps on D_2 faults across the Keno Hill district.

A: Slickenfibres oriented 28°/222° with steps indicating sinistral strike-slip movement on D_2 fault surface oriented 70°/212° along Galena Creek (UTM 471911mE 7085407mN); B: Slickenfibres oriented 34°/064° with steps indicating sinistral strike-slip movement on D_2 fault surface oriented 66°/041° at the Sime open pit (UTM 482379mE, 7088714mN); C: Slickenfibres oriented 55°/036° with steps indicating dextral-normal oblique-slip movement on D_2 fault surface oriented 80°/212° at the Sime open pit (UTM 489852mE, 7086858mN). White arrows indicate slickenline orientation.

D_2 Fault Geometry

The relationship between fault strike and slip plunge is well preserved at the summit of Keno Hill. Here a pair of first order faults are associated with Ag-Pb-Zn veins and are named the Nabob and Comstock faults, respectively (Figure 5.20 and Figure 5.21). An additional first order fault occurs south of the Comstock Fault and is named the Porcupine Fault. At the summit of Keno Hill, the Nabob and Comstock faults are

subparallel and strike ENE; the Porcupine Fault strikes slightly more NE, and tapers into the Comstock Fault to the east.

The Nabob Fault trends subparallel to the ENE-trending steep scarp of Keno Hill and outcrops more or less continuously for 600 metres. Immediately south of the fault at the signpost locality are a series of subordinate, shorter strike-length faults and associated Ag-Pb-Zn veins that are subparallel to the Nabob Fault and include the No. 6 Fault. The Nabob Fault is oriented 68°/075° with subhorizontal slickenlines (L_{2sl}). Some sulfidation is associated with the Nabob and No. 6 faults. Vein width could not be determined at surface; however, underground mapping by Boyle (1965) indicates that vein width associated with the No. 6 Fault varies between 5 and 10 feet (1.5 to 3.0 metres). The Comstock and Porcupine faults occur 400 to 600 metres south of the Nabob Fault on Keno Hill and outcrop in various locations. The Porcupine Fault varies in character along its length and has orientations varying from 71°/080° at the base of Monument Hill, to 74°/052° in the Porcupine open pit. At the base of Monument Hill, the fault was observed to be a discrete, well-polished fault surface with L_{2sl} slickenlines oriented 14°/275° and steps indicating sinistral movement. No Pb-Zn veining was observed at this locality. In the Porcupine open pit, the fault was observed to be associated with a 0.4 metre wide vein associated with galena-sphalerite-arsenopyrite ± pyrite mineralisation, and manganese oxide alteration.

A series of second order, NE-striking faults that splay off the larger Nabob Fault form a linkage between the Nabob and Comstock faults. These faults are named the No. 9, No.

10, and No. 13 veins, and can be observed in trenches near the NNW-facing scarp of Keno Hill (Signpost locality) (Figure 5.20), where they are associated with Ag-Pb-Zn mineralised veins. The No. 9 Fault is oriented 61°/022° and is associated with breccia, pseudotachylyte, sphalerite mineralisation and chlorite alteration. Vein width could not be determined at surface; however, underground mapping by Boyle (1965) suggests that at depth, the width of the No.9 vein may reach 15 feet (4.5 metres) or more.

The No.9 Fault has a pair of slickenlines (L_{2sl}) oriented 61°/113°, and 26/036° with steps indicating normal and sinistral movement, respectively (Figure 5.20C). The lineation that defines normal movement is much more prevalent and better developed than that defines sinistral movement. As such normal displacement is considered to be the dominant movement on the second order fault.

The fault geometry and kinematic indicators on Keno Hill suggest that the Nabob, Comstock, and Porcupine faults are first order, sinistral strike-slip faults that are directly linked by second order, dominantly extensional, sinistral-normal oblique slip faults of the No. 9 Fault system at a left-stepping fault step-over (Figure 5.21). Maximum dilation of the fault system occurred along the second order faults and promoted Pb-Zn ± Ag precipitation. Locally, the Porcupine Fault may bend to strike NE, resulting in local extension and Pb-Zn ± Ag at the Porcupine open pit.

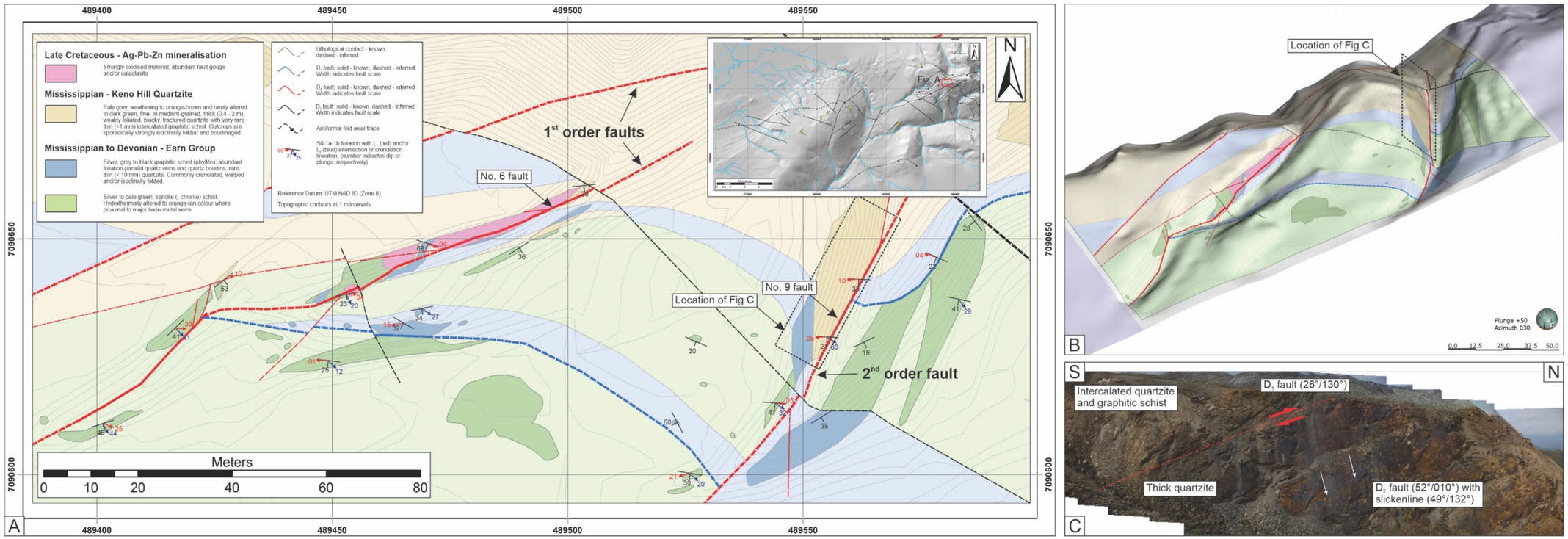

Figure 5.2: Simplified geological maps of the No.6 and No.9 faults at the summit of Keno Hill with associated foliation, lineation, and fault orientation data.

A: Simplified geological map with inset location map; B: Simplified geological map overlain on topographic data (inclined view); C: Panoramic photograph of footwall of the No.9 fault showing dominant, steep-plunging slickenline (L_{2sl}) orientation. Figures D to H: Density contoured, Lambert equal area lower hemisphere projections of measured structural elements. A: $S_{0\text{-}1a\text{-}1b}$ foliations (polar data, 92 measurements, contour intervals 2σ); E: Undifferentiated L_1 lineations (polar data, 48 measurements, contour intervals 2σ); F: Undifferentiated L_2 lineations (polar data, 28 measurements, contour intervals 2σ); G: D_1 faults (polar data, 11 measurements, contour intervals 2σ); H: D_2 faults (polar data, 33 measurements, contour intervals 2σ).

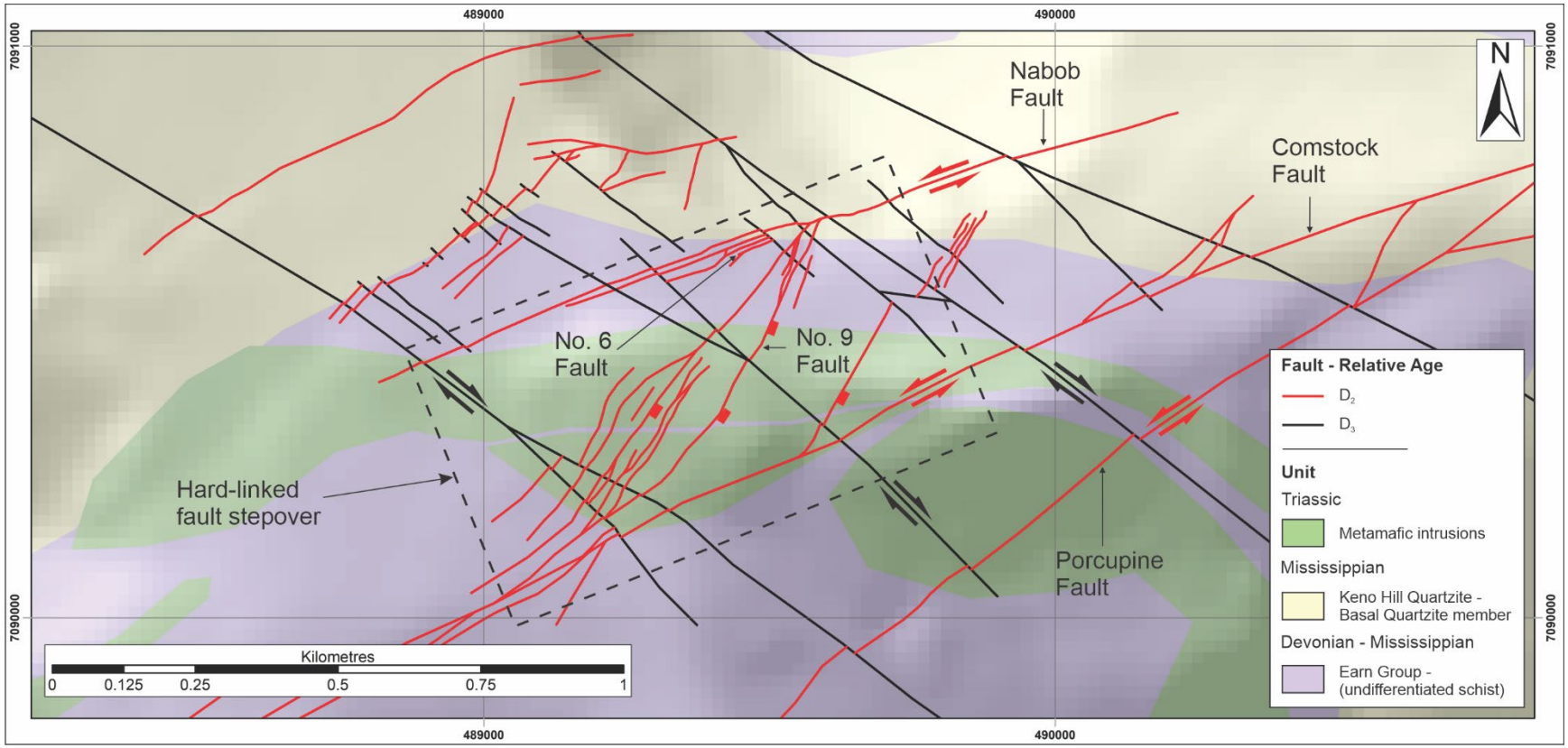

Figure 5.21: Simplified geological map of the 1st order Nabob and Comstock-Porcupine fault network on Keno Hill. First order faults are hard-linked by a set of 2nd order faults including the No.9 Fault. Fault network geometry is compiled from field observations by the author, Boyle (1965), and Murphy (1997). Overlaid on regional geological map of Alexco (2021).

A similar relationship between D_2 fault strike and D_2 fault kinematics is observed at the district-scale on Galena Hill. Measurements of 62 Pb-Zn (galena – sphalerite) mineralised faults and associated veins were measured across the summit of Galena Hill between the Sime and Bermingham deposits (Figure 5.22 to Figure 5.25). Orientation (stereographic) analysis of mineralised faults shows that faults have a bimodal distribution of orientations with fault sets striking ENE and NE to NNE (Figure 5.22A). These faults are subdivided into two sets: 1) ENE-stringing first order faults; and 2) NE to NNE-striking second or third order faults. Both fault sets are steep- to moderate-dipping. Comparison of the faults sets to measured vein width shows that first order, ENE-striking faults are associated with veins measuring less than 0.2 metres wide, while the second-third order, NE- to NNE-striking faults are associated with veins measuring 0.2 metres to greater than 1 metre wide (Figure 5.22A). Slickenlines (L_{2sl} or L_{2g}) were measured where possible, on the mineralised faults. A linear relationship is observed between fault strike and lineation plunge, whereby as fault strike varies from approximately 080° to 020°, lineation plunge increases from 15° to 80° (Figure 5.22B). This shows that as first order faults developed with a more NE strike or were linked by NE-striking second order structures, the faults moved from a regional strike-slip stress regime into local extension.

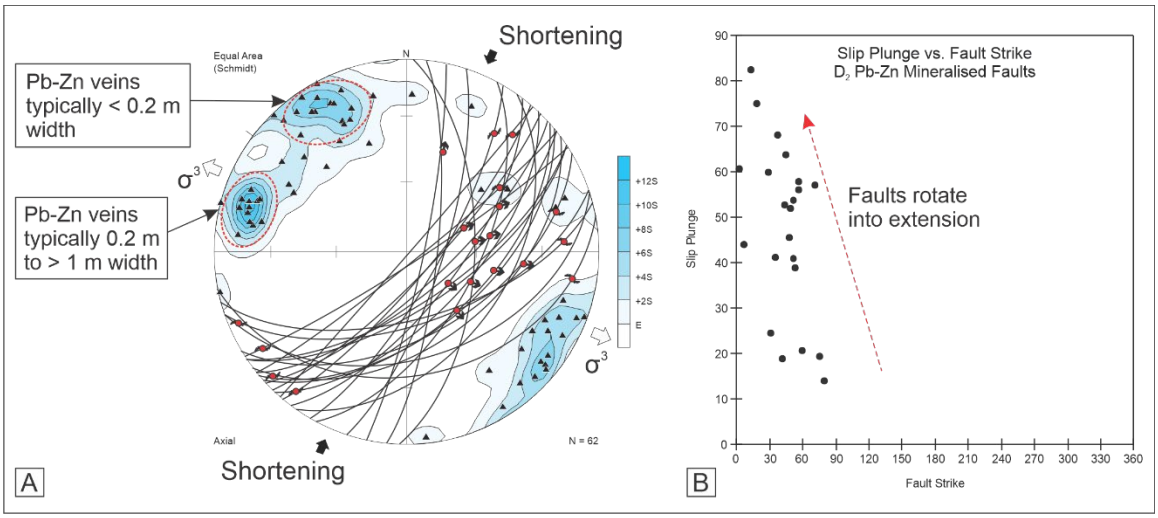

Figure 5.22: Fault strike and dilation on Galena Hill.

A: Density contoured, Lambert equal area lower hemisphere projection of combined measured Pb-Zn mineralised veins and faults on Galena Hill. Great circles represent measured D_2 faults and veins; Red symbols indicate measured slip vectors on faults; triangles and contours represent poles to veins and faults (polar data, 62 measurements, contour intervals 2σ); B: Scatter plot of D_2 fault strike against slickenline (L_{2sl}) plunge showing steepening of slip vector as fault strike varies from ENE to NNE.

A D_2 fault was mapped in detail along the base of the Onek open pit (Figure 5.26). This fault defines the footwall to the Onek vein and at this locality it is segmented at the outcrop-scale. Fault segments strike between 035° and 069°, with one segment striking 264°, and dips varying between 55° and 86°. The fault has an average orientation of 72°/064°. L_{2sl} slickenlines on fault segments plunge shallow NE and SW, to moderately east, and steps on slickensides indicate sinistral strike-slip to sinistral-normal oblique-slip fault movement. Fault segments are typically less than 10 metres in length and form an en echelon array. The fault segments are linked either by rotation of fault segment tips or are hard linked by subordinate faults that form either left or right stepping jogs and offset the Onek Fault by typically less than 0.5 metres.

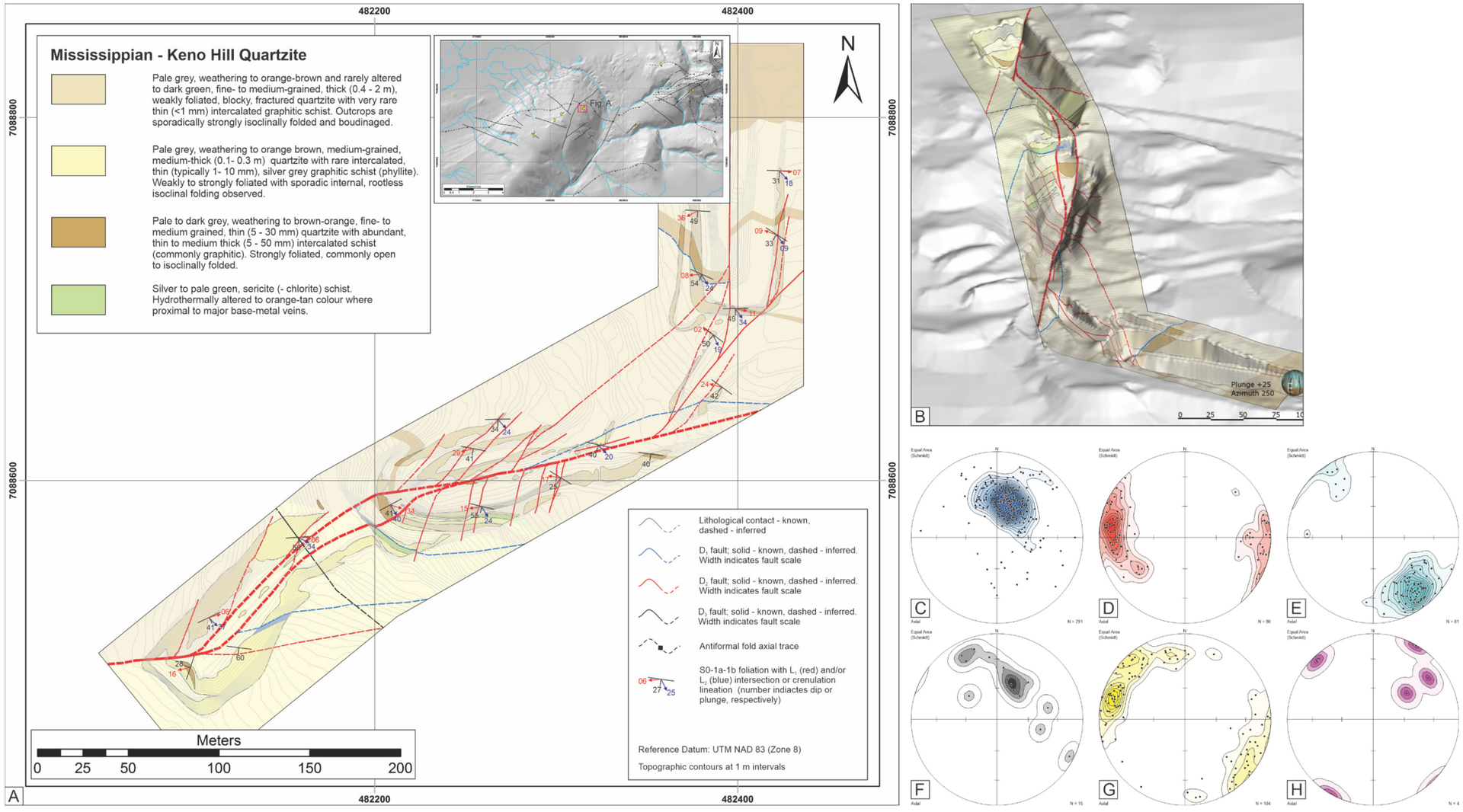

Figure 5.3: Simplified geological maps of the Sime open pit with associated foliation, lineation, and fault orientation data.

A: Simplified geological map with inset location map; B: Simplified geological map overlain on topographic data (inclined view). Figures C to H: Density contoured, Lambert equal area lower hemisphere projections of measured structural elements. C: $S_{0\text{-}1a\text{-}1b}$ foliations (polar data, 291 measurements, contour intervals 2σ); D: Undifferentiated L_1 lineations (polar data, 80 measurements, contour intervals 2σ); E: Undifferentiated L_2 lineations (polar data, 81 measurements, contour intervals 2σ); F: D_1 faults (polar data, 15 measurements, contour intervals 2σ); G: D_2 faults (polar data, 104 measurements, contour intervals 2σ); H: D_3 faults (polar data, 4 measurements, contour intervals 2σ).

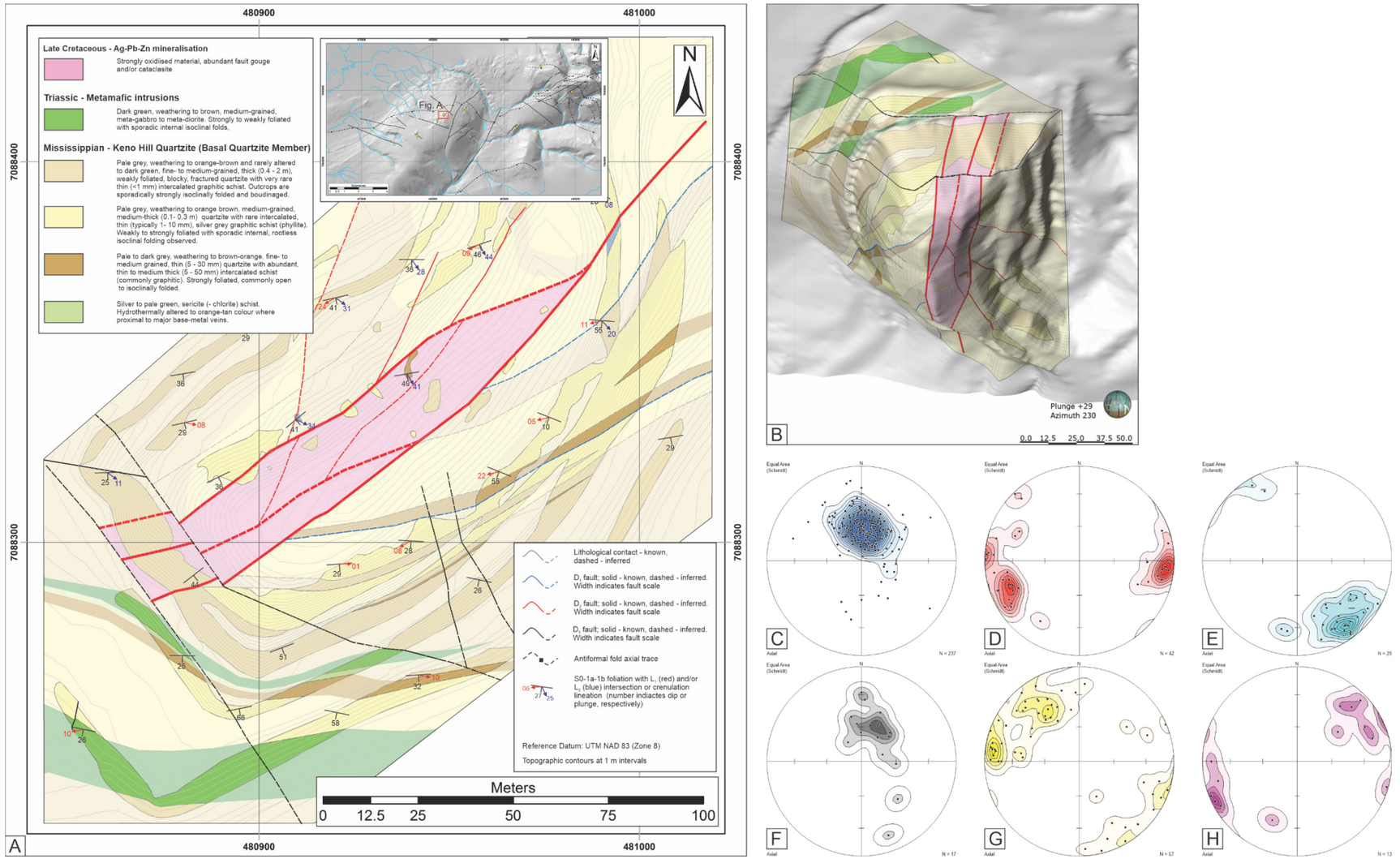

Figure 5.4: Simplified geological maps of the Calumet open pit with associated foliation, lineation, and fault orientation data.

A: Simplified geological map with inset location map; B: Simplified geological map overlain on topographic data (inclined view). Figures C to H: Density contoured, Lambert equal area lower hemisphere projections of measured structural elements. C: $S_{0\text{-}1a\text{-}1b}$ foliations (polar data, 237 measurements, contour intervals 2σ); D: Undifferentiated L_1 lineations (polar data, 42 measurements, contour intervals 2σ); E: Undifferentiated L_2 lineations (polar data, 29 measurements, contour intervals 2σ); F: D_1 faults (polar data, 17 measurements, contour intervals 2σ); G: D_2 faults (polar data, 57 measurements, contour intervals 2σ); H: D_3 faults (polar data, 13 measurements, contour intervals 2σ).

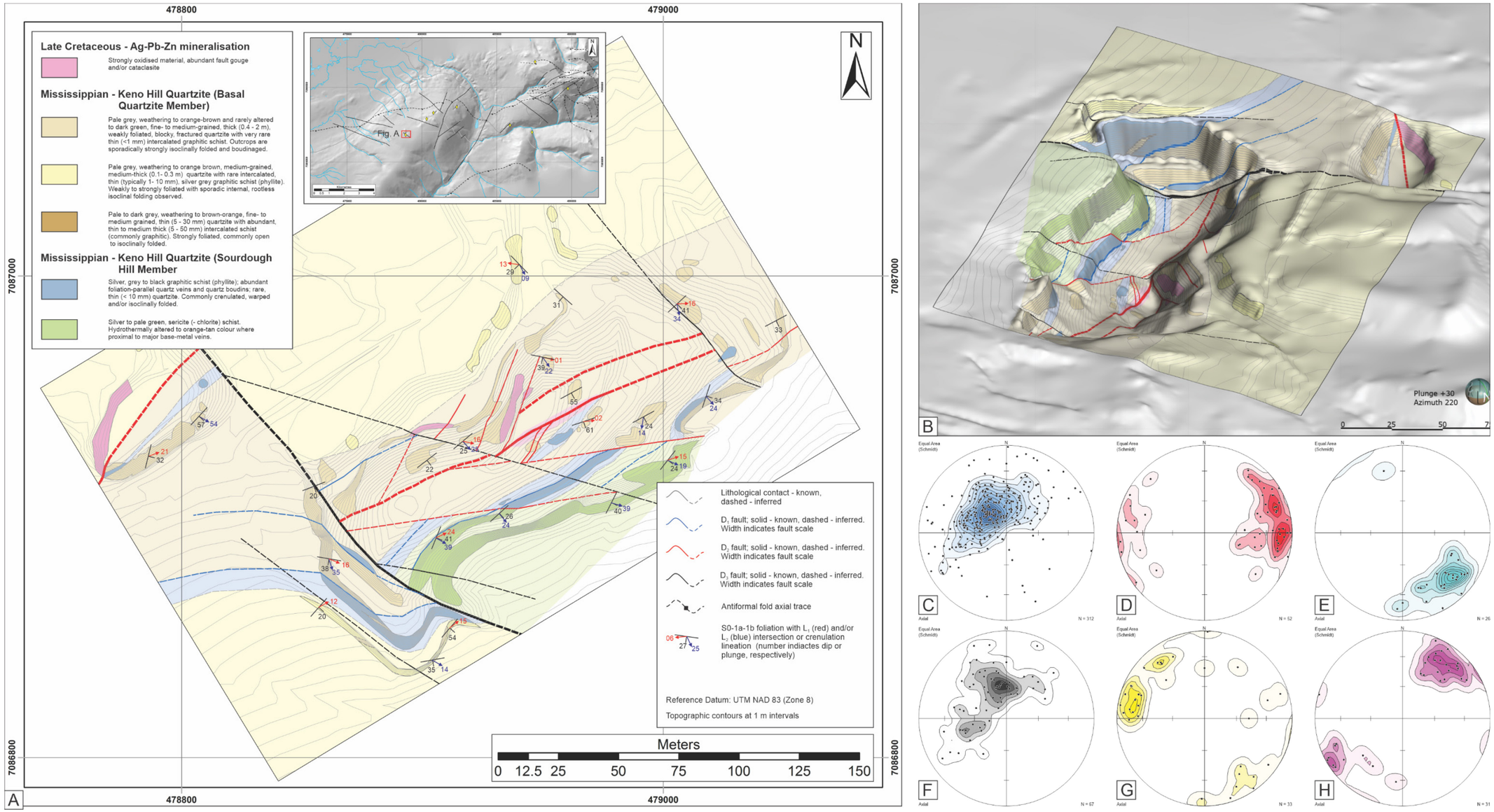

Figure 5.5: Simplified geological maps of the Bermingham open pit with associated foliation, lineation, and fault orientation data.

A: Simplified geological map with inset location map; B: Simplified geological map overlain on topographic data (inclined view). Figures C to H: Density contoured, Lambert equal area lower hemisphere projections of measured structural elements. C: $S_{0\text{-}1a\text{-}1b}$ foliations (polar data, 312 measurements, contour intervals 2σ); D: Undifferentiated L_1 lineations (polar data, 52 measurements, contour intervals 2σ); E: Undifferentiated L_2 lineations (polar data, 26 measurements, contour intervals 2σ); F: D_1 faults (polar data, 67 measurements, contour intervals 2σ); G: D_2 faults (polar data, 33 measurements, contour intervals 2σ); H: D_3 faults (polar data, 31 measurements, contour intervals 2σ).

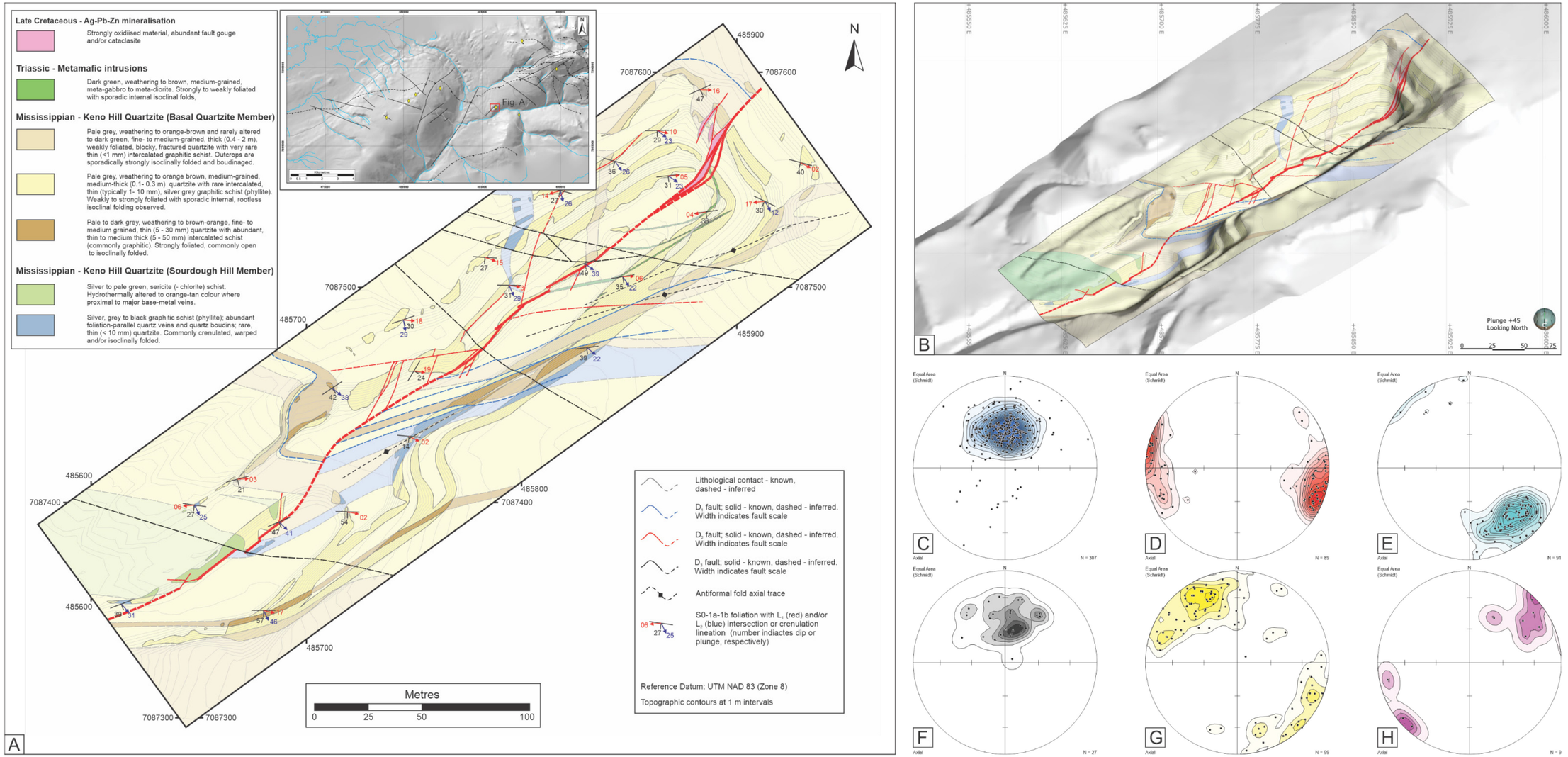

Figure 5.6: Simplified geological maps of the Onek open pit with associated foliation, lineation, and fault orientation data.

A: Simplified geological map with inset location map; B: Simplified geological map overlain on topographic data (inclined view). Figures C to H: Density contoured, Lambert equal area lower hemisphere projections of measured structural elements. C: $S_{0\text{-}1a\text{-}1b}$ foliations (polar data, 307 measurements, contour intervals 2σ); D: Undifferentiated L_1 lineations (polar data, 88 measurements, contour intervals 2σ); E: Undifferentiated L_2 lineations (polar data, 91 measurements, contour intervals 2σ); F: D_1 faults (polar data, 27 measurements, contour intervals 2σ); G: D_2 faults (polar data, 99 measurements, contour intervals 2σ); H: D_3 faults (polar data, 9 measurements, contour intervals 2σ).

D_2 Vein Characteristics

D_2 faults are commonly associated with Pb (galena) and Zn (sphalerite) ± carbonate (siderite) and Ag mineralised veins (Figure 5.17 and Figure 5.18). Local bladed calcite was observed at the Onek (Figure 5.27) and Wernecke deposits. This is indicative of boiling of mineralised fluids associated with rapid decompression (Etoh et al., 2002), likely as a result of fault dilation. At surface, Fe-Mn oxide alteration is common within veins, however altered margins within wall rock are typically narrow to absent. Vein widths range from less than one centimetre to greater than eight metres (i.e., at the Calumet open pit, and the 750-1 crosscut in the Bellekeno underground workings (Figure 5.28).

Figure 5.27: Cross-section view of bladed calcite on open fracture surface at the Onek open pit. Vein orientation 77°/217° (UTM 485713mE, 7087405mN).

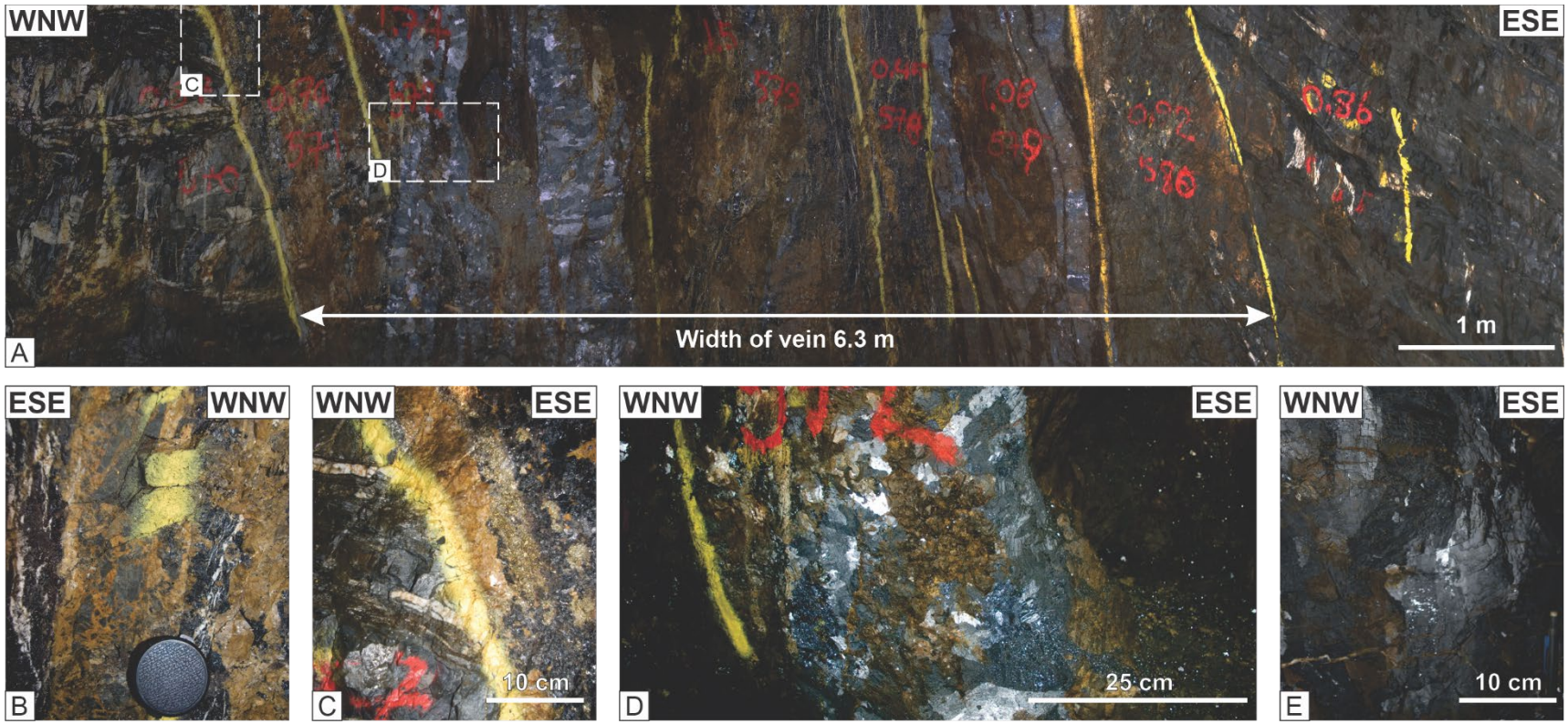

Figure 5.28: Panoramic photograph (A) of a cross-section through an Ag-Pb-Zn vein at the 750-1 cross-cut in the Bellekeno underground workings with close-up photographs (B to E) showing characteristics of vein.

B: Quartz-carbonate-supported breccia at vein margin; C: Siderite, pyrite, and galena at vein margin. Note lack of alteration in wall rock; D: Massive galena with siderite in vein centre; E: Massive euhedral galena in vein centre.

A vein paragenesis study by Hantelmann (2013) indicated that five different episodes of fluid injection/infiltration occurred into the Keno Hill fault system. This correlates with the locally large vein widths, and the observations of multiple overprinting D_2-related slickenline and slickenfibre lineations on a given fault that indicate multiple D_2 slip-events.

In addition to the common Pb-Zn ± Ag veins across the Keno Hill district, rare quartz veins were observed associated with D_2 faults. Thick (greater than 0.2 metres wide) quartz veins were only observed in the east of the district on Keno Hill (in the No. 6 Fault trench at the summit of Keno Hill) and on Sourdough Hill at the Homestake prospect. Some evidence for D_2 associated quartz veining was also observed at the Lucky Queen deposit. Anecdotal evidence suggests that the quartz veins are associated with minor Au mineralisation. Scorodite ($FeAsO_4 \cdot 2H_2O$) and limonite ($FeO(OH) \cdot nH_2O$) alteration (supergene (paleo)weathering) is associated with the quartz veins. At the summit of Keno Hill quartz veining is spatially coincident with the footwall of the No. 6 Fault; however, it appears to be slightly discordant, and possibly truncated by the Ag-Pb-Zn-bearing No. 6 fault-associated vein. This suggests that quartz-Au mineralisation pre-dated Ag-Pb-Zn mineralisation but exploited the same structure. At the Homestake prospect, a wide (greater than one metre), extensional quartz vein is associated with a second order, NE-striking D_2 fault, and is associated with sulfosalts, including jamesonite ($Pb_4FeSb_6S_{14}$), a late-stage hydrothermal mineral commonly associated with Ag-Pb-Zn veins (Figure 5.29).

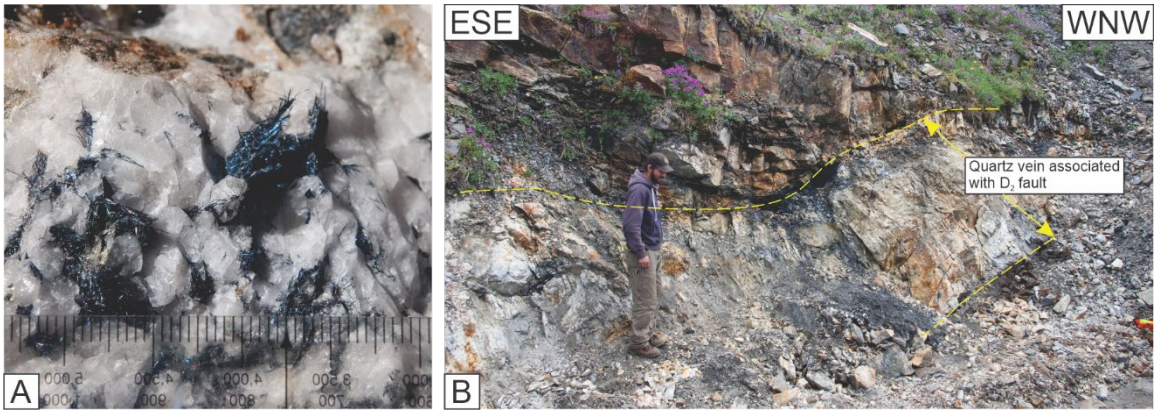

Figure 5.29: Quartz veins associated with D_2 faults at the Homestake prospect.

A: Jamesonite sulfosalts crystals observed within the large extensional quartz vein. B: Approximately 2 metre wide quartz ± Au vein parallel to, and coincident with the D_2 fault at the Homestake prospect (UTM 490237 mE, 7086900 mN).

Pb-Zn ± Ag veins exhibit evidence of fluid overpressure locally (Figure 5.30). Within the Sime open pit (Figure 5.23) a 0.1 metre wide vein, discordant to the $S_{0\text{-}1a\text{-}1b}$ foliation, was observed to intersect and become subparallel to a moderately SE-dipping, D_1 thrust fault. The vein was observed to run subparallel to the D_1 thrust to the north for five metres, and subsequently became discordant to foliation above the thrust fault. This suggests that as the D_2 vein/fault propagated upward and intersected the D_1 fault, the mechanical anisotropy was sufficient such that the vein was forced parallel to the D_1 fault and caused local dilation of the thrust.

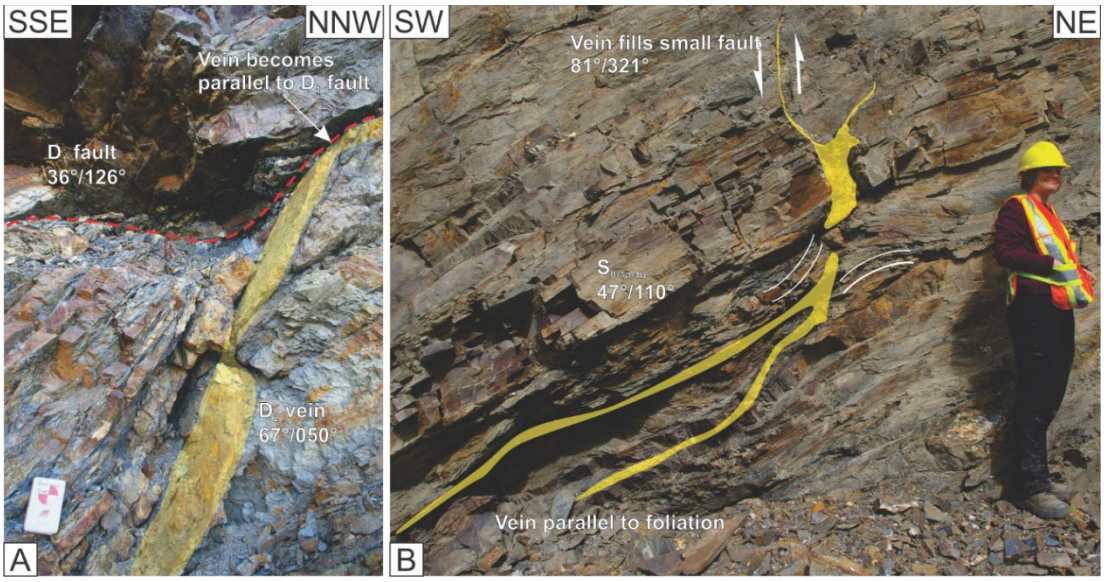

Figure 5.30: Examples of fluid overpressure-mineralisation at the Sime and Onek open pits.

A: D_2 vein discordant with foliation rotates to become subparallel to a D_1 thrust fault at the Sime open pit (UTM 482202mE, 7088572mN); B: $S_{0\text{-}1a\text{-}1b}$ -parallel vein becomes discordant to foliation coincident with small fault at the Onek open pit (UTM 485685mE, 7087425mN).

F_2 Fold Characteristics

D_2 deformation is associated with broad, open folding to warping (F_2) of the $S_{0\text{-}1a\text{-}1b}$ foliation. F_2 fold axes, L_2 intersection (L_{2int}), and crenulation lineations (L_{2cr}) plunge shallow SE with an average orientation of 25°/140° (Figure 5.31). F_2 fold axial surfaces are commonly steeply dipping to subvertical and striking NW or SE (with an average orientation of 80°/336°). While some variation in fold axial surface orientation exists, generally they appear compatible with a NE-shortening direction. At the mesoscale, F_2 folds have long (greater than 10 metre) wavelengths, low (less than 1 metre) amplitudes, and interlimb angles commonly greater than 130°, although locally (such as at the Homestake and Bermingham deposits) F_2 folds appear to tighten (Figure 5.32 and Figure 5.33). F_2 wavelength is dependant on lithology with schistose layers folding on shorter

wavelengths than quartzite or greenstone layers. Rare, east-west plunging slickenlines were observed on $S_{0\text{-}1a\text{-}1b}$ foliations and D_1 thrust faults that are not compatible with D_1 north to NW-directed thrust development. These slickenlines are considered to have formed during flexural slip along $S_{0\text{-}1a\text{-}1b}$ foliations during F_2 fold development.

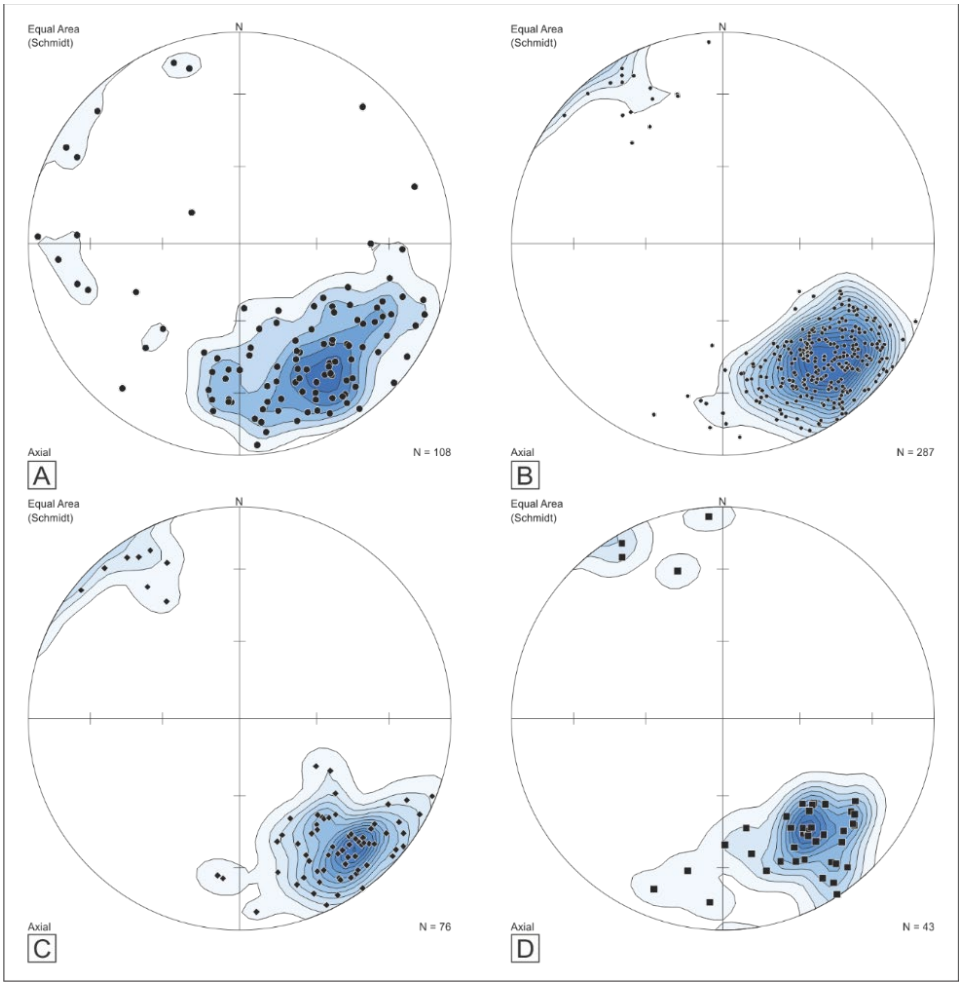

Figure 5.31: Lambert equal area lower hemisphere projections of F_2 fold axes, and L_2 lineation in the Keno Hill district.

A: Density contoured, all measured F_2 fold axes; peak density plunges 25°/144° (polar data, 108 measurements, contour intervals 2σ); B: Density contoured, all measured L_2 lineations; peak density plunges 29°/141° (polar data, 108 measurements, contour intervals 2σ); C: Density contoured, all measured S_1-S_2 intersection lineations (L_{2int}); peak density plunges 18°/135° (polar data, 76 measurements, contour intervals 2σ); D: Density contoured, all measured L_2 crenulation lineations (L_{2cr}); peak density plunges 33°/141° (polar data, 43 measurements, contour intervals 2σ).

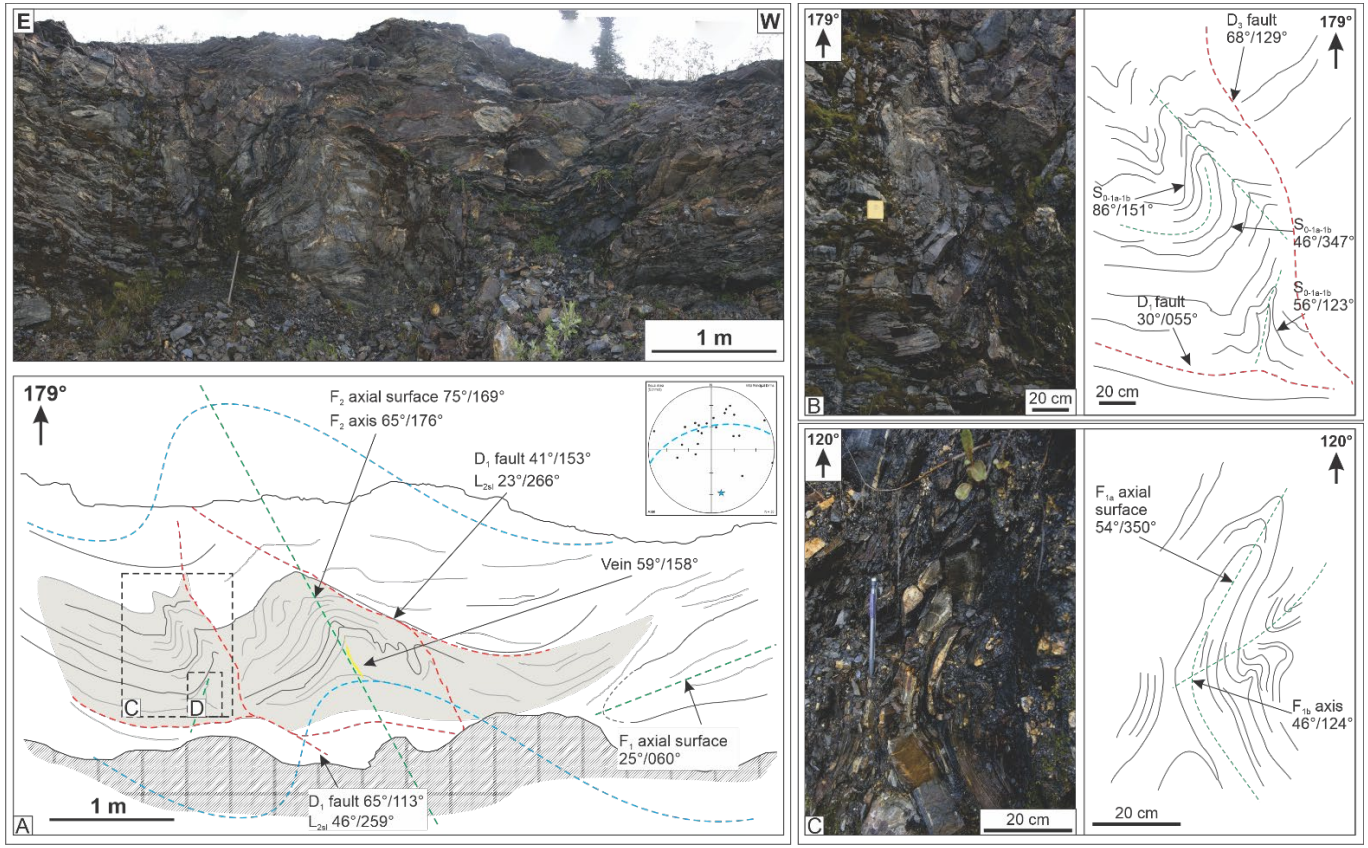

Figure 5.32: F_2 fold architecture at the Bermingham open pit (UTM: 478897 mE, 7086836 mN).

A: Photograph (top) and photograph interpretation (bottom) showing large, open, asymmetric, east-vergent F_2 fold with inset Lambert equal area lower hemisphere projection of $S_{0\text{-}1a\text{-}1b}$ foliations about fold axis. Dashed line on lower hemisphere project represents π-girdle, star indicates calculated fold axis; B: Photograph (left) and photograph interpretation (right) of F_2 fold truncated by D_3 fault; C: Photograph (left) and photograph interpretation (right) of F_{1a}-F_{1b} fold interference pattern in limb of F_2 fold. Blue dashed lines on photograph interpretations represent fold enveloping surfaces, green dashed lines indicate fold hinge surfaces, red dashed lines indicate faults.

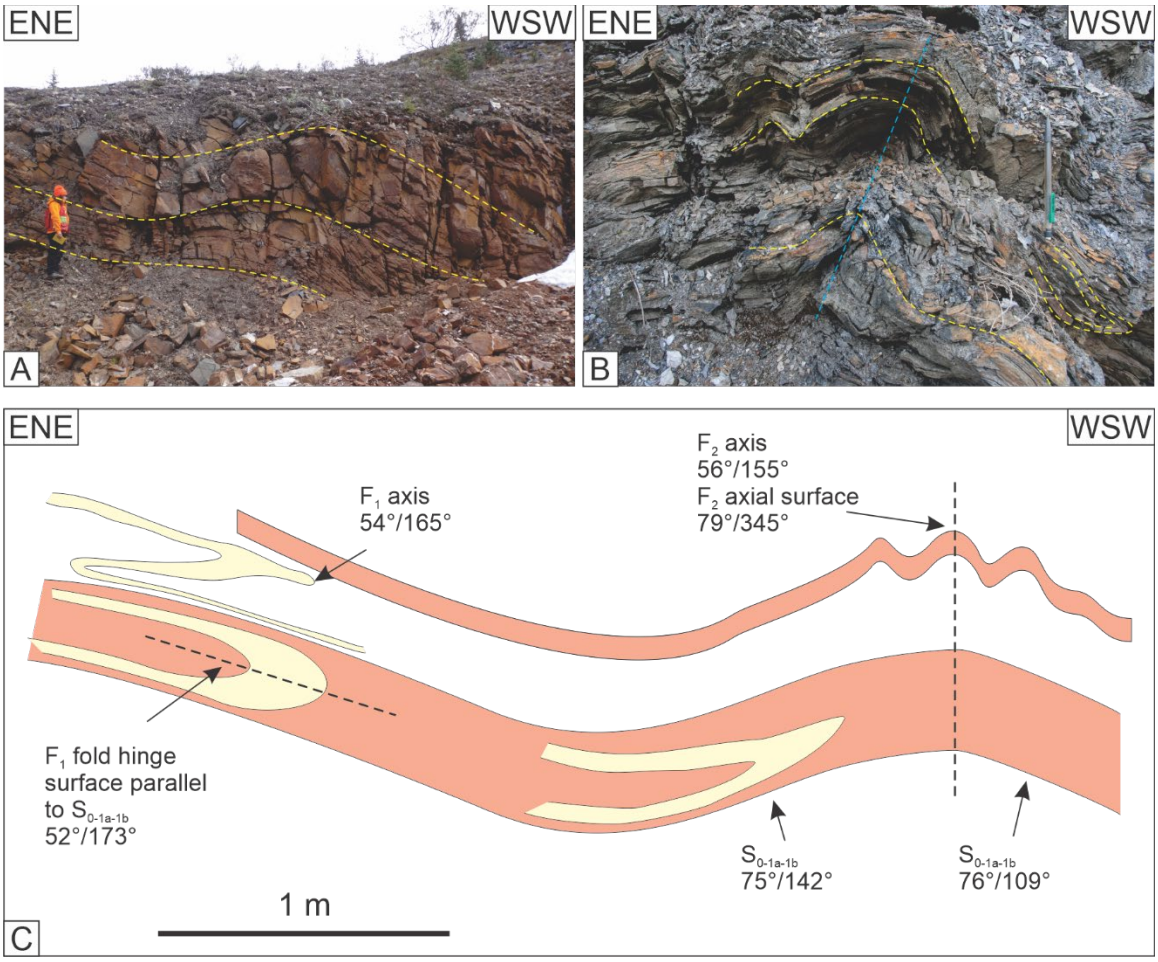

Figure 5.33: Examples of F_2 folding across the Keno Hill district.

A: Cross-section photograph through F_2 fold at Homestake prospect, with hinge surface 85°/330° and shallow, approximately south plunging axis in thick quartzite (UTM 489981mE, 7086774mN); B: F_2 fold at Onek deposit with fold axial surface 57°/343° and fold axis 05°/175°, parasitic crenulations observed about around fold hinge (UTM 485686mE, 7087356mN); C: Sketch of cross-section view through F_1-F_2 fold interference pattern in the South wall of the Silver King open pit (UTM 472063m E 7085483mN).

Regional variations in L_{1int} confirm the presence of SE-plunging F_2 folds; however, they do not accurately predict the location of F_2 fold hinges (Figure 5.34). $S_{0\text{-}1a\text{-}1b}$ foliation data is generally consistent across the district, except for within and proximal to the Bermingham deposit (Figure 5.35). Here foliations are rotated about a shallow SE-

plunging axis. This suggests that the Bermingham deposit is proximal to a regional-scale F_2 fold hinge.

Structural complexity is greatest proximal to the Bermingham open pit, with abundant F_{1a-b} fold, and F_2 folds, major lithological contacts present at surface and a late, D_3, cross-cutting fault observed. D_3 deformation will be discussed in Chapter 5.1.4, but it is thought likely that the inherent, pre-D_3, structural complexity at the Bermingham deposit likely promoted, and focussed the propagation of late, post-mineralisation deformation.

The localisation of boudin necks and F_2 folds may be important, but secondary to fault orientation and lithology, for focussing fluid flow during deformation. At the Homestake prospect D_2 associated veins were observed to exploit both boudin necks and open F_2 fold hinges (Figure 5.36).

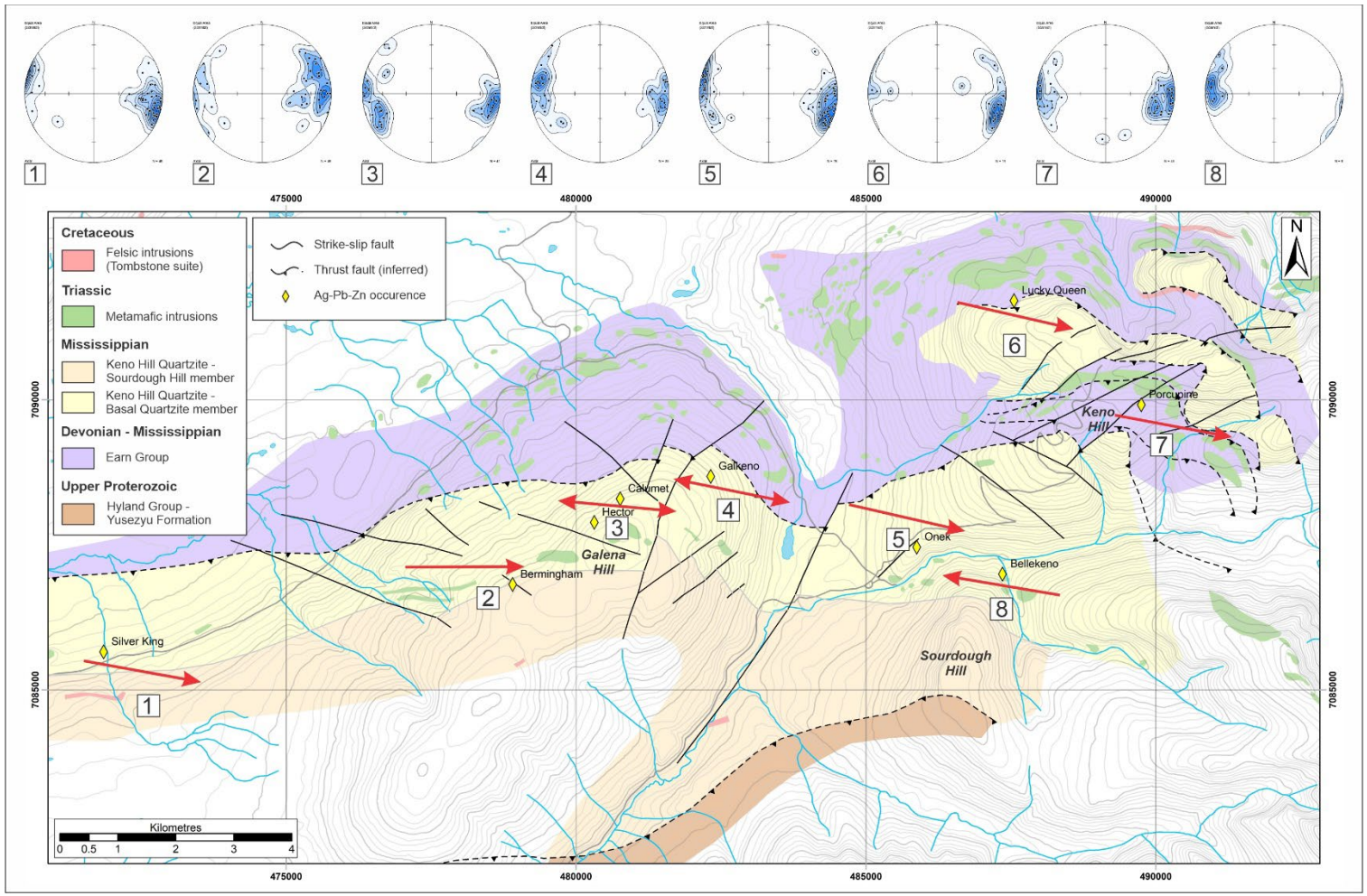

Figure 5.34: Variations in L_{1int} orientation across the Keno Hill district. Numbers refer to equivalent density contoured Lambert equal area lower hemisphere projection showing orientations of L_{1int} lineations. Red arrows show approximate azimuth for density peak. Base data from Alexco (2021).

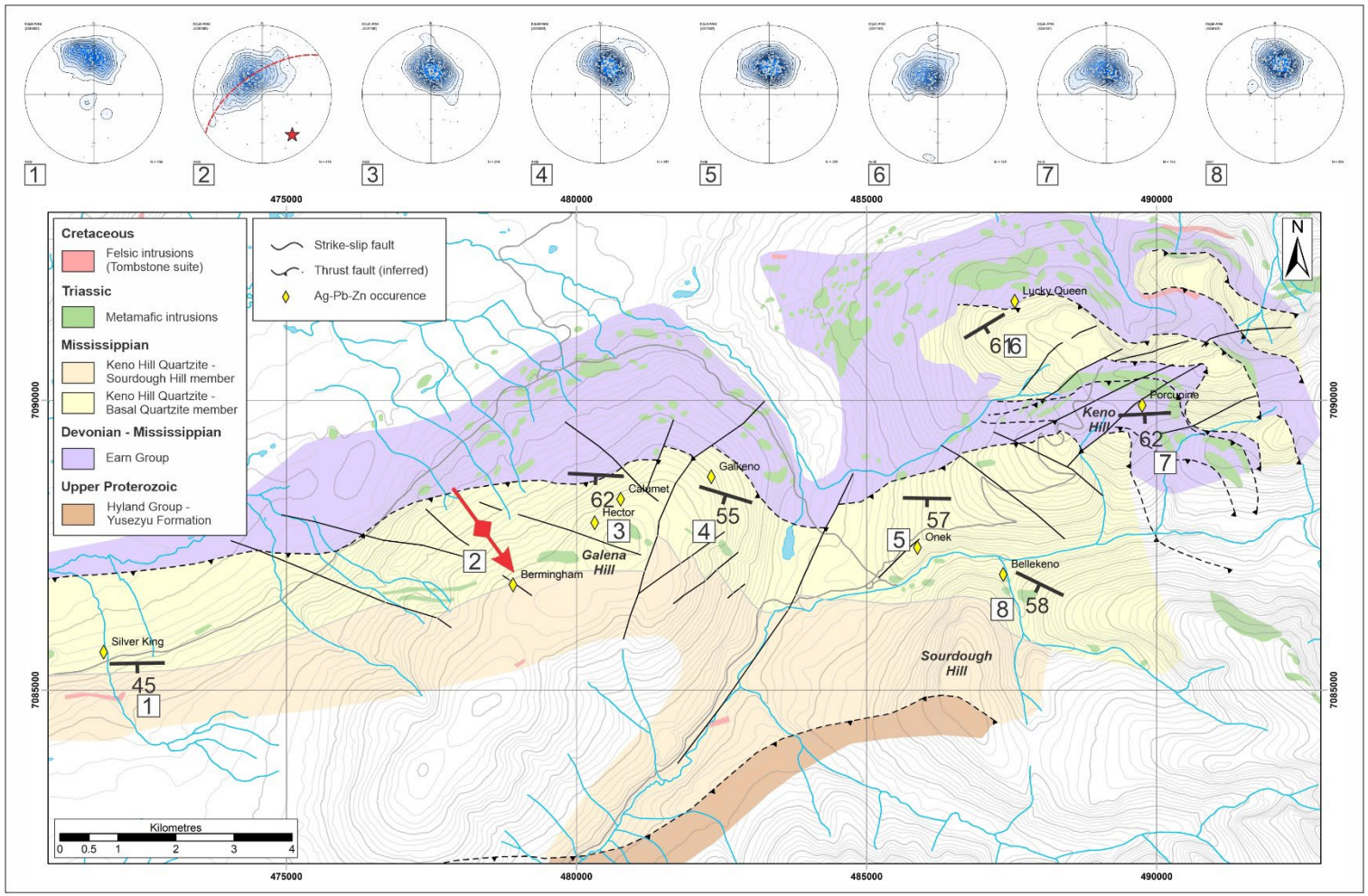

Figure 5.35: Variations in $S_{0\text{-}1a\text{-}1b}$ orientation across the Keno Hill district. Numbers refer to equivalent density contoured Lambert equal area lower hemisphere projection showing poles to $S_{0\text{-}1a\text{-}1b}$. Red arrow shows approximate location of regional F_2 fold axis. Base data from Alexco (2021).

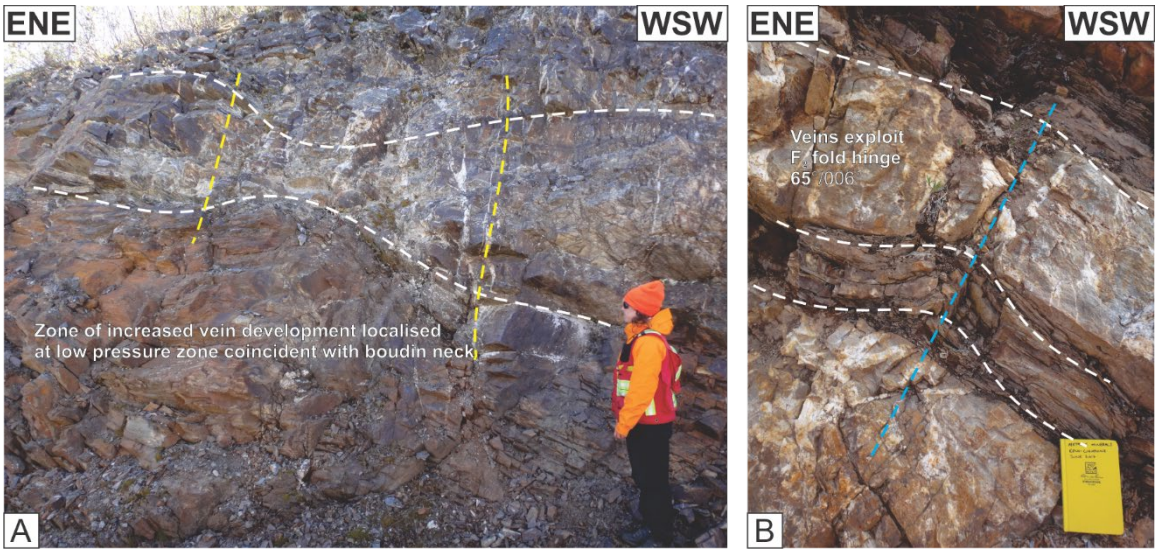

Figure 5.36: Photographs showing examples of veins exploiting boudin necks and fold axes.

A: Quartz veins focussed through boudin necks at the Homestake prospect (UTM 489860 mE, 7086862 mN); B: Quartz veins focused through small, open F_2 fold hinge at the Homestake prospect (UTM 489990 mE, 7086789 mN).

Controls on Ag-Pb-Zn Mineralisation

The spatial distribution of high-grade, high tonnage Ag-Pb-Zn mineralisation is controlled by the location and orientation of second order D_2 faults at left-stepping, first order fault step-overs (such as at the summit of Keno Hill), and the interaction of complex lithological geometry with D_2 faults, such as at the Bermingham deposit. However, high-grade Ag-Pb-Zn mineralisation is also controlled by structural complexity driven by D_2 fault interactions. The Hector-Calumet system is historically the most productive area in the district with over 96 M ounces Ag, 406 M pounds Pb, and 334 M pounds Zn recovered from the system between 1913 and 1990 (Cathro, 2006). Here, the Basal Quartzite member of the KHQ is prevalent and is consistently SSE-dipping with no major F_2 folds apparent. The main vein observed on the SW wall of the pit is very large.

Historic level plan data suggest that the Hector-Calumet area was host to a system of anastomosing veins. The Hector-Calumet system is discussed in detail in Chapter 5.2.5, but here it should be noted that the structural complexity is driven by D_2 fault interaction and Ag-Pb-Zn-mineralisation is controlled by the intersection of first and second order faults within a preferred host rock, rather than by fault-fold interactions. Modelled Ag grade shows that higher grades are more abundant along a NE-striking second order fault, although high-grade ore shoots have a steep SE-plunge that is coincident with the line of intersection between ENE-striking, first order faults, and NE-striking second order faults (Figure 5.37).

While orientation of the host faults is critical in forming dilatant, low pressure zones for the precipitation of Ag-Pb-Zn mineralisation, the role of rheology cannot be understated. Within the district large Pb-Zn ± Ag veins are almost exclusively associated with thick, competent quartzite layers of the Basal Quartzite member. Anecdotal evidence suggests that rare, significant Pb-Zn ± Ag veins are present towards the NE of the district, within greenstone units, although in this area there is a marked absence of quartzite and an abundance of schist. As such, in this area the greenstone would act in a brittle manner relative to the more ductile schist units and provide the required rheological contrast for Ag-Pb-Zn precipitation.

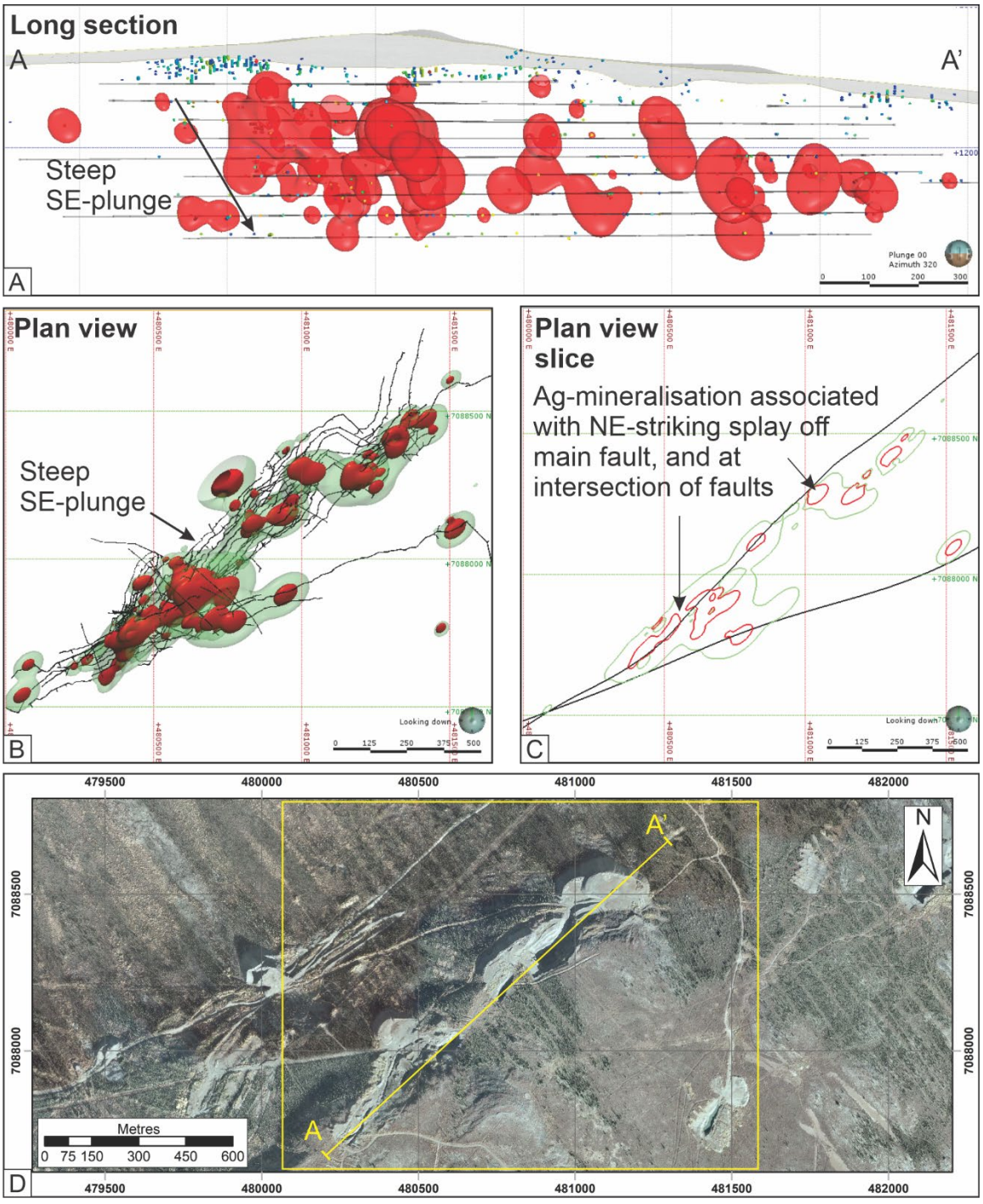

Figure 5.37. Anisotropic model of Ag grade at the Calumet mine shows steep SE plunge to high-grade zones (A), with grade highest along a NE-striking splay fault and at intersection of faults (B and C). Grade isoshells: Green > 400 g/t Ag; Red > 600 g/t Ag. D: Location map showing line of section for Figure A and plan view area of Figures B and C.

Pb-Zn ± Ag veins are in general thickest within the Basal Quartzite member (Boyle, 1965), and are narrower up-stratigraphic section as rocks become more intercalated with schist in the Sourdough member (McOnie and Read, 2009). Seymour Isles (personal communication, June 1, 2016) noted that veins deflect and become more shallowly dipping across more schistose horizons in the Bellekeno underground workings. No significant mineralisation is present in the schistose and phyllitic rocks of the overthrust Yusezyu Formation, above the Robert Service Thrust (A. McOnie personal communication, June 18, 2009). D_2 faults and their associated veins are highly oblique to, crosscut, and offset D_1 deformation fabrics, faults, and shear zones; kinematics of D_1 and D_2 deformation are not compatible, as such it is clear that D_2 associated Ag-Pb-Zn mineralisation post-dated D_1 deformation. Because mineralisation post-dated the D_1 Robert Service Thrust, the rheology of the schist and a mechanical anisotropy due to alignment of platy minerals oblique to fluid flow is expected to have impeded fluid propagation in the finer grained, platy mineral-rich rocks (Gudmundsson, 2001).

5.1.4 Post-Ag-Pb-Zn-Mineralisation (D_3)

D_3 Fault Characteristics and Geometry

Post-mineralisation deformation (D_3) is characterised by brittle fault development. D_3 faults are typically linear, laterally continuous, SE- to locally south-striking, steep SW- to NE-dipping, unmineralised faults (Figure 5.38A). Major (first order) D_3 faults have a regular spacing of between 400 and 800 metres across the district. D_3 faults are

orthogonal to first order D_2 faults. This indicates that D_2 and D_3 faults are not kinematically compatible, and as such represent discrete phases of deformation.

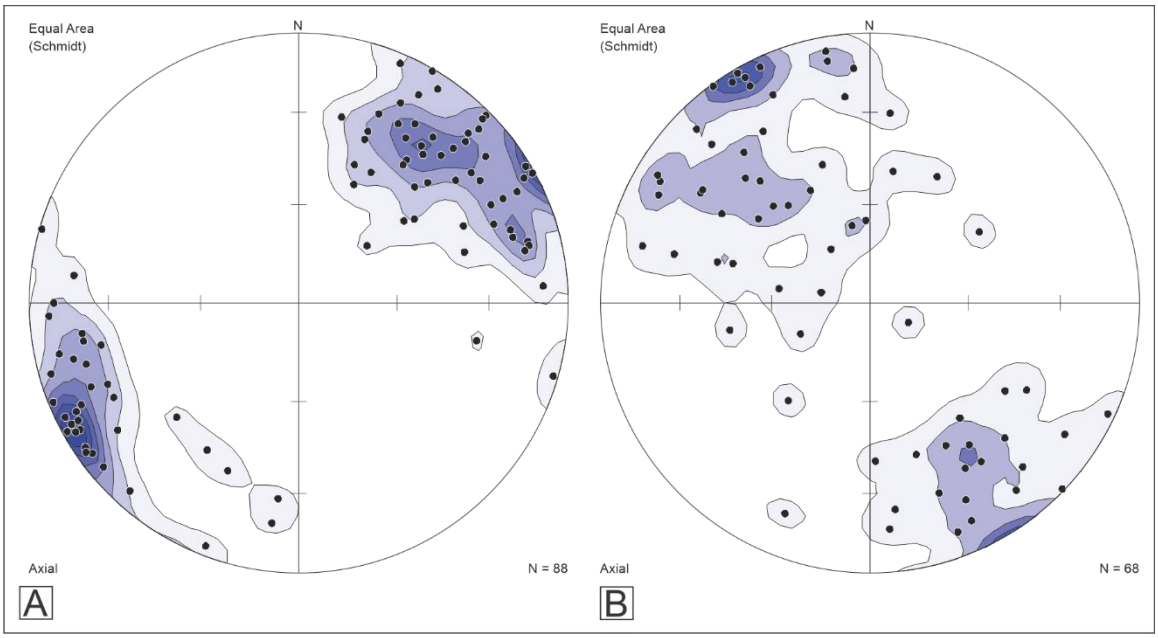

Figure 5.38: Lambert equal area lower hemisphere projections of D_3 faults and L_{3sl} lineations in the Keno Hill district.

A: Density contoured, poles to planes of all measured D_3 faults; peak densities have dip/strike of 86°/331° and 63°/129° (polar data, 88 measurements, contour intervals 2σ); B: Density contoured, all measured L_3 lineations (slickenlines); peak density plunges 04°/329° (polar data, 68 measurements, contour intervals 2σ).

Kinematic indicators associated with D_3 faults comprise slickenlines, slickenfibres, and steps on slickensides indicating fault movement. In addition, offset markers, such as Pb-Zn ± Ag mineralised veins, cataclastic or gouge fabrics, and rotation of foliations into D_3 faults are observed locally across the district. Lineations are moderate to shallow, NW- to SE-plunging (Figure 5.38B). Steps associated with lineations on individual fault surfaces can give ambiguous fault slip vectors and fault surfaces commonly preserve multiple

orientations of slickenline that is indicative of multiple slip events, however in general steps indicate dextral strike-slip to dextral-normal oblique-slip kinematics. Locally, D_1 and D_2 faults show lineations that are incompatible with their interpreted movement and associated stress-regime, but are compatible with D_3 movement, providing evidence of reactivation of D_1 and D_2 structures during D_3 deformation.

D_3 faults are observed across the district with faults of varying scales recorded along Galena Creek and in the Silver King open pit to the west, in the Bermingham, Hector, Calumet, and Sime open pits on Galena Hill, at the Onek open pit, and Signpost trenches on Keno Hill, and at the Bellekeno and Ram deposits and Homestake prospect on Sourdough Hill.

At the Silver King deposit, a D_3 fault offsets a Pb-mineralised vein and is characterised by a 0.3 metre wide zone of strong Fe-oxide alteration. Towards the NE margin of the Bermingham open pit, a D_3 fault is characterised by a highly polished, slickensided surface, while in the Hector open pit a large D_3 fault is characterised by brecciation of wall rock. Along the Bellekeno East access drive, small D_3 faults were observed that are associated with quartz-supported breccia. Breccia zones and associated veins commonly widen along steeper dipping segments of faults indicating an element of normal, dip-slip movement (Figure 5.39).

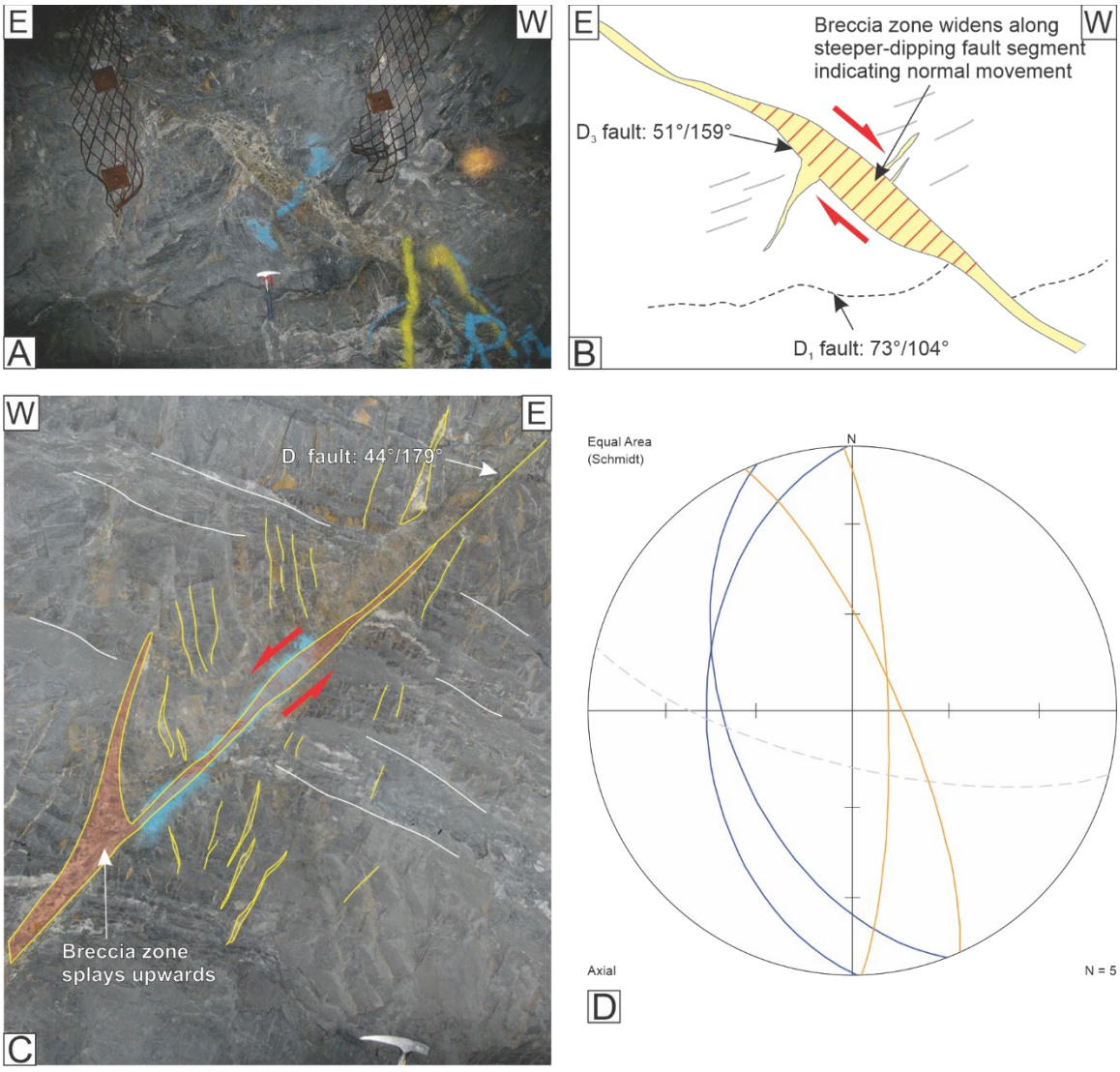

Figure 5.39: Example of a D_3 fault measured in both north and south walls of the Bellekeno East mine access drive.

A: Photograph and photograph interpretation (B) of D_3 fault with quartz-supported breccia in south wall of Bellekeno East access drive (135 m from access drive portal; C: Photograph of D_3 fault with splaying breccia zone in north wall of Bellekeno East access drive (140 m from access portal); D: Lambert equal area lower hemisphere projection of principal D_3 fault (blue great circles), D_1 fault (grey dashed great circle), and vein (orange great circles) orientations (polar data, 5 measurements).

D_3 faults offset Pb-Zn ± Ag-mineralised veins with an apparent dextral strike separation in plan view. The best observed example of a D_3 fault is in the Bermingham open pit where the NW-striking, Mastiff Fault (84°/303°) has slickenlines oriented 36°/301°, and steps indicating dextral-normal oblique-slip kinematics. It is characterised by a wide (greater than two metre) zone of gouge and breccia (Figure 5.40A). The fault transects the Bermingham open pit along its southwestern margin and appears to truncate Pb-Zn ± Ag mineralisation (Figure 5.25). In the south wall of the pit, a marked change in lithology is observed across the fault, from dominantly sericite schist in the footwall to graphitic schist in the hangingwall. Eighty to 100 metres NW along strike of the Mastiff Fault is a small open pit (the Bermingham West open pit). At the western end of this pit is a 0.2 to 0.3 metre wide, D_2, Pb-mineralised vein with strong sericite alteration in the footwall. It is likely that this vein is associated with veining in the main Bermingham pit and has been offset with dextral strike separation along the Mastiff Fault (Figure 5.25).

In addition, along the NE wall of the Bermingham pit, a highly polished D_3 fault surface was observed (Figure 5.40B and C). A pair of slickenlines were observed on this fault surface with steps indicating dextral-normal oblique-slip movement, and dextral strike-slip movement. It is likely that this fault offsets or D_2-mineralised structures at the Bermingham deposit, however the amount of offset is not known.

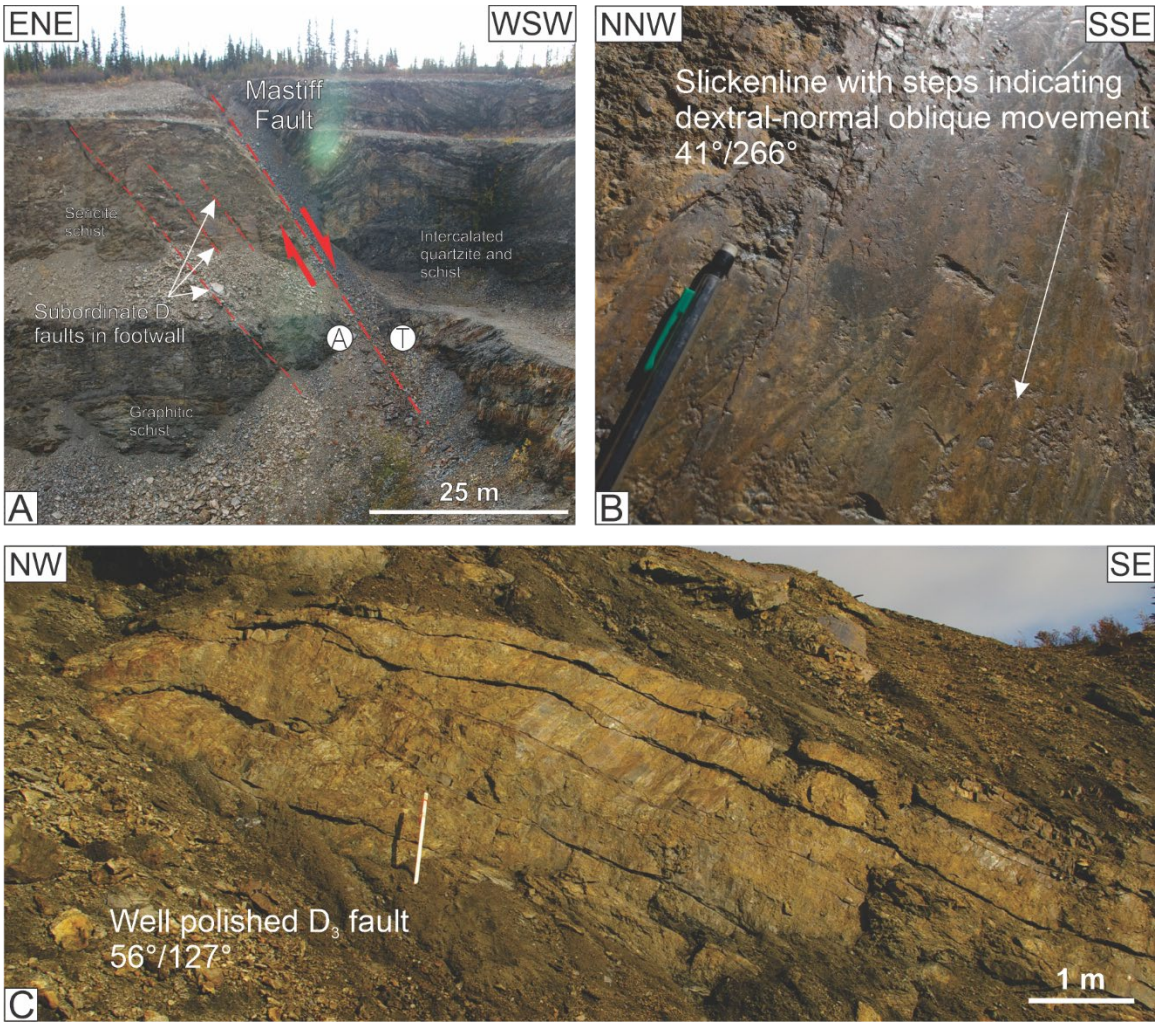

Figure 5.40: Photographs showing D_3 fault characteristics in the Bermingham open pit.

A: Photograph of the Mastiff Fault at the south corner of the Bermingham open pit (UTM 478909 mE, 7086863 mN); B: Photograph of slickenlines with steps on well-polished D_3 fault surface (C) indicating dextral-normal oblique movement along fault in the NE wall of the Bermingham open pit (UTM 479031 mE, 7086981 mN).

D_3 faults are parallel to, and show compatible kinematics with, the major, regional-scale, Cordillera-parallel Tintina Fault (Gabrielse et al., 2006), and as such are considered to be associated with the same to Eocene deformation event.

F_3 Fold Characteristics

D_3 associated folding (F_3) is rare, however, in the hangingwall of the Mastiff Fault in the Bermingham open pit F_3 folding was observed. At this locality F_3 folds plunge shallow SE with axes subparallel to the strike of the Mastiff Fault, and upright axial surfaces (Figure 5.41). Folds are developed exclusively in the carbonaceous to graphitic schist in the fault hangingwall and are polyclinal to chevron in shape (Figure 5.42). F_3 folds were uniquely observed at this locality, and as such are inferred to represent a roll-over antiform that developed as a direct result of the interaction between normal movement along the D_3 Mastiff Fault and the graphitic schist.

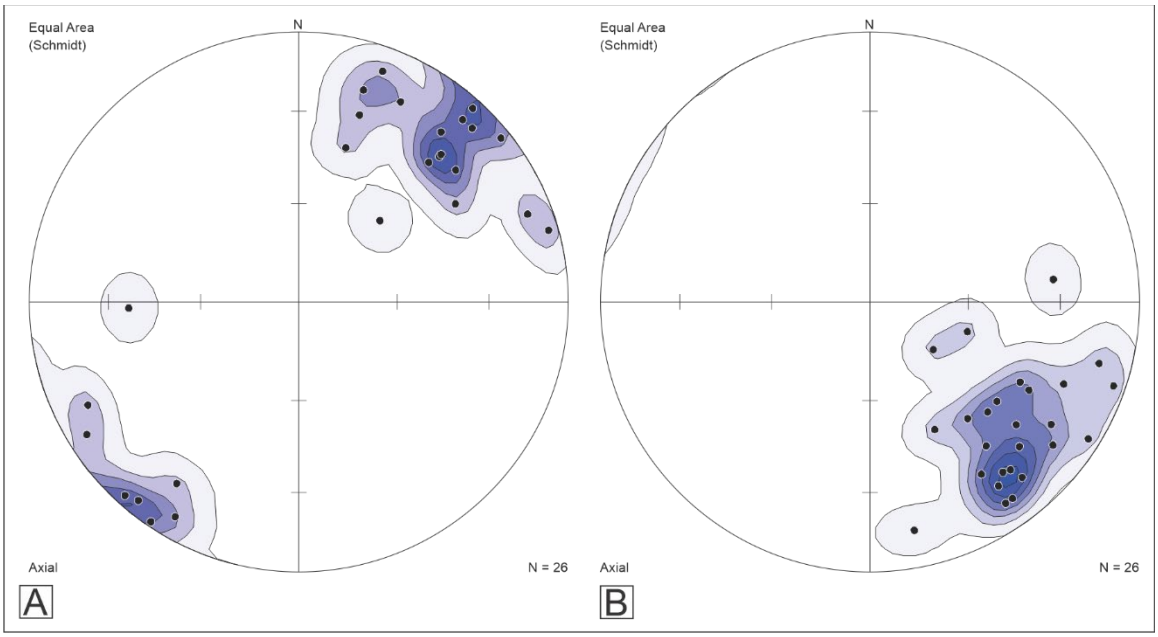

Figure 5.41: Lambert equal area lower hemisphere projections of F_3 fold axial surfaces, and F_3 fold axes in the Bermingham deposit.

A: Density contoured, poles to planes of all measured F_3 fold axial surfaces; peak density has dip/strike of 65°/134° (polar data, 26 measurements, contour intervals 2σ); B: Density contoured, all measured F_3 fold axes; peak density plunges 18°/141° (polar data, 108 measurements, contour intervals 2σ).

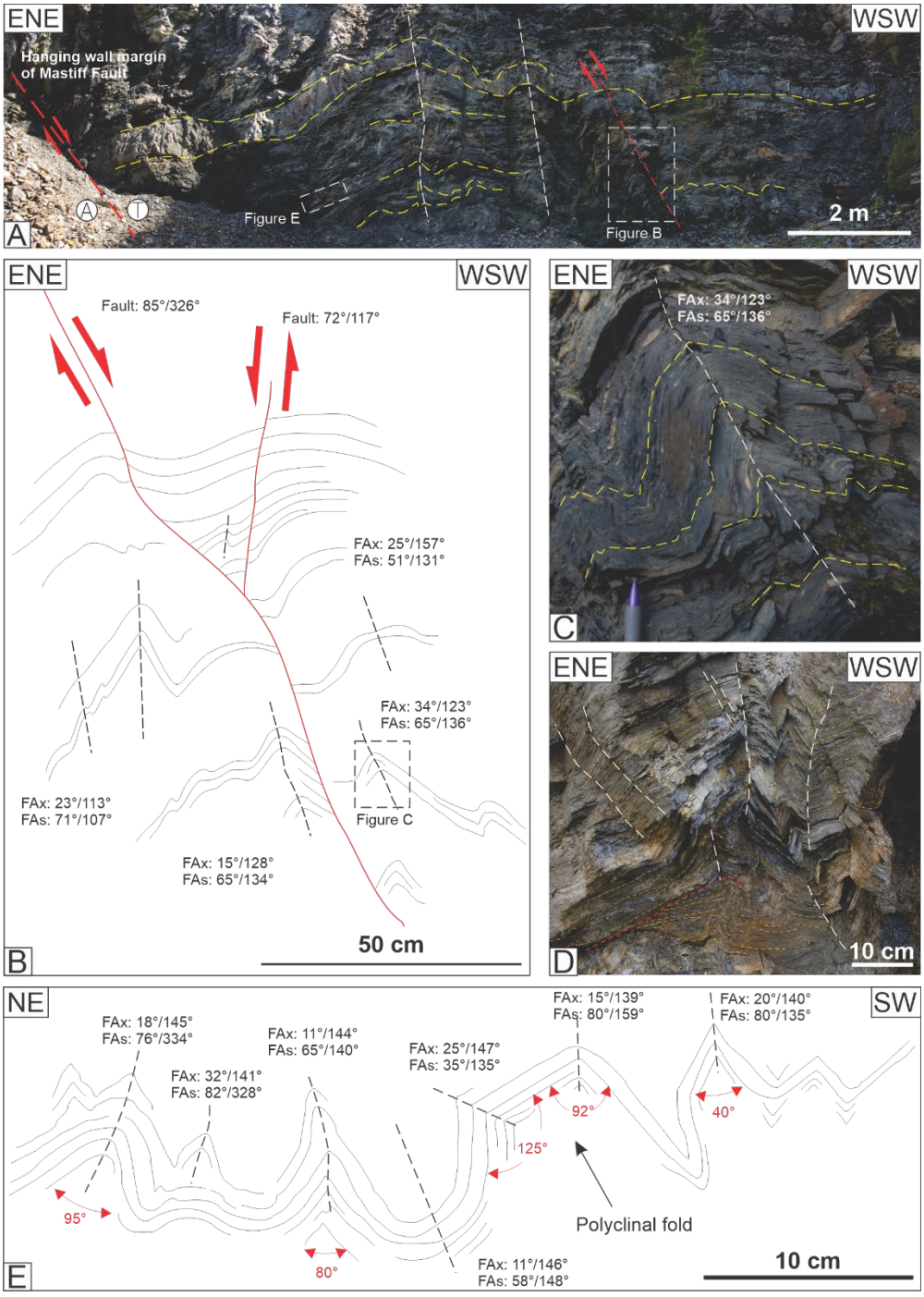

Figure 5.42: Characteristics of F_3 folds in the Bermingham deposit.

A: Photograph of F_3 folded graphitic schist and rare quartzite in hanging wall of the Mastiff Fault (UTM 478902 mE, 7086857 mN); B: Sketch of interaction between F_3 chevron folds and D_3 normal faults (UTM 478900 mE, 7086853 mN); C: Photograph of polyclinal fold in graphitic schist (UTM 478900 mE, 7086853 mN); D: Photograph of polyclinal and chevron folds in graphitic schist (UTM 4786981 mE, 7086981); E: Sketch of F_3 fold geometry in hangingwall of Mastiff Fault showing interlimb angles (UTM 4786981 mE, 7086981). FAx: Fold axis; FAs: Fold axial surface.

5.2 2D and 3D Interpretation of Structural Geology

District- and regional-scale interpretations of fault architecture were completed using digital elevation data (DEM) supplied by Alexco and airborne magnetic data supplied by Alexco, Metallic Minerals, and publicly available data acquired from the Yukon Geological Survey. The interpretations of airborne magnetic data were based on the first vertical derivative (1VD) datasets supplied.

The 2D interpretations of airborne magnetic and DEM data were iterative with a program of 3D modelling of vein architecture in the eastern and central portions of Galena Hill. The 3D modelling program used the 2D interpretations as a guide along with borehole assay data, surface mapping data acquired by the author, historic mine infrastructure data (i.e., drift, ramp, and rare stope geometry), and historic level plan maps and cross-sections supplied by Alexco.

5.2.1 District-Scale Interpretation of Airborne Magnetic Data

The district-scale 2D interpretation of magnetic data broadly agrees with field observations on structural relationships. Three deformational events were identified in the interpretation that correspond with D_1 (pre-Ag-Pb-Zn-mineralisation), D_2 (syn-Ag-Pb-Zn-mineralisation), and D_3 (post-Ag-Pb-Zn-mineralisation) fault development in the district. Faults were classified by age and order based on the criteria outlined in

Magnetic Form Line Interpretation

Prior to the fault interpretation a form line interpretation was completed. Tectono-stratigraphic form lines were drawn using the 1VD data (Figure 5.43). Form lines trace the geometry of stratigraphy within metasedimentary rocks, the tectonic fabric, or the internal fabric (foliation) within intrusive rocks. Discontinuities between form lines, particularly stratigraphic form lines (e.g., intersecting form lines), highlight structures (faults, folds), unconformities, or intrusive contacts. Interpreted form lines vary in trend from NE to east-west trending, and as such are considered to represent a combination of stratigraphic geometry and the geometry of a tectonic fabric associated with D_2 deformation. In broad terms the form lines are more uniformly east-west- to ENE-trending at the eastern and western limits of the study area, while more variation in trend is apparent in the central part of the area. The form lines appear to define a lazy-s-shaped, sigmoidal lens centred on the Keno Hill area. Given the observed sinistral strike-slip to sinistral-normal oblique-slip kinematics on D_2 faults in the study area, the sigmoidal lens defined by the form lines is interpreted to represent a district-scale releasing bend (Figure 5.43).

Table 5.3: Characteristics of faults defined in the interpretation of airborne magnetic data

Fault Age	Fault Order	Geophysical Signature	Characteristics	Kinematics
D_1	1	Short, to moderate length, typically wide magnetic low, defining a single fault or fault segment.	Major, linear to curvilinear faults. Offset or truncated by D_2 and D_3 faults.	Reverse
	2	Typically, short length, moderate to narrow width, subtle magnetic low, defining a single fault or fault segment.	Linear to curvilinear faults. Offset or truncated by D_2 and D_3 faults.	Reverse
	3	Short length, narrow, subtle magnetic low, defining a single fault or fault segment.	Minor curvilinear faults. Offset or truncated by D_3 and D_3 faults. Rarely folded about an east-west fold axis.	Reverse
D_2	1	Linear, segmented, wide magnetic low, defining a single fault or fault segment.	Major, ENE-, to NNE-trending, linear faults. Truncate or offset D_1 faults. Offset or truncated by D_3 faults.	Sinistral-Normal
	2	Linear, to curvilinear, moderate length, moderate width magnetic low, defining a single fault or fault segment. May form sigmoidal faults linking 1st order D_2 faults.	Moderate, ENE-, to NNE-trending, linear to curvilinear faults. Truncate or offset D_1 faults. Offset or truncated by D_3 faults.	Sinistral-Normal
	3	Typically, short, linear to curvilinear, narrow, rarely subtle, magnetic low, defining a single fault or fault segment. May form sigmoidal faults linking 1st and 2nd order D_2 faults.	Minor, ENE-, to NNE-trending, linear to curvilinear faults. Truncate or offset D_1 faults. Offset or truncated by D_3 faults.	Sinistral-Normal
D_3	1	Long, linear, typically wide magnetic low defining a single through-going fault that truncates and offsets magnetic high anomalies oblique to the fault.	Major, linear, NW-trending faults. Truncates or offsets D_1 and D_2 faults.	Dextral-Normal
	2	Moderate to rarely long, moderate to narrow width, commonly subtle magnetic low that defines a single fault that truncates and offsets magnetic high anomalies oblique to the fault.	Moderate linear, NW-trending faults. Truncates or offsets D_1 and D_2 faults. Forms a network with 1st order D_3 faults.	Dextral-Normal
	3	Short to moderate length, narrow, subtle magnetic low that defines a single fault that truncates and offsets magnetic high anomalies oblique to the fault.	Minor, linear, NW-trending faults. Truncates or offsets D_1 and D_2 faults. May link between 1st and 2nd order D_3 faults	Dextral-Normal

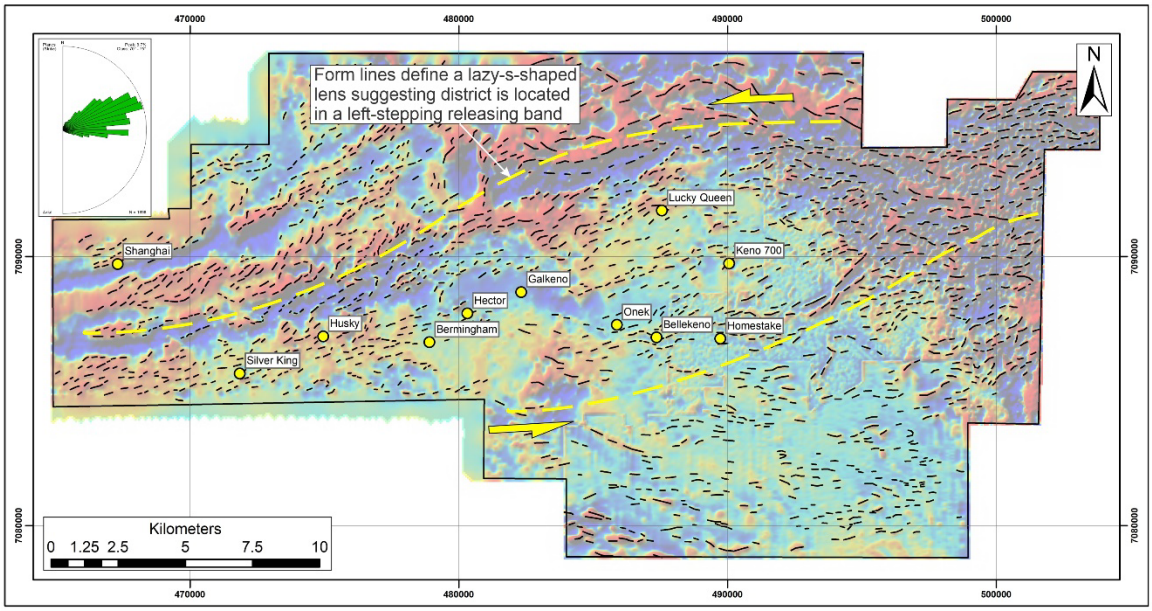

Figure 5.43: District-scale form line interpretation of 1VD data showing interpreted lazy-s-shaped restraining bend. Inset rose diagram showing trend of all interpreted form lines.

Airborne Magnetic Fault Interpretation

Faults were subdivided into three groups based on age and deformation style (Figure 5.44). The first group (D_1) is characterized as early, brittle-ductile faults and shear zones that typically trend east-west, and the second group (D_2) is characterized as a network of brittle faults that trend approximately ENE to NNE. The third group (D_3) is characterised as a network of typically regional-scale brittle faults that trend NW.

Field mapping of the district indicates that D_1 thrust faults are common throughout the area, are subparallel to the regional foliation, and dip shallowly south to SSE. In the airborne magnetic data, D_1 faults have a range in strike from 025° to 147° and length-weighted peaks striking 075° to 080° and 105° to 110° (Figure 5.44B). Given their

apparent abundance observed during field investigations, D_1 structures in the interpretation of magnetic data appear to be under-represented. Eighty D_1 fault segments were interpreted that range in length from approximately 300 to 4,700 metres. The under-representation of D_1 structures is likely due to the high angle of incidence between the data acquisition system and the shallow dip of the faults. It should also be noted that in some areas D_1 faults may be masked by the presence of cross-cutting D_2 and D_3 faults.

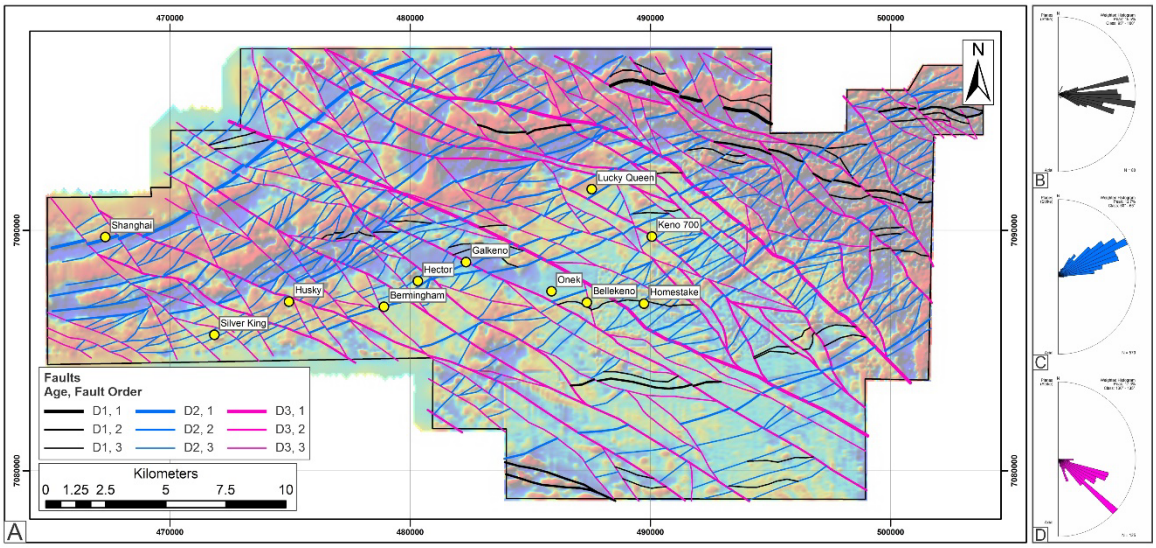

Figure 5.44: District-scale fault interpretation of 1VD data (A) with rose diagrams showing the trends of all interpreted D_1 (B), D_2 (C), and D_3 (D) faults.

Where identified, D_1 faults are characterised by weak to strong, segmented, ENE-, to ESE-trending, curvilinear, magnetic lows. Rarely, D_1 faults appear to be folded about an east-west trending axis that correlates with the mapped orientation of F_1 fold axes. As with the D_1 faults, F_1 fold axes appear to be under-represented in the data, with only 11 F_1 fold axes identified.

D_2 brittle faults were the most abundant structures (570 fault segments) identified in the interpretation. D_2 deformation produced a network of approximately ENE- to NNE-trending faults. Interpreted faults range in orientation from 013° to 093° with a length-weighted peak striking between 060° and 065° (Figure 5.44C). D_2 faults are characterised by weak to strong, linear to curvilinear, magnetic lows that are segmented by later, post-mineralisation D_3 faults. D_2 fault segments are short to moderate in length and range from approximately 250 metres to greater than 3,900 metres in length.

Overall, the spacing and distribution of D_2 faults is consistent across the study area; however, few D_2 structures are interpreted towards the south of the study area. Towards the south of the district, the lithology is dominated by rocks of the Keno Hill Quartzite and the Precambrian Yusezyu Formation. These rocks have a magnetic response that is subdued relative to the NE of the area where schistose rocks of the Earn Group dominate (Figure 5.45). As such, fault accuracy may be greater in areas dominated by Earn Group rocks, and fault frequency may, in reality, be greater than interpreted in areas dominated by the Keno Hill Quartzite and Yusezyu Formation. In areas with good fault definition, the spacing between first or second order faults ranges from approximately 800 to 1800 metres and increases to greater than 4300 metres in areas with a subdued magnetic response.

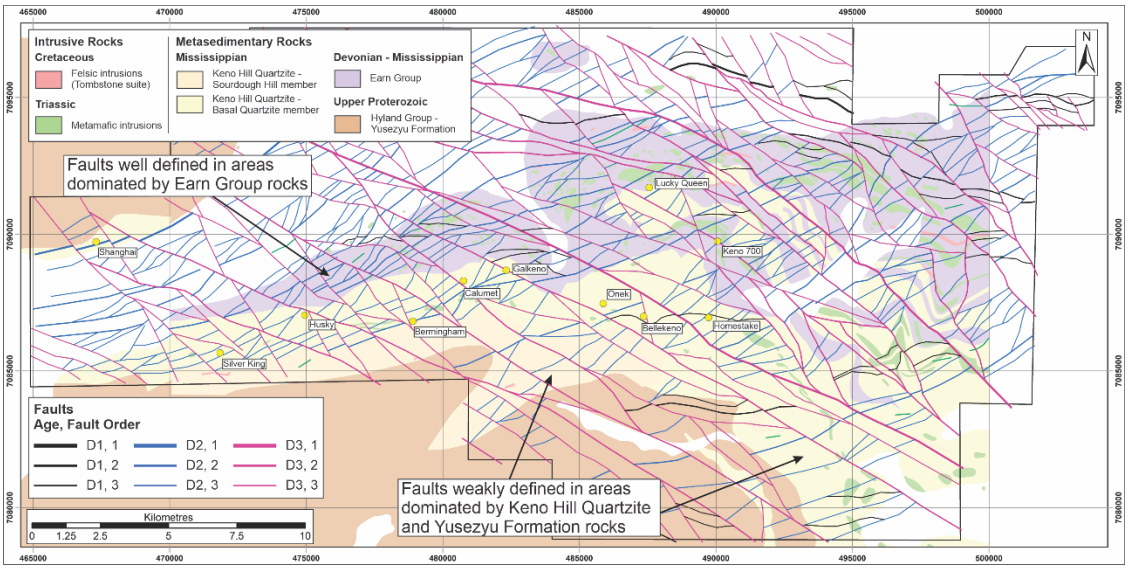

Figure 5.45: District-scale fault interpretation overlain on simplified geological map (combined from Murphy, 1997; and Alexco, 2021) showing variations in interpreted fault frequency dependant on underlying lithology.

D_3 faults are typically long, regional-scale faults that transect the study area and range in length from approximately 800 m to greater than 29.5 km. D_3 faults may appear as subtle magnetic lows but are characterised by sharp breaks between high magnetic anomalies. D_3 faults broadly trend NW-SE to NNW-SSE and range in trend between 013° and 177° with a length-weighted peak between 130° and 135° (Figure 5.44D). D_3 faults segment all D_1 and D_2 structures. D_3 structures typically offset D_1 and D_2 structures with a dextral strike-separation of less than 150 metres. This strike-separation correlates well with observations made on post-mineralisation faults during field studies.

In the study area, D_3 faults appear to be regularly spaced with spacing between first or second order faults commonly 1,100 to 1,900 metres. It should be noted that the flight

lines for the acquisition of the magnetic data are approximately parallel to the trend of the D_3 faults, which may cause the fault frequency to be underestimated.

Fault Density and Orientation Analyses

A series of analyses were conducted on the fault interpretation that include fault density and fault orientation analyses. Considering D_2 faults are known to control Ag-Pb-Zn mineralisation, to avoid biasing the analyses towards D_1 and D_3 faults, a query was run to select only D_2 faults for the analyses (Figure 5.46). Assessment of fault density data should identify areas of increased structural complexity, and thus identify areas of increased prospectivity. The lineament density calculations were done using the spatial analyst tool for ArcGIS™ software. The output cell size was set to 25 metres, and the search radius was set to 1,000 metres.

The lineament density analysis on all D_2 faults shows small areas of elevated fault density east of the Keno 700 deposit, on the north flank of Mount Hinton, and an area along the crest of Galena Hill encompassing the Galkeno, Calumet, Hector, and Bermingham deposits (Figure 5.47). A large, ENE-trending area of high fault density is interpreted along strike from the Husky deposit, in the valley north of Galena Hill. The lithology in this area is not well documented; however, it is thought likely to be dominantly comprised of Earn Group metasedimentary rocks and as such is not thought to be highly prospective. Comparison of the fault density data to all faults suggests that D_3 faults have a strong impact on the distribution of D_2 faults. Numerous D_3 faults, and in particular a

first order, NW-trending D_3 fault through the centre of the district, appear to truncate areas of high D_2 fault density (Figure 5.48).

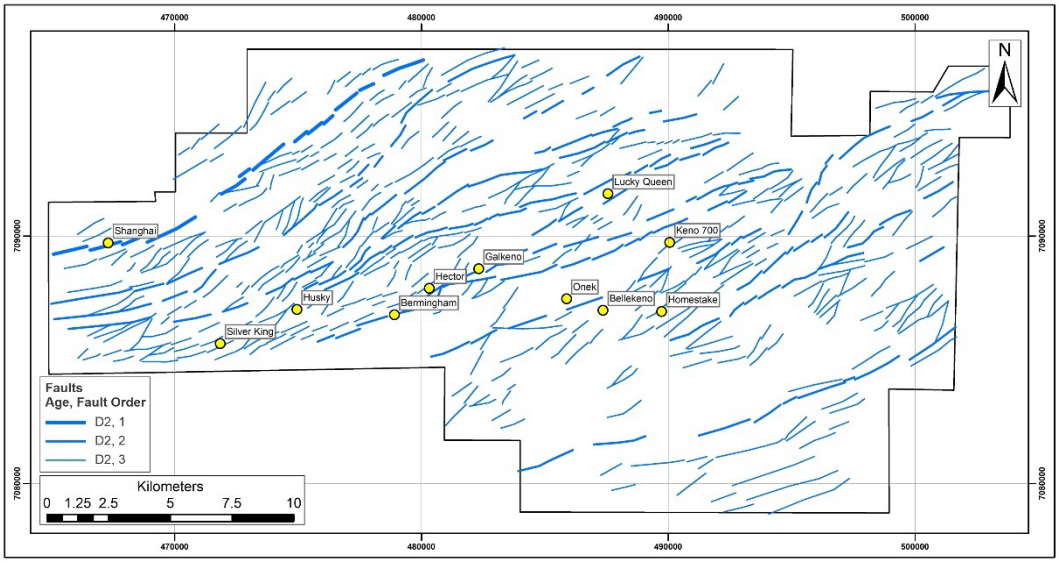

Figure 5.46: District-scale fault interpretation showing only D_2 faults.

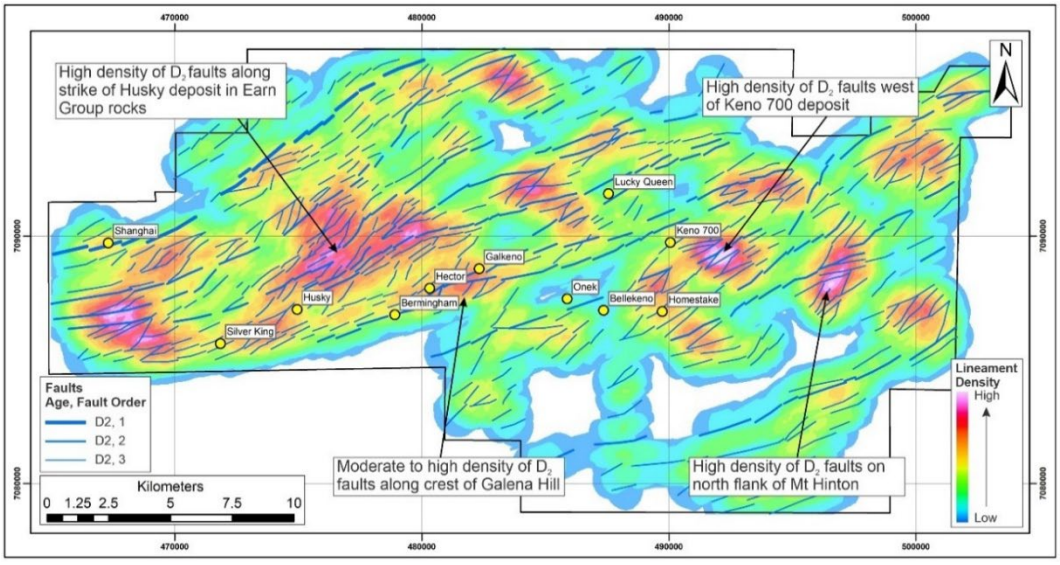

Figure 5.47: Fault density analysis for D_2 faults interpreted from district-scale 1VD data.

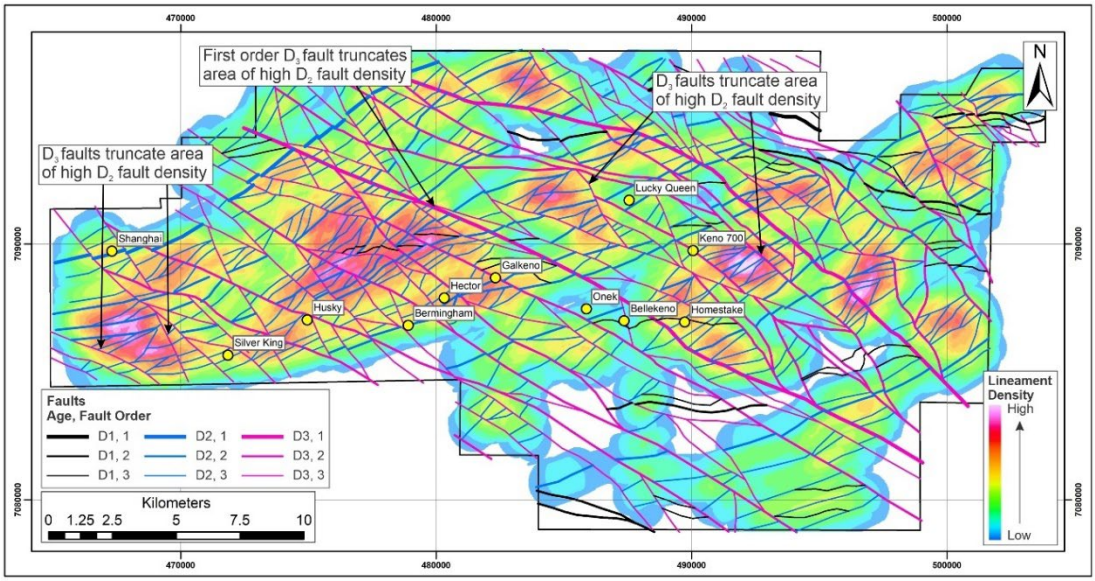

Figure 5.48: Fault density analysis for D_2 faults overlain by all interpreted faults.

Field observations indicate that lower order, NE- to NNE-striking faults developed as extensional structures during Ag-Pb-Zn-mineralisation, and as such host wider veins. To assess the distribution of NE- to NNE-striking D_2 faults interpreted faults were classified based on orientation. The orientation of a given line was calculated from the midpoint of an interpreted fault using the polyline_Get_Azimuth function of Easy Calculate 10 plugin for ArcGIS^{TM}. Faults were classified into two bins that were fault striking ≤ 050° and > 050°. A query was run to select only faults oriented ≤ 050° and the lineament density calculation was rerun (Figure 5.49 and Figure 5.50). The results of the lineament density calculation for NE- to NNE-striking faults are similar to the results for all D_2 faults, with an area of high fault density present along strike and NE of the Husky deposit, and areas of high or moderately high density present on the south flank of Keno Hill, the north flank of Mt Hinton, and along the crest of Galena Hill (Figure 5.50).

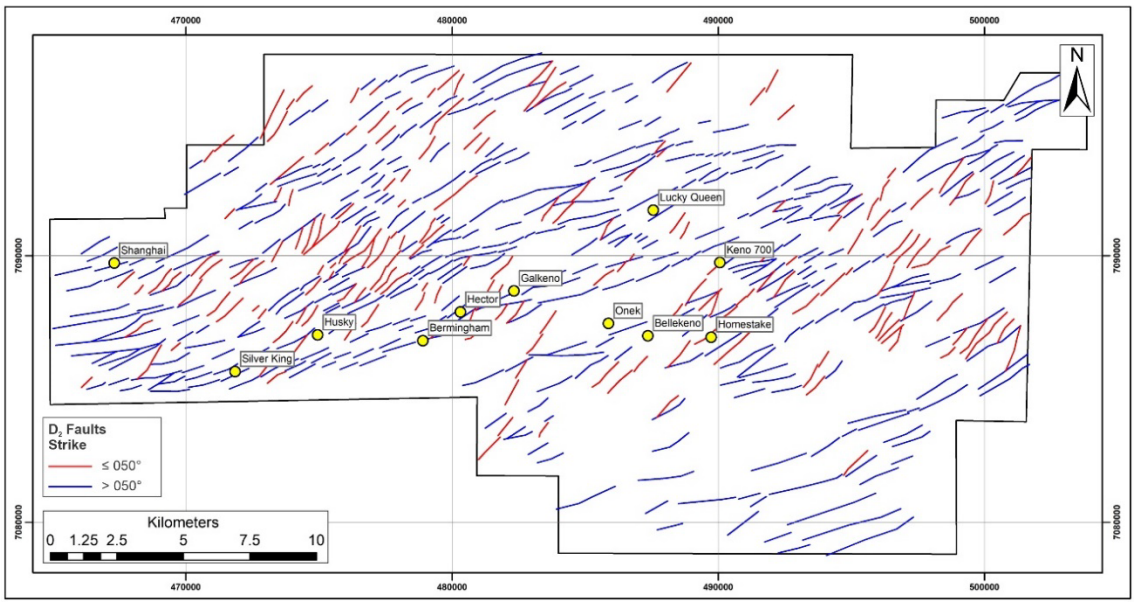

Figure 5.49: District-scale fault interpretation showing D_2 faults classified by orientation.

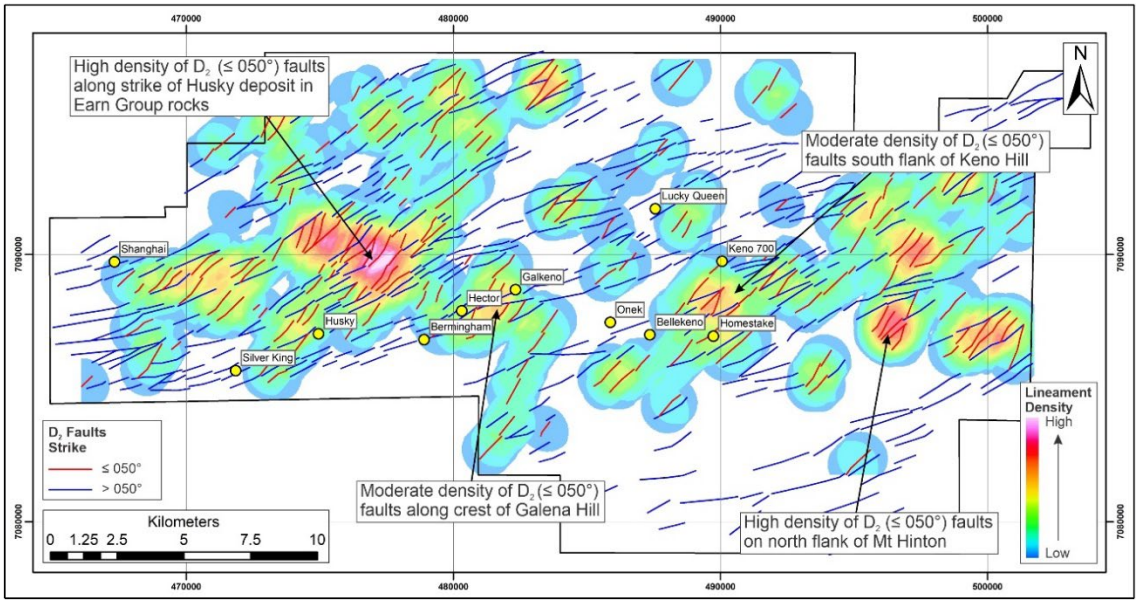

Figure 5.50: Fault density analysis for D_2 faults with a strike of ≤ 050° interpreted from district-scale 1VD data.

5.2.2 Regional-Scale Interpretation of Airborne Magnetic Data

A regional interpretation of publicly available airborne magnetic data was completed over an area in the northwestern Selwyn basin (Figure 5.51). The area is bound to the NE by the Dawson Thrust and to the SW by the Tintina Fault. The interpretation followed the same process as the district-scale interpretation of airborne magnetic data, and the results are similar with D_1, D_2, and D_3 faults present and of a similar orientation and relative abundance.

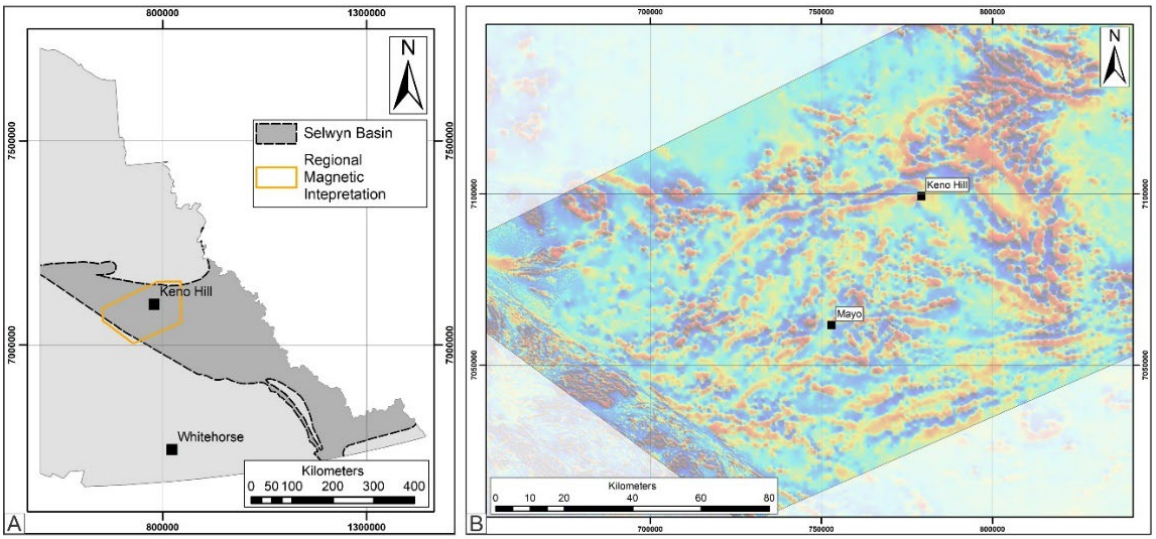

Figure 5.51: Location (A) and 1VD regional airborne magnetic data (B) used for the regional fault interpretation.

Tectonostratigraphic form lines for the regional interpretation are more chaotic than for the district-scale interpretation; however, they broadly show an ENE-trend (Figure 5.52). Towards both the Dawson Thrust and Tintina Fault form lines become strongly fault/thrust-parallel. D_1 faults are slightly better represented in the regional data and

appear relatively abundant towards the south of the interpretation areas, near the city of Mayo.

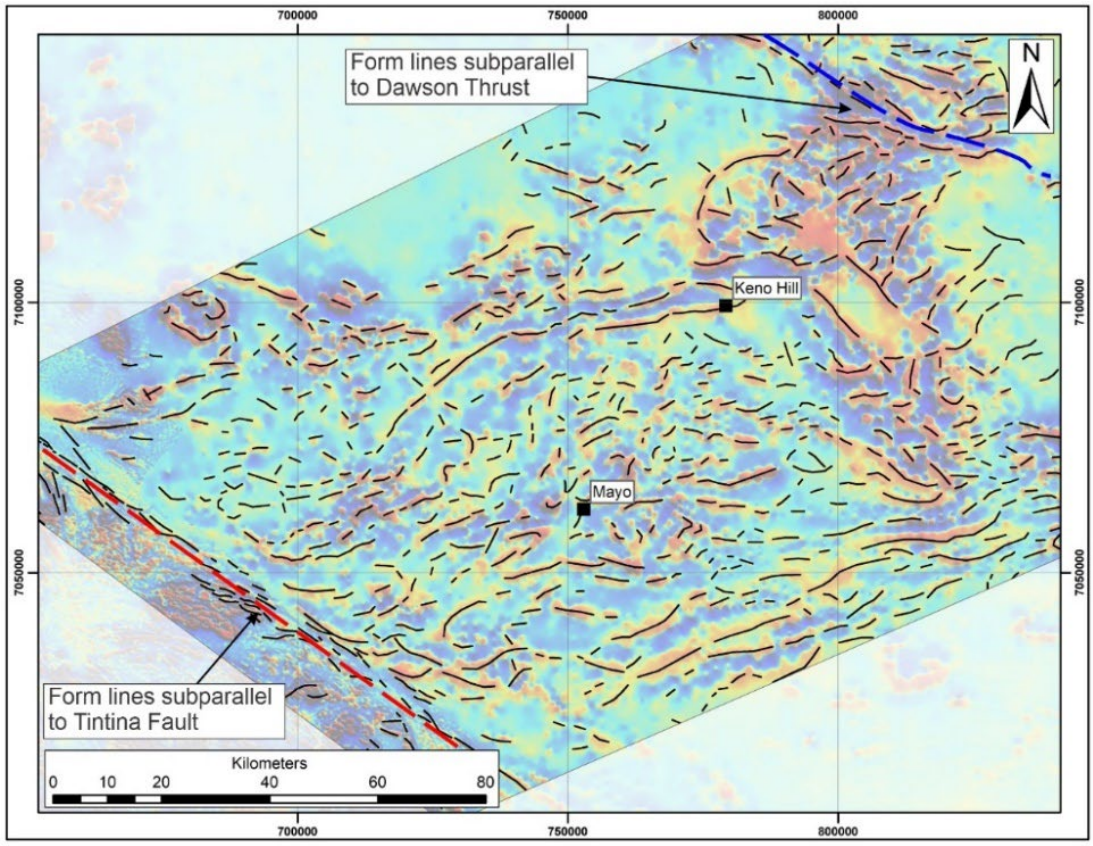

Figure 5.52: Regional-scale form line interpretation of 1VD data. Red dashed line: Tintina Fault; Blue dashed line: Dawson Thrust.

D_2 faults show the same pattern observed in the field as at the district-scale interpretation of airborne magnetic data, with commonly linear, laterally continuous, ENE-striking faults linked by curvilinear NE-striking faults (Figure 5.53). The geometry of the D_2 faults at the regional-scale suggests that the D_2 fault system forms a series of left-stepping releasing bends (Figure 5.54). The Keno Hill district sits approximately near the centre of one interpreted releasing bend. This suggests that the Keno Hill district was located in a

local region of extension and dilation during propagation of the mineralised veins, and as such would in part explain the abundance of wide, mineralised veins, and high metal endowment of the district.

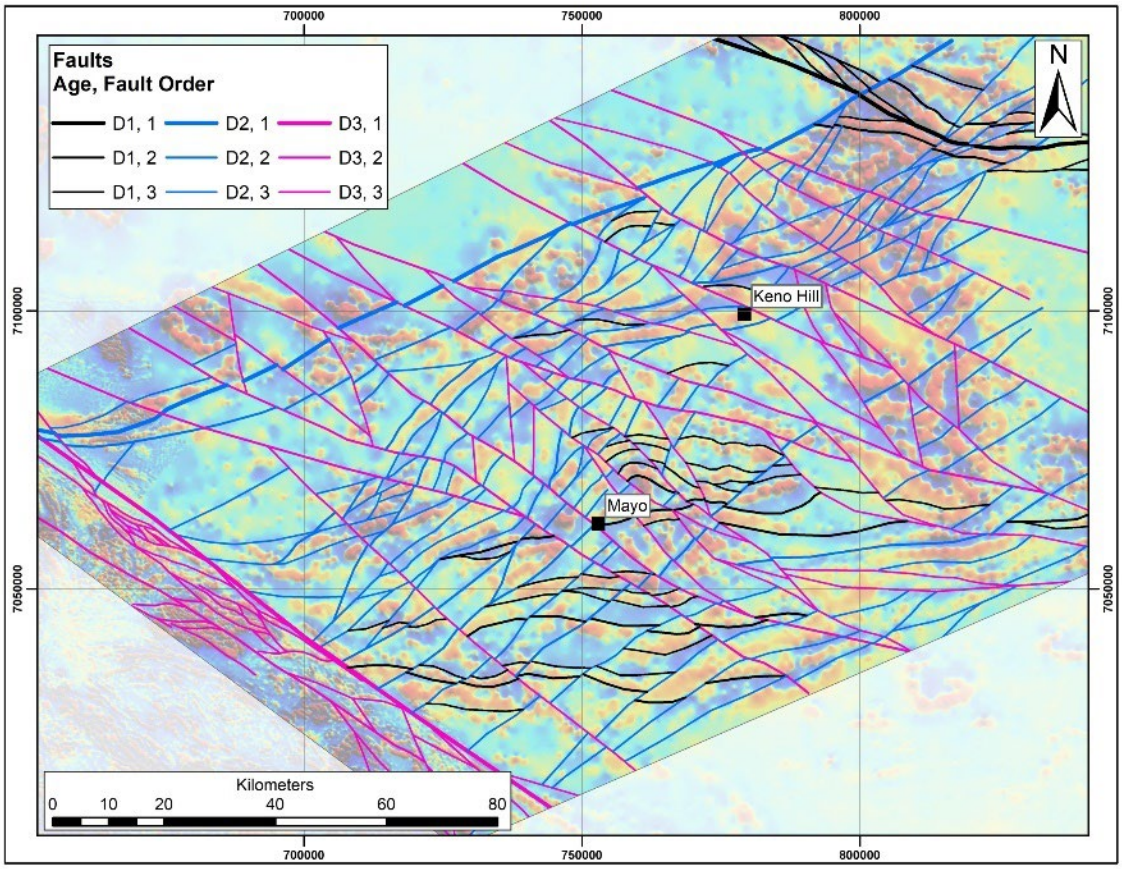

Figure 5.53: Regional-scale fault interpretation of 1VD data.

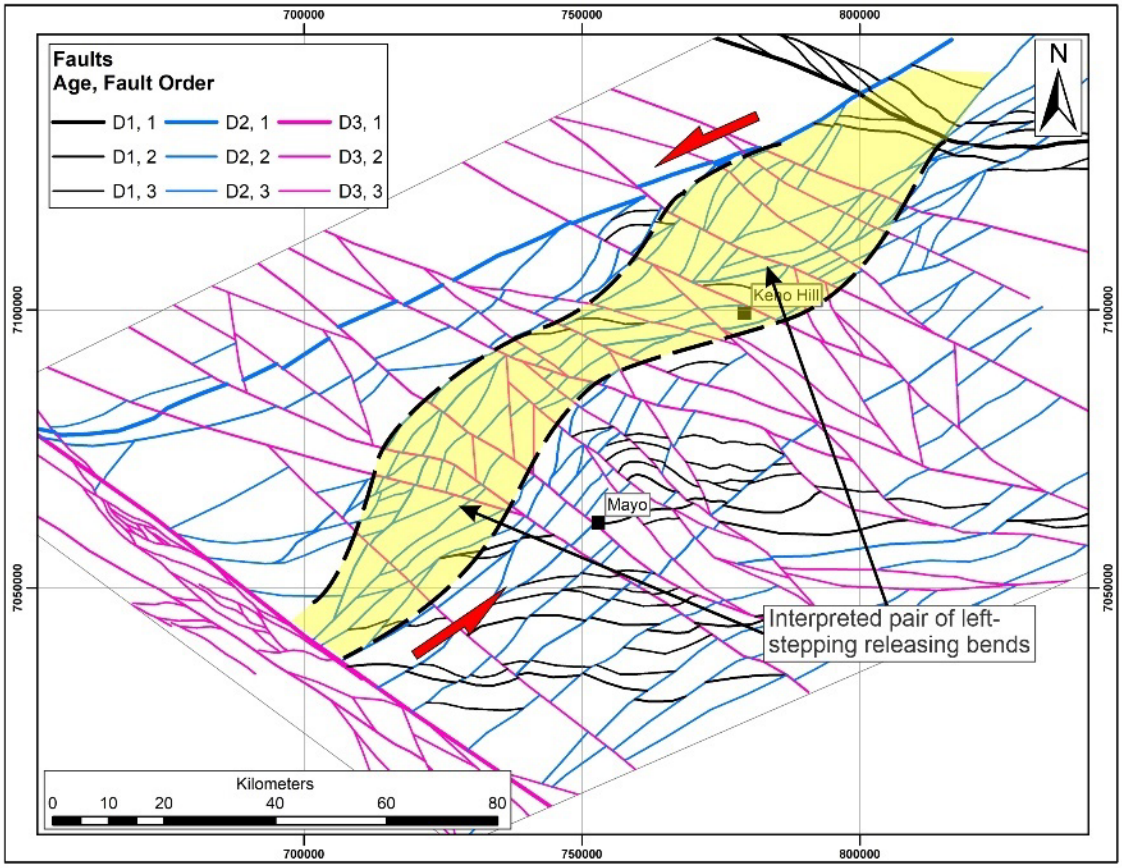

Figure 5.54: Regional-scale fault interpretation showing interpreted left-stepping releasing bends.

5.2.3 District-Scale Interpretation of Digital Elevation (DEM) Data

The boundaries for the lineament interpretation of the Keno Hill area are limited by the DEM coverage supplied by Alexco, and as such do not cover as wide an area as the interpretation of the district-scale airborne magnetic data. The interpretation shows a more fragmented pattern of lineaments than the interpretation of magnetic data due to the commonly weak surface expression of faults (Figure 5.55).

Differentiation between D_1 and D_2 faults is difficult due to their broad similarity in strike; however, certain large ENE-trending faults observed in the DEM data correlate well with D_2 structures in the airborne magnetic data; as such, they are considered to be equivalent. Several laterally continuous D_2 structures are identified trending ENE on Keno Hill, including a major lineament along Lightning Creek. These correlate well with lineaments observed in the airborne magnetic data, with surface observations at the summit of Keno Hill, and the Wernecke and Lucky Queen deposits (Figure 5.55), and with historic mapping by Boyle (1965). In addition, they are proximal to various prospects and deposits in the area.

At the summit of Galena Hill, DEM lineaments are quite rare; however, those identified correlate well with the locations of the Bermingham, Hector, and Calumet deposits (Figure 5.55). Towards the base of Galena Hill, a series of short lineaments are interpreted that trend approximately NE. To the far west of the district, between the Silver King and Husky deposits, these lineaments appear to correlate with veins mapped by Boyle (1965), and as such are expected to be of D_2 age. However, towards the north of Galena Hill, these lineaments are subparallel to both glacial lineaments and McOnie and Read's (2009) interpreted boundary between the KHQ and structurally lower Earn Group. As such it is unclear whether they represent glacial lineaments, D_1 thrust faults, or D_2 brittle faults.

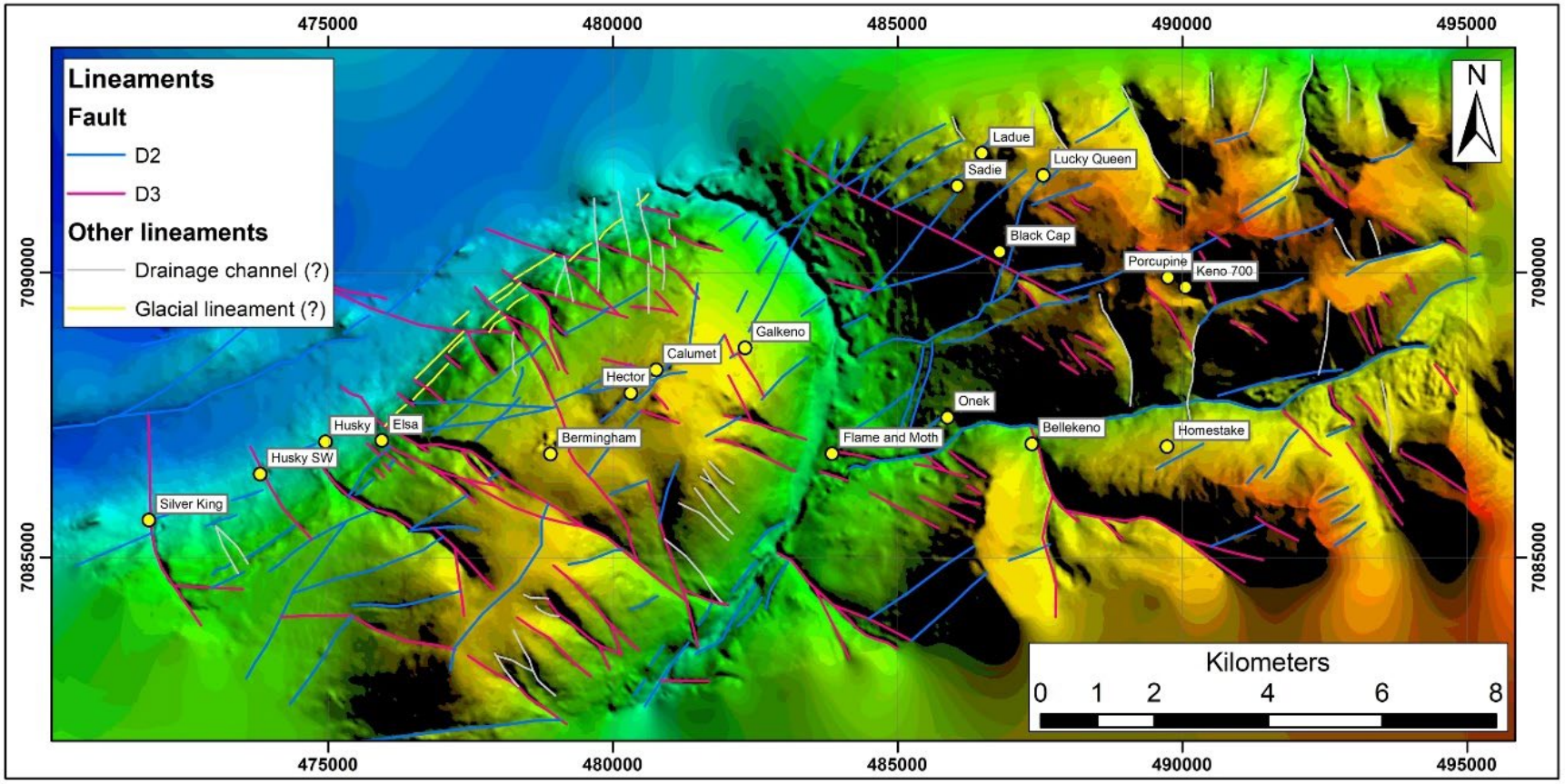

Figure 5.55: Lineament interpretation of DEM data.

D_3 structures are well represented in the DEM data with numerous short to long, NW- to north-south-trending fault segments interpreted. Some caution should be used with the interpreted D_3 lineaments that are perpendicular to the crests of Galena Hill and Keno Hill. These may represent drainage channels and not underlying structures. This is particularly evident on the southeastern flank of Galena Hill (Figure 5.55).

5.2.4 2D Vein Geometry

At the district-scale, Ag-Pb-Zn vein geometry is largely defined by D_2 fault geometry. Vein width is controlled by a combination of D_2 fault orientation and host lithology, with KHQ rocks overwhelmingly hosting thicker veins. At deposit- and smaller scales vein geometry is generally controlled by D_2 fault geometry; however, rheological variations may cause small-scale deviation in vein dip (S. Isles, personal communication, June 1, 2016), and locally fluid overpressure during D_2 may have caused pre-existing D_1 faults to dilate, permit fluid flow, and promote Ag-Pb-Zn precipitation. This section exclusively discusses the large-scale vein geometry.

A 2D analysis of historic mapping and borehole data was conducted (Figure 5.56 and Figure 5.57). The data used for the analysis included historic vein mapping (Boyle, 1965), assays and collar data for all drilling completed in the district between 1930 and 2009, the 2D interpretations of airborne magnetic and DEM data, and the 3D modelling of vein architecture on Galena Hill (discussed in Chapter 5.2.5). It should be noted that

there is an inherent bias in the interpretation, in that drilling, historic mapping, and mining activities only define areas of high-volume mineralisation.

The interpretation shows an *en echelon* network of narrow, ENE-trending structures linked by apparently wider NE-trending veins and segmented by post-mineralisation D_3 faults. On Galena Hill vein geometry appears to be anastomosing, with relatively little variation in vein width between the ENE- and NE-trending veins. However, NE-trending veins appear to be better defined.

On Keno Hill, around the Signpost area, a classic fault step-over is defined, with narrow ENE-trending faults (associated with the Nabob and Comstock-Porcupine faults) linked by wider NE-trending structures associated with the No. 9 fault system. The Bellekeno structure appears to be a splay between a NE- and more north-south-trending structure. The vein geometry over larger areas as defined by borehole data and mapping is replicated at the over smaller areas with sphalerite veins at the Sime deposit showing a near identical pattern (Figure 5.58).

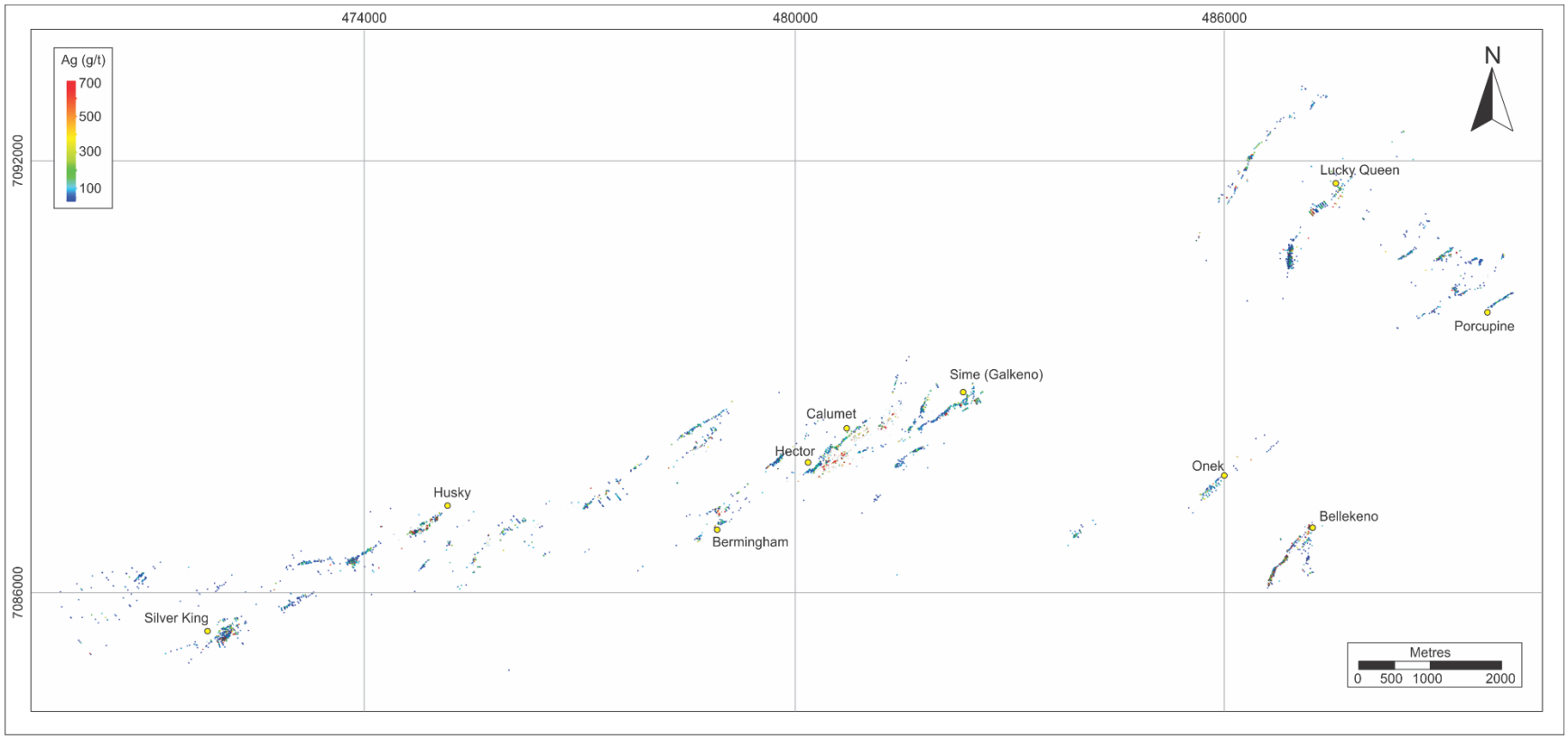

Figure 5.56: Plan view of all supplied assay data for the Keno Hill district. Assay data show a pattern of en echelon, anastomosing vein systems.

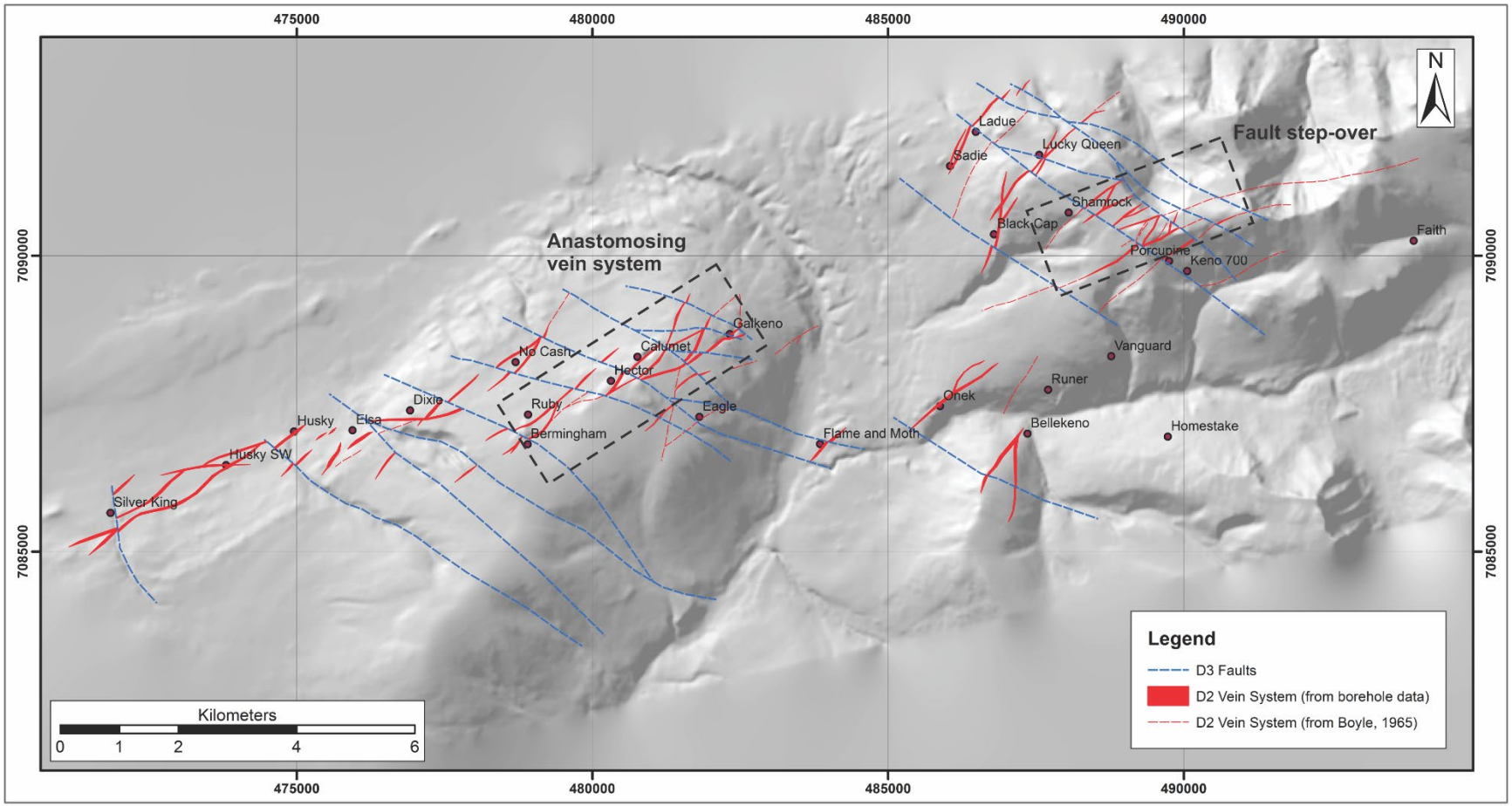

Figure 5.57: Interpretation of 2D vein geometry based on borehole assay data and regional, historic vein mapping (modified after Boyle, 1965).

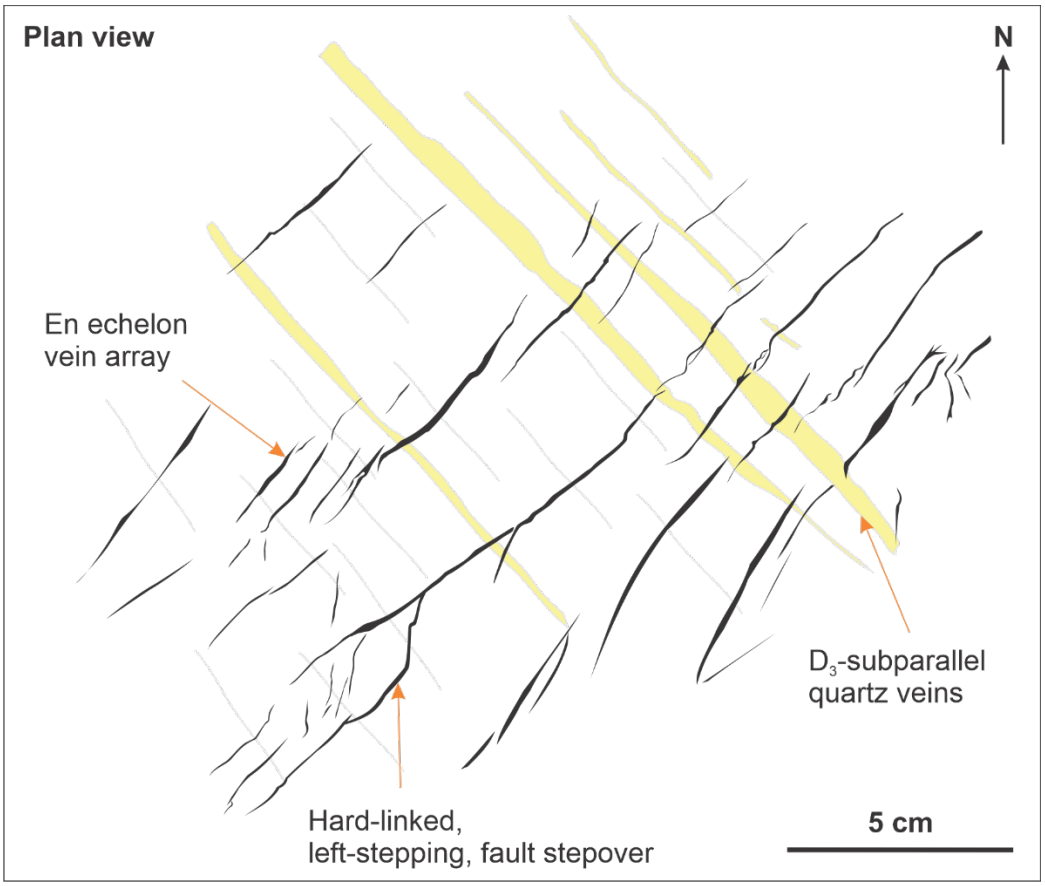

Figure 5.58: Sketch of small-scale en echelon vein architecture defined by sphalerite stringer veins in KHQ outcrop at the Sime deposit (UTM 482374mE, 7088658mN).

5.2.5 3D Vein Geometry

The 3D interpretation of vein architecture was completed for the Galena Hill summit area between the Sime (Galkeno) and Bermingham deposits (Figure 5.59 and Figure 5.60). The vein model was built based on historic infrastructure data, historic level plans, surficial mapping data collected by the author, and borehole assay data (up to 2009). The vein model defines the known, existing vein geometry, and predicts areas that are of interest for future exploration. The model was built to a depth of 950 masl (metres above

sea level). Rare borehole data is present to a depth of approximately 817 masl, although the sparsity of the data removes confidence in the accuracy of the model below 950 masl.

The 3D model shows a network of NNE- to ENE-trending D_2 vein/faults, segmented by a network of NW- to WNW-trending D_3 faults (Figure 5.59 and Figure 5.60). Due to data density, the model is best constrained between the Sime (Galkeno) deposit in the east and the Hector deposit in the west.

A large D_2, ENE-trending fault transects the model that in historic mapping is variously termed the No. 23 and No. 10 veins. The model suggests that the No. 23 and No. 10 veins represent a single, discrete, albeit segmented structure and as such it is here termed the D2-1 vein (Figure 5.59 and Figure 5.60). The D2-1 vein appears truncated in the east by the D_3 Calumet Fault; however, there is a lack of data along strike of the vein east of the Calumet Fault and it is expected that the fault continues to the east. The D2-1 vein persists to the western margin of the model.

The D2-1 vein is relatively narrow with a maximum measured width of approximately 3.5 metres and a typical width of approximately one metre. Despite its narrow width, the D2-1 vein appears to be the principal, controlling D_2 structure in the model, with subordinate D_2 veins splaying off or attaching to the main structure. A similar relationship is observed in the No Cash area where a small ENE-trending fault truncates a set of NE-trending veins (Figure 5.59 and Figure 5.60).

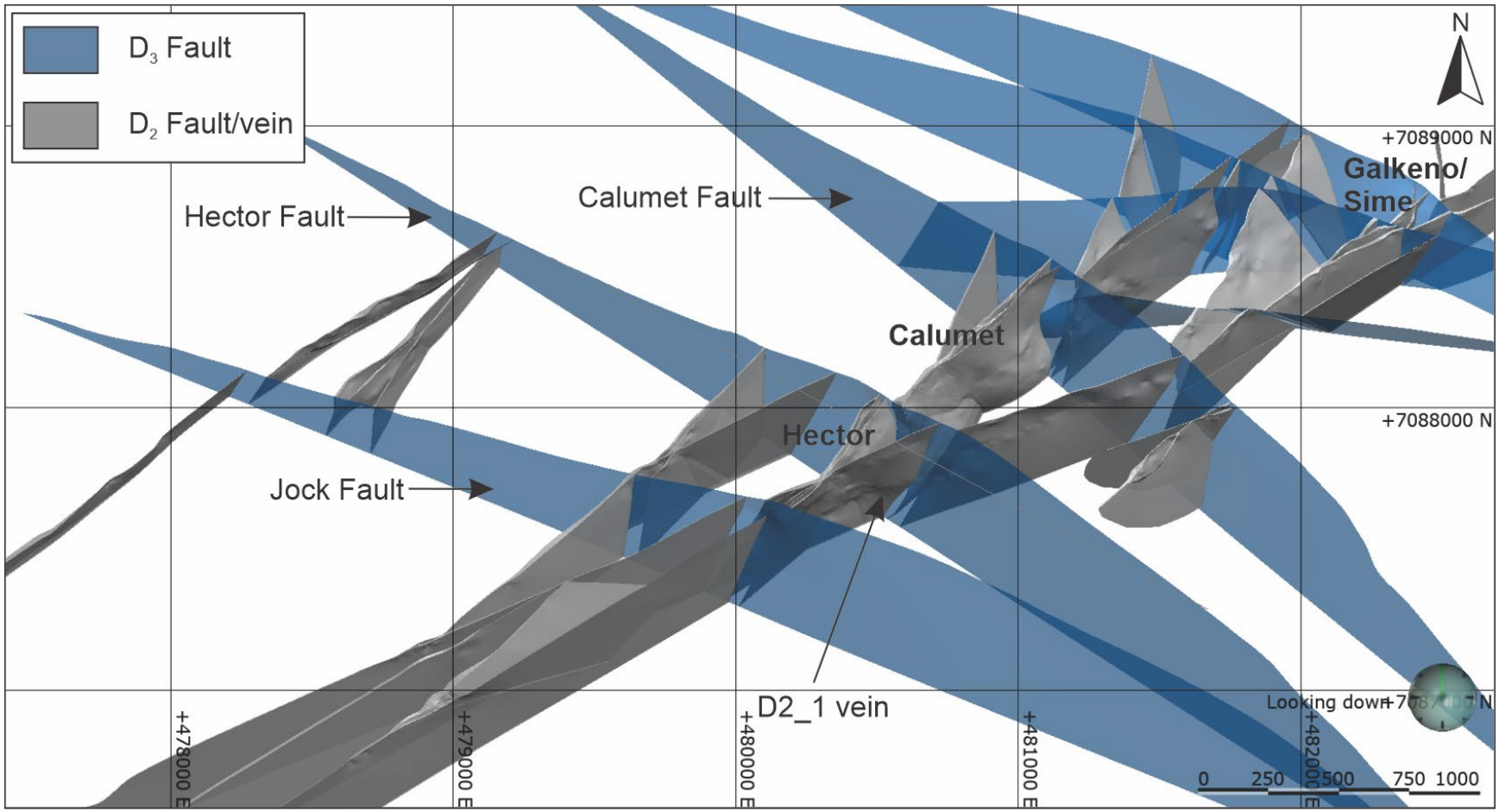

Figure 5.59: Plan view of 3D model of D_2 faults/veins and cross-cutting D_3 faults in the Galena Hill area.

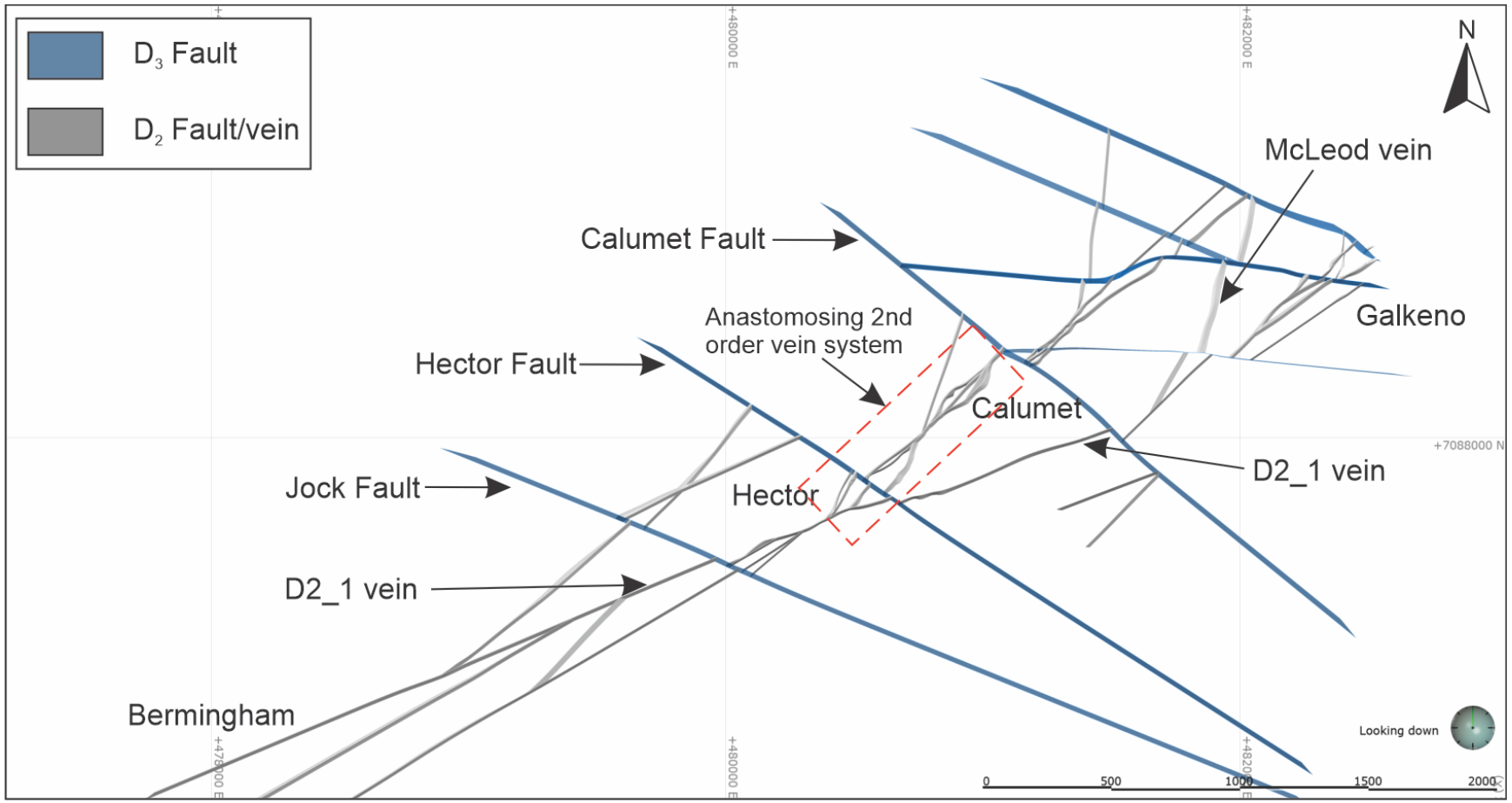

Figure 5.60: Plan view slice through 3D fault/vein model. 1160 masl.

NE-trending veins are common throughout the model. In the Hector and Calumet areas, a series of NE-trending veins form an anastomosing geometry in both plan view and cross-section and appear to form a flower structure (Figure 5.60 and Figure 5.61). The areas with maximum dilation along the anastomosing structures are coincident with the locations of the subsurface Hector and Calumet deposits.

In addition to the NE-trending second order veins, a relatively rare set of NNE-trending veins are modelled, particularly towards the east of the area. These include the historic McLeod veins, a splay off the historic No. 18 vein, and the vein observed and mapped in the north pit of the Sime deposit. The NNE-trending veins typically splay off the NE-trending structures and are thus considered to be third order structures (Figure 5.59 and Figure 5.60).

Ag-grade was modelled within the modelled veins. A structural trend was applied to the grade modelling that was parallel to the veins, decaying away from the veins, and strongly isotropic in an attempt to model only grade present in individual veins, and prevent the influence of grade outside modelled veins. Despite this, due to the narrow spacing of most veins, it is evident that the grade model is influenced, in part by assay data outside individual veins. Grades of greater than 100, 200, 500, and 1000 g/t Ag were modelled (Figure 5.62).

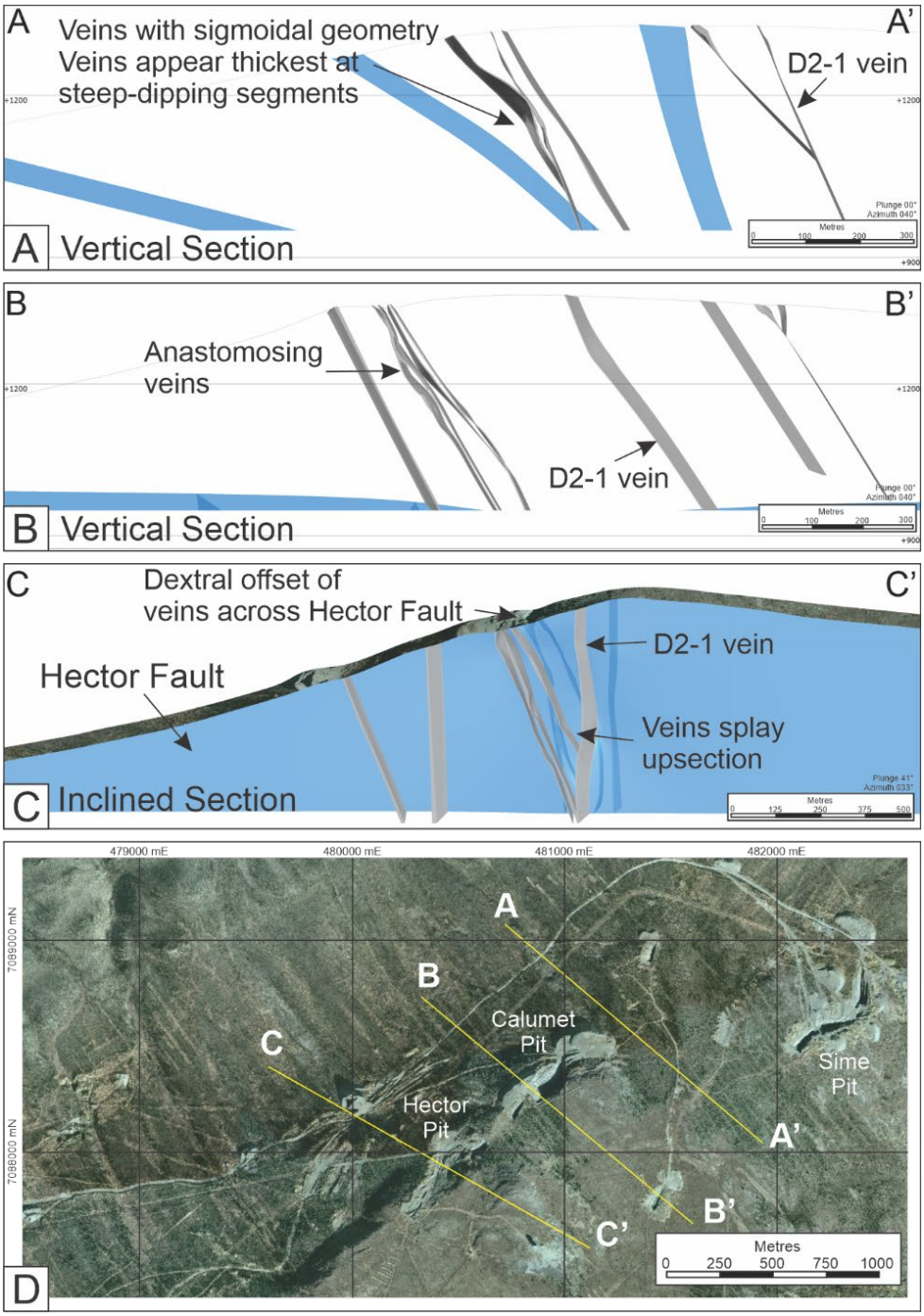

Figure 5.61: Vertical (A and B) and inclined (C) sections through the 3D fault/vein model. D: location map showing lines of section at surface.

The grade modelling shows that the majority of Ag-mineralisation is present in the NE-trending, second order structures (Figure 5.62). No significant mineralisation is

associated with ENE-trending veins, including the first order D2-1 vein. Some Ag mineralisation is associated with the third order McLeod vein, although this is limited to grades of less than 500 g/t Ag (Figure 5.62). This suggests that during the mineralising event(s), the NE-trending second order faults were in a local extensional stress field, and thus more dilatory than the first and third order faults. The third order faults carry some minor grade, and as such were likely in partial dilation, whereas the first order ENE-trending faults do not appear to have produced major dilational sites and were thus likely purely strike-slip faults.

High-grade ore shoots are steep and plunge approximately SE (Figure 5.62C). The high-grade shoots are typically coincident with the intersection of second order faults with either first or third order faults. Structural complexity would be greatest in these areas, and as such would create zones of inherent high structural permeability and low pressure leading to enhanced fluid-wall rock interaction and Ag-precipitation.

D_3 faults segment the D_2 veins. D_3 faults are typically NW-trending and SE-dipping, however a pair of small D_3 faults between the Sime and Calumet deposits trend east-west, dip south, and link between larger D_3 faults. Offsets across the D_3 faults appear relatively consistent with typical measured offsets of between 50 and 65 metres. The Calumet Fault appears to have the largest offset of approximately 95 metres. Offsets across D_3 faults consistently have a dextral strike separation (Figure 5.59 and Figure 5.60). Vertical displacement is difficult to determine but may be as much as 100 metres across the Hector Fault.

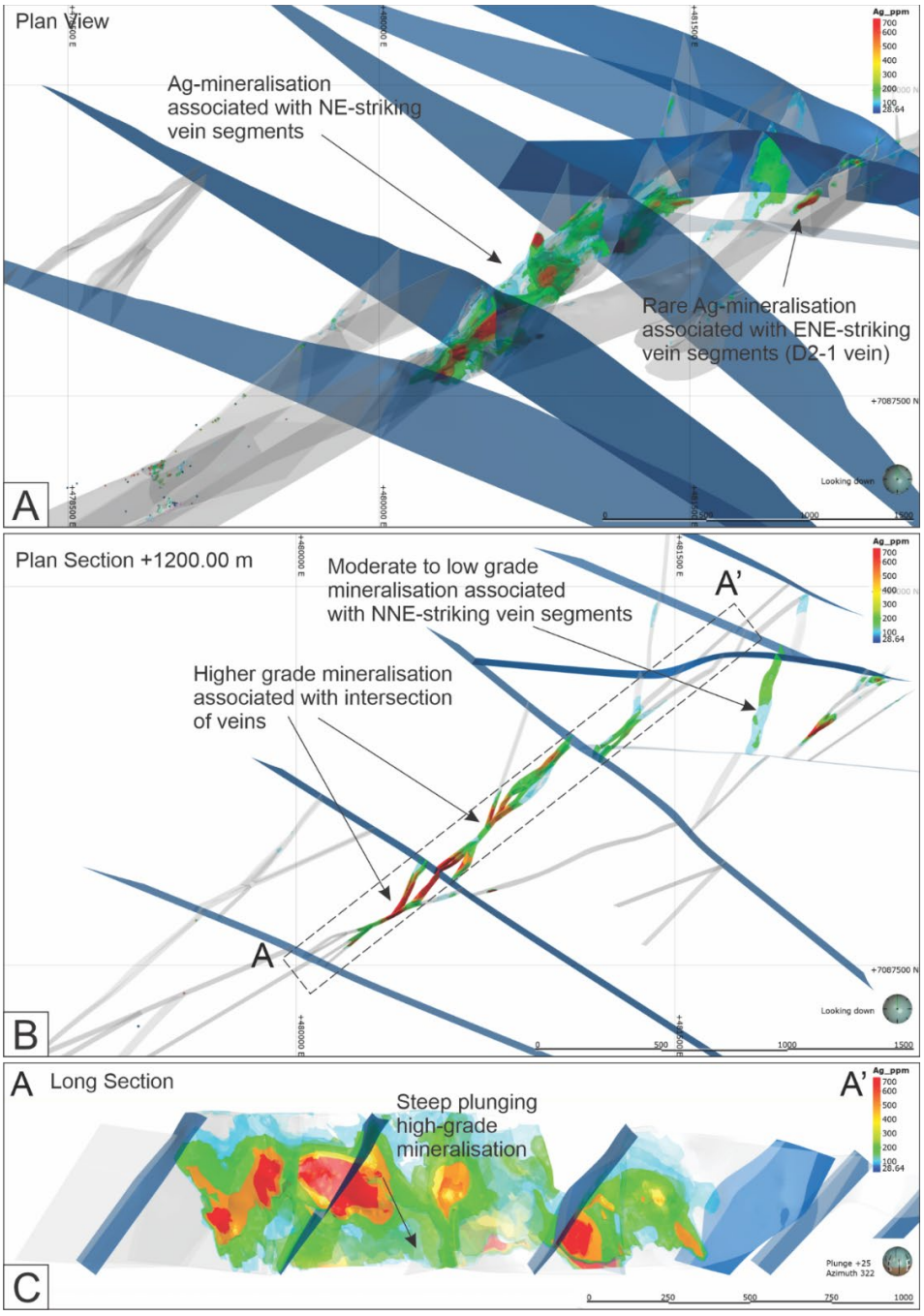

Figure 5.62: Anisotropic modelling of Ag grade in D_2 veins in 3D fault/vein model. Model created in Leapfrog Geo™.

A: Plan view of 3D model showing Ag grade isoshells within D_2 veins; B: Plan view section showing Ag grade isoshells within D_2 veins. Section has a width of 30 metres and is cut at 1200 masl; C: Long section through Hector-Calumet vein system showing Ag grade isoshells within D_2 veins. Modelling shows steep plunging high-grade mineralisation. Ag grade modeling was anisotropic, using a structural trend parallel to the Hector-Calumet vein system, and used a "strongest along inputs" trend type. Grade isoshells: light blue > 100 g/t Ag; green > 200 g/t Ag; orange > 500 g/t Ag; red > 1000 g/t Ag.

6. Geochronological Analysis

A geochronology study was undertaken to augment the structural geology study and to attempt to identify any temporal affinity, or lack thereof, between emplacement of Ag-Pb-Zn veins and a local intrusive body. The geochronology study used the $^{40}Ar/^{39}Ar$ method to assess the age of sericite alteration proximal to veins, and the U-Pb CA-TIMS analytical method was used to determine the age of the intrusive body.

6.1 Previous Geochronological Studies in the Keno Hill District and Surrounding Area

Prior to this study, three geochronological studies have been conducted within the study area. Two studies used the K/Ar (whole rock) method. Wanless et al. (1967) retrieved an age of 86 ± 8 Ma from chloritic sericite schist near the No Cash adit, while Sinclair et al. (1980) retrieved ages from five samples collected at the Husky, Keno, Ruby, and Elsa mines. The Sinclair et al. (1980) data were collected from stockwork or quartzitic wall rock in or near Ag-Pb-Zn veins and produced ages of between 85.1 ± 5.1 Ma and 103 ± 5.0 Ma. An age of 87 ± 3 Ma was interpreted to represent the age of Ag-Pb-Zn mineralisation within the Keno Hill district. In addition, Hantelmann (2013) attempted to define the age of mineralisation using a Pb isotope study and interpreted a model age of 82.0 ± 31.0 Ma.

Mair et al. (2006) retrieved $^{40}Ar/^{39}Ar$ ages from three muscovite samples in strongly deformed Hyland Group rocks in the lower Robert Service thrust sheet. The samples were considered to be thermally undisturbed by mid Cretaceous plutonism, and were analysed by both *in situ* and step-heating of mineral separates. Mair et al. (2006) retrieved ages of between 100.47 ± 0.40 Ma and 104.60 ± 2.00 Ma from those samples and consider these ages to represent the cessation of ductile deformation in the lower Robert Service thrust sheet. No dates were retrieved for the age of metamorphism during this study, however the spatial proximity and similarity in structural style between the fold- and thrust-related deformation documented by Mair et al. (2006) and that documented by the author in the Keno Hill district suggest that it is reasonable to assume a similar late Middle Cretaceous age (circa 100 Ma) for the end of D_1 deformation and associated greenschist facies metamorphism. The $^{40}Ar/^{39}Ar$ ages obtained from this study range between approximately 83 and 69 Ma, and as such are not considered to be representative of regional metamorphism.

Prior to this study, 35 isotopic ages have been retrieved from rocks within approximately 50 km of the Keno Hill district (Table 6.1). These include cooling, crystallisation, and alteration ages from plutonic, metamorphic, and hydrothermally altered rocks.

6.2 Sampling for the Geochronological Study

For this study, five samples were selected for analysis by the $^{40}Ar/^{39}Ar$ method, and one sample was selected for analysis by the U-Pb CA-TIMS method (Figure 6.1). Samples for the $^{40}Ar/^{39}Ar$ analysis were collected at D_2 vein selvages or within D_2 vein-associated breccia in drill core and from the 750-1 crosscut in the Bellekeno underground mine (samples 0187-005, U0160-009, and K-BX-007), and in strongly sericite-altered rocks within the D_2 fault zone associated with the Onek vein. The sample selected for U-Pb CA-TIMS analysis was collected from a quartz-feldspar porphyritic dyke on the north flank of Keno Hill (sample K-KH-003). This was the sole occurrence of felsic intrusive rock observed in the study area during field work.

A summary of the theory and methodology employed for each analytical technique is given in section 3.6 and Appendix A. Below is a summary of the results of $^{40}Ar/^{39}Ar$ and U-Pb CA-TIMS results.

Table 6.1: Summary of geochronology studies within 50 km of Keno Hill district (data from Breitsprecher and Mortensen, 2004).

Age (Ma)	Method	Mineral	Interpretation	Rock Class	Rock type	Source
85.1 ± 10.2	K/Ar	Whole Rock	Alteration	Hydrothermal	Quartzite within stockwork zone at Husky mine.	Sinclair et al. (1980)
88.9 ± 7.8	K/Ar	Whole Rock	Alteration	Hydrothermal	Quartzite within stockwork zone at Keno mine. Age interpreted as age of alteration related to veining	Sinclair et al. (1980)
91.5 ± 0.6	Ar/Ar	Biotite	Hydrothermal	Hydrothermal	Coarse-grained biotite in quartz-moly vein in granite.	Joyce et al. (2015)
96.5 ± 0.8	Ar/Ar	Biotite	Hydrothermal	Hydrothermal	Coarse-grained biotite in quartz-moly vein in granite.	Joyce et al. (2015)
82 ± 31	Pb isotope	Galena	Mineralisation	Hydrothermal		Hantelmann (2013)
86 ± 8	K/Ar	Muscovite	Cooling	Metamorphic	Chloritic sericite schist near top of Lower Schist unit, well above the Keno Hill Quartzite	Wanless et al. (1967)
95 ± 12	K/Ar	Muscovite	Cooling	Metamorphic	Sericite schist near base of Upper Schist unit, well above the Keno Hill Quartzite	Wanless et al. (1967)
104 ± 6	K/Ar	Muscovite	Cooling	Metamorphic	Sericite-quartz schist of the Upper Schist unit, well above the Keno Hill Quartzite	Wanless et al. (1967)
91.1 ± 6.4	K/Ar	Whole Rock	Cooling	Metamorphic	Quartzite wall rock at Elsa mine, 30 m from mineralization	Sinclair et al. (1980)
102 ± 8	K/Ar	Whole Rock	Cooling	Metamorphic	Quartzite wall rock at Ruby mine; 1.5 m from vein	Sinclair et al. (1980)
103 ± 10	K/Ar	Whole Rock	Cooling	Metamorphic	Quartzite wall rock at Keno mine; 152 m from mineralization	Sinclair et al. (1980)
83.1 ± 7	K/Ar	Biotite	Cooling	Plutonic	Porphyritic quartz diorite	Leech et al. (1963)
104.5 ± 8.0	K/Ar	Biotite	Cooling	Plutonic	Biotite quartz monzonite	Leech et al. (1963)
108.6 ± 8.0	K/Ar	Biotite	Cooling	Plutonic	Granodiorite boulder in Dublin Gulch; believed to be from a stock exposed at the head of the Gulch	Leech et al. (1963)
83 ± 5	K/Ar	Biotite	Cooling	Plutonic	Granitic porphyry sill at Mount Haldane	Wanless et al. (1967)
89.0 ± 2.6	K/Ar	Biotite	Cooling	Plutonic	Narrow (2-3m-wide) quartz-feldspar porphyry dyke cutting Keno Hill Quartzite	Stevens et al. (1982a)
90.4 ± 5.8	K/Ar	Biotite	Cooling	Plutonic	Quartz monzonite	Kuran et al. (1982)
98.9 ± 3.7	K/Ar	Biotite	Cooling	Plutonic	(Hornblende-)biotite quartz monzonite	Stevens et al. (1982b)

99.3 ± 3.8	K/Ar	Biotite	Cooling	Plutonic	Porphyritic hornblende-biotite quartz monzonite	Stevens et al. (1982b)
613 ± 15	K/Ar	Biotite	Cooling	Plutonic	Lamprophyre dyke intruding the lower Quartet Lake Group (Wernecke Supergroup)	Stevens et al. (1982a)
93.8 ± 2.0	K/Ar	Biotite	Cooling	Plutonic	(Hornblende-)biotite quartz monzonite	Hunt and Roddick (1987)
85.3 ± 2.1	K/Ar	Whole Rock	Cooling	Volcanic	Weakly altered quartz-plagioclase-biotite-phyric rhyolite flow unconformably overlying metamorphic rocks	Hunt and Roddick (1987)
511 ± 82	Rb/Sr	Whole Rock	Crystallization	Metamorphic	Six samples of metasediments (mostly pelitic schists) from the Scheelite Dome property.	Kuran et al. (1982)
377.9 ± 2.9	U-Pb	Zircon	Crystallization	Metamorphic	Felsic metavolcanic; gritty chloritic feldspathic augen phyllite, augen up to 3 mm.	Roots (1997)
91 ± 0.3	U-Pb	Zircon	Crystallization	Plutonic	Quartz monzonite	Murphy (1997)
91.2 ± 0.9	U-Pb	Titanite	Crystallization	Plutonic	Medium-grained porphyritic quartz monzonite, locally exhibits miarolitic cavities	Murphy (1997)
92.1 ± 0.5	U-Pb	Zircon	Crystallization	Plutonic	Medium-grained porphyritic quartz monzonite, locally exhibits miarolitic cavities	Murphy (1997)
92.2 ± 0.3	U-Pb	Zircon	Crystallization	Plutonic	Quartz monzonite	Murphy (1997)
92.3 ± 0.3	U-Pb	Zircon	Crystallization	Plutonic	Quartz monzonite	Murphy (1997)
92.5 ± 2.5	U-Pb	Titanite	Crystallization	Plutonic	Quartz monzonite	Murphy (1997)
92.8 ± 0.5	U-Pb	Titanite	Crystallization	Plutonic	Coarse-grained porphyritic granite (also referred to as the Mayo Lake batholith)	Roots (1997)
92.8 ± 0.5	U-Pb	Titanite	Crystallization	Plutonic	Quartz monzonite	Murphy (1997)
93.5 ± 5.8	U-Pb	Zircon	Crystallization	Plutonic	Quartz monzonite	Murphy (1997)
91.7 ± 0.5	U-Pb	Zircon	Crystallization	Volcanic	Pink to brown, siliceous fine-grained biotite felsite (flow)	Roots (1997)
94.20 ± 0.02	U-Pb	Zircon	Crystallization	Plutonic	Biotite granodiorite	Breitsprecher and Mortensen (2004)

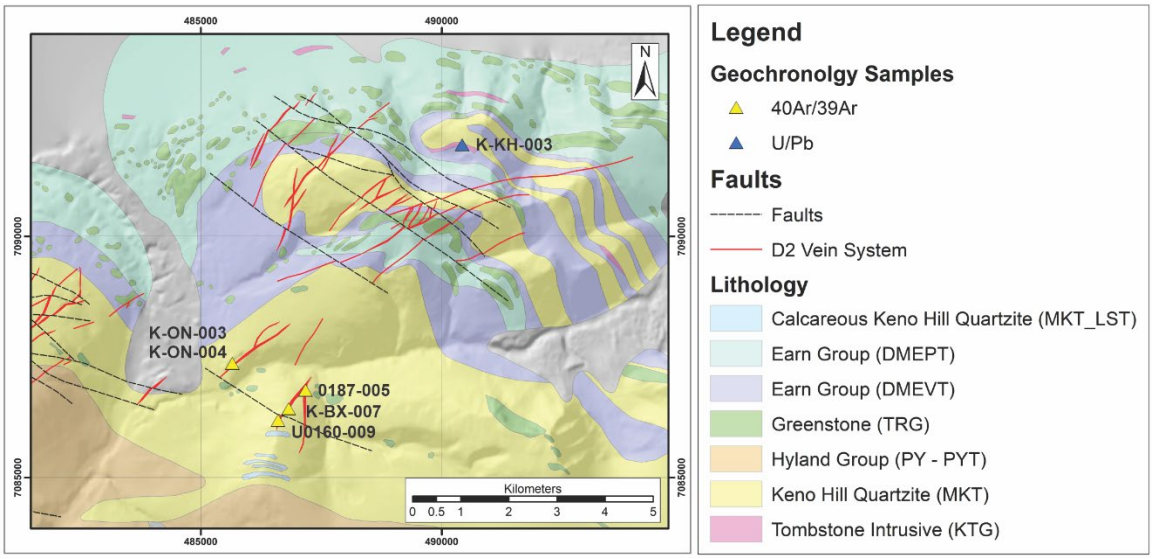

Figure 6.1: Simplified geological map showing locations of samples collected for geochronological analysis. Base data from Murphy (1997).

6.3 Sample Descriptions and Results

Below are descriptions of, and results for the samples analysed.

6.3.1 $^{40}Ar/^{39}Ar$ Analysis

Sample: K-ON-003

Location:

Surface sample – Onek deposit; footwall of the Onek fault, collected within 1 metre of main fault surface. UTM 485651 mE, 7087367 mN.

Sample description:

Highly altered chlorite-(white) mica schist composed of fine-grained anhedral quartz (50 to 55%) with abundant fine-grained sericite (25 to 30 %) and chlorite (5 %) along foliations. Coarse muscovite grains of metamorphic origin appear absent or have been pervasively overprinted by sericite alteration. The schist hosts bands (up to 6 mm) and pods of quartzite composed of oblate quartz with minor sericite and flooded by late carbonate (ankerite; 15%) and foliation-parallel quartz segregations. Disseminated pyrite (2%) is also present along foliations.

Results:

The age-spectra and inverse isochron (Table 6.2; Figure 6.2) show a higher integrated age (77.1 ± 0.4 Ma) and plateau age (72.1 ± 0.2 Ma) than the inverse isochron age (69.64 ± 0.63 Ma). A ^{40}K decay constant of (5.5545 (±0.0109) x 10^{-10} $a^{-1)}$ (Renne et al., 2010) yields an inverse isochron age of 69.49 ± 0.62 Ma. In this sample two plateaus appear to be defined by the age spectrum. A plateau is present at approximately 85 Ma that is interpreted to represent initial growth and cooling of the hydrothermal mica possibly during Ag-Pb-Zn-mineralisation. A second plateau is evident at approximately 72 Ma that may indicate the sample was reset due to hydrothermal alteration and associated fluid flow along the Onek Fault.

Table 6.2: Summary of $^{40}Ar/^{39}Ar$ dates for sample K-ON-003.

Integrated Age (Ma)	2-sigma (Ma)			
77.1	0.4			
Plateau or Plateau Segment Age (Ma)	2-sigma (Ma)	$\%^{39}Ar$	MSWD	
72.1	0.2	49.0	1.8	
Inverse Isochron Age (Ma)	2-sigma (Ma)	Initial Ratio	2-sigma (Ma)	MSWD
69.6	0.6	719	66	1.7
Min Step Date (Ma)	2-sigma (Ma)	Max High-T Step Date (Ma)	2-sigma (Ma)	
53	2	85	1	

The inverse isochron has an acceptable MSWD of 1.7. The inverse isochron shows an abundance of radiogenic Ar ($^{40}Ar^*$) suggesting the presence of excess argon and may indicate contamination and inheritance from older source material. The excess argon may pull the plateau and integrated ages up, and thus produce an artificially older age. As such, the inverse isochron age of 69.64 ± 0.63 Ma is considered to be more robust than the circa 72 Ma plateau age for possible hydrothermal alteration defined by the age spectra. However, the 72 Ma age observed in the age spectrum may define the maximum age of hydrothermal alteration (D. Archibald, personal communication, May 12, 2016).

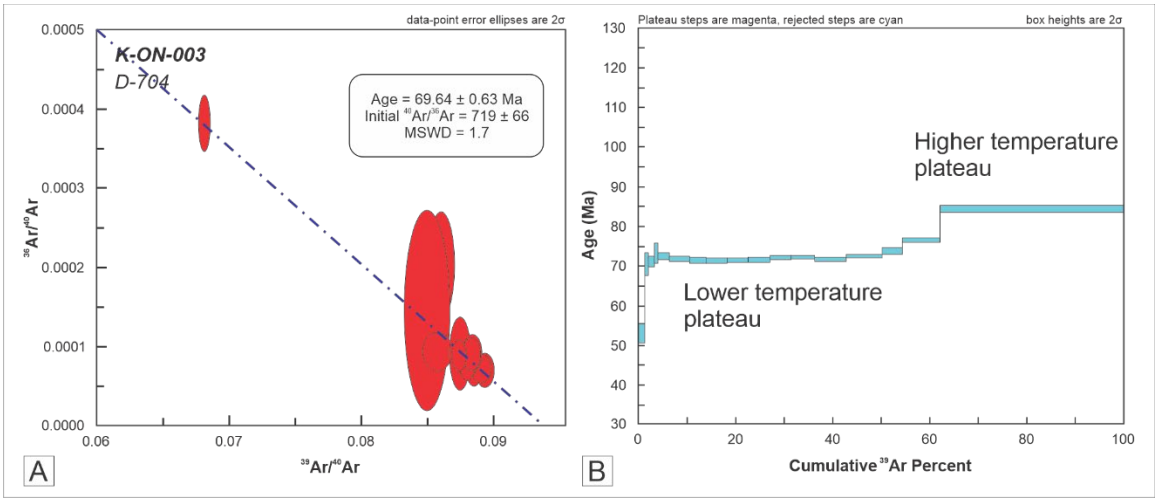

Figure 6.2: Inverse isochron (A) and age spectrum (B) for sample K-ON-003.

Sample: K-ON-004

Location:

Surface sample – Onek deposit; footwall of major fault, collected within 1 metre of main fault surface. UTM 485665 mE, 7087377 mN.

Sample description:

Highly altered chlorite-mica schist composed of fine-grained anhedral quartz (50 to 55%) with coarsely crystalline muscovite (5%), fine-grained sericite (20 %), and chlorite foliations (10 -15 %). The schist hosts bands and pods of quartzite composed of quartz with minor muscovite, foliation-parallel quartz segregations, and foliation is cross-cut by late carbonate (ankerite) veinlets. The schist and quartzite are altered by patchy and disseminated subhedral to euhedral cubic crystals and lesser interlocking crystal clusters of pyrite (1 to 2 %) up to 0.3 mm in diameter.

Results:

No inverse isochron was produced for this sample. The age spectrum does not define a single plateau, however numerous plateau segments are apparent. The best-defined plateau segment has an age of 85.5 ± 0.6 Ma and an MSWD of 1.2 (Table 6.3; Figure 6.3). The minimum age for this plateau is approximately 80 Ma. This plateau segment correlates with the apparent age of initial cooling in sample K-ON-003. As with sample K-ON-003, abundant radiogenic argon was present in the sample that may indicate the presence of excess argon (D. Archibald, personal communication, May 12, 2016). The presence of excess argon and coarse crystalline muscovite (presumably of metamorphic origin) may account for the lack of a coherent plateau, and may suggest the incorporation of metamorphic mica into the analysis.

Table 6.3: Summary of $^{40}Ar/^{39}Ar$ dates for sample K-ON-004.

Integrated Age (Ma)	2-sigma (Ma)			
87.7	0.3			
Plateau or Plateau Segment Age (Ma)	2-sigma (Ma)	$\%^{39}Ar$	MSWD	
85.5	0.6	29.5	1.2	
Inverse Isochron Age (Ma)	2-sigma (Ma)	Initial Ratio	2-sigma (Ma)	MSWD
n/a	n/a	n/a	n/a	n/a
Min Step Date (Ma)	2-sigma (Ma)	Max High-T Step Date (Ma)	2-sigma (Ma)	
49	4	98	1	

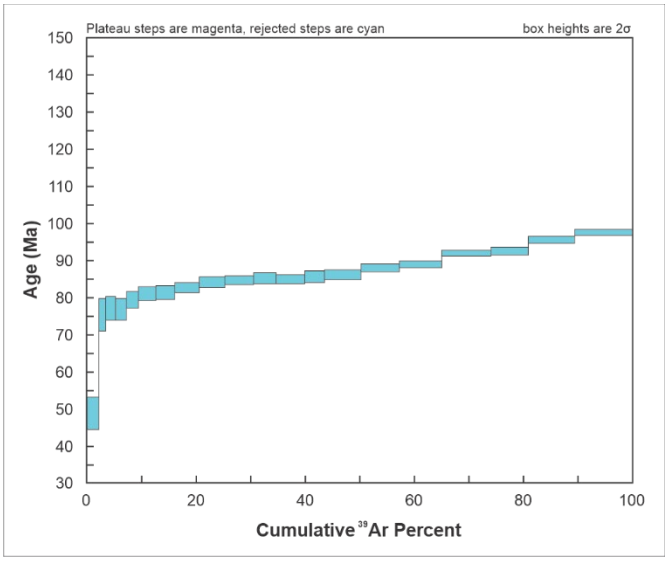

Figure 6.3: Age spectrum for sample K-ON-004.

Sample 0187-005

Location:

Drill core sample – Bellekeno East Zone; surface drill hole K-09-0187; downhole distance 197.96 m

Sample description:

Sphalerite-bearing siderite cement supported breccia with clasts of pale grey, fine-grained, foliated, granoblastic quartzite with equigranular interlocking anhedral quartz and minor discontinuous foliated muscovite and accessory zircon. Schistose layers, 2 to 13 mm thick, are composed of quartz with thick foliations of abundant crystalline muscovite, some of which is internally deformed. Both quartzite and schistose layers are locally host to disseminated by subhedral to euhedral pyrite. The quartzite hosts two thin foliation parallel bands of medium- to coarse-grained quartz that display sutured grains

and undulatory extinction. These bands are truncated at clast boundaries and thus predate hydrothermal alteration; however, it is not clear if the bands simply reflect a coarser-grained portion of the quartzite or if these features represent a metamorphic quartz vein. Furthermore, a portion of the quartzite within the carbonate cemented breccia appears micro-brecciated and cemented by finely crystalline chlorite. Siderite vein texture is open and vuggy in places, with rare large vuggy sphalerite crystals (up to 6mm). Minor quartz occurs as segregations and as siderite vein-concordant or cross-cutting veins with minor pyrite. Modal mineralogy: Quartz (78 to 80 %), Muscovite (6 to 8 %), Chlorite (4 to 5 %), Pyrite (1 to 2 %), Amphibole (<0.1 %), and Zircon (<0.01 %).

Results:

The age spectrum and inverse isochron (Table 6.4; Figure 6.4) show that the sample yielded a higher integrated age (91.0 ± 4.0 Ma) and plateau age (82.4 ± 2.5 Ma) than the inverse isochron age (81.1 ± 4.9 Ma). A ^{40}K decay constant of 5.5545 (±0.0109) x 10^{-10} a^{-1} (Renne et al., 2010) yields an inverse isochron age of 80.9 ± 4.9 Ma. The integrated age is older than the plateau age due to the retention of older dates. The MSWD values for the plateau (0.9) and inverse isochron (2.3) are acceptable. Overall, there is a good correlation between the plateau and inverse isochron ages.

Table 6.4: Summary of $^{40}Ar/^{39}Ar$ dates for sample 187-005.

Integrated Age (Ma)	2-sigma (Ma)			
91.0	4.0			
Plateau or Plateau Segment Age (Ma)	2-sigma (Ma)	$\%^{39}Ar$	MSWD	
82.4	2.5	88.3	0.9	
Inverse Isochron Age (Ma)	2-sigma (Ma)	Initial Ratio	2-sigma (Ma)	MSWD
81.1	4.9	330	20	2.3
Min Step Date (Ma)	2-sigma (Ma)	Max High-T Step Date (Ma)	2-sigma (Ma)	
77	8	119	11	

The sample had low potassium, but also low radiogenic ^{40}Ar. While the inverse isochron indicates that mica growth occurred at circa 81 Ma, the age spectra shows that with increasing temperature the plateau age appears to decrease (Figure 6.4). This apparent age decrease suggests that recoil loss occurred in the surface of analysed grains. Loss or relocation of ^{39}Ar can occur as a result of recoil of the nucleus of ^{39}K caused by the emission of a proton during the (*n,p*) reaction (Faure and Mensing, 2005). If a significant fraction of the ^{39}Ar is lost from the irradiated sample, its $^{40}Ar/^{39}Ar$ ratio is increased correspondingly, and the total-release date would be older than its "geological age" (Faure and Mensing, 2005). Given the lack of multiple plateaus recorded in this sample, the "geological age" is considered to represent the initial growth of mica during hydrothermal alteration.

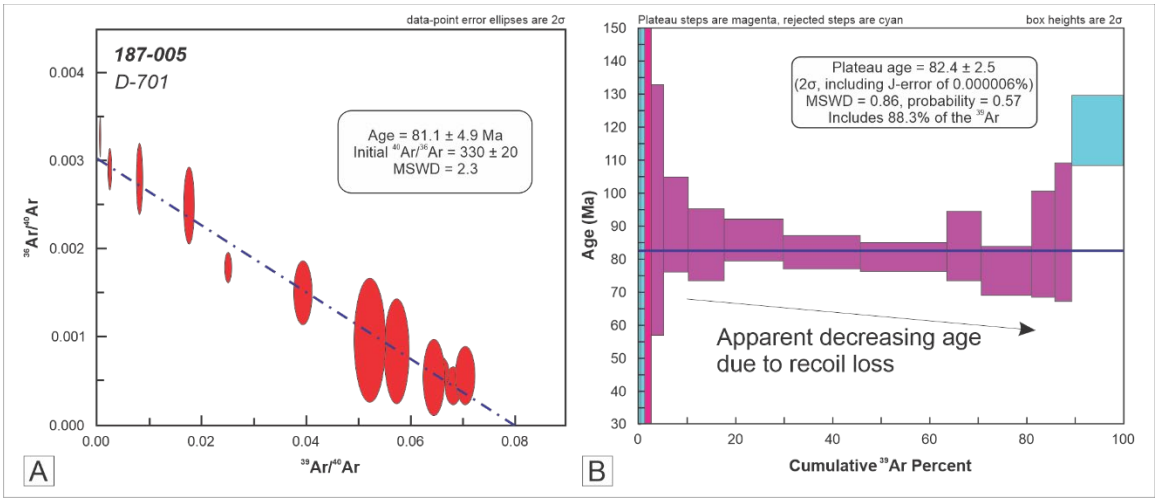

Figure 6.4: Inverse isochron (A) and age spectrum (B) for sample 187-005.

Sample U0160-009

Location:

Drill core sample – Bellekeno Southwest Zone; underground drill hole BKUD09-0160; downhole distance 56.79 m

Sample description:

Contact between host rock quartzite and cross-cutting sulfide vein material. Vein is siderite with quartz, galena, pyrite, and sphalerite. Quartzite is strongly foliated with sporadic intercalated schistose layers. The quartzite consists essentially of granoblastic, fine-grained equigranular interlocking quartz intergrown with minor foliated sericite (5%) plus trace/accessory amphibole and zircon. Quartz grains typically have undulatory extinction and sutured grain boundaries that are typical of metamorphic recrystallization, with grains displaying preferential orientation. Schistose layers, 2 to 13 mm thick, are

composed of quartz with thick foliations defined by abundant crystalline, metamorphic muscovite, some of which is internally deformed.

Results:

The sample analysed was almost pure muscovite. It contained abundant ^{39}Ar, and very little ^{36}Ar. Due to the low concentration of ^{36}Ar, the data clustered along the $^{39}Ar/^{40}Ar$ axis, and non-radiogenic ^{40}Ar could not be distinguished from radiogenic ^{40}Ar. As such no inverse isochron was produced for this sample. No excess argon was identified in Isoplot. The age spectrum does not define a single plateau, and no plateau segments are apparent (Figure 6.5). The sample yielded an integrated age of 83.0 ± 0.4 Ma (Table 6.5). Little meaningful information can be gleaned from this sample, although the age spectrum appears to show an inflection point at around 80 Ma that could be indicative of a mid Cretaceous overprinting event, and the growth of new mica between 70 and 80 Ma (D. Archibald, personal communication, May 12, 2016). The crystalline mica in the sample suggests it is of metamorphic, rather than hydrothermal origin. Overprinting of the metamorphic mica by hydrothermal alteration may be responsible for the incoherent age spectrum.

Table 6.5: Summary of $^{40}Ar/^{39}Ar$ dates for sample U0160-009.

Integrated Age (Ma)	2-sigma (Ma)			
83.0	0.4			
Plateau or Plateau Segment Age (Ma)	2-sigma (Ma)	$\%^{39}Ar$	MSWD	
n/a	n/a	n/a	n/a	
Inverse Isochron Age (Ma)	2-sigma (Ma)	Initial Ratio	2-sigma (Ma)	MSWD
n/a	n/a	n/a	n/a	n/a
Min Step Date (Ma)	2-sigma (Ma)	Max High-T Step Date (Ma)	2-sigma (Ma)	
64	8	122	2	

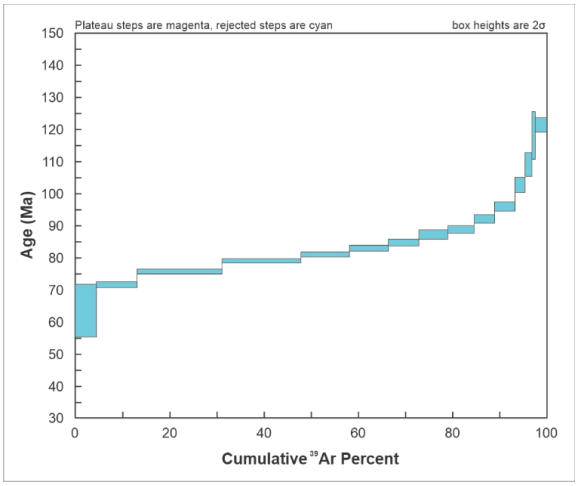

Figure 6.5: Age spectrum for sample U0160-009.

Sample K-BX-007

Location:

Underground sample – Bellekeno underground workings, 750-1 crosscut; footwall vein selvage, sample collected within 0.1 metres of the main fault zone.

Sample description:

Foliated and folded, granoblastic fine-grained quartzite composed essentially of equigranular interlocking anhedral quartz with minor discontinuous foliated fine-grained sericite (5 %) and accessory grains of zircon. Quartz grains typically have undulatory extinction and sutured grain boundaries that are characteristic of metamorphic recrystallization, with grains displaying preferential orientation aligned with the foliation. Sericite commonly defines the foliation, and is present at quartz-grain boundaries, and sporadically appears to overgrow quartz grains. Minor chlorite, pyrite, and galena at vein selvage and rare, < 1 mm, cross-cutting, siderite veins. Weak manganese oxide alteration observed.

Results:

Two analyses were conducted on this sample. The first analysis (D-700) was a whole rock analysis of the sample. The second analysis (JF-151617) was conducted on quartz grains from the sample. Three separate runs were completed on quartz grains of different sizes, and the data were combined to produce the age spectrum and inverse isochron (Table 6.6; Figure 6.6).

Table 6.6: Summary of $^{40}Ar/^{39}Ar$ dates for sample K-BX-007.

Analysis D-700				
Integrated Age (Ma)	2-sigma (Ma)			
86.6	3.2			
Plateau or Plateau Segment Age (Ma)	2-sigma (Ma)	$\%^{39}Ar$	MSWD	
77.9	2.3	89.2	1.3	
Inverse Isochron Age (Ma)	2-sigma (Ma)	Initial Ratio	2-sigma (Ma)	MSWD
77.9	2.6	297	7	1.3
Min Step Date (Ma)	2-sigma (Ma)	Max High-T Step Date (Ma)	2-sigma (Ma)	
72	11	303	28	
Analysis JF-151617				
Integrated Age (Ma)	2-sigma (Ma)			
985.0	29.0			
Plateau or Plateau Segment Age (Ma)	2-sigma (Ma)	$\%^{39}Ar$	MSWD	
n/a	n/a	n/a	n/a	
Inverse Isochron Age (Ma)	2-sigma (Ma)	Initial Ratio	2-sigma (Ma)	MSWD
69.0	33.0	418	8	1.5
Min Step Date (Ma)	2-sigma (Ma)	Max High-T Step Date (Ma)	2-sigma (Ma)	
n/a	n/a	n/a	n/a	

The age spectrum and inverse isochron for analysis D-700 (whole rock) yielded a near identical plateau (77.9 ± 2.3 Ma) and inverse isochron age (77.9 ± 2.6 Ma), and a higher integrated age (86.6 ± 3.2 Ma) (Table 6.6; Figure 6.6A and B). A ^{40}K decay constant of 5.5545 (±0.0109) x 10^{-10} a^{-1} (Renne et al., 2010) yields an inverse isochron age of 77.8 ± 2.6 Ma. The integrated age is older than the plateau age due to the retention of older dates. The MSWD values for the plateau (1.3) and inverse isochron (1.3) are acceptable. The inverse isochron shows a good regression and no excess argon was detected in the analysis. Overall, the excellent correlation between the step heating plateau and inverse

isochron ages indicates that a weighted age of approximately 78.0 ± 2.5 Ma is robust. The lack of a secondary plateau indicates that this sample was not reset, and as such this date likely represents the cooling age of sericite that grew during Ag-Pb-Zn vein propagation. It should be noted that this age is statistically younger than that of sample 187-005, despite the spatial proximity of the two samples.

The inverse isochron for analysis JF-151617 indicates an age of 69.0 ± 33.0 Ma with an MSWD value of 1.3 (Figure 6.6C). A ^{40}K decay constant of 5.5545 (±0.0109) x 10^{-10} a^{-1} (Renne et al., 2010) yields an identical inverse isochron age. The age spectrum shows no plateau and does not yield any valuable information (Figure 6.6D). The large errors associated with the isochron age mean that any interpretation based on this result should be treated with caution, although it should be noted that the isochron age derived from the sample correlates well with the isochron age recorded in sample K-ON-003.

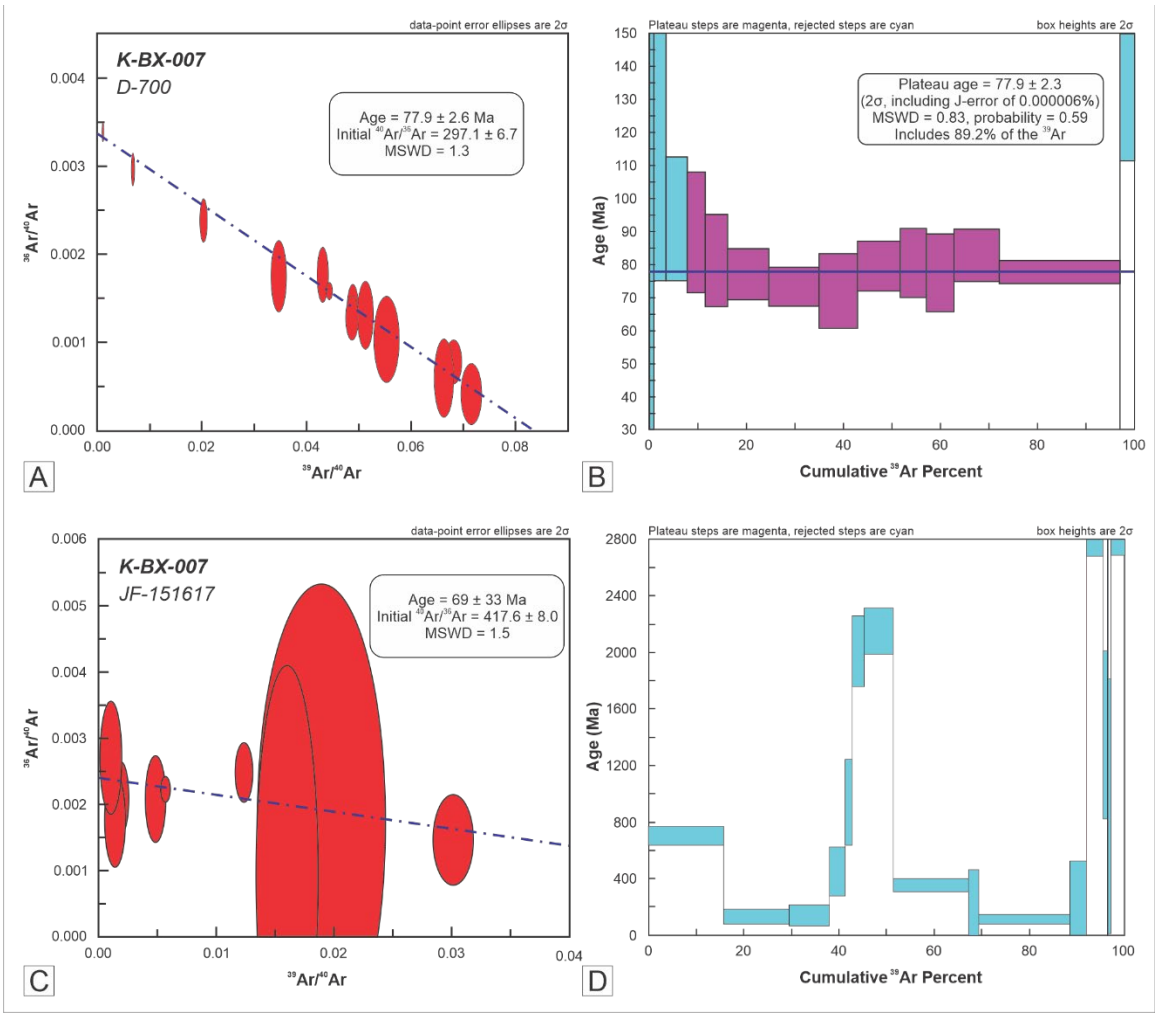

Figure 6.6: Inverse isochron and age spectra for sample K-BX-007. A: inverse isochron for analysis D-700; B: age spectrum for analysis D-700; C: inverse isochron for analysis JF-151617; D: age spectrum for analysis JF-151617.

6.3.2 U-Pb CA-TIMS Analysis

Sample K-KH-003

Location:

Surface sample - ridge above and west of Faro Gulch, north flank of Keno Hill. UTM 490420 mE, 7091898 mN.

Sample description:

Unfoliated, equigranular to porphyritic, grey to pink biotite-hornblende granite (Figure 6.7A). Two to 20 mm potassium feldspar phenocrysts in a fine- to medium-grained groundmass of quartz, plagioclase, potassium feldspar, biotite, and hornblende groundmass. Rare calcite crystals may be associated with post-emplacement fracturing and alteration. Euhedral to subhedral zircon is common and up to 50 micrometres in size (Figure 6.7B). Rare, coarse titanite was also observed.

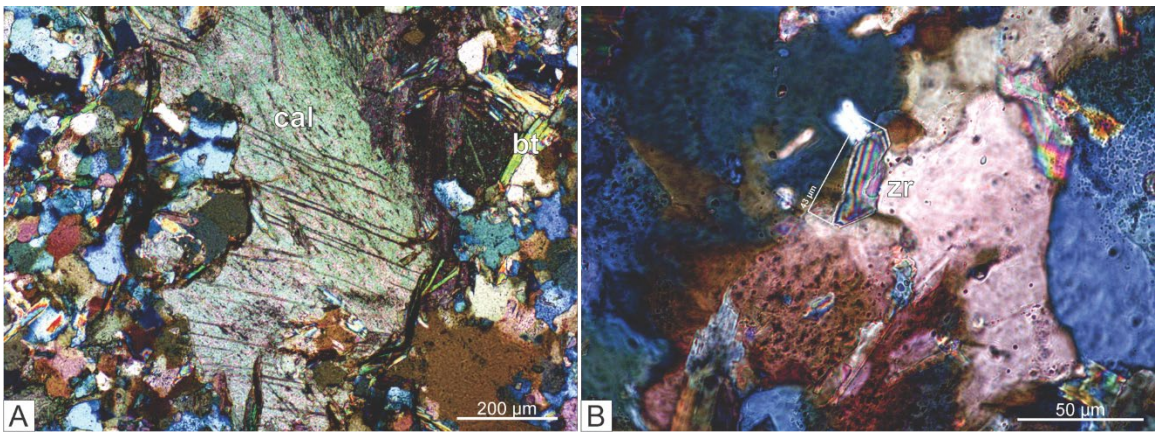

Figure 6.7: Photomicrographs (XPL) of sample K-KH-003 showing (A) calcite in a biotite-quartz-feldspar groundmass; and (B) example of zircon crystals present.

Results:

The concordia diagram for this sample yields an age of 94.7 ± 0.1 Ma from six single zircon grains or grain fragments. The six-point weighted average gives an age of 94.706 ± 0.073 with an MSWD of 1.0 (Table 6.7; Figure 6.8). This is considered to be a robust age for the intrusion and correlates with either the age of Tombstone suite intrusions (90 to 94 Ma; e.g., Murphy, 1997) or Mayo suite intrusions (96-93 Ma; Murphy, 1997; Hart et al., 2004a, b; Tupper and Bennett, 2010) recorded nearby.

Table 6.7: U-Pb isotopic ages for sample K-KH-003

Fractions	$\frac{^{207}Pb}{^{206}Pb}$ (a)	± (b)	$\frac{^{207}Pb}{^{235}U}$ (a)	± (b)	$\frac{^{206}Pb}{^{238}U}$ (a)	± (a)
A	85.43	16.57	94.21	0.71	94.55	0.21
B	120.76	28.77	95.63	1.22	94.63	0.25
C	195.18	53.99	98.02	2.32	94.07	0.28
D	84.96	9.52	94.45	0.44	94.82	0.16
E	63.53	27.94	93.49	1.13	94.67	0.17
F	83.43	10.16	94.29	0.46	94.72	0.16

A: Calculations are based on the decay constants of Jaffey et al. (1971). $^{206}Pb/^{238}U$ and $^{207}Pb/^{206}Pb$ ages corrected for initial disequilibrium in $^{230}Th/^{238}U$ using Th/U [magma] = 3.

B: Errors are 2-sigma, propagated using the algorithms of Schmitz and Schoene (2007) and Crowley et al. (2007).

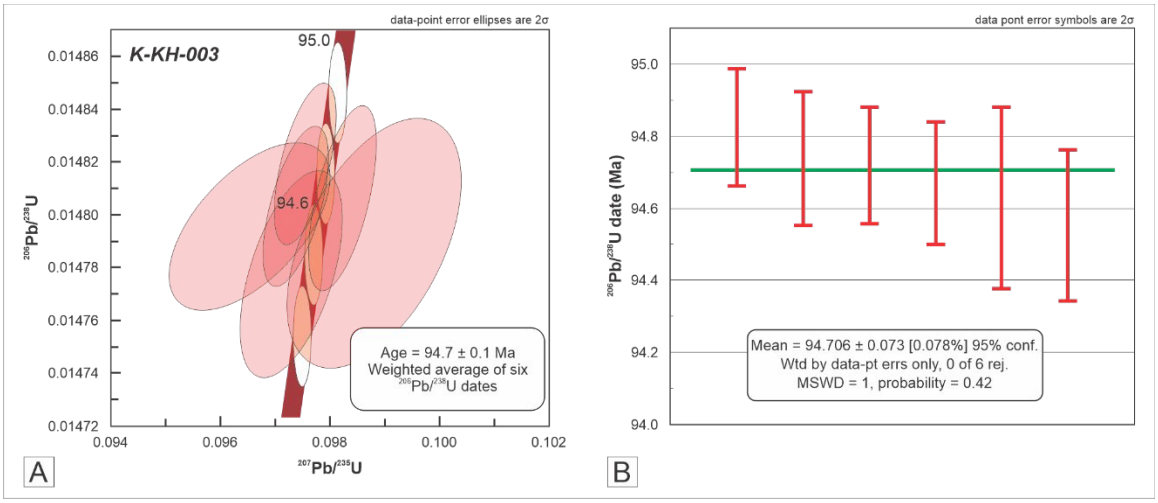

Figure 6.8: Concordia diagram and weighted six-point average chart for sample K-KH-003.

6.4 Summary and Discussion of Geochronology Analysis

The ages established by the $^{40}Ar/^{39}Ar$ dating are of variable confidence, with three samples (K-ON-003, 187-005, and K-BX-007 [analysis D-700]) yielding the most robust results. The data show two separate ages, both of which are younger than the 104 to 100 Ma age for the cessation of metamorphism (Mair et al., 2006).

Initial growth of the hydrothermal mica is interpreted as having occurred in the 78 to 81 Ma range. This range of cooling ages is constrained by sample K-BX-007 (analysis D-700) yielding an age of approximately 77.9 Ma from both the age spectrum and inverse isochron (Figure 6.6), and sample 187-005 yielding an inverse isochron age of 81.1 ± 4.9 Ma (Figure 6.4A). The plateau age for sample 187-005 is slightly older (82.4 ± 2.5), although argon loss by recoil is suspected in this sample, and as such the plateau age may

be artificially older than the geological age (Figure 6.4B) and the inverse isochron age is considered to be more robust. The higher temperature plateau for sample K-ON-003, and the plateau segment for sample K-ON-004 give ages of approximately 85 Ma and 85.5 ± 0.6 Ma, respectively, but excess argon was detected in both samples, and as such the plateau age is likely older than the geological age (Figure 6.2 and 6.3). Sample U0160-009 produced no plateaus, however, an apparent inflection occurs at approximately 80 Ma correlates with the initial cooling dates of the other samples (Figure 6.5).

Single plateau ages of 77.9 ± 2.3 Ma and 82.4 ± 2.5 Ma are observed in the age spectra of samples K-BX-007 (analysis D-700) and 187-005, respectively, indicating that the samples only recorded initial mica growth and were not reset (Figure 6.4B and 6.6B). Both samples were collected from the Bellekeno deposit. Sample K-BX-007 was collected from the contact of an approximately 8 metre wide D_2 galena-siderite-sphalerite vein, while sample 187-005 collected from a siderite-hosted breccia associated with a D_2 fault.

Unlike at the Bellekeno deposit, the $^{40}Ar/^{39}Ar$ analysis of sericite at the Onek deposit (sample K-ON-003) records two hydrothermal events (Figure 6.2B). An initial cooling of mica at approximately 85 Ma, and a subsequent resetting of the geochronometer at 69.6 ± 0.6 Ma (inverse isochron age). While there are significant errors associated with analysis JF-151617, the inverse isochron age (69.0 ± 33 Ma; Figure 6.6C) for this sample is remarkably similar to that from sample K-ON-003; this appears to suggest that a later hydrothermal event occurred. A McQuesten intrusive suite cooling age of 67.03 ± 0.40

Ma ($^{40}Ar/^{39}Ar$ biotite; Rasmussen, 2013) and a crystallisation age of 67.3 ± 0.4 Ma (U-Pb zircon; Murphy, 1997) may indicate heat generated by early stage McQuesten plutonism was responsible for the hydrothermal alteration observed at Keno Hill. Widespread hydrothermal alteration and remagnetisation of underlying rocks at between 70 and 68 Ma is recorded in southwestern Yukon, and is associated with Carmacks volcanism (Johnston et al., 1996b; Wynne et al., 1998; YGS, 2020a). However, remnants of Carmacks volcanism have not been recorded in the Selwyn Basin, and as such no causal link between Carmacks volcanism and hydrothermal alteration at Keno Hill can be reached. Recently, Davis et al. (2019) documented U-Pb ages of calcite veins associated with Au-mineralisation at the Carlin-type Conrad and Sunrise prospects in the Nadeleen trend, approximately 75 km NE of the Keno Hill district. The dates collected by Davis et al. (2019) indicate that Au-mineralisation along the Nadeleen trend occurred between 70 and 75 Ma. While temporally similar, no other link between this mineralising event and the circa 69 Ma hydrothermal event in the Keno Hill district has been reached.

Comparison with previous geochronological studies in the Keno Hill district shows that the approximately 83 to 78 Ma $^{40}Ar/^{39}Ar$ age for initial mica growth and circa 69 Ma age for subsequent hydrothermal alteration defined in this study are routinely younger than the 87 to 85 Ma ages acquired by Wanless et al. (1967) and Sinclair et al. (1980) using the K-Ar method. However, the interpreted maximum initial mica growth age does appear to correlate with the Hantelmann (2013) 82.0 ± 31.0 Pb isotope model age. The U-Pb age derived for the felsic dyke correlates well with the range of ages defined for the Tombstone intrusive suite (Figure 6.9).

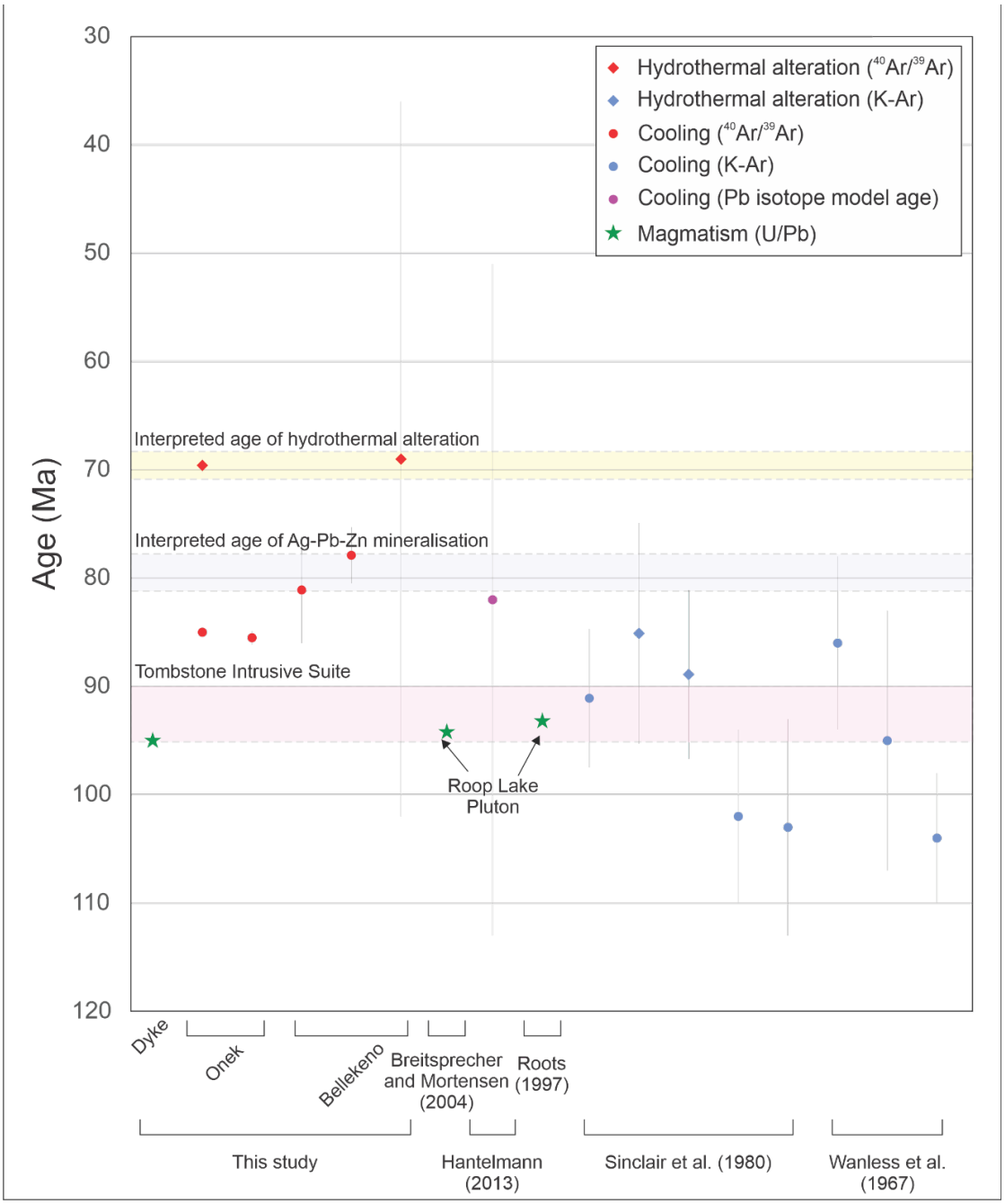

Figure 6.9: Comparison between ^{40}Ar/^{39}Ar and U-Pb ages acquired in this study, and K-Ar and U-Pb ages acquired in or near the Keno Hill district by previous authors.

Sources of historic data: Wanless et al., (1967); Sinclair et al., (1980); Roots (1997); Breitsprecher and Mortensen (2004); and Hantelmann (2013).

7. Discussion

The intent of this study was to elucidate the structural geology of the Keno Hill district, the structural controls and tectonic processes in place at the time of Ag-Pb-Zn mineralisation in the district, and to assess the timing of mineral endowment. The results contribute to understanding the tectonic evolution of the western Selwyn Basin and more specifically the Keno Hill area, and to assist with identifying potential targets for future exploration. In this chapter, the principal elements of the deformation phases and controls on Ag-Pb-Zn mineralisation are discussed within the context of the regional tectonics. The implications of this study for regional prospectivity are also be examined.

The Keno Hill district has a complex, but largely systematic structural geometry that resulted from three discrete phases of deformation. These included pre-, syn-, and post-Ag-Pb-Zn-mineralisation deformation phases (D_1, D_2, and D_3, respectively). These deformation phases record the ductile to brittle-ductile deformation, exhumation, and subsequent brittle deformation of the Keno Hill district between at least the Early Cretaceous and the Eocene (Figure 7.1; Gabrielse et al., 2006).

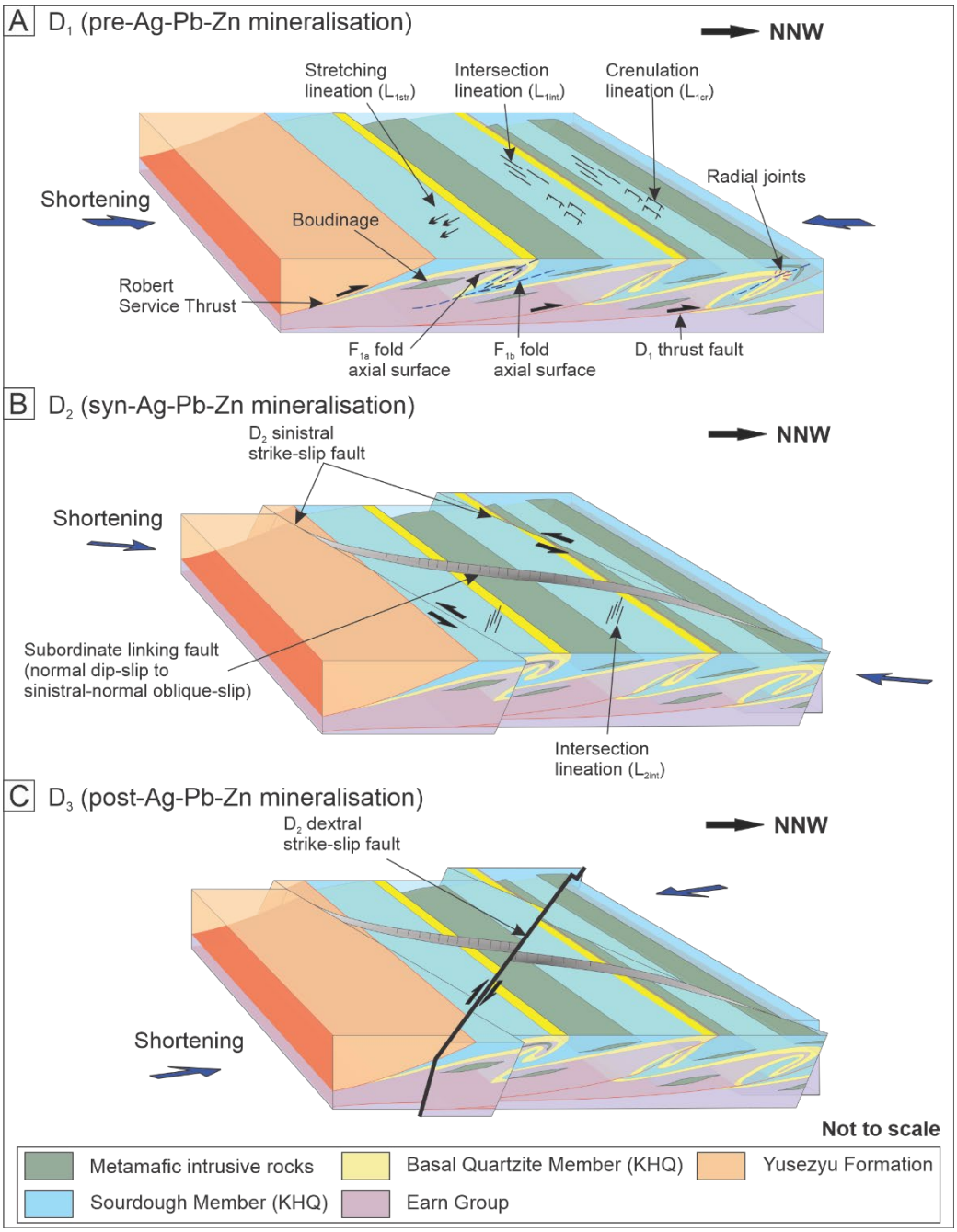

Figure 7.1: Schematic block models showing the essential elements and structural architecture of D_1 (A), D_2 (B), and D_3 (C) deformation in the Keno Hill district. Not to scale.

Rocks in the Keno Hill district comprise a sequence of metasedimentary, basinal rocks that were deposited along the northwestern (present co-ordinates) margin of Laurentia

between the Neoproterozoic to early Cambrian (Yusezyu Formation), and the Mississippian (Keno Hill Quartzite and Earn Group). The sedimentary sequence was intruded by Late Triassic (Carnian) back-arc gabbroic and basaltic rocks (Mortensen and Thompson, 1990), then deformed by ductile to brittle-ductile, and brittle deformation processes (Figure 7.1). Subsequent to ductile to brittle-ductile deformation, the sequence was intruded by rare felsic intrusive rocks.

7.1 Controls on Ag-Pb-Zn-Mineralisation

The localisation of Ag-Pb-Zn-mineralisation is primarily controlled by the complex interplay between fault geometry and orientation, and the rheological contrast between varying rock types in the district. D_2 faults are the most prospective structures in the area, and their associated veins thicken when subordinate faults strike approximately NNE to NE into an orientation approximately subparallel to the (local) D_2 shortening direction and sub-perpendicular to the (local) D_2 extension direction. In addition, where subordinate NNE- to NE-trending structures link with their controlling east-west- to ENE-trending faults Ag-Pb-Zn-mineralisation can be enhanced (Figure 5.22).

Lithology is a critical consideration when defining areas of increased prospectivity. Ag-Pb-Zn-mineralisation is preferentially hosted in thick, competent quartzite units within the Keno Hill Quartzite, and to a lesser extent in deformed Triassic greenstone units. Within the Keno Hill Quartzite, thicker quartzite units are dominantly hosted in the

structurally lower Basal Quartzite Member and are less common in the schist (phyllite), grit, and limestone dominated, structurally higher Sourdough Hill Member. As such, the Basal Quartzite Member is considerably more prospective than the Sourdough Hill Member, the Yusezyu Formation, the Earn Group, and the Triassic metamafic (greenstone) intrusive rocks in the district. Anecdotal evidence suggests that Ag-Pb-Zn-mineralisation may occur within greenstone rocks towards the NE of the district where they intrude Earn Group schistose rocks. It is thought that in this case, in the absence of quartzitic rocks, the greenstone rocks would have had a more brittle response to D_2 deformation than the surrounding schistose rocks, and thus provided the requisite rheological contrast for dilatancy and conduit for fluids responsible for Ag-Pb-Zn precipitation.

A secondary control on the localisation of Ag-Pb-Zn-mineralisation is the pre-D_2 structural architecture in the district. D_1 thrust repetition can increase the apparent thickness of all units in the district, including the thicker quartzitic units of the Basal Quartzite Member. Similarly, fold repetition resulting from two generations of near coaxial, tight to isoclinal folding (F_{1a-b}) has the potential to thicken quartzite units by up to a factor of four. While pre-D_2 thickening of quartzite units by thrust and/or fold repetition is not considered to be a requirement for Ag-Pb-Zn-mineralisation, the thickened units provide a larger volume of preferential host rock that is more likely to focus brittle deformation and localise fluids that then form economic Ag-Pb-Zn deposits.

7.2 Deformation Phases

7.2.1 Pre-Ag-Pb-Zn-Mineralisation Structural Elements and Associated Tectonism

Pre-Ag-Pb-Zn-mineralisation, D_1 deformation is characterised by ductile to brittle-ductile structural elements and is associated with greenschist facies metamorphism described in Chapter 5.1.2. D_1 records the progressive exhumation of the metasedimentary and metamafic sequence, with both ductile elements and brittle structural elements preserved and is associated with regional fold and thrust belt development in the Selwyn Basin.

No dates were retrieved for the age of metamorphism during this study, however correlation of structures observed in the Keno Hill district with work by previous authors suggests that D_1 deformation is bracketed within an approximately 132 Ma period between the early Late Triassic (Carnian) and earliest Late Cretaceous (Cenomanian), but likely initiated during the Late Jurassic. The maximum age for D_1 deformation is defined by the Carnian emplacement of gabbroic to basaltic sills (Mortensen and Thompson, 1990), however the first post-Triassic deformation event documented in the northern Cordillera is associated with Early Jurassic exhumation of the Yukon Tanana Terrane (e.g. Hansen et al., 1991; Johnston et al., 1996a; Dusel-Bacon et al., 2002; McCausland et al., 2002; Villeneuve et al., 2003; Berman et al., 2007; Knight et al., 2013; Nelson et al., 2013) and thus the onset of D_1 deformation in the district almost certainly significantly post-dates greenstone emplacement. Poulton and Tempelman-Kluit (1982) suggested that isolated occurrences of Late Jurassic (Oxfordian) quartz-mica schist, informally termed

the Lower schist, in the northwestern Selwyn Basin represent the youngest passive margin strata in the basin and Mair et al., (2006) suggest that fold and thrust-related deformation migrated northward from the early to latest Jurassic. As such, the onset of D_1 deformation in the Keno Hill district was likely no earlier than the end of the Oxfordian (circa 157 Ma).

Mair et al. (2006) indicate cessation of ductile deformation in the northern Selwyn Basin at circa 100 Ma, this correlates with K-Ar (whole rock) cooling ages collected by Wanless et al. (1967) and Sinclair et al. (1980) within the Keno Hill district. The spatial proximity and similarity in structural style between the fold- and thrust-related deformation presented by Mair et al. (2006) and that documented by this author suggest that it is reasonable to assume a similar Cenomanian age for the end of D_1 deformation and associated greenschist facies metamorphism in the Keno Hill district.

The broad age bracket for D_1 deformation at Keno Hill is coincident with the Early Jurassic accretion and exhumation of the Yukon Tanana Terrane, Middle Jurassic imbrication of the Slide Mountain Terrane, and middle to late Early Cretaceous collision of the Insular Terrane (e.g., Hansen and Dusel-Bacon, 1998; Mihalynuk et al., 1994; 2004; Follo, 1992; White et al., 1992; Clift et al., 2005).

7.2.2 Syn-Ag-Pb-Zn-Mineralisation Structural Elements and Associated Tectonism

Ag-Pb-Zn-mineralisation concomitant with D_2 deformation is characterised by brittle structural elements described in Chapters 5.1.3 and 5.2. D_2 fault propagation was coeval with the genesis of Ag-Pb-Zn-bearing (galena-sphalerite-siderite) veins and rare Au-bearing quartz ± sulfosalt veins.

D_2 fault propagation occurred within a regional sinistral strike-slip fault system; as such, Ag-Pb-Zn-bearing veins are thickest along NE to NNE-striking fault segments at left-stepping bends or linking zones between major sinistral strike-slip faults (Figure 5.22; Figure 5.37; and Figure 5.62). In these areas fault dilation is greatest and produces a low-pressure zone promoting fluid in-flux, mixing, and precipitation of precious and base metals. Anisotropic, 3D modelling of Ag grade within D_2 veins shows a steep SE-plunge to high-grade zones within linking structures that confirms the sinistral strike-slip model for fault propagation and coeval Ag-Pb-Zn mineralisation (Figure 5.37 and Figure 5.62). Additional high-grade zones are recorded at intersections between ENE-striking sinistral strike-slip faults and NE to NNE-striking linking faults (Figure 5.37 and Figure 5.62). In these areas, high-grade mineralisation plunges steep SE, parallel to the line of intersection between the faults and is associated with inherent structural complexity, and the resultant increase in permeability in these areas.

Fault kinematics, F_2 fold axes, and L_2 intersection lineations indicate that the expected shortening direction for D_2 deformation was approximately oriented NE to NNE. A

district wide strain calculation was completed on all D_2 faults in FaultKin™ software that contained slickenfibres with associated steps. The results of the strain calculation indicate a shortening (P) direction of 30°/357° (plunge/azimuth) and an extensional (T) direction of 09°/092° (Figure 7.2A to C). This orientation is somewhat surprising given the field observations of fault kinematics, and the high angle (circa 60°) between the calculated shortening azimuth and the measured strike of sinistral strike-slip, first order faults. An explanation for this discrepancy may be that no weighting was applied to any faults in the calculation. First order faults are, by definition, less common than lower order faults, and as such the calculation was likely biased towards the greater number of NNE-striking lower order faults. To correct this, the calculation was rerun including only faults that strike between 050° and 080°, and faults striking between 230° and 260°. This calculation gives a P-direction of 25°/018° and a T-direction of 03°/287° (Figure 7.2D to E). This orientation appears to correlate better with field observations, and thus is thought to be more accurate.

District- to regional-scale interpretations of airborne magnetic data indicate that the Keno Hill district is located within a regional-scale, left-stepping bend within a major, ENE-trending, sinistral strike-slip structural zone that is truncated by the Tintina Fault (Figure 5.54). The implications of displacement of this structural zone by the Tintina Fault will be discussed in Chapter 7.3. The strain analysis completed on district-wide data (Figure 7.2), and data from the Galena Hill area (Figure 5.22) correlates well with deposit-scale fault and vein analyses across the district, the steep SE plunge of mineralisation derived from 3D modelling, and with the district- to regional-scale structural geometry in

airborne magnetic data. This suggests that the structural requirements for elevated base or precious metal endowment are reproduced at all scales at left-stepping bends along the length of the regional-scale structural zone.

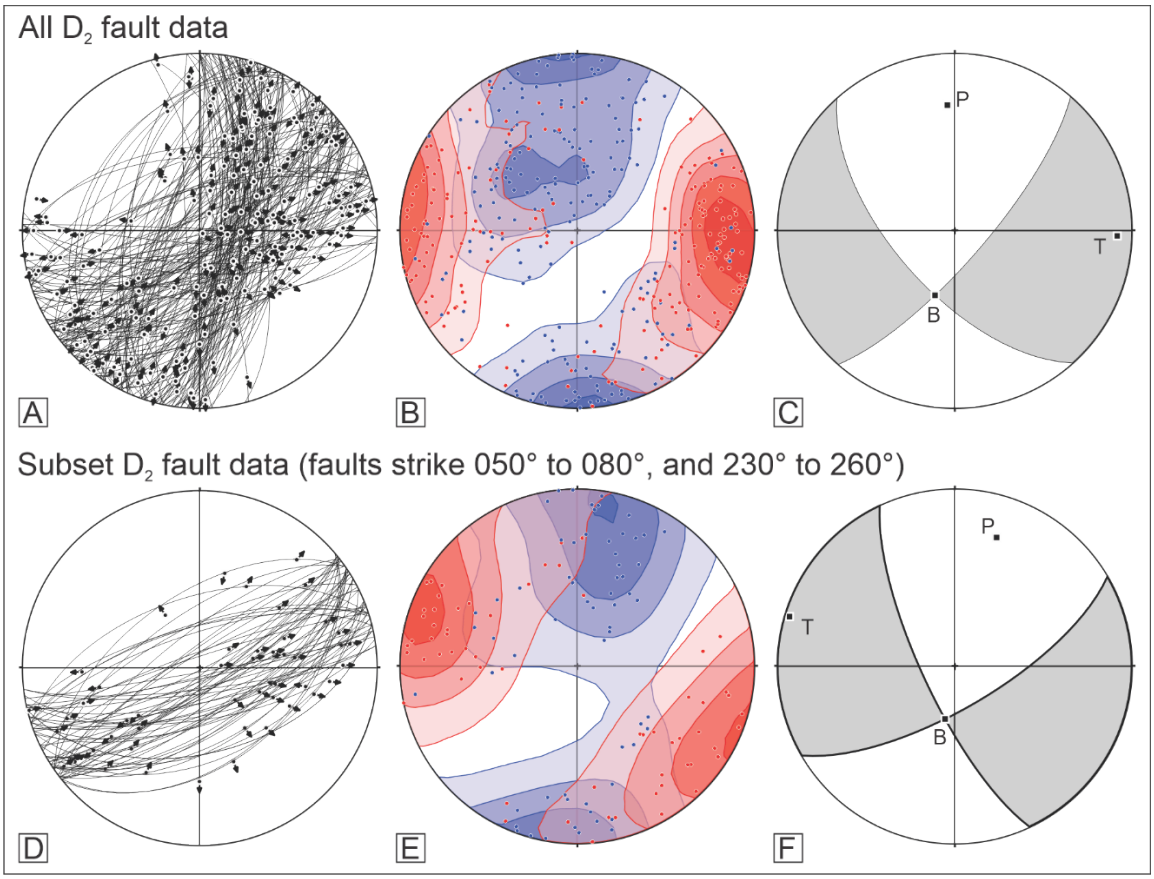

Figure 7.2: Lambert equal area projections of D_2 fault measurements and associated inversions using FaultKin™ software (Marrett and Allmendinger, 1990; Allmendinger et al., 2012).

A: All measured D_1 faults (great circles; polar data, 116 measurements) with slickenline measurements (dots), and hanging wall slip direction (arrows); B: All shortening axes (blue dots) with Kamb contours of shortening axes (blue contours), and extension axes (red dots) with Kamb contours of extension axes (red contours); C: Kinematic axes overlain on P-T dihedra plot calculated with Linked Bingham statistics for all D_2 faults; D: Subset of measured D_1 faults (great circles; polar data, 34 measurements) with slickenline measurements (dots), and hanging wall slip direction (arrows); E: Subset of shortening axes (blue dots) with Kamb contours of shortening axes (blue contours), and extension axes (red dots) with Kamb contours of extension axes (red contours); D: Kinematic axes overlain on P-T dihedra plot calculated with Linked Bingham statistics in for subset D_2 faults. Statistics calculated in FaultKin™ software (Allmendinger et al., 2012). P: shortening axis, T: extensional axis, B: intersection of nodal planes.

D_2 faults were active coevally with Ag-Pb-Zn-mineralisation, and five phases of fluid injection have been recorded during D_2 deformation (Hantelmann, 2013). The ages established by the $^{40}Ar/^{39}Ar$ dating in this study are of variable quality, although three samples (K-ON-003, 187-005, and K-BX-007 [analysis D-700]) yielded interpretable results. The data show two clusters of dates at circa 81 to 78 Ma and circa 69 Ma, respectively. Since these ages are substantially younger than the approximate 104 – 100 Ma age for the cessation of D_1-associated greenschist metamorphism (Mair et al., 2006), it is considered that the sampled micas either grew during D_2 deformation or that their geochronometers were completely reset during D_2 deformation. As such, the two ages established by $^{40}Ar/^{39}Ar$ dating during this study are thought to represent mica growth during Ag-Pb-Zn-mineralisation at circa 81 to 78 Ma, and a subsequent hydrothermal overprinting event at circa 69 Ma.

In terms of regional magmatism, the circa 81 to 78 Ma age for initial mica growth, and presumably Ag-Pb-Zn-mineralisation is interesting. Previous geochronological studies on the age of Ag-Pb-Zn-mineralisation or hydrothermal alteration in the Keno Hill district have yielded K/Ar (whole rock) ages of 86.6 ± 8.0 Ma (Wanless et al., 1967) and 87.0 ± 3.0 Ma (Sinclair et al., 1980), and a Pb isotope model age of 82.0 ± 31.0 Ma (Hantelmann, 2013). The younger ages retrieved in this study, relative to the K/Ar ages retrieved by Wanless et al. (1967) and Sinclair et al. (1980), may be attributable to the methods used for the geochronological study (K/Ar vs $^{40}Ar/^{39}Ar$), as well as to advances in geochronological techniques. However, in terms of the regional magmatism that may

have driven Ag-Pb-Zn-mineralisation, the results of Wanless et al. (1967) and Sinclair et al. (1980) studies, and this study are intriguing.

Ag-Pb-Zn-mineralisation at the Keno Hill district has been associated with emplacement of the Tombstone intrusive suite, and in particular the 92.8 ± 0.5 Ma (U/Pb titanite; Roots, 1997) Roop Lake stock (Lynch, 2006, 2010). An age range of 94 to 90 Ma suggested for emplacement of the Tombstone magmatic suite (e.g., Murphy, 1997) does not correlate with data obtained in this study or with ages reported by the Wanless et al. (1967) and Sinclair et al. (1980) studies.

A time series chart of geochronological data from Ancestral North American (Laurentian Realm) basinal rocks (NAb on Figure 2.4), including the Selwyn, Kechika, and Richardson basins was compiled to assess the timing of recorded mineralisation against the measured age of plutonic rocks in Yukon, Alaska, and British Columbia (Figure 7.3). The time series chart indicates a major pulse of plutonism between 100 and 90 Ma in Yukon. This pulse broadly correlates with successive intrusions of the 115 – 96 Ma Anvil-Hyland-Cassiar belt (Hart et al., 2004a; Rasmussen, 2013), the 98 – 94 Ma Tungsten suite (Gordey and Anderson, 1993; Hart et al., 2004a, b), the 98-93 Ma Mayo suite (Murphy, 1997; Hart et al., 2004a, b; Rasmussen, 2013), and 94-90 Ma the Tombstone suite (Murphy, 1997; Hart et al., 2004a, b; Rasmussen, 2013). A saddle is observed in the data that indicates a waning of magmatism between approximately 90 and 67 Ma. This is followed by an increase in magmatism that is correlated with the McQuesten Suite intrusions (67-64 Ma; Murphy, 1997; Rasmussen, 2013).

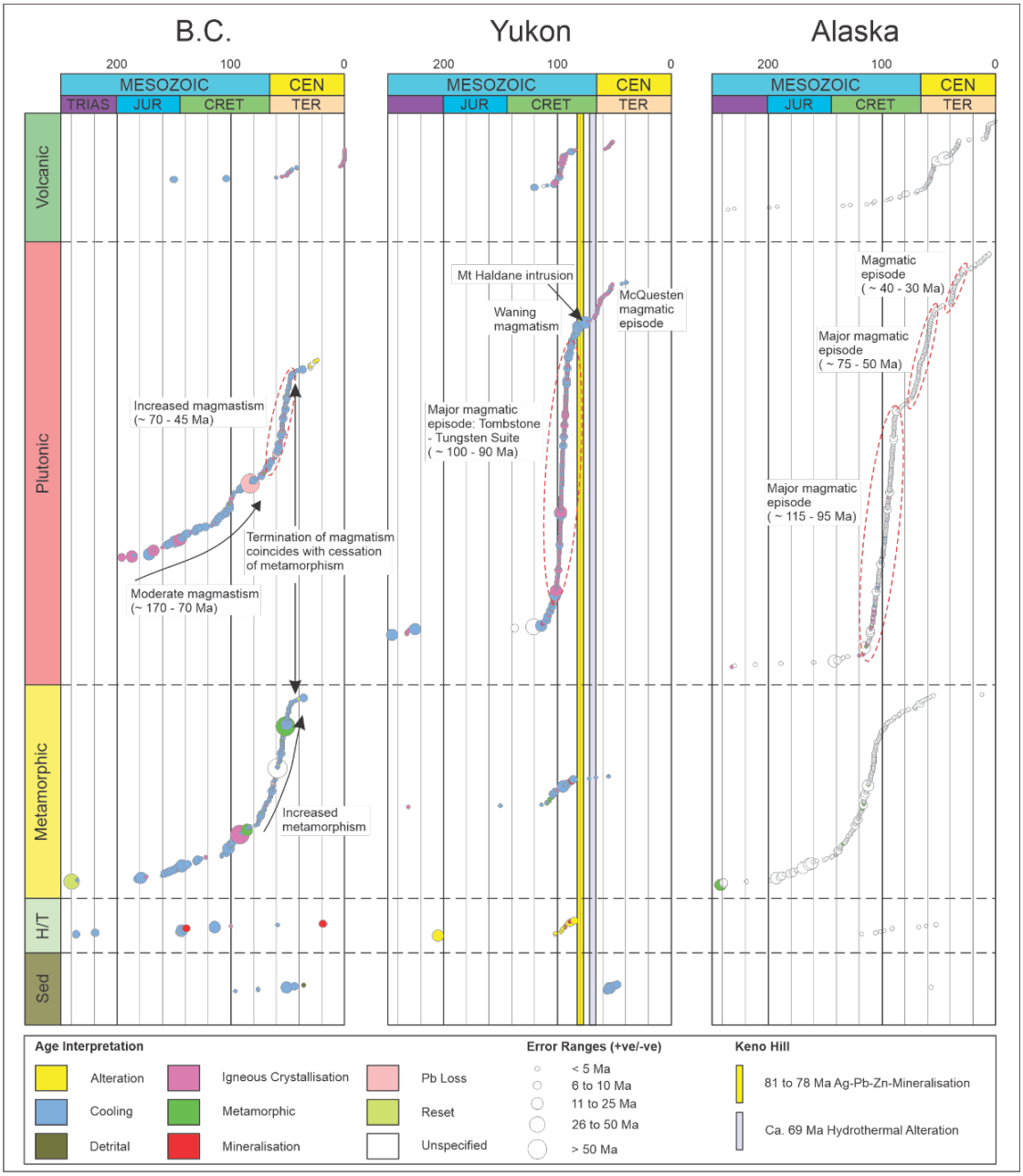

Figure 7.3: Time series chart showing publicly available geochronological data for Ancestral North American (Laurentian Realm) basinal rocks.

Chart is subdivided by volcanic, plutonic, metamorphic, hydrothermal (H/T), and sedimentary (Sed) rocks based on information available in databases. Vertical axis is sorted by rock type only; steeply trending data clusters indicate an abundance of data points for that rock type within a given age bracket, while shallow trending data clusters indicate fewer data points associated with that age. Given the abundance of data available and assuming there is no bias in data collection, this permits an assessment of the timing of major volcanic, magmatic, and metamorphic episodes. Not enough data is available to permit interpretation of depositional or hydrothermal alteration events. Source data: Alaska: USGS (2020); Yukon: YGS (2020a): B.C.: GSC (2013).

A similar quiet period in magmatic activity is recorded in the Alaskan data between approximately 95 and 75 Ma (Figure 7.3). Magmatic activity in B.C. appears to have been moderate from 170 to 70 Ma; however, apparent increases in magmatism occurred at circa 100 Ma and between 70 Ma and 45 Ma. Cessation of the 70 to 45 Ma magmatic episode in B.C. appear to correlate with the cessation of metamorphism, while in Alaska metamorphism appears to have ceased approximately midway through the 115 to 95 Ma magmatic episode (Figure 7.3). Data for metamorphism in the Yukon is sparse and as such no correlation is made.

The estimated age of 81 to 78 Ma for Ag-Pb-Zn-mineralisation in the Keno Hill district sits in a lull between magmatic events, and as such does not appear to correlate with any known major magmatic event in the Selwyn Basin (Figure 7.3). The Tungsten, Mayo, and Tombstone suite intrusive events were all relatively short pulses of magmatism, ranging from approximately 3 to 4 Ma with the bulk of pluton emplacement completed by circa 90 Ma (Gordey and Anderson, 1993; Murphy, 1997; Hart et al., 2004a, b; Rasmussen, 2013). As such, it is thought unlikely that residual heat from these magmatic episodes would have been sufficient to drive Ag-Pb-Zn-mineralisation. Emplacement of the McQuesten Suite (67-64 Ma; Murphy, 1997) occurred too late to be associated with 81 to 78 Ma Ag-Pb-Zn-mineralisation. However, while an overall lull in plutonism is observed between 90 and 70 Ma, rare plutons have been recorded in this window within the basin. One data point is particularly intriguing; approximately 20 km west of Elsa on Mount Haldane, a granitic sill attributed to the Tombstone intrusive suite intrudes the Keno Hill Quartzite and was initially dated at 81 ± 5 Ma (K/Ar biotite; Wanless et al.,

1967) and subsequently recalibrated to Steiger and Jäger (1977) to 83 ± 5 Ma by the Yukon Geological Survey (YGS, 2020a). The fact that this datum was acquired over 50 years ago, and the disparity in age between this intrusion and other Tombstone intrusions suggests that this date, as well as its correlation with the Tombstone intrusive suite, should be treated with some caution. However, the spatial proximity of the intrusion, and apparent similarity in age suggest that magmatic activity associated with emplacement of the sill is a more likely candidate for the source of the Ag-Pb-Zn-bearing fluids than the U-Pb zircon 92.8 ± 0.5 Ma Roop Lakes stock (Roots, 1997).

A hydrothermal resetting of the sericite $^{40}Ar/^{39}Ar$ geochronometer at 69.6 ± 0.6 Ma (inverse isochron age) is apparent in sample K-ON-003 from the Onek deposit. A similar age of 69 ± 33 Ma (inverse isochron age) was retrieved from sample K-BX-007 (analysis JF-151617) at the contact of an approximately 6 metre wide vein in the Bellekeno underground mine, although the large error associated with measurement indicates that this age should be treated with an abundance of caution. As with the 81 to 78 Ma age of initial mica growth, it is not immediately clear with what magmatic episode this hydrothermal event is associated, if any. The earliest recorded ages for the McQuesten Intrusive Suite are 67.03 ± 0.40 Ma ($^{40}Ar/^{39}Ar$ biotite; Rasmussen, 2013) and 67.3 ± 0.4 Ma (U-Pb zircon; Murphy, 1997). These ages are interpreted as cooling and crystallisation ages, respectively, and as such it is possible that heat generated by early stage McQuesten plutonism may have been responsible for the hydrothermal alteration observed at Keno Hill.

It should be noted that the circa 69 Ma hydrothermal alteration at Keno Hill occurred coevally with widespread Late Cretaceous Carmacks Group volcanism in southwestern Yukon (72 to 69 Ma; Grond et al., 1984; Lowey et al., 1986; Hart, 1995; Johnston et al., 1996b). However, despite their temporal affinity, to the author's knowledge remnants of Carmacks volcanism have not been recorded anywhere in the Selwyn Basin. As such no causal link between the Carmacks volcanic event and the circa 69 Ma hydrothermal alteration in the Keno Hill district can be reached.

Concurrent with D_2 deformation and the circa 81 to 78 Ma Ag-Pb-Zn mineralisation in the Keno Hill district, the Yukon-Tanana Terrane experienced extension of the orogen core and dextral transtension. This was a result of approximately north-south directed shortening (Mair et al., 2006; M. Grimshaw, personal communication, September 04, 2020) and produced orogen-parallel, NW-striking, dextral strike-slip faults, such as the 77 – 70 Ma Big Creek Fault (Sánchez et al., 2014; Friend et al., 2017; Mottram et al., 2020) and orogen-orthogonal, NE-striking sinistral strike-slip faults, such as the Dip Creek and Sixtymile-Pika faults (Sánchez et al., 2013). The importance and implications of orogen-orthogonal faults will be discussed in Chapter 7.4, but here it should be noted that the trend and interpreted kinematics of orogen-orthogonal faults correlate well with the interpreted and measured D_2 structures in the Keno Hill district. However, it should also be noted that since the NW-striking, dextral strike-slip faults and NE-striking, sinistral strike slip faults in the Yukon Tanana Terrane have an orthogonal geometric relationship, they are kinematically incompatible. As such, unless the orogen-orthogonal faults have experienced significant clockwise rotation post-initial fault propagation

coeval propagation of the orogen-parallel and orogen-orthogonal faults should not be implied.

7.2.3 Post-Ag-Pb-Zn-Mineralisation Structural Elements and Associated Tectonism

Post-Ag-Pb-Zn-mineralisation, D_3 deformation is characterised by unmineralised brittle structural elements described in Chapter 5.1.4. Strain analysis using FaultKin™ software of all D_3 faults exhibiting slickenfibres and associated steps indicates that D_3 deformation occurred in an almost pure dextral strike-slip system with a P-direction of 09°/006° and a T-direction of 04°/097° (Figure 7.4).

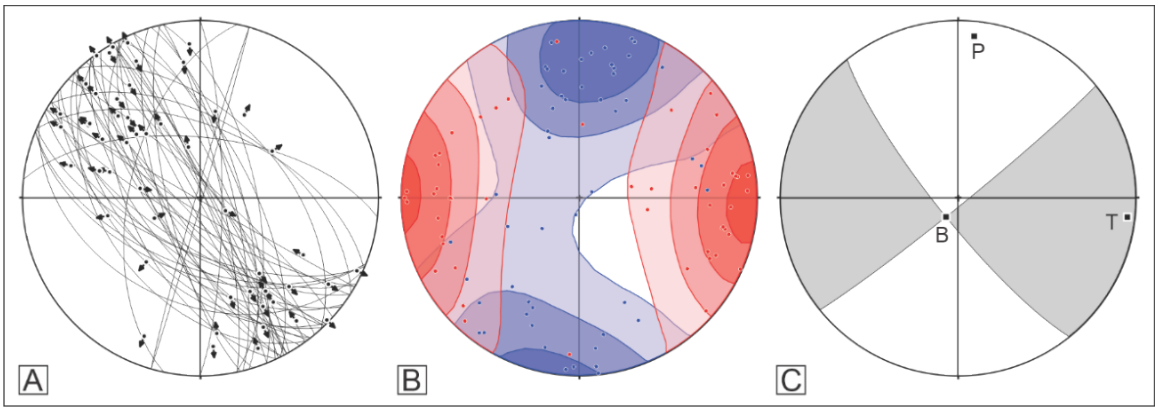

Figure 7.4: Lambert equal area projections of D_3 fault measurements and associated inversions using FaultKin™ software (Marrett and Allmendinger, 1990; Allmendinger et al., 2012).

A: All measured D_3 faults (great circles; polar data, 41 measurements) with slickenline measurements (dots), and hanging wall slip direction (arrows); B: All shortening axes (blue dots) with Kamb contours of shortening axes (blue contours), and extension axes (red dots) with Kamb contours of extension axes (red contours); C: Kinematic axes overlain on P-T dihedra plot calculated with Linked Bingham statistics for all D_2 faults. Statistics calculated in FaultKin™ software (Allmendinger et al., 2012). P: shortening axis, T: extensional axis, B: intersection of nodal planes.

Post-accretion (D_1), NW-trending (orogen-parallel), dextral strike-slip faults are documented throughout Yukon and B.C. by various authors (e.g., Dickinson, 2004; Gabrielse et al., 2006; Nelson et al., 2013; Sánchez et al., 2014). Major structures include the late Early Cretaceous Teslin-Thibert, Hess-Macmillan, and Pinchi faults, and the Cenozoic Tintina and Denali faults (Figure 2.10). The Northern Rocky Mountain Trench (NRMT) Fault is generally considered to be of Cenozoic age; however, some Early Cretaceous displacement is also interpreted to have occurred along this fault (Gabrielse et al., 2006). Cenozoic (mainly Eocene) orogen-parallel faults show elements of both strike-slip and extensional movement, and are spatially associated with alkalic Eocene volcanic and subvolcanic rocks, particularly the Tintina and NRMT faults (Gabrielse et al., 2006). Offset of the 67 – 64 Ma McQuesten plutonic suite indicates that movement along the Tintina Fault initiated no earlier than the latest Cretaceous (Murphy and Mortensen, 2003; Gabrielse et al., 2006), and ceased at circa 43 Ma coincident with the final subduction of the Kula Plate (Gabrielse et al., 2006). In the Keno Hill district, NW-trending, dextral strike-slip faults contain no Ag-Pb-Zn-mineralisation and routinely offset Ag-Pb-Zn-bearing D_2 faults. The timing of mineral emplacement (circa 81 – 78 Ma) shows that propagation of the NW-trending, dextral strike-slip faults cannot have been associated with early Late Cretaceous fault development, and thus must be associated with development of the Cenozoic faults, and in particular the Tintina Fault that occurs approximately 100 km WSW of the district.

Cenozoic strike-slip faults were generated in a broad subduction-related setting (Roeske et al., 2003; Gabrielse et al., 2006) with orogen-parallel displacement attributed to some

degree of coupling between the North American continental plate and the obliquely subducting, offshore oceanic Kula plate (Gabrielse et al., 2006). The Kula plate fused with the Pacific plate between 60 and 55 Ma (Brass et al., 1983), and was completely subducted by 43 Ma. The final subduction of the Kula plate coincides with the cessation of movement along the Tintina and NRMT faults (Gabrielse et al., 2006).

7.3 Post-Ag-Pb-Zn-Mineralisation Transport and its Impact on Regional Prospectivity

Interpretation of regional magnetic data suggests that the Keno Hill fault system is truncated or offset by the Tintina Fault. As such, any assessment of regional prospectivity along the fault system must account for post-mineralisation, orogen-parallel displacement. The amount of orogen-parallel displacement is critical for understanding the relationship between potentially prospective areas and the Keno Hill Fault system. Estimates of post-accretion displacement of, and within, the North American Cordillera have proved highly contentious for decades, and resolution among conflicting datasets has yet to be reached. Brief synopses of the two competing models (the Baja BC and moderate translation models) for the amount of northward translation of the outboard Terranes are given in Chapter 2.1.4. Observations of rocks in Keno Hill district and the wider central Yukon area, and rocks of the Livengood, Pogo, and Tok areas of Alaska observed by this author during the course of this study and subsequent proprietary studies, coupled with work by previous authors (e.g., Blusson, 1978; Weber et al., 1992;

Wiltse et al., 1995; Gabrielse et al., 2006; Colpron and Nelson, 2011; Hayward, 2019; Hayward and Paradis, 2021) suggest that the moderate translation model provides the most reasonable explanation for the observed lithological and/or structural similarities between Keno Hill district and rocks in eastern Alaska.

7.3.1 Palinspastic Restoration of the Tintina Fault

To test the validity of the geological observations an assessment of palinspastic restorations of geological mapping data, elevation data, and airborne magnetic data were completed. Palinspastic restoration of 430 km of dextral strike-slip movement along the Tintina Fault was completed on regional geological maps by N. Hayward (personal communication, January 27, 2017; Figure 7.5). The geological maps used for the restoration were Colpron et al. (2016) for the Yukon data, and Wilson et al. (2015) and Foster et al. (1983) for the Alaska data. Data from the Yukon is substantially more detailed than the Alaskan data and is based on more recent mapping data. As such, caution should be exercised when correlating small-scale geological elements across maps (J. Ryan, personal communication, January 27, 2017).

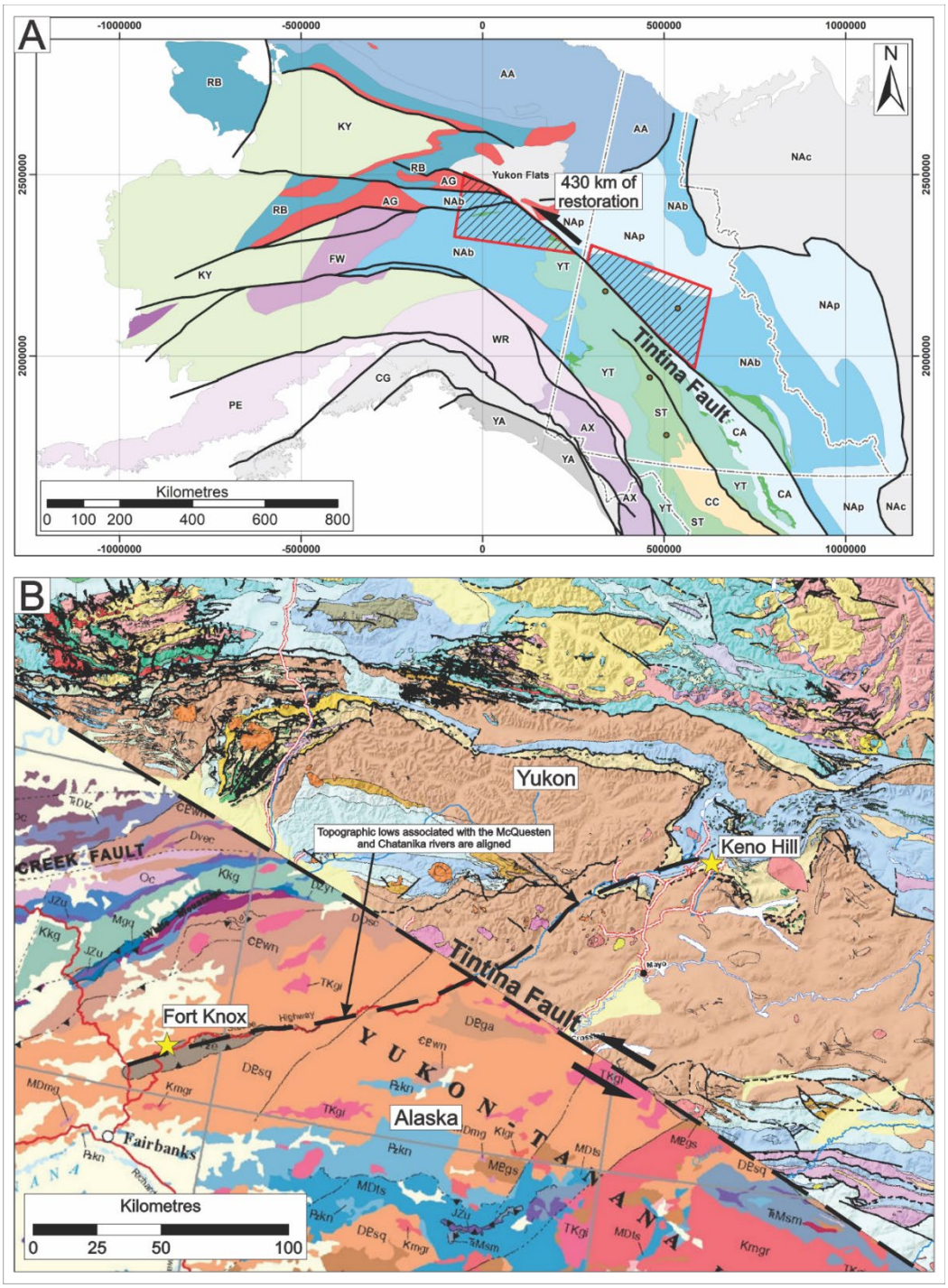

Figure 7.5: Palinspastic restoration of 430 kilometres of dextral strike-slip movement along Tintina Fault of geological mapping data (N. Hayward, personal communication, January 27, 2017).

A) Approximate boundaries of palinspastically restored geological mapping data overlain on Cordilleran terrane map terrane (Colpron and Nelson, 2011); B) Palinspastic restoration of Yukon geological mapping data (Colpron et al., 2016) and Alaska geological mapping data (Wilson et al., 2015).

The restoration juxtaposes clastic, basinal facies of the Laurentian realm Selwyn Basin against metasedimentary, clastic rocks in Alaska (Figure 7.5). In Foster et al.'s (1983) map the metasedimentary rocks in the Alaskan portion of the data were assigned to the Yukon-Tanana crystalline complex, however, more recently have been assigned to basinal facies of the Laurentian realm (Colpron and Nelson, 2011). Descriptions of rocks on either side of the Tintina Fault appear similar with phyllite, shale, sandstone, grit, conglomerate, and limestone of the Hyland Group mapped NE of the Tintina Fault, and pelitic schist, quartzite, and interbedded mafic units mapped in Alaska. In addition, a well-defined, ENE-trending linear topographic low associated with the McQuesten River in the Yukon aligns with an ENE-trending linear topographic low in Alaska that runs parallel to the Steese highway and is associated with McManus Creek and the Chatanika River (Figure 7.5). The McQuesten River defines a topographic lineament that is strongly associated with interpreted first order D_2 faults in the regional-scale airborne magnetic interpretation, and as such it is likely that the aligned, and subparallel topographic lineament identified in Alaska represents the surface expression of the same fault system.

Regional interpretation of airborne magnetic data between the Keno Hill district and the Tintina Fault shows the presence of a wide ENE-trending zone of deformation that is associated with Ag-Pb-Zn-mineralisation in the Keno Hill district (Figure 5.53). The interpretation agrees with the deposit-scale sinistral strike-slip interpretation of D_2 faults in that numerous left-stepping releasing bends are identified in the data. In Yukon, mineralisation at Keno Hill is interpreted to be associated with a macro-scale left-

stepping bend along this fault system (Figure 5.43 and Figure 5.54). Palinspastic restoration of 435 km of dextral strike-slip movement along the Tintina Fault of 1VD airborne magnetic data shows excellent alignment and correlation between the interpreted zone of (magnetite destructive) D_2 deformation between the Keno Hill district and the Tintina Fault, and a zone of subparallel deformation extending WSW of the Tintina Fault from approximately 10 km west of the city of Central, AK, towards the city of Fairbanks, AK (Figure 7.6). The airborne magnetic data for Alaska is of typically lower resolution than that acquired in Yukon, however, patchy areas of higher resolution are available. The data show that the interpreted zone of ENE-trending deformation has the same characteristics as that observed in the interpretation of regional 1VD airborne magnetic data in Yukon. Major (first order) faults are ENE-trending and are linked by zones of NE- to NNE-trending faults that define left-stepping jogs in the fault system. This suggests that the Keno Hill Fault system, prior to Eocene dextral displacement, was through-going and extended well into Alaska.

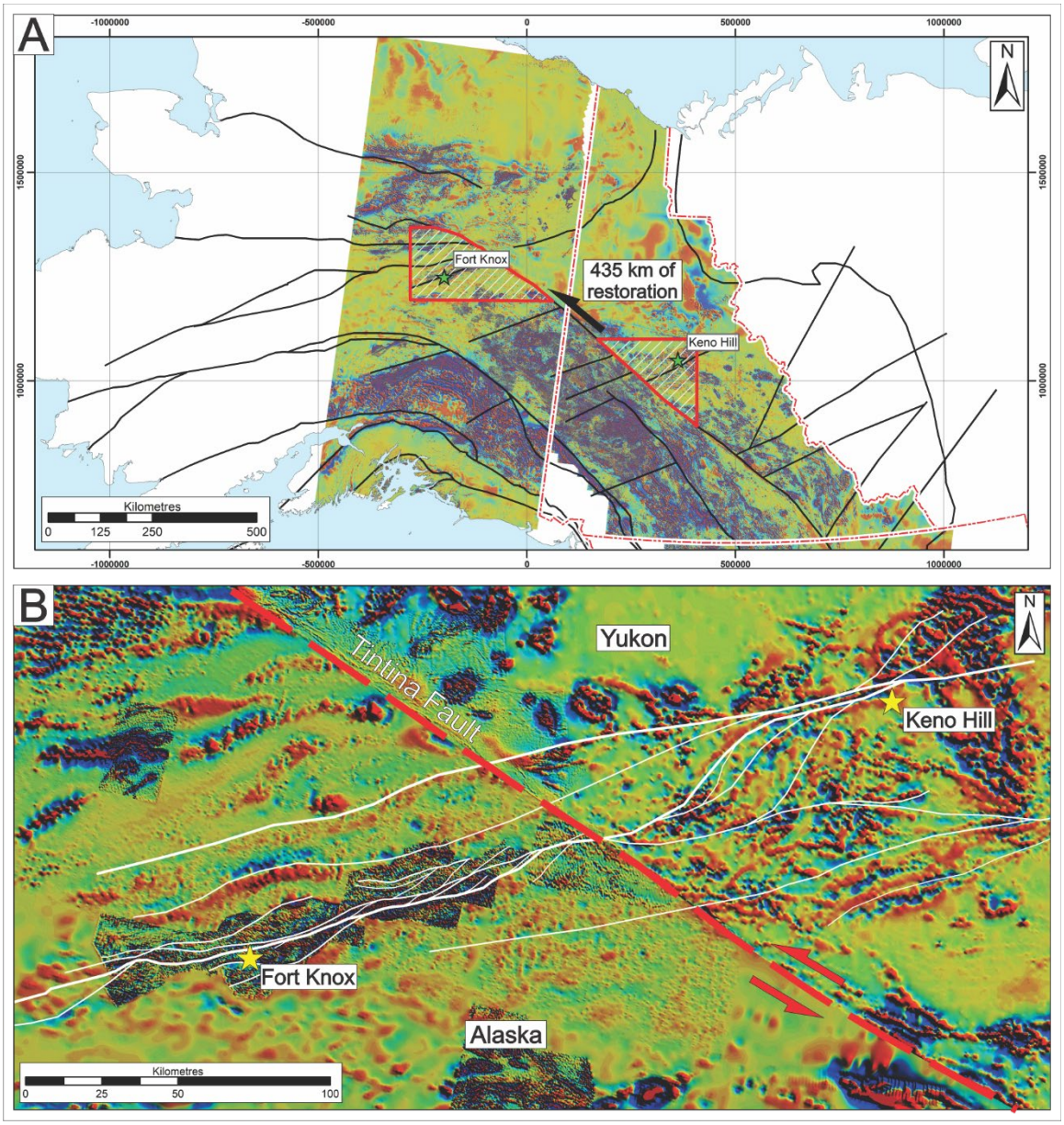

Figure 7.6: Palinspastic restoration of 430 kilometres of dextral strike-slip movement along Tintina Fault of 1VD airborne magnetic data (A) and interpretation of through-going ENE-trending lineaments in palinspastically restored (B). Interpretation shows potential structural link between the Keno Hill and Fort Knox deposits. Source data: Oneschuk et al. (2019).

Regional lithological mapping (Foster et al., 1983) along the trend of this postulated major zone of D_2 deformation offers little in terms of correlation with units in the Selwyn Basin; however sporadic occurrences of gneiss, amphibolite, schist, quartzite, and marble may suggest equivalence to rocks in the Tombstone high strain zone (Murphy, 1997). Detailed geological mapping of an area approximately 30 km WSW of Central, AK (Wiltse et al., 1995), within a left-stepping bend of the interpreted zone of D_2 deformation shows a remarkable similarity to the Keno Hill district (Figure 7.7). In this area a medium to dark grey, slightly calcareous lower schist is overthrust by intercalated, dark to medium grey quartz-muscovite schist and thin to thick layered quartzite, which is overthrust by quartzite with lesser schist and grits up to tens of metres thick, which is in turn overthrust by an upper schist with interlayered marble (Wiltse et al., 1995). The similarity between this sequence and the structurally bottom-to-top sequence of Earn Group schist, basal quartzite member of the KHQ, and Sourdough Hill member of the KHQ (McOnie and Read, 2009) is striking. As in the Keno Hill district, the area mapped by Wiltse et al. (1995) is mapped as being cross-cut by numerous sinistral strike-slip (to presumable sinistral-normal, oblique-slip) faults (Figure 7.7). Numerous mineral occurrences are documented in this area, including occurrences for Au, Ag, and Sn. That these mineral occurrences are within, or proximal to, an interpreted left-stepping of a major ENE-trending deformation zone, and within a package of rock similar to that observed within the Keno Hill district is not considered coincidental, and thus the area should be considered highly prospective.

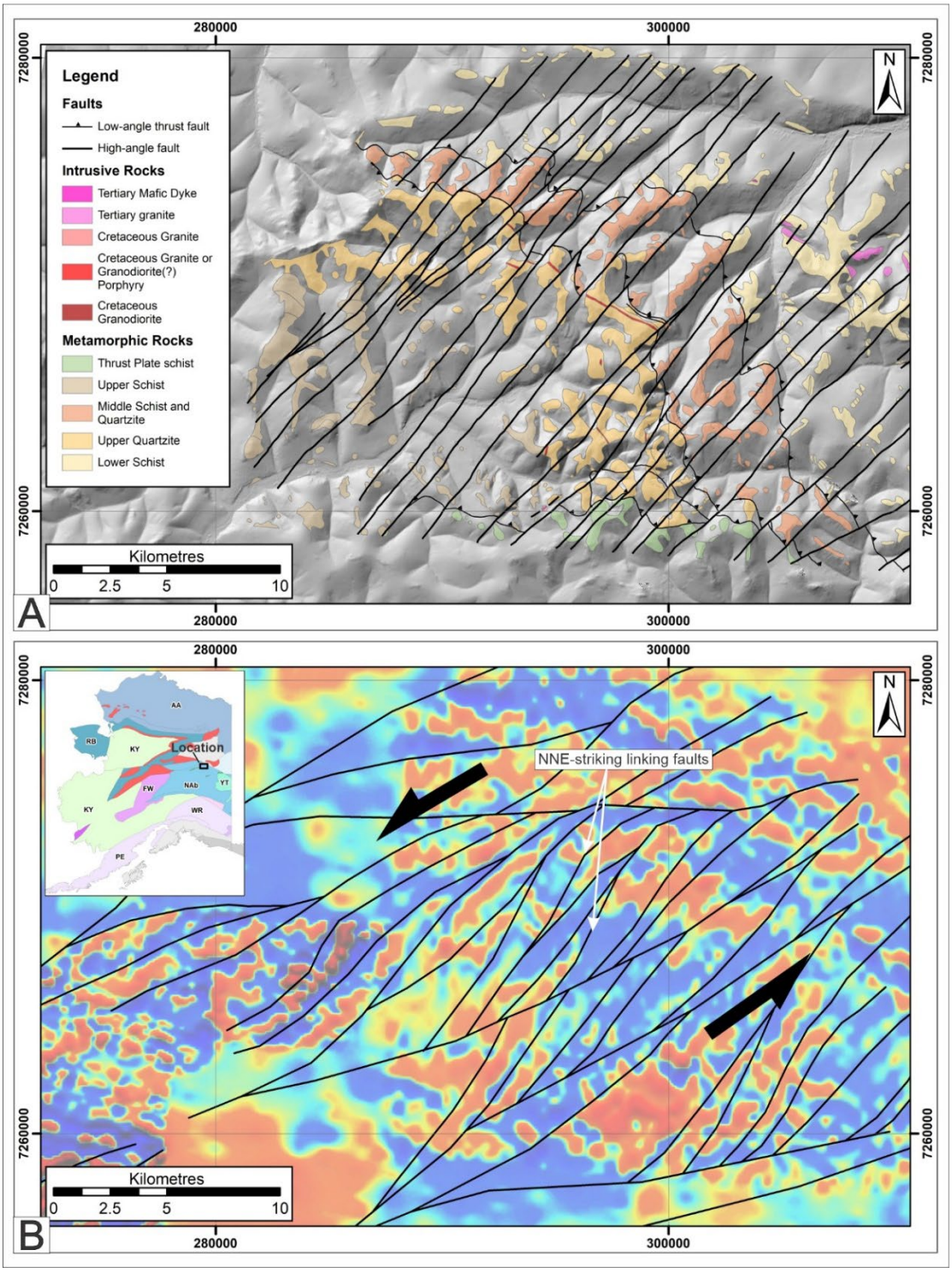

Figure 7.7: A: Geological map (Wiltse et al., 1995) overlain on DEM data; and B; interpretation of 1VD airborne magnetic data (Oneschuk et al., 2019) showing ENE-striking faults linked by NNE-striking faults in an apparent left-stepping, releasing bend approximately 30 km WSW of Central, AK.

7.4 Potential Precambrian Control on Mesozoic Mineralisation

Overall, the tectonic grain of the Cordillera, as defined by airborne magnetic data, follows an orogen-parallel, arcuate trend that delineates the syn-accretionary tectonic history of the orogen; however, numerous, prominent structural trends are apparent at a high angle to the orogen and trend approximately NE (Figure 7.8). The NE-trending structures are laterally continuous and can be traced in basement rocks from Alberta in the east (well beyond the Cordilleran deformation front), underneath Cordilleran cover rocks to at least the Rocky Mountain trench in the west (Ross, 1991, 2002; Nelson et al., 2013; Hayward, 2015; 2019; Hayward and Paradis, 2021).

The orogen-oblique structural trends include the Vulcan structure in Alberta (Price, 1981, 2004), the Red Deer Zone and Hay River Fault in British Columbia and NWT (Nelson et al., 2013), the Liard line in northern British Columbia, southern Yukon, and the Northwest Territories, and the Fort Norman Fault in central Yukon (Figure 7.8; Cecile et al., 1997; Nelson et al., 2013). These structural trends are considered to be long-lived basement structures that likely initiated in response to the assembly of the Paleoproterozoic supercontinent that encompassed Laurentian and Siberian cratons (circa 2000 to 1700 Ma; Price, 2004), and were subsequently reactivated during Neoproterozoic to early Cambrian rifting (circa 600 to 530 Ma; Price, 2004). Reactivation of these structures occurred again during accretion of the Cordilleran orogen (Price, 2004).

These basement structures likely play a significant role in localising major and world class mineral deposits in the Cordillera. Nelson et al. (2013) suggest that in the Eskay mining district in British Columbia, the Eskay rift exploited a pre-existing basement structure and developed as a regional-scale cross-fracture. Elsewhere the Highland Valley Copper porphyry, Sullivan, and Galore Creek deposits in British Columbia, the Howards Pass SEDEX deposit in Yukon, and the intrusion-related Fort Knox deposit in Alaska, all appear to be spatially associated with large, approximately NE-trending, basement structures (Figure 7.8).

If one traces the palinspastically restored, interpreted D_2 Keno Hill fault system along strike, WSW, it intersects and continues beyond the Fort Knox deposit (Figure 7.6). The Fort Knox deposit is considered to be a rare world class example of an intrusion-related gold system (IRGS; Groves et al., 2016). IRGSs are associated with a single, prolonged pulse of magmatic hydrothermal activity related to emplacement of hybrid, reduced granitic intrusions, and comprise sheeted vein networks, and surrounding magmatic As-Au, Sb, and Ag-Pb-Zn hydrothermal skarn deposits (Hart et al., 2002; Hart, 2007). Geochronology by Re-Os and U-Pb indicate mineralisation at the Fort Knox deposit at between 94.5 and 91.2 Ma (Hart, 2004) and hydrothermal resetting between 88.9 and 86.8 Ma ($^{40}Ar/^{39}Ar$; Hart, 2004). The interpreted ages of mineralisation, and hydrothermal resetting at Fort Knox are significantly earlier (at least 10 Ma) than that interpreted for mineralisation and hydrothermal resetting at the Keno Hill district (81-78 Ma, and around 70 Ma, respectively); however, their proximity, after palinspastic restoration, to the same interpreted structural zone is compelling.

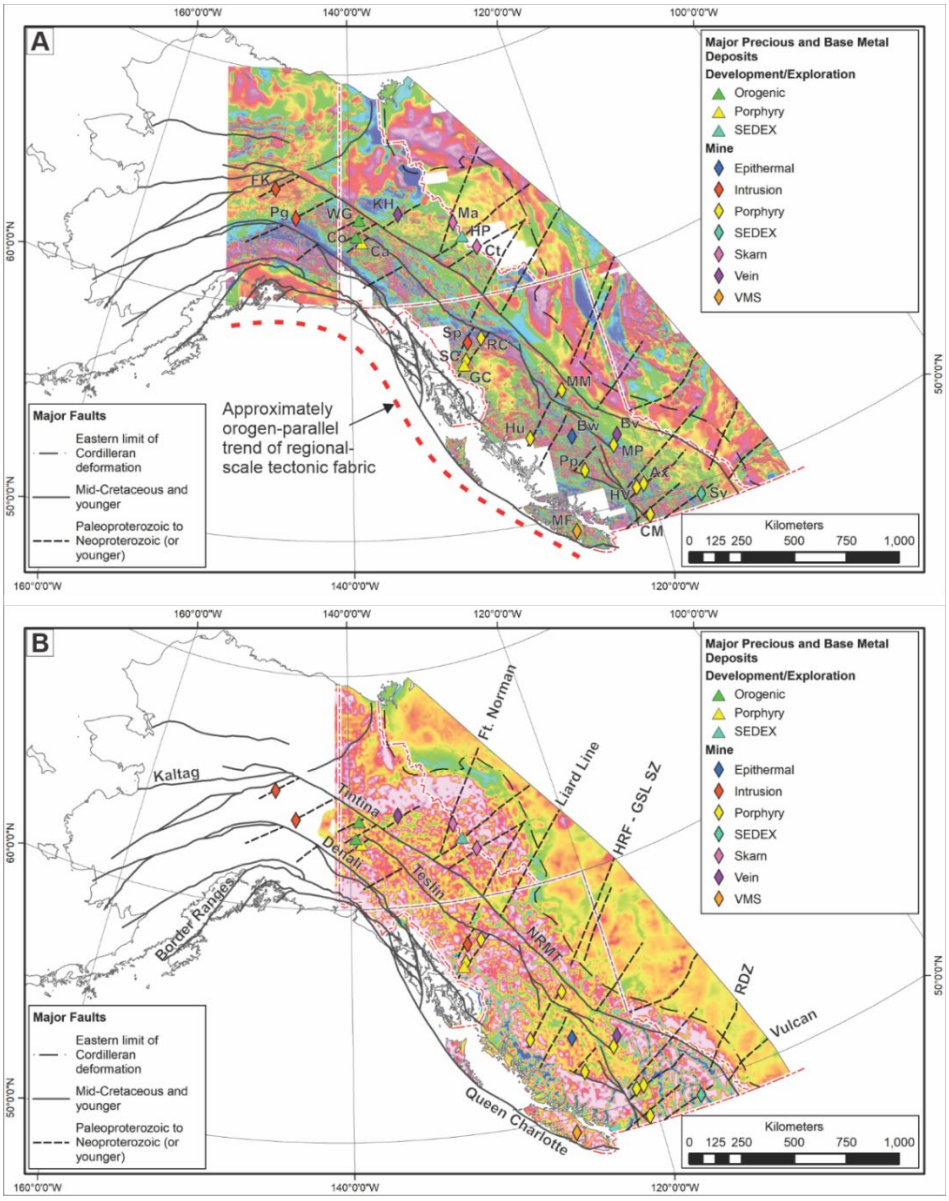

Figure 7.8: Distribution of major precious and base metal deposits in the northern Cordillera, and their spatial association with orogen-oblique, likely Paleoproterozoic-age faults.

A: Composite, regional, residual total field airborne magnetic data. Source data from Miles and Oneschuk (2016) and Oneschuk et al. (2019). B: Regional, free air gravity anomaly data. Source data from Jobin et al. (2017). Raw magnetic and gravity data were compiled, levelled, and shaded in Geosoft Viewer™ software. Mid-Cretaceous and younger faults data from Colpron and Nelson (2011); Paleoproterozoic fault data modified from Nelson et al. (2013). Deposit location data from Nokleberg et al. (2005). Deposit abbreviations: FK, Fort Knox (Au); Pg, Pogo (Au); WG, White Gold (Au); Co, Coffee (Au); Ca, Casino (Au-Cu-Mo); KH, Keno Hill (Ag-Pb-Zn); Ma, Mactung (W); HP, Howards Pass (Pb-Zn); Ct, Cantung (W); Sp, Snip (Au)); SC, Shaft Creek (Cu-Au); RC, Red Chris (Cu-Au); GC, Galore Creek (Cu-Au); MM, Mount Milligan (Cu-Au); Hu, Huckleberry (Co-Mo); Bw, Blackwater (Au-Ag); Bv, Barkerville (Au); Pp, Prosperity (Cu-Au); MP, Mount Polley (Cu-Au); Ax, Ajax (Mo); HV, Highland Valley (Cu); MF, Myra Falls (Cu-Pb-Zn); CM, Copper Mountain (Cu-Au); Sv, Sullivan (Pb-Zn).

While the source of magmatism that may have driven mineralising fluids at Keno Hill remains uncertain, Au-mineralisation at Fort Knox is associated with a Fairbanks suite monzogranitic to granodioritic intrusion (Thompson et al., 1999; Hart, 2004, 2007; Goldfarb et al., 2007). The Fairbanks intrusive suite is considered to be the Alaskan equivalent of the Tombstone intrusive suite in Yukon (Thompson et al., 1999). The Fort Knox deposit lies close to the long-lived craton margin (Groves et al., 2016), and isotropic and geochemical data from the Fairbanks suite indicate the presence of significant crustal components in the magma (Thompson et al., 1999). The presence of more primitive magmas, and carbonic fluid inclusions suggest the involvement of asthenospheric or lithospheric mantle magmatic processes, and as such the intrusion associated with the Fort Knox is considered to have been emplaced at intermediate to deep crustal levels (between 3 and 6 km; Thompson et al., 1999).

In the Keno Hill district, rare lamprophyre dykes have been observed. The precise timing of lamprophyre dyke emplacement is unknown. Offset of a lamprophyre dyke by a mineralised D_2 fault at the Formo deposit indicates that they were emplaced pre-Ag-Pb-Zn-mineralisation (Boyle, 1965), and Murphy (1997) suggests that the lamprophyre dykes are associated with emplacement of the Tombstone intrusive suite. Lamprophyres are of mantle origin and originate from up to 100 km depth in subduction zones and continental rifts and have been reported as components of bimodal dyke suites in hydrothermal Pb-Zn deposits (Štemprok and Seifert, 2011). The coincidence between both the world class Keno Hill and Fort Knox deposits, and a single, major structural zone suggests that magmatism, hydrothermal fluid circulation, and mineralisation at are

fundamentally controlled by the same ENE-trending fault zone. The approximate 10 Ma age difference between the deposits suggests that the fault zone was a long-lived structure, while the interpreted intermediate to deep depth of emplacement of the Fort Knox intrusion, and the occurrence of post-metamorphic lamprophyre dykes at Keno Hill suggest that the fault zone is a crustal-scale structure.

The Keno Hill Fault system and its possible extension into Alaska are broadly ENE-trending and approximately orogen-orthogonal. An inherent problem with determining the regional abundance and extent of orogen-orthogonal faults is that regional- and smaller-scale magnetic and gravity surveys, and seismic profiles are commonly acquired along the same, broadly NE-trend, and orthogonal to the regional structural grain. While this does not prohibit delineation of orogen-orthogonal structures, their magnetic or gravity signatures are commonly diminished. Large or very large structures are still apparent in data, however smaller structures may be missed. In the available data orogen-orthogonal structures appear to be rare in the Selwyn Basin and more abundant in the pericratonic terranes where they are considered to be of Late Cretaceous age (Sánchez et al., 2013, 2014). It is not clear if this is simply due to the availability of higher resolution magnetic data in the pericratonic terranes, if this is a true reflection of their relative abundances, or if this is due to the generally crystalline pericratonic rocks more readily fractured in this orientation than the metaclastic rocks of the Selwyn Basin.

Three-dimensional gravity models suggest that extended North American basement continuously underlies a thin carapace of accreted terranes in western Yukon and eastern

Alaska (Hayward, 2015), including the Selwyn Basin. These basement structures likely play a significant role in localising Mesozoic mineral deposits in the Cordillera (Figure 7.8). Hayward (2015) suggests that the spatial relationship between mineral occurrences and post-accretionary, Cretaceous lithospheric lineaments indicates that late Proterozoic lineaments influenced Mesozoic mineralization through influence on the development of the shallow crustal structure, intrusion, and exhumation and erosion.

Three, named, major basement lineaments have previously been identified in geophysical data within or at the margins of the Selwyn Basin (Figure 7.8). Towards the southern margin of the basin, the Liard Line and Beaver River structures are coincident with a plan-view narrowing of basinal strata across which the laterally extensive Selwyn Basin to the NW pinches-out and becomes the Kechicka Trough to the SE. The Liard Line intersects the northern Cordillera near the platformal to basinal transition of the Ancestral North American basement and is interpreted as a transfer zone that separated a zone of lower plate extension in the Selwyn Basin from upper plate extension in the Kechicka Trough (Hayward, 2015). The Beaver River structure is sub-parallel to the Liard Line, and is interpreted to be related to be a Precambrian structure associated with thickness variations in the Proterozoic basement and to have episodically influenced the deformation of younger strata (Hayward, 2015). The Fort Norman Line trends NE and cuts through the central part of the Selwyn Basin. It is interpreted to be a NW side down structure that underlies the Mackenzie Mountains (Hayward, 2015).

To the author's knowledge, no Precambrian basement structure has been interpreted in the area around Keno Hill; however regional gravity, magnetic, and topographic data suggest this may be a possibility (Figure 7.9). A well-defined, ENE-trending lineament in gravity and RTF magnetic data is spatially coincident and aligns closely with the zone of D_2 deformation in the Keno Hill district. The gravity lineament is well-defined in the Selwyn Basin, cuts across the Dawson Thrust, and can be traced as a subtle gravity low across the Mackenzie Platform and into cratonic rocks in N.W.T (Figure 7.9A). The gravity lineament defines the boundary between an area of high gravity to the north from moderate to low gravity to the south and broadly coincides with a moderate change in topographic relief, with higher elevations occurring north of the lineament (Figure 7.9C). The acquired gravity data do not extend into Alaska; however, the well-defined lineament in regional RTF and 1VD magnetic data mentioned above is coincident with the gravity lineament in the Selwyn Basin and the magnetic lineament appears to extend at least 230 km WSW into Alaska after palinspastic restoration of 430 km dextral strike-slip along the Tintina Fault (Figure 7.6). The total length of the lineament after palinspastic restoration of magnetic data is between 435 and 450 km but may be greater than 840 km if the subtle gravity low in the Mackenzie Platform is included (Figure 7.9A). As such, it is suggested here that emplacement of the Keno Hill and Fort Knox deposits are related to a long-lived, Precambrian basement structure that is present beneath the North American margin platformal and basinal and possibly pericratonic rocks, that was reactivated and controlled the spatial, and geometric development of faults in the overlying rocks during the Late Cretaceous (as per Price, 2004). In the Selwyn Basin, this proposed structure may also be related to Au-mineralisation at the Tombstone intrusive suite-associated

Dublin Gulch (Eagle mine), Scheelite Dome, and Tertiary plutonism-associated at the Rackla project, all of which are proximal to, or along strike of the Keno Hill deposit, and within the envelope of deformation associated with the basement structure, as defined by regional magnetic data (Figure 5.53 and Figure 7.9).

In the Selwyn Basin, in addition to the D_2 fault system, the postulated basement fault is spatially coincident with the D_1 Tombstone high strain zone. It is possible that structural complexity generated by Jurassic to mid-Cretaceous development of the Tombstone high strain zone focussed the subsequent D_2 deformation. This would not necessarily require the presence of a deep-seated, controlling basement structure. However, the apparent continuity of the gravity lineament ENE beyond the Dawson Thrust and the lack of certainty regarding the extent of Tombstone high strain zone-associated rocks in Alaska suggests that the coincidence of the basement structure with rapid changes in lithology in the basin may have instead focussed D_1 deformation, and subsequently focussed D_2 brittle deformation and dilatancy enhancing regional Ag-Pb-Zn-bearing fluid flow.

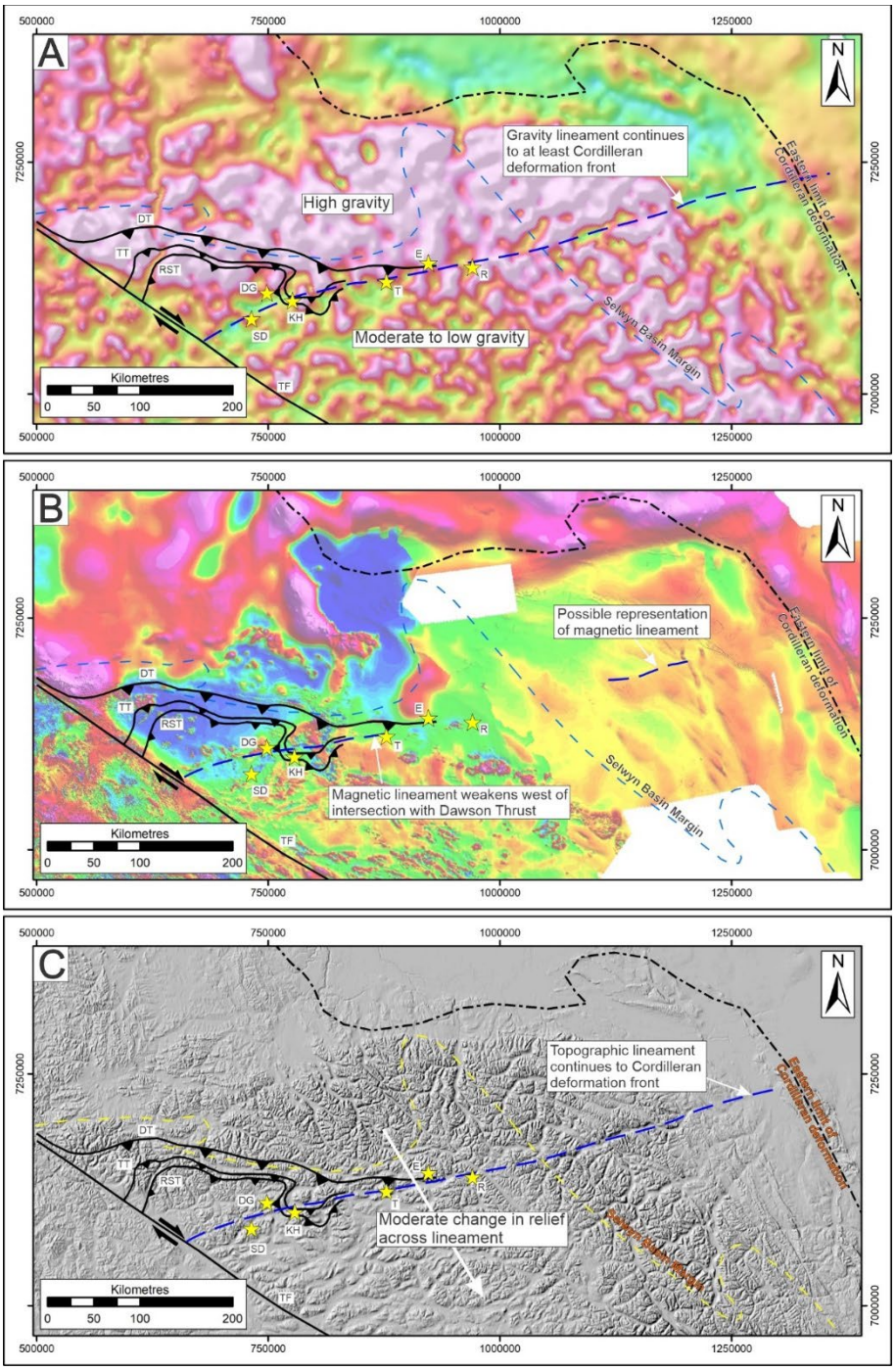

Figure 7.9: Proposed location of Precambrian basement structure that controls deformation in overlying basinal rocks, based on observations from regional free air gravity anomaly data (A), regional airborne magnetic RTF data, and topographic data.

Structural elements: DT: Dawson Thrust; RST: Robert Service Thrust; TF: Tintina Fault; TT: Tombstone Thrust (source Gabrielse et al., 2006). Deposit/exploration locations (yellow star): DG: Dublin Gulch; E: Einarson; KH: Keno Hill; R: Rackla; SD: Scheelite Dome; T: Tell (source YGS (2020b). Gravity source data from Jobin et al. (2017); regional airborne magnetic RTF source data from Oneschuk et al. (2019).

8. Conclusions

The following concluding remarks summarise the objectives, and findings of this thesis and make recommendations on future work. The objective of this study was to understand the structural geology of the historic Keno Hill mining district, the structural controls and tectonic processes in place at the time of Ag-Pb-Zn mineralisation in the district, and to assess the timing of mineral endowment through field, laboratory, and desktop analysis. The results of the work are intended to help understand the tectonic evolution of the western Selwyn Basin and more specifically the Keno Hill area, and to assist with identifying potential targets for future exploration. The scope of work comprised detailed structural analysis of open pit, underground deposits, and outcrops; geochronological analysis of intrusive and fault-related rocks; and analysis of deposit to regional-scale airborne magnetic, gravity, and digital elevation data.

8.1 Deformation in the Keno Hill District

The structural history of the Keno Hill district is comprised of three discrete phases of deformation. These included pre-, syn-, and post-Ag-Pb-Zn-mineralisation deformation phases (D_1, D_2 and D_3, respectively). These deformation phases record the ductile to brittle-ductile deformation, exhumation, and subsequent brittle deformation of the Keno Hill district between at least the Late Jurassic and the Eocene.

Pre-Ag-Pb-Zn-mineralisation, D_1 deformation is characterised by ductile to brittle-ductile structural elements and is associated with greenschist facies metamorphism, and records the progressive exhumation of the metasedimentary and metaigneous sequence present in the study area. Structural elements include (but are not limited to) a transposed, composite $S_{0\text{-}1a\text{-}1b}$ foliation, two generations of near coaxial, tight to isoclinal, upright to recumbent, commonly asymmetric folds (F_{1a} and F_{1b}), and thrust faults. $F_{1a\text{-}b}$ fold axes, mineral stretching lineations, and strain analysis of D_1 faults indicate NNW-directed shortening with sub-vertical extension.

D_1 deformation is bracketed to an approximately 132 Ma period between the early Late Triassic (Carnian) and earliest Late Cretaceous (Cenomanian), but likely initiated during the Late Jurassic. This is coincident with the Early Jurassic accretion and exhumation of the Yukon Tanana Terrane, Middle Jurassic imbrication of the Slide Mountain Terrane, and middle to late Early Cretaceous collision of the Insular Terrane (e.g., Follo, 1992; White et al., 1992; Mihalynuk et al., 1994; 2004; Hansen and Dusel-Bacon, 1998; Clift et al., 2005).

Syn-Ag-Pb-Zn-mineralisation, D_2 deformation is characterised by brittle structural elements that include ENE-striking, sinistral strike slip faults, NE- to NNE-striking, sinistral-normal oblique-slip linking faults. The orientation of D_2 faults has a bimodal distribution, with larger (first order), commonly more through-going faults striking between 050° and 060°, and commonly small, linking faults striking between 010° and 020°. Observations of D_2 fault, L_2 lineation, and F_2 fold relationships in the field, and

subsequent strain analysis indicates a shallow to moderate, NNE-plunging shortening direction and a shallow to subhorizontal ESE extension direction.

D_2 faults developed in a regional sinistral strike-slip fault system where fault dilation was greatest along NE- to NNE-striking fault segments at left-stepping bends or linking zones between major sinistral strike-slip faults. Low-pressure zones associated with fault dilation promoted fluid in-flux, mixing, and precipitation of precious and base metals, and as such Ag-Pb-Zn-bearing veins are thickest along NE- to NNE-striking fault segments. Ag grade within D_2 veins shows a steep SE-plunge to high-grade zones within linking structures that confirms the sinistral strike-slip model for fault propagation and coeval Ag-Pb-Zn mineralisation. Additional high-grade zones are recorded at intersections between ENE-striking sinistral strike-slip faults and NE- to NNE-striking linking faults where mineralisation plunges steep SE, parallel to the line of intersection between the faults.

D_2 deformation in the Keno Hill district may be associated with NNE-SSE directed shortening, extension of the orogen core, and dextral transtension in the Yukon Tanana Terrane (Mair et al., 2006; M. Grimshaw, personal communication, September 04, 2020) that occurred as a result of spreading between the Kula and Pacific plates at circa 85 Ma. Spreading was associated with north-directed subduction of the Kula Plate along the Aleutian Trench, oblique convergence with the more southerly portion of the North American margin (Woods and Davies, 1982; Engebretson et al., 1985), and relative south-directed movement of the North American continent (Hildebrand, 2013). Extension

of the orogen core and dextral transtension produced orogen-parallel, NW-striking, dextral strike-slip faults, such as the Big Creek Fault (Sánchez et al., 2014), and orogen-orthogonal, NE-striking sinistral strike-slip faults, such as the Dip Creek and Sixtymile-Pika faults (Sánchez et al., 2013) in the Yukon Tanana Terrane.

Post-Ag-Pb-Zn-mineralisation, D_3 deformation is characterised by brittle structural elements that include linear, commonly laterally continuous, SE- to locally south-striking, steep SW- to NE-dipping faults. D_3 faults commonly show dextral strike-slip to dextral-normal oblique-slip kinematics, are unmineralised, and offset Ag-Pb-Zn-mineralised veins by up to approximately 100 to 150 metres. Strain analysis indicates a shallow to subhorizontal, north-plunging shortening direction, and a shallow to subhorizontal, west-plunging extension direction.

D_3 dextral strike-slip was associated with development of the Cenozoic, orogen-parallel faults, and in particular the Tintina Fault that occurs approximately 100 km WSW of the district.

8.2 Structural Controls and Timing of Ag-Pb-Zn-Mineralisation

Ag-Pb-Zn-mineralisation occurred coevally with D_2 fault propagation, and mineralisation is primarily controlled by the complex interplay between fault geometry and orientation, and the rheological contrast between varying rock types in the district. Veins thicken

when subordinate (2^{nd} or 3^{rd} order) faults strike approximately NNE to NE and are orientated approximately subparallel to the (local) D_2 shortening direction and sub-perpendicular to the (local) D_2 extension direction. Ag-Pb-Zn-mineralisation is preferentially hosted in thick, competent quartzite units of the Basal Quartzite member of the Keno Hill Quartzite. F_1 fold and thrust repetition likely thickened units prior to D_2 fault propagation and provided a locally larger volume of preferential host rock that focussed brittle deformation and localised economic Ag-Pb-Zn deposits. Two generations of pre-D_2, near coaxial, tight to isoclinal folding (F_{1a} and F_{1b}) potentially locally thickened stratigraphic units by a factor of four.

Cessation of D_1-associated greenschist metamorphism occurred at circa 104 to 100 Ma (Mair et al., 2006). $^{40}Ar/^{39}Ar$ (sericite) geochronological data from D_2 vein selvages or within D_2-vein associated breccia show two sets of dates at circa 81 to 78 Ma and circa 69 Ma, respectively. These ages are substantially younger than the age of metamorphism and as such either micas grew during D_2 deformation, or their geochronometers were completely reset during D_2 deformation. The 81 to 78 Ma age is thought to reflect mica growth during the Ag-Pb-Zn-mineralising event, and the circa 69 Ma age represents a subsequent hydrothermal overprinting event during further deformation.

Previous studies have associated Ag-Pb-Zn-mineralisation at the Keno Hill district with emplacement of the Tombstone age (92.8 ± 0.5 Ma) Roop Lake stock (Lynch, 2006; 2010). This does not correlate with ages obtained in this thesis or ages obtained by previous authors (Wanless et al., 1967; Sinclair et al., 1980; Hantelmann, 2013).

Available geochronological data for the Selwyn Basin indicates that the 81 to 78 Ma age for Ag-Pb-Zn-mineralisation in the Keno Hill district occurred during a regional lull in magmatism and as such does not appear to correlate with any known major magmatic event. Sporadic Ag-Pb-Zn-mineralisation coeval intrusions have been recorded in the Selwyn Basin, including a granitic sill (83 ± 5 Ma; Wanless et al., 1967) on Mount Haldane, approximately 20 km west of the study area. However, while temporally and spatially similar, no definitive causal link between the Mount Haldane intrusion and Ag-Pb-Zn-mineralisation at Keno Hill has been established, and as such this correlation should be treated with caution.

The circa 69 Ma age retrieved from sample K-ON-003 in the Onek deposit is considered to represent hydrothermal resetting of the $^{40}Ar/^{39}Ar$ sericite geochronometer. As with the 81 to 78 Ma age of initial mica growth, it is not immediately clear with what magmatic episode, if any, this hydrothermal event is associated. A McQuesten suite cooling age of 67.0 ± 0.4 Ma ($^{40}Ar/^{39}Ar$ biotite; Rasmussen, 2013) and a crystallisation age of 67.3 ± 0.4 Ma (U-Pb zircon; Murphy, 1997) may indicate heat generated by early stage McQuesten plutonism was responsible for the hydrothermal alteration observed at Keno Hill. The circa 69 Ma hydrothermal alteration age is temporally coincident with widespread Carmacks volcanism-associated hydrothermal alteration and remagnetisation of rocks in SW Yukon (Johnston et al., 1996b; Wynne et al., 1998; YGS, 2020a). However, remnants of Carmacks volcanism have not been recorded in the Selwyn Basin, and as such no causal link between Carmacks volcanism and hydrothermal alteration at Keno Hill can be reached.

Regional- to district-scale interpretation of airborne magnetic data indicates that the Keno Hill district is located within a macro-scale left-stepping, releasing bend of a sinistral strike-slip fault system associated with D_2 fault propagation and Ag-Pb-Zn-mineralisation. Palinspastic restoration of circa 430 kilometers of offset along the Cenozoic (Eocene) Tintina Fault (as per Gabrielse et al., 2006) aligns the Keno Hill fault system with a sub-parallel fault system SW of the Tintina Fault in Alaska. Numerous, left-stepping, releasing bends are evident in airborne magnetic data along the strike of the fault system in Alaska that indicate kinematic equivalence. In addition, lithological similarities are observed. This suggests that the structural and lithological controls on Ag-Pb-Zn-mineralisation present at the Keno Hill district are present along the length of the palinspastically restored structure, and that similar, as yet undiscovered deposits are present along the structure.

Palinspastic restoration of airborne magnetic data indicates the presence of a through-going ENE-trending, D_2 fault-subparallel, magnetic lineament of at least 435 to 450 km in length. The magnetic lineament is coincident with sub-parallel gravity and topographic lineaments that extend east of the Selwyn Basin margin, across Mackenzie Platform rocks, and possibly into cratonic rocks of North America. The lineament is thought to be at least 840 km in length. The extension of the gravity lineament into cratonic North America rocks, suggests that the Keno Hill fault system (and D_2 fault movement) may be associated with a large-scale zone of weakness inherited from an underlying Precambrian fault zone. The world class Fort Knox (IRGS) deposit, along with numerous historic

mines, current mines, or advanced exploration projects (e.g., Scheelite Dome, Dublin Gulch, and Rackla) are aligned along the same (palinspastically restored) lineament as the world class Keno Hill district. Ages of mineralisation differ between projects from the Tombstone related Fort Knox and Dublin Gulch, to the 81 to 78 Ma Keno Hill deposit, to the Tertiary Rackla deposit. This suggests that the lineament has a long history of movement. The depth of emplacement of the Fort Knox deposit and presence of associated lamprophyres at Keno Hill suggests that the structure is crustal-scale. The spatial coincidence of the interpreted lineament with the northern limit of the (D_1-associated) Tombstone strain zone suggests that the lineament may have focussed both D_1 and D_2 deformation.

The results of this thesis raise numerous questions that should be investigated to further advance the understanding of the evolution of the Selwyn Basin and the Northern Cordillera. The possibility of a deep-seated Precambrian structure that controls regional-scale localisation of Mesozoic mineralisation in the northern Selwyn Basin, and equivalent rocks of Alaska is suggested in this thesis. Evidence for this feature is largely based on regional-scale gravity data, and the correlation between the results of this study and that of Gabrielse et al. (2006) that indicate approximately 430 km of Cenozoic dextral offset along the Tintina Fault. As previously stated in this thesis, an inherent problem with mineral exploration in the northern Cordillera is that geophysical surveys in the Cordillera are commonly acquired perpendicular to the regional, orogen-parallel fabric, and as such limit the ability to accurately identify orogen-orthogonal, or orogen-oblique structures. A series magnetic or gravity geophysical surveys perpendicular to the

strike of the postulated structure would help to delineate its extent. The surveys should be acquired with approximately NW-oriented flight lines. Subsequent inversion of the geophysical data would help to define the depth extent of the structure. Similarly, a series of NW-oriented, 2D seismic profiles across the structure would help to define its depth extent and geometry, confirm its presence, and clarify its importance in controlling mineralisation in the overlying basinal or accreted terranes.

The Selwyn Basin-equivalent rocks present SW of the Tintina Fault in Alaska are generally considered to be underexplored. Geological mapping in eastern Alaska is commonly less detailed that in equivalent areas in Yukon, and correlation between terranes across the Yukon-Alaska border appears outdated. Similarly, available geophysical surveys are commonly of coarser resolution in Alaska than in Yukon. The potential for economic-scale Au or Ag mineralisation within rocks SW of the restored Tintina Fault is considered to be high, and has been documented in this thesis, particularly in an area WSW of the city of Central, AK. Updated geological mapping and geophysical surveys should help delineate additional prospective areas and confirm correlation between units in the Selwyn Basin and those mapped in Alaska.

The age of emplacement of metamafic (greenstone) sills in the Keno Hill district is generally assumed to be early Late Triassic (Murphy, 1997), although this is based on a single U-Pb (baddeleyite) age of similar rocks in the Ogilvie Mountain range (Mortensen and Thompson, 1990). Metamafic rocks in the Keno Hill district have been observed to contain metamict zircon and rare baddeleyite. U-Pb dating of one sample containing

baddeleyite was attempted during this study, however, no age was recovered. A systematic study of metamafic units in the Keno Hill district may provide dateable samples, and as such would clarify their temporal relationship with similar rocks in the Selwyn Basin. In addition, petrographic study of metamafic units across the Keno Hill district showed the presence of abundant, deformed titanite. A geochronological study of deformed titanite in these units may provide additional confidence in the age of metamorphism within the district.

Further geochronological studies should be completed to assess the age of D_2 fault movements in the Keno Hill district. This study has defined an age of between 81 and 78 Ma for D_2 fault movement and the associated Ag-Pb-Zn-mineralisation event, although the sample size is recognised to be small, and the quality of the recovered data is variable. Re-Os studies of sulfides present at Keno Hill would provide better resolution on the age of mineralisation. It is understood that Alexco is in the process of commissioning a U-Pb study into the age of calcite within D_2 fault zones. While the application of the U-Pb technique to calcite is currently in its infancy, this has the potential to add substantial weight to the data acquired during this thesis and historically (Wanless et al., 1967; Sinclair et al., 1980; Hantelmann, 2013). The rare occurrence of bladed calcite associated with D_2 faults was documented in this thesis, and the association between bladed calcite and flash boiling of fault-associated fluids suggests that U-Pb (calcite) geochronology has the potential to provide a definitive age for D_2 fault dilation and associated mineralisation.

The heat source responsible for driving Ag-Pb-Zn-mineralisation at Keno Hill remains unknown. The 81 to 78 Ma age for mineralisation proposed by this study does not correlate with previous hypotheses that the source of heat was derived from the Roop Lakes stock (Lynch, 1986, 2006; 2010), nor does it correlate with any other known major magmatic events in the Selwyn Basin. The presence of a similar aged granitic sill on Mount Haldane (Wanless et al., 1967) is intriguing, although the age of this sill, and its proposed association with Tombstone intrusive suite should be treated with caution. An updated geochronological study of this sill, and any additional granitic sills proximal to the Keno Hill district should be completed to confirm a temporal relationship between granite emplacement and Ag-Pb-Zn mineralisation event at Keno Hill. Furthermore, a U-Th-He geochronological study should provide details on rates of differential uplift and may provide insight into the source of the geothermal gradient responsible for Ag-Pb-Zn mineralisation.

Bibliography

Abbott, J. G., 1990, Geological Map of Mt. Westman map area (106D/1): Exploration and Geological Services Division, Yukon, Indian and Northern Affairs Canada, Open File 1990-1, 1 sheet.

Abbott, J. G., 1997, Geology of the Upper Hart River Area, Eastern Ogilvie Mountains, Yukon Territory (116A/10, 116A/11): Exploration and Geological Services Division, Yukon, Indian and Northern Affairs Canada, Bulletin 9, 92 p.

Abbott, J. G., Gordey, S. P., and Tempelman-Kluit, D. J., 1986, Setting of stratiform, sediment hosted lead-zinc deposits in Yukon and northeastern British Columbia, in Morin, J. A., ed., Mineral Deposits of Northern Cordillera, Special Volume 37: Canadian Institute of Mining and Metallurgy, p. 1-18.

Abbott, J. G., and Turner, R. J., 1990, Character and paleotectonic setting of Devonian stratiform sediment-hosted Zn-Ph-Ba deposits, Macmillan Fold Belt, Yukon, in Abbott, J. G., and Turner, R. J., eds., Mineral Deposits of the Northern Cordillera, Yukon, northeastern British Columbia. Guidebook for Field Trip 14, Open File 2169: Geological Survey of Canada, p. 99-136.

Aho, A. E., 1949, Mineralogy of some heavy sands of the McQuesten River area, Yukon: unpublished BSc thesis, University of British Columbia, 48 p.

Alexco Resource Corporation (Alexco), 2021, NI 43-101 Technical report on updated mineral resource and reserve estimate of the Keno Hill silver district: unpublished report, 403 p.

Allmendinger, R. W., Cardozo, N., and Fisher, D. M., 2012, Structural Geology Algorithms: Vectors and Tensors: Cambridge University Press, 302 p.

Allmendinger, R. W., Gephart, J. W., and Marrett, R. A., 1989, Notes on Fault Slip Analysis: "Quantitative Interpretation of Joints and Faults". Cornell University, Ithaca, New York, Geological Society of America Workshop, 56 p.

Alsop, G. I., and Holdsworth, R. E., 2002, The geometry and kinematics of flow pertubation folds: Tectonophysics, v. 350, p. 99-125.

Beck, M. E., 1991, Case for northward transport of Baja and coastal southern California: Paleomagnetic data, analysis, and alternatives: Geology, v. 19, p. 506-509.

Beck, M. E., Burmester, R. F., and Schoonover, R., 1981, Paleomagnetism and tectonics of the Cretaceous Mt. Stuart Batholith of Washington: translation or tilt?: Earth and Planetary Science Letters, v. 56, p. 336-342.

Beck, M. E., and Noson, L., 1972, Anomalous palaeolatitudes in Cretaceous granitic rocks: Nature Physical Science, v. 235, p. 11-13.

Berman, R. G., Ryan, J.J., Gordey, S.P., and Villeneuve, M., 2007, Permian to Cretaceous polymetamorphic evolution of the Stewart River region, Yukon-Tanana

terrane, Yukon: P-T-t evolution linked with in situ SHRIMP monazite geochronology: Journal of Metamorphic Geology, v. 25, p. 803–827.

Blusson, S. L., 1978, Geologic setting of lead-zinc deposits in Selwyn Basin, Yukon, in Current Research, Part A: Geological Survey of Canada Paper 78-1A, p. 77-80.

Bogue, S. W., and Grommé, C. S., 2004, Structural correction of paleomagnetic vectors dispersed about two fold axes and application to the Duke Island (Alaska) ultramafic complex: Journal of Geophysical Research: Solid Earth, v. 109, p 1-13.

Bogue, S. W., Grommé, S., and Hillhouse, J. W., 1995, Paleomagnetism, magnetic anisotropy, and mid-Cretaceous paleolatitude of the Duke Island (Alaska) ultramafic complex: Tectonics, v. 14, p. 1133-1152.

Booysen, R., Gloaguen, R., Lorenz, S., Zimmermann, R., and Nex, P., 2021, Geological remote sensing, in Alderton, D., and Elias, S., eds., Encyclopedia of Geology, 2nd edition, v. 6, p. 301-314.

Boyle, R. W., 1965, Geology, geochemistry, and origin of the lead-zinc-silver deposits of the Keno Hill - Galena Hill area, Yukon Territory (with short descriptions of the tin, tungsten, and gold deposits): Geological Survey of Canada, Bulletin 111, 161 p.

Brass, G. W., Mattes, B. W., Reid, R. P., and Whitman, J. M., 1983, Mesozoic interaction of the Kula plate and the western margin of North America: Tectonophysics, v. 99, p. 231-239.

Breitsprecher, K., and Mortensen, J. K., 2004, Yukonage 2004: A database of isotopic age determinations for rock units from Yukon Territory, Canada: Yukon Geological Survey, Microsoft AccessTM database.

Brown, C. M., Oliver, N., and Dickens, G., 2004, Veins and hydrothermal fluid flow in the Mt. Whaleback Iron Ore District, eastern Hamersley Province, Western Australia: Precambrian Research, v. 128, p. 441-474.

Brown, D., and McClay, K., 1994, Structural geology of the Vangorda Pb-Zn-Ag orebody, Yukon, Canada: Ore Geology Reviews, v. 9, p. 61 - 78.

Butler, R. F., Gehrels, G. E., and Bazard, D. R., 1997, Paleomagnetism of Paleozoic strata of the Alexander Terrane, southeastern Alaska: GSA Bulletin, v. 109, p. 1372-1388.

Butler, R. F., Gehrels, G. E., and Kodama, K. P., 2001, A modern translation alternative to the Baja British Columbia Hypothesis: GSA Today, v. 11, p. 4-10.

Campbell, R. B., 1967, Reconnaissance Geology of Glenlyon map area, Yukon Territory (105L); Geological Survey of Canada Memoir 352, Geological Survey of Canada, 92 p.

Carreras, J., and Druguet, E., 2019, Complex fold patterns developed by progressive deformation: Journal of Structural Geology, v. 125, p. 195-201.

Carreras, J., Druguet, E., and Griera, A., 2005, Shear zone-related folds: Journal of Structural Geology, v. 27, p. 1229-1251.

Cathro, R. J., 2006, Great Mining Camps of Canada 1: The History and Geology of the Keno Hill Silver Camp, Yukon Territory: Geoscience Canada, v. 33, p. 103-134.

Cawood, P. A., Kröner, A., Collins, W. J., Kusky, T. M., Mooney, W. D., and Windley, B. F., 2009, Accretionary orogens through Earth history: Geological Society, London, Special Publications, v. 318, p. 1-36.

Cecile, M. P., Morrow, D. W., and Williams, G. K., 1997, Early Paleozoic (Cambrian to Early Devonian) tectonic framework, Canadian Cordillera: Bulletin of Canadian Petroleum Geology, v. 45, p. 54-74.

Chamberlain, V. E., and Lambert, R. S. J., 1985, Cordilleria, a newly defined Canadian microcontinent: Nature, v. 314, p. 707-713.

Clift, P. D., Pavlis, T., DeBari, S. M., Draut, A. E., Rioux, M., and Kelemen, P. B., 2005, Subduction erosion of the Jurassic Talkeetna-Bonanza arc and the Mesozoic accretionary tectonics of western North America: Geology, v. 33, p. 881-884.

Colpron, M., Israel, S., Murphy, D. C., Pigage, L. C., and Moynihan, D., 2016, Yukon bedrock geology map, Yukon Geological Survey.

Colpron, M., Logan, J., and Mortensen, J.K., 2002, U-Pb zircon age constraint for late Neoproterozoic rifting and initiation of the lower Paleozoic passive margin of western Laurentia: Canadian Journal of Earth Sciences, v. 39, p. 133–143

Colpron, M., Moynihan, D., Israel, S., and Abbott, J. G., 2013, Bedrock geology of the Rackla belt, east-central Yukon (106C/1-4, 106D/1): Yukon Geological Survey, Open File 2013-13, 1:50,000 scale.

Colpron, M., and Nelson, J. L., 2011, A Digital Atlas of Terranes for the Northern Cordillera: British Columbia Ministry of Energy and Mines, BCGS GeoFile 2011-11.

Colpron, M., Nelson, J. L., and Murphy, D. C., 2007, Northern Cordilleran terranes and their interactions through time: GSA Today, v. 17, p. 4-10.

Cowan, D. S., Brandon, M. T., and Garver, J. I., 1997, Geological tests of hypotheses for large coastwise displacements; a critique illustrated by the Baja British Columbia controversy: American Journal of Science, v. 297, p. 117-173.

Cox, K. G., Bell, J. D. & Pankhurst, R. J., 1979, The interpretation of igneous rocks: George Allen & Unwin, London, 450 p.

Craw, D., Begbie, M., and MacKenzie, D., 2006, Structural controls on Tertiary orogenic gold mineralization during initiation of a mountain belt, New Zealand: Mineral Deposita, v. 41, p. 645-659.

Creaser, R. A., Goodwin-Bell, J. S., and Erdmer, P., 1999, Geochemical and Nd isotopic constrains for the origin of eclogite protoliths, northern Canadian Cordillera: Implications for the Paleozoic tectonic evolution of the Yukon-Tanana terrane: Canadian Journal of Earth Sciences, v. 36, p. 1697–1709.

Crowley, J., Schoene, B., and Bowring, S., 2007, U-Pb dating of zircon in the Bishop Tuff at the millennial scale: Geology, v. 35, p. 1123-1126.

Dalrymple, R. W., and Narbonne, G. M., 1996, Continental slope sedimentation in the Sheepbed Formation (Neoproterozoic, Windermere Supergroup), Mackenzie Mountains, N.W.T: Canadian Journal of Earth Sciences, v. 33, p. 848-862.

Davidson, C., Rosenberg, C., and Schmid, S. M., 1996, Synmagmatic folding of the base of the Bergell pluton, central Alps: Tectonophysics, v. 265, p. 213-238.

Davis, W. J., Pinet, N., Petts, D. C., Jackson, S. J., and Mercier-Langevin, P., 2019, U-Pb ages of hydrothermal calcite associated with Carlin-type gold mineralization, Nadeleen trend, north Central Yukon: GAC-MAC-IAH abstract, Quebec City, Quebec, Canada, 2019.

de la Roche, H., Leterrier, J., Grandclaude, P., and Marchal, M., 1980, A classification of volcanic and plutonic rocks using R1-R2 -diagram and major-element analyses; its relationships with current nomenclature: Chemical Geology, vol. 29, p. 183-210.

Deer, R. A., Howie, R. A., and Zussman, J., 1997, Rock Forming Minerals, Volume 2B, Double-Chain Silicates: The Geological Society, 759 p.

Dickinson, W. R., 2001, Tectonic setting of the Great Basin through geologic time: implications for metallogeny, in Shaddrick, D. R., Zbinden, E., Mathewson, D. C., and Prenn, C., eds., Regional Tectonics and Structural Control of Ore: The Major Gold Trends of Northern Nevada, 33: Geological Society of Nevada, p. 27-53.

Dickinson, W. R., 2004, Evolution of the North American Cordillera: Annual Review of Earth and Planetary Sciences, v. 32, p. 13-45.

Driver, L. A., Creaser, R. A., Chacko, T., and Erdmer, P., 2000, Petrogenesis of the Cretaceous Cassiar batholith, Yukon–British Columbia, Canada: Implications for magmatism in the North American Cordilleran Interior: GSA Bulletin, v. 112, p. 1119-1133.

Druguet, E., 2019, Deciphering the presence of axial-planar veins in tectonites: Geoscience Frontiers, v. 10, p. 2101-2115.

Dusel-Bacon, C., Lanphere, M. A., Sharp, W. D., Layer, P. W., and Hansen, V. L., 2002, Mesozoic thermal history and timing of structural events for the Yukon–Tanana Upland, east-central Alaska: $^{40}Ar/^{39}Ar$ data from metamorphic and plutonic rocks: Canadian Journal of Earth Sciences, v. 39, p. 1013–1015.

Edelman, N., 1973, Tension cracks parallel with the axial plane: Bulletin of the Geological Society of Finland, v. 45, p. 61-65.

Eisbacher, G. H., 1976, Sedimentology of the Dezadeash flysch and its implications for strike-slip faulting along the Denali Fault, Yukon Territory and Alaska: Canadian Journal of Earth Sciences, v. 13, p. 1495-1513.

Engebretson, D. C., Cox, A., and Gordon, R. G., 1985, Relative motions between oceanic and continental plates in the Pacific Basin: Geological Society of America Special Papers, v. 206, p. 1-60.

Enkin, R. J., 2006, Paleomagnetism and the case for Baja British Columbia, in Haggart, J. W., Enkin, R. J., and Monger, J. W. H., eds., Paleogeography of the North American Cordillera: Evidence For and Against Large-Scale Displacements: Geological Association of Canada, Special Paper 46, p. 233-253.

Enkin, R. J., Johnston, S. T., Larson, K. P., and Baker, J., 2006a, Paleomagnetism of the 70 Ma Carmacks Group at Solitary Mountain, Yukon, confirms and extends controversial results: Further evidence for the Baja British Columbia model, in Haggart, J. W., Enkin, R. J., and Monger, J. W. H., eds., Paleogeography of the North American Cordillera: Evidence for and against Large-Scale Displacements: Geological Association of Canada, Special Paper 46, p. 221–232.

Enkin, R. J., Mahoney, J. B., and Baker, J., 2006b, Paleomagnetic signature of the Silverquick/Powell Creek succession, south-central British Columbia: Reaffirmation of Late Cretaceous large-scale terrane translation, in Haggart, J. W., Enkin, R. J., and Monger, J. W. H., eds., Paleogeography of the North American Cordillera: Evidence for and Against Large-Scale Displacements: Geological Association of Canada Special Paper 46, p. 201-220.

Etoh, J., Izawa, E., Watanabe, K., Taguchi, S., and Sekine, R., 2002, Bladed quartz and its relationship to gold mineralization in the Hishikari Low-Sulfidation Epithermal Gold Deposit, Japan: Economic Geology, v. 97, p. 1841-1851.

Evenchick, C. A., McMechan, M. E., McNicoll, V. J., Carr, S. D., Sears, J. W., Harms, T. A., and Evenchick, C. A., 2007, A synthesis of the Jurassic–Cretaceous tectonic evolution of the central and southeastern Canadian Cordillera: Exploring links across the orogen, whence the mountains? Inquiries into the evolution of orogenic systems: A volume in honor of Raymond A. Price: Geological Society of America Bulletin, v. 433, p. 117-145.

Faure, G., and Mensing, T. M., 2005, Isotopes: principles and applications: John Wiley & Sons Inc., 897 p.

Feenstra, A., and Franz, G., 2015, Regional Metamorphism: Reference Module in Earth Systems and Environmental Sciences, Elsevier, p.407-413.

Fernandes, N. A., Gleeson, S. A., Magnall, J. M., Creaser, R. A., Martel, E., Fischer, B. J., and Sharp, R., 2017, The origin of Late Devonian (Frasnian) stratiform and stratabound mudstone-hosted barite in the Selwyn Basin, Northwest Territories, Canada: Marine and Petroleum Geology, v. 85, p. 1-15.

Fingler, J., 2005, Technical report on the McQuesten Property, Mayo mining district, Yukon Territory, Canada, NTS 105M/13 for Alexco Resources Corporation: Alexco Prospectus, 86 p.

Follo, M. F., 1992, Conglomerates as clues to the sedimentary and tectonic evolution of a suspect terrane: Wallowa Mountains, Oregon: GSA Bulletin, v. 104, p. 1561-1576.

Fossen, H., Cavalcante, G. C. G., Pinheiro, R. V. L., and Archanjo, C. J., 2019, Deformation – progressive or multiphase?: Journal of Structural Geology, v. 125, p. 82-99.

Fossen, H., Teyssier, C., and Whitney, D.L., 2013, Transtensional folding: Journal of Structural Geology, v. 56, p. 89-102.

Foster, H. L., Laird, J., Keith, T. E. C., Cushing, G. W., and Menzies, W. D., 1983, Preliminary geologic map of the Circle quadrangle, Alaska: Menlo Park, California, United States Department of Interior Geological Survey.

Friend, M.A., Allan, M.M., and Hart, C.J.R., 2017, New contributions to the bedrock geology of the Mount Freegold district, Dawson Range, Yukon (NTS 115I/2, 6 and 7), *in* MacFarlane, K.E., ed., Yukon Exploration and Geology 2017: Whitehorse, Yukon Geological Survey, p. 47–68.

Fritz, W. H., Cecile, M. P., Norford, B. S., Morrow, D. W., and Geldsetzer, H. H. J., 1991, Cambrian to Middle Devonian assemblages, in Gabrielse, H., and Yorath, C. J., eds., Geology of the Cordilleran orogen in Canada: Geological Survey of Canada, Decade of North American Geology 4, p. 151-218.

Fritz, W. H., Narbonne, G. M., and Gordey, S. P., 1983, Strata and trace fossils near the Precambrian-Cambrian boundary, Mackenzie, Selwyn and Wernecke mountains, Yukon and Northwest Territories: Current Research, Part B Paper 83-1B: Geological Survey of Canada, p. 365–375.

Gabrielse, H., 1967, Tectonic evolution of the northern Canadian Cordillera: Canadian Journal of Earth Sciences, v. 4, p. 271-298.

Gabrielse, H., 1985, Major dextral transcurrent displacements along the northern Rocky Mountain Trench and related lineaments in north-central British Columbia: Geological Society of America Bulletin, v. 96, p. 1-14.

Gabrielse, H., Blusson, S. L., and Roddick, J. A., 1973, Geology of Flat River, Glacier Lake, and Wrigley Lake map areas, District of Mackenzie and Yukon Territory: Geological Survey of Canada, Memoir 366, p. 153.

Gabrielse, H., Murphy, D. C., and Mortensen, J. K., 2006, Cretaceous and Cenozoic dextral orogen-parallel displacements, magmatism, and paleogeography, north-central Canadian Cordillera, in Haggart, J. W., Enkin, R. J., and Monger, J. W. H., eds., Paleogeography of the North American Cordillera: Evidence for and Against Large-Scale Displacements: Geological Association of Canada, Special Paper 46, p. 255-276.

Gabrielse, H., and Yorath, C. J., 1991, Tectonic synthesis, Chapter 18, in Gabrielse, H., and Yorath, C. J., eds., Geology of the Cordilleran Orogen in Canada: DNAG Geological Survey of Canada, p. 97–124.

Garzione, C. N., Patchett, P. J., Ross, G. M., and Nelson, J., 1997, Provenance of Paleozoic sedimentary rocks in the Canadian Cordilleran miogeocline: a Nd isotopic study: Canadian Journal of Earth Sciences, v. 34, p. 1603-1618.

Geological Survey of Canada (GSC), 2013, Canadian Geochronology Knowledgebase: Geological Survey of Canada, Earth Science Sector, Natural Resources Canada, https://www.nrcan.gc.ca/maps-tools-publications/tools/geodetic-reference-systems/canadian-geochronology-knowledgebase/18211

Ghosh, S.K., 1993, Structural Geology. Fundamentals and Modern Developments. Pergamon Press, Oxford, 598 p.

Ghosh, S. K., Khan, D., and Sengupta, S., 1995, Interfering folds in constrictional deformation: Journal of Structural Geology, v. 17, p. 1361-1373.

Ghosh, S. K., Mandal, N., Sengupta, S., Deb, S. K., and Khan, D., 1993, Superposed buckling in multilayers: Journal of Structural Geology, v. 15, p. 95–111.

Ghosh, S. K., and Ramberg, H., 1968, Buckling experiments on intersecting fold patterns: Tectonophysics v. 5, p. 89-105.

Ghosh, S. K., and Sengupta, S., 1996, Hinge migration and hinge replacement: Tectonophysics v. 263, p. 319-337.

Gleeson, C. F., and Boyle, R. W., 1980, The lithogeochemistry of the Keno Hill district, Yukon Territory: Geological Survey of Canada, Paper 77-31, 23 p.

Godfrey, N. J. and Dilek, Y., 2000, Mesozoic assimilation of oceanic crust and island arc into the North American continental margin in California and Nevada, in Dilek, Y., Moores, E. M., Elthon, D. and Nicolas, A., eds. Insights from geophysical data in ophiolites and oceanic crust: new insights from field studies and the ocean drilling program: Geological Society of America, Special Paper 349, p. 365-382.

Goldfarb, R. J., Marsh, E. E., Hart, C. J. R., Mair, J. L., Miller, M. L., and Johnson, C., 2007, Geology and origin of epigenetic lode gold deposits, Tintina Gold Province, Alaska and Yukon: Chapter A in Recent U.S. Geological Survey studies in the Tintina Gold Province, Alaska, United States, and Yukon, Canada--results of a 5-year project, in Gough, L. P., and Day, W. C., eds., Scientific Investigations Report: Reston, VA, USGS, 22 p.

Gordey, S. P., 2013, Evolution of the Selwyn Basin region, Sheldon Lake and Tay River map areas, central Yukon: Geological Survey of Canada, Bulletin 599, 190 p.

Gordey, S. P., and Anderson, R. G., 1993, Evolution of the northern Cordilleran miogeocline, Nahanni map area (105I): Yukon and Northwest Territories, Geological Survey of Canada Memoir 428, 214 p.

Grasemann, B., Wiesmayr, G., Draganits, E., and Fusseis, F., 2004, Classification of refold structures: Journal of Geology, v. 112, p. 119-125.

Green, L. H., 1971, Geology of Mayo Lake, Scougale Creek and McQuesten Lake map areas, Yukon Territory (105M/15, 106/D2, 106/D3): Geological Survey of Canada, Memoir 357, 72 p

Green, L. H., and McTaggart, K. C., 1960, Structural studies in the Mayo District, Yukon Territory: Proceedings of the Geological Association of Canada, v. 12, p. 119-134.

Grond, H. C., Churchill, S. J., Armstrong, R. L., Harakal, J. E., and Nixon, G. T., 1984, Late Cretaceous age of the Hutshi, Mount Nansen, and Carmacks groups, southwestern Yukon Territory and northwestern British Columbia: Canadian Journal of Earth Sciences, v. 21, p. 554–558.

Groves, D. I., Goldfarb, R. J., and Santosh, M., 2016, The conjunction of factors that lead to formation of giant gold provinces and deposits in non-arc settings: Geoscience Frontiers, v. 7, p. 303-314.

Grujic, D., 1993, The influence of initial fold geometry on Type 1 and Type 2 interference patterns: an experimental approach: Journal of Structural Geology, v. 15, p. 293-307.

Grujic, D., Walter, T. R., and Gärtner, H., 2002, Shape and structure of (analogue models of) refolded layers: Journal of Structural Geology, v. 24, p. 1313-1326.

Gudmundsson, A., 2001, Fluid overpressure and flow in fault zones: field measurements and models: Tectonophysics, v. 336, p. 183-197.

Guest, B., Matthews, W., Coutts, D. S., Bain, H., and Hubbard, S. M., 2015, Geological evidence that resolves the Baja-BC controversy: detrital zircons indicate that Vancouver Island was adjacent to southern California in the Late Cretaceous: American Geophysical Union 2015, p. T13A-2979.

Haeussler, P. J., Bradley, D. C., Wells, R. E., and Miller, M. L., 2003, Life and death of the Resurrection plate: Evidence for its existence and subduction in the northeastern Pacific in Paleocene–Eocene time: GSA Bulletin, v. 115, p. 867-880.

Hansen, V. L., and Dusel-Bacon, C., 1998, Structural and kinematic evolution of the Yukon-Tanana upland tectonites, east-central Alaska: A record of late Paleozoic to Mesozoic crustal assembly: GSA Bulletin, v. 110, p. 211-230.

Hansen, V. L., 1990, Yukon-Tanana terrane: A partial acquittal: Geology, v. 18, p. 365-369.

Hansen, V. L., Goodge, J. W., Keep, M., and Olive, D. H., 1993, Asymmetric rift interpretation of the western North America margin: Geology, v. 21, p. 1067-1070.

Hansen, V.L., Heizler, M.T., and Harrison, T.M., 1991, Mesozoic thermal evolution of the Yukon-Tanana composite terrane: new evidence from $^{40}Ar/^{39}Ar$ data: Tectonics, v. 10, p. 51-76.

Hantelmann, J. J., 2013, The paragenesis and geochemistry of the Bellekeno Ag-Pb-Zn vein, Keno Hill district, Yukon, Canada, unpublished MSc thesis, University of Alberta, 81 p.

Hart, C. J. R., 2004, Mid-Cretaceous Magmatic Evolution and Intrusion-Related Metallogeny of the Tintina Gold Province, Yukon and Alaska: unpublished PhD thesis, University of Western Australia, 198 p.

Hart, C. J. R., 2007, Reduced intrusion-related gold systems, in Goodfellow, W. D., ed., Mineral deposits of Canada: a synthesis of major deposit types, district

metallogeny, the evolution of geological provinces, and exploration methods Special Publication No. 5, Geological Association of Canada, Mineral Deposits Division, p. 95-112.

Hart, C. J. R., Baker, T., and Burke, M. J., 2000, New exploration concepts for country-rock-hosted intrusion-related gold systems: Tintina Gold Belt in Yukon. The Tintina Gold Belt: Concepts, Exploration, and Discoveries: British Columbia and Yukon Chamber of Mines, Special Volume 2, p. 145–171.

Hart, C. J. R., Goldfarb, R. J., Lewis, L. L., and Mair, J. L., 2004a, The Northern Cordilleran Mid-Cretaceous Plutonic Province: Ilmenite/Magnetite-series Granitoids and Intrusion-related Mineralisation: Resource Geology, v. 54, p. 253-280.

Hart, C. J. R., Mair, J. L., Goldfarb, R. J., and Groves, D. I., 2004b, Source and redox controls on metallogenic variations in intrusion-related ore systems, Tombstone-Tungsten Belt, Yukon Territory, Canada: Earth and Environmental Science Transactions of the Royal Society of Edinburgh, v. 95, p. 339-356.

Hart, C. J. R., McCoy, D. T., Goldfarb, R. J., Smith, M., Roberts, P., Hulstein, R., Bakke, A. A., Bundtzen, T. K., Goldfarb, R. J., and Nielsen, R. L., 2002, Geology, Exploration, and Discovery in the Tintina Gold Province, Alaska and Yukon, in Goldfarb, R.J., and Nielsen, R.L., eds., Integrated Methods for Discovery, Global Exploration in the Twenty-First Century, Special Publication 9, Society of Economic Geologists, p. 241-274.

Haskin, M. L., Enkin, R. J., Mahoney, J. B., Mustard, P. S., and Baker, J., 2003, Deciphering shallow paleomagnetic inclinations: Implications from correlation of Albian volcanic rocks along the Insular/Intermontane Superterrane boundary in the southern Canadian Cordillera: Journal of Geophysical Research: Solid Earth, v. 108, p 1-18.

Hayward, N., 2015, Geophysical investigation and reconstruction of lithospheric structure and its control on geology, structure, and mineralization in the Cordillera of northern Canada and eastern Alaska: Tectonics, v. 34, p. 2165-2189.

Hayward, N., 2019, The 3D Geophysical Investigation of a Middle Cretaceous to Paleocene Regional Décollement in the Cordillera of Northern Canada and Alaska: Tectonics, v. 38, p. 307-334.

Hayward, N., and Paradis, S., 2021, Geophysical reassessment of the role of ancient lineaments on the development of the western Laurentian margin and its sediment hosted Pb-Zn deposits, Yukon and Northwest Territories, Canada: Canadian Journal of Earth Sciences, v. 58, p. 1283-1300.

Heffernan, R. S., 2004. Temporal, geochemical, isotopic, and metallogenic studies of “mid”-Cretaceous magmatism in the Tintina Gold Province, southeastern Yukon and southwestern Northwest Territories, Canada: unpublished PhD thesis, University of British Columbia, Vancouver, 83p.

Heffernan, S., and Mortensen, J. K., 2000, Age, geochemical and metallogenic investigations of Cretaceous intrusions in southeastern Yukon and southwestern NWT: A preliminary report, in Emond, D. S., and Weston, L. H., eds., Yukon Exploration and Geology 1999: Exploration and Geological Services Division, Yukon, Indian and Northern Affairs Canada, p. 145–149.

Hildebrand, R. S., 2015, Dismemberment and northward migration of the Cordilleran orogen: Baja-BC resolved: GSA Today, v. 25, p. 4-11.

Housen, B. A., and Beck, J. M. E., 1999, Testing terrane transport: An inclusive approach to the Baja B.C. controversy: Geology, v. 27, p. 1143-1146.

Housen, B. A., Beck Jr, M. E., Burmester, R. F., Fawcett, T., Petro, G., Sargent, R., Addis, K., Curtis, K., Ladd, J., Liner, N., Molitor, B., Montgomery, T., Mynatt, I., Palmer, B., Tucker, D., and White, I., 2003, Paleomagnetism of the Mount Stuart batholith revisited again: What has been learned since 1972?: American Journal of Science, v. 303, p. 263-299.

Hunt, P. A., and Roddick, J. C., 1987, Radiogenic age and isotopic studies: report 1: Geological Survey of Canada, Paper no. 87-2, p. 143-210.

Ingersoll, R.V., 2000, Models for origin and emplacement of Jurassic ophiolites of Northern California, in Dilek, Y., Moores, E. M., Elthon, D. and Nicolas, A., eds. Insights from geophysical data in ophiolites and oceanic crust: new insights from field studies and the ocean drilling program: Geological Society of America. Special Paper 349: p. 395-402.

Irvine, T. N., and Baragar, W. R. A., 1971. A guide to the chemical classification of the common volcanic rocks: Canadian Journal of Earth Sciences, vol. 8, p. 523-548.

Irving, E., 1985, Tectonics: Whence British Columbia?: Nature, v. 314, p. 673-674.

Irving, E., Thorkelson, D. J., Wheadon, P. M., and Enkin, R. J., 1995, Paleomagnetism of the Spences Bridge Group and northward displacement of the Intermontane Belt, British Columbia: A second look: Journal of Geophysical Research: Solid Earth, v. 100, p. 6057-6071.

Irving, E., Wynne, P. J., Thorkelson, D. J., and Schiarizza, P., 1996, Large (1000 to 4000 km) northward movements of tectonic domains in the northern Cordillera, 83 to 45 Ma: Journal of Geophysical Research: Solid Earth, v. 101, p. 17901-17916.

Jaffey, A. H., Flynn, K. F., Glendenin, L. E., Bentley, W. C., and Essling, A. M., 1971, Precision Measurement of Half-Lives and Specific Activities of 235U and 238U: Physical Review C, v. 4, p. 1889-1906.

Jobin, D. M., Véronneau, M., and Miles, W., 2017, Gravity anomaly map, Canada / Carte des anomalies gravimétriques, Canada, in Geological Survey of Canada, Open File 8081: Natural Resources Canada, p. 1 sheet.

Johnston, S. T., 1999, Large-scale coast-parallel displacements in the Cordillera: a granitic resolution to a paleomagnetic dilemma: Journal of Structural Geology, v. 21, p. 1103-1108.

Johnston, S. T., Mortensen, J. K., and Erdmer, P., 1996a, Igneous and metaigneous age constraints on the Aishihik metamorphic suite, SW Yukon: Canadian Journal of Earth Sciences, v. 33, p. 1543-1555.

Johnston, S. T., Wynne, P. J., Francis, D., Hart, C. J. R., Enkin, R. J., and Engebretson, D. C., 1996b, Yellowstone in Yukon: The Late Cretaceous Carmacks Group: Geology, v. 24, p. 997-1000.

Jones, D. L., Silberling, N. J., and Hillhouse, J., 1977, Wrangellia—A displaced terrane in northwestern North America: Canadian Journal of Earth Sciences, v. 14, p. 2565-2577.

Jones, R. R., Holdsworth, R. E., Clegg, P., McCaffrey, K., and Travarnelli, E., 2004, Inclined transpression: Journal of Structural Geology, v. 26, p. 1531-1548.

Joyce, N. L., Ryan, J. J., Colpron, M., Hart, C. J. R., and Murphy, D. C., 2015, A compilation of $^{40}Ar/^{39}Ar$ age determinations for igneous and metamorphic rocks, and mineral occurrences from central and southeast Yukon: Geological Survey of Canada, Open File 7924, 229 p.

Kania, E. A., 1926, Origin and paragenesis of the silver-lead ores of the Mayo District, Yukon Territory. Unpublished thesis, University of British Columbia.

Kerr, R. A., 1995, How far did the west wander?: Science, v. 268, p. 635-637.

Kim, B., and Kodama, K. P., 2004, A compaction correction for the paleomagnetism of the Nanaimo Group sedimentary rocks: Implications for the Baja British Columbia hypothesis: Journal of Geophysical Research: Solid Earth, v. 109, p 1-17.

King, P. B., 1987, Cordilleran orogenic belt, in Structural Geology and Tectonics. Encyclopedia of Earth Science: Springer Berlin Heidelberg, p. 132-141.

Kingston, S. P., 2009, Nature and origin of gold-rich carbonate replacement deposits at the Rau occurrence, central Yukon: unpublished BSc thesis, University of British Columbia, 63 p.

Kingston, S., Mortensen, J. K., Gabites, J., and Dumala, M., 2010, Ar-Ar geochronology and Pb isotopic constraints on the origin of the Rau gold-rich carbonate replacement deposit, central Yukon, in MacFarlane, K. E., Weston, L. H., and Blackburn, L. R., eds., Yukon Exploration and Geology 2009: Yukon Geological Survey, p. 213-222.

Klepacki, D. W., and Wheeler, J. O., 1985, Stratigraphic and structural relations of the Milford, Kaslo and Slocan Groups, Goat Range, Lardeau and Nelson map areas, British Columbia: Geological Survey of Canada, Paper 85-1A, p. 277–286.

Knight, E., Schneider, D.A., and Ryan, J., 2013, Thermochronology of the Yukon-Tanana Terrane, west-central Yukon: Evidence for Jurassic extension and exhumation in the Northern Canadian Cordillera: The Journal of Geology, v. 121, p. 371-400.

Kuran, V. M., Godwin, C. I., and Armstrong, R. L., 1982, Geology and geochronometry of the Scheelite Dome tungsten-bearing skarn property, Yukon: Canadian Institute of Mining and Metallurgy, Bulletin 75, p. 137-142.

Laurent, G., Ailleres, L., Grose, L., Caumon, G., Jessell, M., and Armit, R., 2016, Implicit modeling of folds and overprinting deformation: Earth and Planetary Science Letters, v. 456, p. 26-38.

Leech, G. B., Lowdon, J. A., Stockwell, C. H., and Wanless, R. K., 1963, Age determinations and geological studies (including isotopic ages-report 4): Geological Survey of Canada, Paper no. 63-17, 146 p.

Lowey, G. W., 1998, A new estimate of the amount of displacement on the Denali Fault system based on the occurrence of carbonate megaboulders in the Dezadeash Formation (Jura-Cretaceous), Yukon, and the Nutzotin Mountains Sequence (Jura-Cretaceous), Alaska: Bulletin of Canadian Petroleum Geology, v. 46, p. 379-386.

Lowey, G.W., Sinclair, W.D., and Hills, L.V., 1986, Additional K-Ar isotopic dates for the Carmacks Group (Upper Cretaceous), west central Yukon: Canadian Journal of Earth Sciences, v. 23, p. 1857-1859.

Lund, K., 2008, Geometry of the Neoproterozoic and Paleozoic rift margin of western Laurentia: Implications for mineral deposit settings: Geosphere, v. 4, p. 429–444.

Lynch, J. V. G., 1986, Mineral zoning in the Keno Hill Ag-Pb-Zn mining district, Yukon: Yukon Geology, v. 1, p. 89-97.

Lynch, J. V. G., 1989a, Hydrothermal zoning in the Keno Hill Ag-Pb-Zn vein system: a study in structural geology, mineralogy, fluid inclusions, and stable isotope geochemistry: unpublished PhD thesis, University of Alberta, 218 p.

Lynch, J. V. G., 1989b, Large-scale hydrothermal zoning reflected in the tetrahedrite-freibergite solid solution, Keno Hill Ag-Pb-Zn district, Yukon: Canadian Mineralogist, v. 27, p. 383-400.

Lynch, J. V. G., 2006, Sediment-hosted disseminated gold occurrence, northeast Mayo Lake area, in Esmond, D. S., Bradshaw, G. D., Lewis, L. L., and Weston, L. H., eds., Yukon Exploration and Geology 2005: Whitehorse, Yukon Geological Survey, p. 327-339.

Lynch, J. V. G., 2010, Pressure-depth relationships of the Roop Lakes Stock and Keno Hill Ag-Pb-Zn veins, in MacFarlane, K. E., Weston, L. H., and Blackburn, L. R., eds., Yukon Exploration and Geology 2009: Whitehorse, Yukon Geological Survey, p. 229-235.

Lynch, J. V. G., Longstaffe, F. J., and Nesbitt, B. E., 1990, Stable isotopic and fluid inclusion indications of large-scale hydrothermal paleoflow, boiling, and fluid mixing in the Keno Hill Ag-Pb-Zn district, Yukon Territory, Canada: Geochimica et Cosmochimica Acta, v. 54, p. 1045-1059.

Mahoney, B. J., Enkin, R. J., and Haskin, M. L., 2001, Paleomagnetic Constraints on Terrane Translation: the Churn Creek Succession in South Central British Columbia: American Geophysical Union, Fall Meeting 2001, abstract.

Mahoney, B. J., Mustard, P. S., Haggart, J. W., Friedman, R. M., Fanning, C. M., and McNicoll, V. J., 1999, Archean zircons in Cretaceous strata of the western Canadian Cordillera: The "Baja B.C." hypothesis fails a "crucial test": Geology, v. 27, p. 195-198.

Mair, J. L., Hart, C. J. R., and Stephens, J. R., 2006, Deformation history of the northwestern Selwyn Basin, Yukon, Canada: Implications for orogen evolution and mid-Cretaceous magmatism: Geological Society of America Bulletin, v. 118, p. 304-323.

Marrett, R., and Allmendinger, R. W., 1990, Kinematic analysis of fault-slip data: Journal of Structural Geology, v. 12, p. 973-986.

McCausland, P. J. A., Symons, D. T. A., and Hart, C. J. R., 2005, Rethinking "Yellowstone in Yukon" and Baja British Columbia: Paleomagnetism of the Late Cretaceous Swede Dome stock, northern Canadian Cordillera: Journal of Geophysical Research, v. 110, p 1-13.

McCausland, P. J. A., Symons, D. T. A., Hart, C. J. R., and Blackburn, W. H., 2002, Paleomagnetism and geobarometry of the Granite Mountain batholith, Yukon: Minimal geotectonic motion of the Yukon-Tanana Terrane relative to North America, in Emond, D.S., Weston, L.H., and Lewis, L.L., eds., Yukon exploration and geology 2001: Exploration and Geological Services Division, Yukon, Indian and Northern Affairs Canada, p. 163-177.

McClay, K. R., 1991, Deformation of stratiform Zn-Pb (-barite) deposits in the northern Canadian Cordillera: Ore Geology Reviews, v. 6, p. 435-462.

McClay, K. R., 1989, Inversion of the Kechika Trough, Northeastern British Columbia, Canada, in Cooper, M.A. and Williams, G.D., eds, Inversion Tectonics, Geological Society, London, Special Publications 44, p. 235-257.

McOnie, A. W., and Read, P. B., 2009, Stratigraphy, structure and exploration opportunities, Sourdough, Galena and part of Keno hills, Keno Hill mining camp, central Yukon: Unpublished Alexco Resources Corp Report, 142 p.

McPhar Geosurveys Ltd (McPhar), 2006, Final report on a helicopter-borne geophysical survey, Keno Hills, Yukon: unpublished report, Newmarket, Ontario, 36 p.

McTaggart, K. C., 1960, The geology of Keno and Galena Hills, Yukon Territory: Geological Survey of Canada, Bulletin 58, 36 p.

Meschede, M., 1986, A method of discriminating between different types of mid-ocean ridge basalts and continental tholeiites with the Nb-Zr-Y diagram: Chemical Geology, vol. 56, p. 207-218.

Miall, A. D., 2019, The Paleozoic western craton margin, in Miall, A. D., ed, The sedimentary basins of the United States and Canada, 2nd edition, Elsevier, p. 239-266.

Miall, A. D., and Blakey, R. C., 2019, The Phanerozoic Tectonic and Sedimentary Evolution of North America, in Miall, A. D., ed, The sedimentary basins of the United States and Canada, 2nd edition, Elsevier, p. 1-38.

Mihalynuk, M. G., Erdmer, P., Ghent, E. D., Cordey, F., Archibald, D. A., Friedman, R. M., and Johannson, G. G., 2004, Coherent French Range blueschist: Subduction to exhumation in < 2.5 m.y.?: GSA Bulletin, v. 116, p. 910-922.

Mihalynuk, M. G., Nelson, J., and Diakow, L. J., 1994, Cache Creek terrane entrapment: Oroclinal paradox within the Canadian Cordillera: Tectonics, v. 13, p. 575-595.

Miles, W., and Oneschuk, D., 2016, Magnetic anomaly map, Canada / Carte des anomalies magnétiques, Canada: Geological Survey of Canada, Open File 7799, Natural Resources Canada, 1 sheet.

Miller, I. M., Brandon, M. T., and Hickey, L. J., 2006, Using leaf margin analysis to estimate the mid-Cretaceous (Albian) paleolatitude of the Baja BC block: Earth and Planetary Science Letters, v. 245, p. 95-114.

Moore, T. E., Wallace, W. K., Bird, K. J., Karl, S. M., Mull, C. G., and Dillon, J. T., 1994, Geology of northern Alaska, in Plafker, G., and Berg, H. C., eds., The Geology of Alaska: Geological Society of America, The Geology of North America, v. G-1, p. 49–140.

Mortensen, J. K., Hart, C. J. R., Murphy, D. C., and Heffernan, S., 2000, Temporal evolution of early and mid-Cretaceous magmatism in the Tintina Gold Belt: British Columbia and Yukon Chamber of Mines, p. 49–57.

Mortensen, J. K., and Thompson, R. I., 1990, A U-Pb zircon-baddeleyite age for a differentiated mafic sill in the Ogilvie Mountains, west-central Yukon Territory, Radiogenic age and isotopic studies; Report 3: Geological Survey of Canada Paper 89-02, p. 23-28.

Mottram, C.M., Kellet, D.A., Barresi, T., Zwingmann, H., Friend, M., Todd, A., and Percival, J.B., 2020, Syncing fault rock clocks: direct comparison of U-Pb carbonate and K-Ar illite fault dating methods: Geology, v. 48, p. 1179-1183.

Mullen, E.D., 1983, $MnO/TiO_2/P_2O_5$: a minor element discriminant for basaltic rocks of oceanic environments and its implications for petrogenesis: Earth and Planetary Science Letters, vol. 62, p. 53-62.

Murphy, D. C., 1997, Geology of the McQuesten River Region, Northern McQuesten and Mayo Map Area, Yukon Territory (115P/14, 15, 16; 105M/13, 14): Exploration and Geological Services Division, Indian and Northern Affairs Canada, Bulletin 6, 122 p.

Murphy, D.C., and Heon, D., 1995, Geology and mineral occurrences of the Seattle Creek map area (115P/16), western Selwyn Basin: Yukon Exploration and Geology

1994, Exploration and Geological Services Division, Yukon, Indian and Northern Affairs Canada, p. 59-71.

Murphy, D. C., and Mortensen, J. K., 2003, Late Paleozoic and Mesozoic features constrain displacement on Tintina fault and limit large-scale orogen-parallel displacement in the northern Cordillera (abstract): Geological Association of Canada, Mineral Association of Canada and Society of Economic Geologists, Program with Abstracts, CD-ROM, v. 28, p. 151.

Murphy, D. C., Mortensen, J. K., Piercey, S. J., Orchard, M. J., and Gehrels, G. E., 2006, Mid-Paleozoic to early Mesozoic tectonostratigraphic evolution of Yukon-Tanana and Slide Mountain terranes and affiliated overlap assemblages, Finlayson Lake massive sulphide district, southeastern Yukon, in Colpron, M., and Nelson, J., eds., Paleozoic evolution and metallogeny of pericratonic terranes at the ancient Pacific margin of North America, Canadian and Alaskan Cordillera: GAC Special Paper 45, p. 75-105.

Murphy, D. C., and Roots, C. F., 1992, Geology of Keno Hill Map Area (105M/14): Open File 1992-3, Indian and Northern Affairs Canada, Exploration and Geological Services Division, Yukon Region, 1 sheet.

Narbonne, G. M., and Aitken, J. D., 1995, Neoproterozoic of the Mackenzie Mountains, northwestern Canada: Precambrian Research, v. 73, p. 101-121.

Nelson, J. L., Colpron, M., and Israel, S., 2013, The Cordillera of British Columbia, Yukon, and Alaska: Tectonics and Metallogeny, in Colpron, M., Bissig, T., Rusk, B. G., and Thompson, J. F. H., eds., Tectonics, Metallogeny, and Discovery: The North American Cordillera and Similar Accretionary Settings: Society of Economic Geologists, Special Publication 17, p. 52-109.

Nelson, J., and Friedman, R., 2004, Superimposed Quesnel (late Paleozoic–Jurassic) and Yukon-Tanana (Devonian- Mississippian) arc assemblages, Cassiar Mountains, northern British Columbia: Field, U-Pb, and igneous petrochemical evidence: Canadian Journal of Earth Sciences, v. 41, p. 1201–1235.

Nokleberg, W. J., Bundtzen, T. K., Eremin, R. A., Ratkin, V. V., Dawson, K. M., Shpikerman, V. I., Goryachev, N. A., Byalobzhesky, S. G., Frolov, Y. F., Khanchuk, A. I., Koch, R. D., Monger, J. W. H., Pozdeev, A. I., Rozenblum, I. S., Rodionov, S. M., Parfenov, L. M., Scotese, C. R., and Sidorov, A. A., 2005, Metallogenesis and tectonics of the Russian Far East, Alaska, and the Canadian Cordillera: USGS Professional Paper, 428 p.

Nokleberg, W. J., Parfenov, L. M., Monger, J. W. H., Norton, I. O., Khanchuck, A. I., Stone, D. B., Scotese, C. R., Scholl, D. W., and Fujita, K., 2000, Phanerozoic Tectonic Evolution of the Circum-North Pacific: U.S. Department of the Interior, USGS Professional Paper 1626, 122 p.

Oneschuk, D., Miles, W., Saltus, R., and Hayward, N., 2019, Alaska and Yukon magnetic compilation, residual total magnetic field: Geological Survey of Canada, Open File 7862, Natural Resources Canada, 1 sheet.

Orchard, M. J., 1991, Conodonts, time and terranes: An overview of the biostratigraphic record in the western Canadian Cordillera, in Orchard, M. J., and McCracken, A. D., eds.: Ordovician to Triassic conodont paleontology of the Canadian Cordillera: Geological Survey of Canada, Bulletin 417, p. 1-26.

Otto, B. R., 2010, Structural and stratigraphic analysis of the Calumet-Birmingham vein system: unpublished report for Alexco Resource Corp, 11 p.

Park, R. G., 1969, Structural correlation in metamorphic belts: Tectonophysics, v. 7, p. 323-338.

Pearce, J. A., 1996. A user's guide to basalt discrimination diagrams: Geological Association of Canada, Short Course Notes 12, p. 79-113.

Pearce, J. A., and Cann, J. R., 1973, Tectonic setting of basic volcanic rocks determined using trace element analyses: Earth and Planetary Science Letters, vol. 19, p. 290-300.

Pearce, J. A., and Norry, M. J., 1979, Petrogenetic implications of Ti, Zr, Y, and Nb variations in volcanic rocks: Contributions to Mineralogy and Petrology, vol. 69, p. 33-47.

Pearce, J. A., and Parkinson, I. J., 1993, Trace element models for mantle melting: application to volcanic arc petrogenesis. In: Magmatic processes and plate tectonics, H.M. Pritchard, T. Alabaster, N.B.W. Harris and C.R. Cleary (eds.): Geological Society of London, Special Publication 76, p. 373-403.

Piercey, S. J., Mortensen, J.K., and Creaser, R.A., 2003, Neodymium isotope geochemistry of felsic volcanic and intrusive rocks from the Yukon-Tanana terrane in the Finlayson Lake region, Yukon Canada: Canadian Journal of Earth Sciences, v. 40, p. 77–97.

Pigage, L. C., and Anderson, R. G., 1985, The Anvil plutonic suite, Faro, Yukon Territory: Canadian Journal of Earth Sciences, v. 22, p. 1204-1216.

Poole, W. H., 1965, Mount Haldane (105M/13) and Dublin Gulch (106D/4) map areas: Report of Activities: Geological Survey of Canada Paper 65-1, p. 32-34.

Poulton, T. P., and Tempelman-Kluit, D. J., 1982, Recent discoveries of Jurassic fossils in the Lower Schist Division of central Yukon: Geological Survey of Canada, Paper 82-1 C, p. 91-94.

Price, R. A., 1981, The Cordilleran foreland thrust and fold belt in the southern Canadian Rocky Mountains: Geological Society, London, Special Publications, v. 9, p. 427-448.

Price, R. A., 2004, Some Recurring Themes in Cordilleran Orogenic Evolution: Tectonic Heredity, Tectonic Wedging, and Retrograde Mantle Flow: Program and Abstracts, The LITHOPROBE Celebratory Conference: From Parameters to Processes, Revealing the Evolution of a Continent: Toronto.

Ramsay, J. G., 1962, Interference patterns produced by the superposition of folds of similar types: The Journal of Geology, v. 70, p. 466-481.

Ramsay, J. G., 1967, Folding and fracturing of rocks. McGraw-Hill, New York, 568 p.

Ramsay, J.G., and Huber, M.J., 1987, The techniques of modern structural geology, Volume 2: Folds and fractures, Academic Press, New York, 307 p.

Rasmussen, K. L., 2013, The timing, composition, and petrogenesis of syn- to post-accretionary magmatism in the northern Cordilleran miogeocline, eastern Yukon and southwestern Northwest Territories: unpublished PhD thesis, University of British Columbia, 788 p.

Renne, P. R., Swisher, C. C., Deino, A. L., Karner, D. B., Owens, T. L., and DePaolo, D. J., 1998, Intercalibration of standards, absolute ages and uncertainties in $^{40}Ar/^{39}Ar$ dating: Chemical Geology, v. 145, p. 117-152.

Riddell, J., 2011, Lithostratigraphic and tectonic framework of Jurassic and Cretaceous Intermontane sedimentary basins of south-central British Columbia: Canadian Journal of Earth Sciences, v. 48, p. 870-896.

Robert, F., Poulsen, K. H., and Dubé, B., 1994, Structural Analysis of Lode Gold Deposits in Deformed Terranes: Canada. Geological Survey of Canada, Open File 2850, 145 p.

Roddick, J. A., 1967, Tintina Trench: The Journal of Geology, v. 75, p. 23-33.

Roeske, S. M., Snee, L. W., and Pavlis, T. L., 2003, Dextral-slip reactivation of an arc-forearc boundary during Late Cretaceous–Early Eocene oblique convergence in the northern Cordillera, in Sisson, V. B., Roeske, S. M., and Pavlis, T. L., eds., Geology of a transpressional orogen developed during ridge-trench interaction along the North Pacific margin: Geological Society of America, Special Paper 371, p. 141-169.

Roots, C. F., 1997, Geology of the Mayo Map Area, Yukon Territory (105M): Exploration and Geological Services Division, Indian and Northern Affairs Canada, Bulletin 7, 82 p.

Rosenberg, C.L., Berger, A., and Schmid, S.M., 1995, Observations from the floor of a granitoid pluton: Inferences on the driving force of final emplacement: Geology, v. 23, p. 443-446.

Ross, G. M., 1991, Precambrian basement in the Canadian Cordillera: an introduction: Canadian Journal of Earth Sciences, v. 28, p. 1133-1139.

Ross, G. M., 2002, Evolution of Precambrian continental lithosphere in Western Canada: results from Lithoprobe studies in Alberta and beyond: Canadian Journal of Earth Sciences, v. 39, p. 413-437.

Ross, G.M., Bloch, J.D., and Krouse, H.R., 1995, Neoproterozoic strata of the southern Canadian Cordillera and the isotopic evolution of seawater sulphate: Precambrian Research, v. 73, p. 71–99.

Rusmore, M. E., Bogue, S. W., and Woodsworth, G. J., 2013, Paleogeography of the Insular and Intermontane terranes reconsidered: Evidence from the southern Coast Mountains Batholith, British Columbia: Lithosphere, v. 5, p. 521-536.

Sánchez, M. G., Allan, M. M., Hart, C. J. R., and Mortensen, J. K., 2013, Orogen-perpendicular magnetic segmentation of the western Yukon and eastern Alaska cordilleran hinterland: Implications for structural control of mineralization, in MacFarlane, K. E., Nordling, M. G., and Sack, P. J., eds., Yukon Exploration and Geology 2012: Whitehorse, Yukon Geological Survey, p. 133-146.

Sánchez, M. G., Allan, M. M., Hart, C. J. R., and Mortensen, J. K., 2014, Extracting ore-deposit-controlling structures from aeromagnetic, gravimetric, topographic, and regional geologic data in western Yukon and eastern Alaska: Interpretation, v. 2, p. SJ75-SJ102.

Schmitz, M. D., and Schoene, B., 2007, Derivation of isotope ratios, errors, and error correlations for U-Pb geochronology using ^{205}Pb-^{235}U-(^{233}U)-spiked isotope dilution thermal ionization mass spectrometric data: Geochemistry, Geophysics, Geosystems, v. 8, p 1-20.

Shand, S.J., 1943, Eruptive rocks, their genesis, composition, classification, and their relation to ore deposits, 2nd Edition. John Wiley & Sons, New York, 444 p.

Siddorn, J. P., Williams, P. R., Isles, D. J., and Rankin, L. R., 2020, Integrated geologic-geophysical interpretation of district-scale structural frameworks: systematic approaches for targeting mineralizing systems: Reviews in Economic Geology, v. 21, p. 271-313.

Simpson, R. G., Fingler, J., Stammers, M., and Dodd, S., 2007, Annual Information Form: Alexco Resource Corporation., 80 p.

Sinclair, A. J., Tessari, O. J., and Harakal, J. E., 1980, Age of Ag-Pb-Zn mineralization, Keno Hill - Galena Hill area, Yukon Territory: Canadian Journal of Earth Sciences, v. 17, p. 1100-1103.

Skelton, A., Lewerentz, A., Kleine, B., Webster, D., and Pitcairn, I., 2015, Structural channelling of metamorphic fluids on Islay, Scotland: implications for paleoclimatic reconstruction: Journal of Petrology, v. 56, p. 2145-2172.

Spear, F. S., 1993, Metamorphic phase equilibria and pressure-temperature-time paths: Mineralogical Society of America, Monograph 1, 799 pp.

Steiger, R. H., and Jäger, E., 1977, Subcommission on geochronology: Convention on the use of decay constants in geo- and cosmochronology: Earth and Planetary Science Letters, v. 36, p. 359-362.

Štemprok, M., and Seifert, T., 2011, An overview of the association between lamprophyric intrusions and rare-metal mineralization: Mineralogia, v. 42, p. 121-162.

Stephens, J. R., 2003, Structural, mechanical and P-T evolution of intrusion-related gold mineralization at clear Creek and Dublin Gulch, Yukon, Canada: unpublished PhD thesis, James Cook University of North Queensland, 237 p.

Stevens, R. D., Delabio, R. N., and Lachance, G. R., 1982a, Age determinations and geological studies K-Ar isotopic ages, report 15: Geological Survey of Canada, Paper no. 81-2, 56 p.

Stevens, R. D., Lachance, G. R., and Delabio, R. N., 1982b, Age determinations and geological studies K-Ar isotopic ages, report 16: Geological Survey of Canada, Paper no. 82-2, 56 p.

Tempelman-Kluit, D. J., 1966, The stratigraphy and structure of "Keno Hill Quartzite" in the Tombstone area, central Yukon: unpublished PhD thesis, McGill University, 162 p.

Tempelman-Kluit, D. J., 1970, Stratigraphy and structure of the Keno Hill quartzite in Tombstone River-Upper Klondike River map areas, Yukon Territory (1168/7, B/8): Geological Survey of Canada, Bulletin 180, 102 p.

Tessari, O. J., 1979, Model ages and applied whole rock geochemistry of Ag-Pb-Zn veins, Keno Hill - Galena Hill mining camp: unpublished MSc thesis, University of British Columbia, 151 p.

The Earth Resources Research and Analysis Facility (TERRA), 2019, XRF instrument: Memorial University, https://www.mun.ca/creait/TERRA/XRF_Instrument_cs.php, accessed 24/08/20.

Thiessen, R. L., and Means, W. D., 1980, Classification of fold interference patterns: a re-examination: Journal of Structural Geology, v. 2, p. 311-326.

Thompson, J. F. H., Sillitoe, R. H., Baker, T., Lang, J. R., and Mortensen, J. K., 1999, Intrusion-related gold deposits associated with tungsten-tin provinces: Mineralium Deposita, v. 34, p. 323-334.

Tupper, D., and Bennett, V., 2010, Observations of polymetallic Ag-Pb-Zn (± Au ± In) mineralization at the Eagle and Fisher vein-faults, airborne total field magnetics and identification of Tombstone age-equivalent aplite dykes in the Galena Hill area, Keno City, Yukon, in MacFarlane, K. E., Weston, L. H., and Blackburn, L. R., eds., Yukon Exploration and Geology 2009: Yukon Geological Survey, p. 305-330.

Turner, E. C., Roots, C. F., MacNaughton, R. B., Long, D. G. F., Fischer, B. J., Gordey, S. P., Martel, E., and Pope, M. C., 2011, Chapter 3. Stratigraphy: NWT Geoscience Office, NWT Special Volume 1, p. 31–192.

Turner, F. J., and Weiss, L. E., 1963, Structural analysis of metamorphic tectonites. McGraw-Hill, New York, 560 p.

United States Geological Survey (USGS), 2020, National Geochronological Database: United States Geological Survey, https://mrdata.usgs.gov/geochron/, accessed 13/7/2020.

van Staal, C. R., 2007, Pre-Carboniferous tectonic evolution and metallogeny of the Canadian Appalachians, in Goodfellow, W. D., ed., Mineral Deposits of Canada: A synthesis of major deposit-types, district metallogeny, the evolution of geological provinces, and exploration methods, Special Publication No. 5: Geological Association of Canada, Mineral Deposits Division, p. 793-818.

Villeneuve, M.E., Ryan, J.J., Gordey, S.P., and Piercey, S.J., 2003, Detailed thermal and provenance history of the Stewart River area (Yukon-Tanana terrane, western Yukon) through application of SHRIMP, Ar-Ar and TIMS [abs]: Geological Association of Canada/Mineralogical Association of Canada, Abstracts, v. 28, p. 344.

Wanless, R. K., Stevens, R. D., Lachance, G. R., and Edmonds, C. M., 1967, Age determinations and geological studies K-Ar Isotopic ages, report 7: Geological Survey of Canada, Paper 66-17, 120 p.

Ward, P. D., Hurtado, J. M., Kirschvink, J. L., and Verosub, K. L., 1997, Measurements of the Cretaceous Paleolatitude of Vancouver Island: Consistent with the Baja-British Columbia Hypothesis: Science, v. 277, p. 1642-1645.

Weber, F. R., Wheeler, K. L., Rinehart, C. D., Chapman, R. M., and Blodgett, R. B., 1992, Geologic map of the Livengood Quadrangle, Alaska: USGS Open-File Report 92-562, 19 p.

White, J. D. L., White, D. L., Vallier, T., Stanley, G. D., Jr., and Ash, S. R., 1992, Middle Jurassic strata link Wallowa, Olds Ferry, and Izee terranes in the accreted Blue Mountains island arc, northeastern Oregon: Geology, v. 20, p. 729-732.

Whitten, E.H.T., 1966, Structural Geology of Folded Rocks. Rand McNally & Company, Chicago, 663 p.

Wilson, F. H., Hults, C. P., Mull, C. G., and Karl, S. M., 2015, Geologic map of Alaska, U.S. Geological Survey Scientific Investigations Map 3340, pamphlet 196 p., 2 sheets, scale 1:1,584,000.

Wiltse, M. A., Reger, R. D., Newberry, R. J., Pessel, G. H., Pinney, D. S., Robinson, M. S., and Solie, D. N., 1995, Geological map of the Circle mining district, Alaska: Alaska Division of Geological & Geophysical Surveys, Alaska Division of Geological & Geophysical Surveys Report of Investigation 95-2A, 1 sheet, scale 1:63,360.

Winchester, J.A., and Floyd, P.A., 1977, Geochemical discrimination of different magma series and their differentiation products using immobile elements: Chemical Geology, vol. 20, p. 325-343.

Winchester, J.A., Park, R.G., and Holland, J.G., 1980, The geochemistry of Lewisian semipelitic schists from the Gairloch District, Wester Ross: Scottish Journal of Geology, vol. 16, p. 165-179.

Wooley, A. R., Bergman, S. C., Edgar, A. D., Le Bas, M. J., Mitchell, R. H., Rock, N. M. S., and Scott Smith, B. H., 1996, Classification of lamprophyres, lamprolites,

kimberlites, and the kalsilitic, melilitic, and leucocratic rocks: recommendations of the International Union of Geological Sciences (IUGS), Subcommission on the Systematics of Igneous Rocks: The Canadian Mineralogist, v. 34, p. 175-186.

Wynne, P. J., Enkin, R. J., Baker, J., Johnston, S. T., and Hart, C. J. R., 1998, The big flush: paleomagnetic signature of a 70 Ma regional hydrothermal event in displaced rocks of the northern Canadian Cordillera: Canadian Journal of Earth Sciences, v. 35, p. 657-671.

Wynne, P. J., Irving, E., Maxson, J. A., and Kleinspehn, K. L., 1995, Paleomagnetism of the Upper Cretaceous strata of Mount Tatlow: Evidence for 3000 km of northward displacement of the eastern Coast Belt, British Columbia: Journal of Geophysical Research: Solid Earth, v. 100, p. 6073-6091.

Yukon Geological Survey (YGS), 2020a, Yukon Geochronology - A database of Yukon isotopic age determinations: Yukon Geological Survey, http://data.geology.gov.yk.ca/Compilation/22, accessed 15/09/2020.

Yukon Geological Survey (YGS), 2020b, Yukon MINFILE – A database of mineral occurrences: Yukon Geological Survey, http://data.geology.gov.yk.ca/Compilation/24, accessed 2/10/2020.

Zajac, I., 1957, No 6 Vein, Keno Hill, Yukon Territory: unpublished BSc thesis, University of British Columbia, 43 p.

Appendix

Appendices A to F are available as separate digital files.

Curriculum Vitae

Simon David Craggs

Universities Attended

2008 - 2022
University of New Brunswick, Fredericton, New Brunswick
Department of Earth Sciences
Ph.D. Earth Sciences
Supervisors: Dr. D.R. Lentz, University of New Brunswick; Dr. J.C. White, University of New Brunswick
Thesis Title: Structural geological controls and timing of Ag-Pb-Zn Mineralisation at the Keno Hill deposit, Yukon

2004 - 2008
University of New Brunswick, Fredericton, New Brunswick
Department of Earth Sciences
M.Sc. Earth Sciences
Supervisors: Dr. J.G. Spray, University of New Brunswick
Thesis Title: The structural control and tectonic evolution of the Campbellton region, northern New Brunswick, Canada.

1998-2004
University of Leeds, Leeds, UK
Department of Earth Sciences
B.Sc. (Hons) Geological Sciences

Professional Experience

2011 – 2022
SRK Consulting (Canada) Inc.
Senior Consultant – Structural Geology
Structural geology, and deposit- to regional-scale geological mapping in variably deformed terranes in North America, South America, Europe, West Africa, and Australia. Analysis and interpretation of remote sensing data. 3D modelling of fault/fracture networks. Target generation for greenfield and brownfield exploration, and mining projects. Project management and technical collaboration on exploration and mining projects for epithermal vein-type, porphyry, orogenic, and VMS Au, Ag, and base metal deposits, and geotechnical studies for underground and open pit mines.

2011
Bearing Resources Ltd.
Consultant Structural Geologist

Structural and lithological mapping and analysis of the Upper Hyland River area, southeast Yukon, Canada.

2007 – 2008
Royal Holloway University of London, Fault Dynamics Research Group
Post-Graduate Research Assistant
Development of content for the STAR (STructural Analogues for Reservoirs) website and atlases.

Publications:

Craggs, S.D., Keighley, D., Waldron, W.F., and Park, A. 2017. Salt tectonics in an intracontinental transform setting: Cumberland and Sackville basins, southern New Brunswick, Canada. Basin Research, 29: 266-283

Conference Presentations:

Craggs, S.D. 2016. Structural evolution of the Keno Hill mining district. Margins Through Time GAC-MAC, Whitehorse, Yukon, Canada.

Craggs, S.D., Keighley, D., Park, A., and Waldron, W.F. 2013. Stratigraphy and salt tectonics of Mississippian–Pennsylvanian strata of the northern Cumberland Basin, Maringouin Peninsula, southeastern New Brunswick. Atlantic Geoscience, Antigonish, Nova Scotia, Canada.

Craggs, S.D., Lentz, D.R., and White, J.C. 2011. Structural evolution of the Keno Hill Ag-Pb-Zn mining district, Yukon. AMEBC Roundup, Vancouver, BC, Canada.

Craggs, S.D. 2010. Polyphase deformation and vein/fracture geometry in the Keno Hill Ag-Pb-Zn mining district. Yukon Geoscience Forum, Whitehorse, Yukon, Canada.

Craggs, S.D., and Lentz, D.R. 2010. Petrographic, geochemical, and pseudochemostratigraphic analysis of metamafic intrusions in the Keno Hill Ag-Pb-Zn mining district, Yukon, Canada. Yukon Geoscience Forum, Whitehorse, Yukon, Canada.

Craggs, S.D., Lentz, D.R., and White, J.C. 2010. Polyphase folding in the Keno Hill Ag-Pb-Zn mining district, Yukon, Canada. GAC-MAC Joint Annual Meeting, Calgary, Alberta, Canada.

Craggs, S.D., and Lentz, D.R. 2009. A petrological, geochemical and chemostratigraphic analysis of metamafic intrusions in the Keno Hill Ag-Pb-Zn mining district, central Yukon. Yukon Geoscience Forum, Whitehorse, Yukon, Canada.

Craggs, S.D., Dutka, R., Roberts, M, and Lentz, D.R. 2008. The structure and tectonics of the Keno Hill mining district: Proposed work and preliminary observations. Yukon Geoscience Forum, Whitehorse, Yukon, Canada.

Craggs, S.D. 2007. The structural control and tectonic evolution of the Restigouche Syncline, northern New Brunswick, Canada. Geological Society of London, Thames Valley Regional Group, Egham, Surrey, UK.

Craggs, S.D. and Spray, J.G. 2005. Transcurrent Faulting in the Squaw Cap Tectonic Block of the Restigouche Syncline, Campbellton Region, northern New Brunswick. Canadian Tectonics Group workshop, Orillia, Ontario, Canada.